Modification of Zeolites with Self-Assembled Monolayers for Gas Separation

by

Xinpei Zhou

B.S., University of Maryland College Park, 2019

M.S., University of Colorado Boulder, 2021

A thesis submitted to the

Faculty of the Graduate School of the

University of Colorado in partial fulfillment

of the requirements for the degree of

Doctor of Philosophy

Department of Chemical and Biological Engineering

2024

Committee Members:

J. Will Medlin (Chair)

John L. Falconer

Adam Holewinski

Kayla Sprenger

John Pellegrino

Zhou, Xinpei (Ph.D., Chemical Engineering)

Modification of Zeolites with Self-Assembled Monolayers for Gas Separation

Thesis directed by Prof. J. Will Medlin

Abstract

Gas separation processes are important for major industries, such as oil refining, chemical manufacturing, energy production, and environmental engineering. Adsorptive separation is an energy-efficient alternative to traditional distillation. Understanding adsorption mechanisms is essential for the rational design of high-performance adsorbents for gas separation. Surface modification with self-assembled monolayers (SAMs) is an attractive approach to tune material properties because it enables precise control over film thickness at a molecular scale. In this thesis, zeolites were modified with organic phosphonic acids (PAs) to improve gas adsorption selectivity and the structure-function relationships of adsorbents for selective adsorption was investigated. First, the adsorption rates of C_3H_6 and C_3H_8 on zeolite 5A were controlled by varying the properties of PAs, such as ligand chain length and steric configuration. Based on single-gas, pressure-decay adsorption measurements, the PA coatings enhanced the kinetic selectivity of C_3H_6/C_3H_8 by adding diffusion barriers on the zeolite surface. Next, mixture adsorption was measured to investigate the competitive adsorption between C_3H_6 and C_3H_8. On uncoated 5A, C_3H_6 displaced adsorbed C_3H_8 at high gas exposures because C_3H_6 had stronger affinity for the zeolite than C_3H_8; the C_3H_6/C_3H_8 mixture selectivity measured from mixture adsorption was higher than the ideal selectivity from single-

gas adsorption. With an *n*-octadecylphosphonic acid (ODPA) coating, the mixture selectivity was higher than uncoated 5A at low gas exposures, but the selectivity did not improve as rapidly with exposure time. The performances of adsorbents were affected by both barriers to gas diffusion and competition for adsorption sites between adsorbates. Finally, varying the PA functional group (amine or carboxylic acid) and coating density was employed to further tune the structure of coating layer and gas adsorption rates. At low coating densities, the amine group of PA forms a hydrogen bond with the hydroxyl group on the zeolite surface, resulting in high resistance to gas diffusion. The adsorption rates on the zeolite 5A coated with 3-aminopropylphosphonic acid (NH_2C_3PA) varied drastically with coating density compared with ODPA coating. The results provide insight into the design of adsorbents by providing gas-specific resistance for gas adsorptive separation.

Dedication

This work is dedicated to my beloved parents, for their love, support, and encouragement.

Acknowledgments

I would like to sincerely thank my advisor, Will Medlin, for his support and guidance throughout my PhD. Thanks for giving me the opportunity to work on research projects that I am truly interested in. Whenever I needed feedback or suggestions, Will always made himself available and patiently discussed every research idea with me. I have learned a lot, and every step that I have taken in my research could not have been achieved without his mentorship. I would like to thank Professor John Falconer, who contributed to almost every idea in the projects that I have worked on. His passion and attitude towards research have inspired me a lot. I would also like to thank the other committee members: Kayla Sprenger, Adam Holewinski, and John Pellegrino, for their genuine interest in my research and valuable insights and suggestions.

I would like to thank the current and former members of the Medlin group. I truly enjoyed working with them and I appreciate all the help I have received. I would specifically like to thank Alex Jenkins, Mat Rasmussen, and Jiajie Huo for their great mentorship. Special thanks to my cohort: Laura Paz Herrera, Ezra Baghdady, and Zachary Blanchette, for being alongside me; the time we have spent together is a valuable memory to me. I would also like to thank my friend Gesse Roure for all the support.

This work was made possible by the support of the National Science Foundation [grant CBET 1916738].

Finally, I would like to thank my family, Mom and Dad. Thanks for supporting me to study abroad in the U.S. Your encouragement and understanding always meant a lot to me.

Contents

List of Tables

List of Figures

Chapter 1: Introduction

1.1. Gas separation methods

Light olefins, such as ethylene and propylene, are important raw materials for the production of chemicals and polymers [1,2]. They are mainly produced by steam cracking of naphtha, fluid catalytic cracking of gas oils in refineries, catalytic alkane dehydrogenation processes, and methanol-to-olefins reactions [3]. From those processes, other hydrocarbon byproducts such as paraffins and alkynes are produced. Further separation of the mixtures is needed to obtain "polymer-grade" light olefins (minimum purity of 99.5%) for the manufacture of polymers. The separations of olefins and paraffins, such as propylene and propane, have traditionally been carried out by distillation. Due to the similar boiling points of olefins and paraffins with the same number of carbon atoms, their separation usually requires distillation towers with 150–200 stages, temperature of 183–233 K, pressure of 16–20 bar, and high reflux [4,5], which makes it energy-intensive. Chemical separations have been reported to account for 10%–15% of the total energy consumption in the United States, and distillation consumes about half of the energy in chemical separation [2]. Therefore, developing alternative energy-efficient separation processes is highly desired.

Some alternative separation processes have been developed, such as adsorption [6–8], absorption [9,10], and membrane separation [4,11–14], as illustrated in Fig. 1.1. In absorption-based separation, certain components are preferentially transported into the bulk adsorbent phase, while the remaining

components become enriched in the gas phase. Membrane-based separation is a continuous separation process, which is based on the difference in permeability of different components across the membranes, and the permeation rate of gas molecules is determined by the pore size and the chemical properties of porous materials [15]. Adsorption separation is based on the differences in gas uptakes in adsorbents.

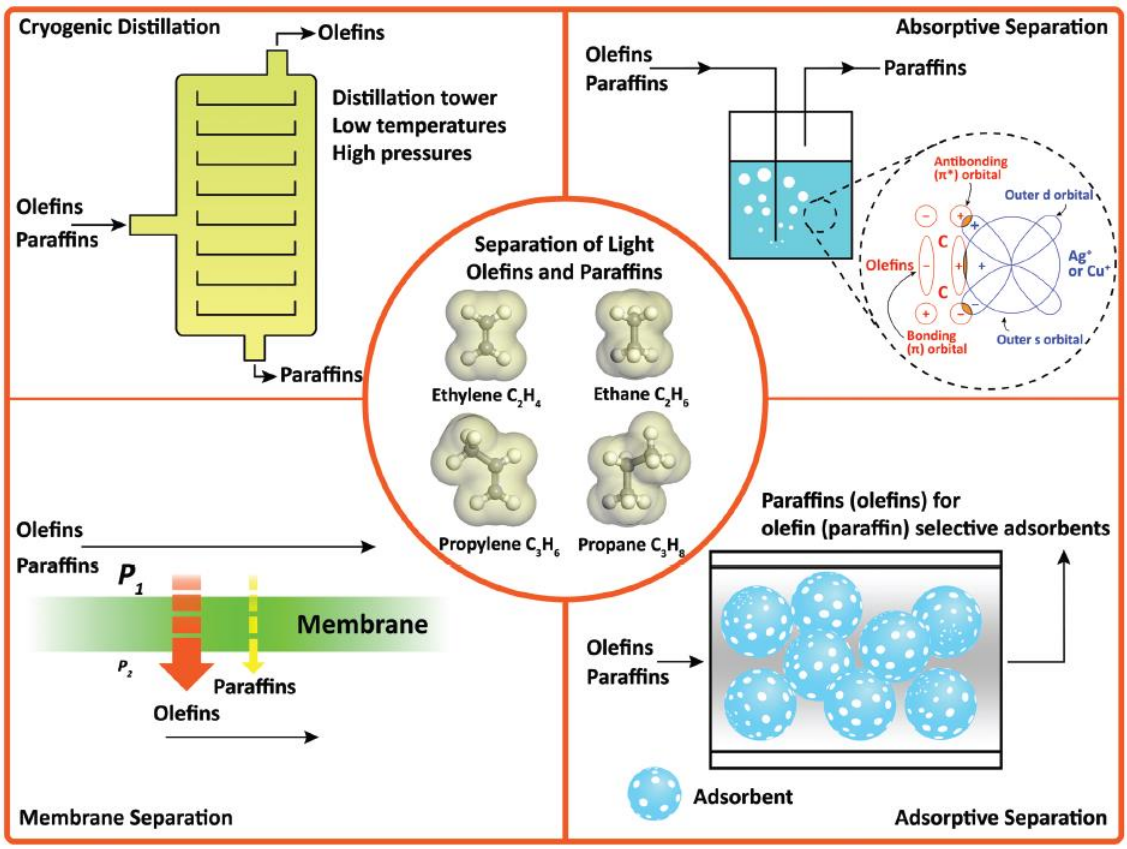

Figure 1.1. A schematic comparison of different processes of light olefin/paraffin separations. Adapted from Bai et. al [16].

1.2. Gas adsorptive separation

Among alternative separation technologies to energy-intensive distillation, adsorptive separation has advantages of low energy consumption and capital cost, easy precursor accessibility, and a facile sorbent regeneration process. In an article

entitled “Seven Chemical Separations to Change the World”, Lively and Sholl listed “alkenes from alkanes”, “greenhouse gases from dilute emission”, and “benzene derivatives from each other” as being separations that can be achieved via adsorption [2].

Adsorption is a surface phenomenon and is defined as the enrichment in the concentration of molecules, atoms, or ions present in a fluid phase in the vicinity of an interface [17]. In the case of a solid-gas system, this interface is the surface of the solid. Molecules that are adsorbable are *adsorptive*; adsorbed molecules are called the *adsorbate*; solid materials for adsorption are called *adsorbent*. The opposite process of adsorption is desorption in which molecules leave the solid surface and go back to the fluid phase. The key to adsorptive separation is to develop advanced adsorbents with high adsorption capacity, high selectivity, good stability, and easy regeneration with low energy input to desorb gas molecules from adsorbents. In industry, a packed bed is commonly used for adsorption, where one component is preferentially adsorbed while the other component breaks through.

1.2.1. Adsorbents

Various adsorbents have been studied for gas adsorptive separation, such as carbons, polymers, zeolites, zeolitic imidazolate frameworks (ZIFs), and metal organic frameworks (MOFs). Among those materials, zeolites have been widely used as adsorbents because they have well-defined pores, high surface area, and high chemical, thermal, and mechanical stabilities [18].

Zeolites are crystalline microporous aluminosilicates with a rigid framework consisting of TO_4 tetrahedra, where T are typically Si or Al, connected by a shared oxygen atom. There are many types of natural and synthetic zeolites, with over 200 zeolite structures that have been recognized by the International Zeolite Association-Structure Commission [19]. Although many structures of zeolites exist, further modification, i.e., post-synthetic treatment, is useful to achieve the desired properties. The modification of zeolites for gas adsorptive separation needs to consider not only the separation selectivity, but also adsorption capacity, adsorption/desorption kinetics, adsorbent regeneration, stability and durability, and cost. In this thesis, LTA-type zeolite 5A was selected for the adsorptive separation of C_3H_6 and C_3H_8 because the pore window of zeolite 5A is ~5 Å, close to the kinetic diameters of C_3H_6 and C_3H_8, 4.31 Å and 4.46 Å, respectively [20].

1.2.2. Adsorption performance measurement methods

Industrial gas adsorption processes employ a technology known as swing adsorption, which involves cycling the adsorbent bed under varying operations conditions, leading to pressure-swing adsorption (PSA), vacuum-swing adsorption (VSA) or temperature-swing adsorption (TSA). PSA involves adsorbing the adsorbates at high pressure, followed by desorption at low pressure, while maintaining a relatively constant temperature at atmospheric levels. VSA is a variation of PSA that operates under vacuum instead of at varying levels of positive pressure. TSA involves selective adsorption of adsorbates onto the adsorbents at low

temperature and subsequently desorbing them at high temperature, with the pressure maintained constant throughout the process.

Many techniques have been developed to evaluate the gas separation performance of adsorbents. Single-component adsorption isotherm measurements are used to obtain the relationship between adsorption loading and gas pressure at a constant temperature, providing metrics such as adsorption capacity, ideal selectivity, and isosteric heat of adsorption, which are important for equilibrium-based separation. Single-gas, pressure-decay adsorption measurements track the change of gas pressure over adsorption time, which can be used to determine adsorption rates, diffusivity, and ideal selectivity, thus providing insights into kinetic separation and diffusion mechanisms. Breakthrough measurements are usually carried out in a fixed-bed column combined with mass spectrometry or gas-chromatography to record adsorbate concentration in the effluent as a function of time. These measurements determine breakthrough times (the points when adsorbate concentrations exceed a specific threshold) and selectivity of mixture adsorption, and thereby help understand the interactions between adsorbates and adsorbents and provide important parameters for the design of separation process.

In an adsorptive separation process, the difference in interactions of gas components with adsorbent surfaces can affect mixture adsorption selectivity, which may be quite different from ideal selectivity measured with single-gas adsorption. The displacement of an adsorbed adsorbate by another adsorbate that has stronger interaction with the adsorbent has been observed in mixture adsorption; this results

in higher mixture selectivity than ideal selectivity [21–23]. Moreover, the enrichment of one component due to its preferential adsorption over other components facilitates the increase of mixture selectivity with adsorption time [16]. The work described in Chapter 3 investigated the competitive adsorption between C_3H_6 and C_3H_8 and discussed the effects of surface coating layers on mixture adsorption.

1.2.3. Adsorptive separation mechanisms

Adsorptive separation mechanisms can be divided into four main categories: equilibrium, kinetic, molecular sieving, and "trapdoor" effect [16,24,25], as illustrated in Fig. 1.2.

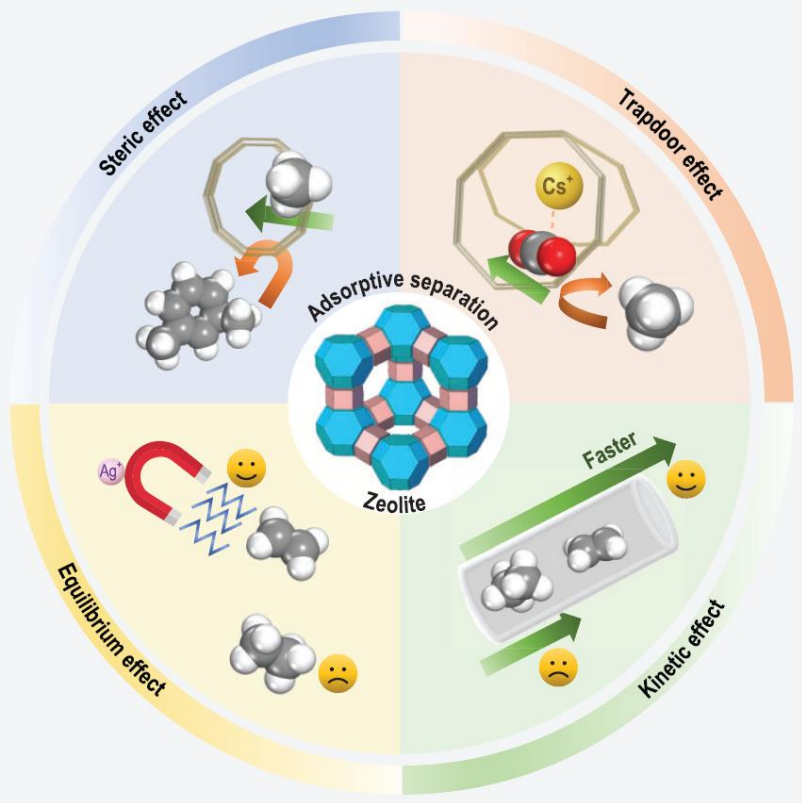

Figure 1.2. Schematic illustration of the adsorptive separation mechanism by zeolites. Adapted from Bai et. al [16].

Equilibrium separation is based on the interaction between the adsorbate and the adsorbent, in which molecules having stronger interactions with the adsorbent are preferentially adsorbed, resulting in selectivity of preferentially adsorbed molecules over less preferentially adsorbed molecules. In equilibrium separation for olefin/paraffin mixtures, the adsorbents generally have stronger affinity towards olefins than paraffins. Cation exchange with Li^+ [26], Cs^+ [27], Ca^{2+} [28], and Ba^{2+} [29] has been used to improve olefin/paraffin separation by changing the interactions between gases and the zeolites or tuning the pore sizes. Transition metals, such as Co(II) [30], Fe(II) [31], and Cu(II) [23] present in adsorbents, can form π-complexation with olefin or alkyne to improve selectivity. Moreover, the presence of double bonds in hexene-covalent triazine framework (CTF) promotes the adsorption of olefins or alkynes due to strong pi-pi interactions [32]. Hydrogen-bonded organic framework (HOF) with free -COOH sites can selectively adsorb olefins [33].

Kinetic separation is based on the differences in the diffusion rates of different molecules. Porous materials, such as zeolites [34–37], carbon materials CMS [38,39], and MOFs [40–42], with suitable aperture windows or pore channels have been utilized [36–38] for olefin/paraffin separation. The kinetic separation process is generally more energy-efficient than equilibrium separation for recovering olefins from adsorbents due to the absence of strong interactions, and it has less serious problems of gas diffusion and adsorbent regeneration in steric separation with strong restriction of the pore structures [40]. The adsorption selectivity of kinetic separation can be improved by tuning the pore structures of adsorbents.

Molecular sieve separations can be regarded as an extreme example of kinetic selectivity in which only small and properly shaped molecules can be diffused into the pores of adsorbents, whereas other components are excluded, resulting in the potential for near-perfect selectivity. To utilize the sieving effect, adsorbents, such as zeolites 4A and SAPO-14 [43], MOF materials KAUST-7 [44] and Y-abtc [3], with precisely controlled rigid pore structures have been used for C_3H_6/C_3H_8 separation. Dynamic molecular sieving materials with flexible gate-openings, such as MOF material JNU-3a, result in high selectivity [45]. Moreover, HOF material HOF-FJU-1 achieves high selectivity and gas capacity benefited from highly discriminating gating effect under elevated temperatures [46]. Although molecular sieve separations yield high selectivity, the diffusion rates are usually slow due to the restricted pores. The design of large local sieving channels in adsorbents, such as ZU-609, enables fast gas diffusion with high selectivity [47].

The "trapdoor" effect is based on a difference in ability of a guest molecule to induce temporary and reversible displacement of cations from the center of pore apertures; the molecules having strong interaction with the cations enter the pore, while other molecules are excluded. This effect has been used for CHA type zeolite with K^+, Rb^+ or Cs^+ ions, resulting in high selectivity of CO_2/CH_4 and CO/N_2 [48].

1.3. Surface modification of adsorbents

Many surface modification techniques have been developed to tune the pore windows of adsorbents and surface properties to enhance adsorptive separation

selectivity. One approach is to modify adsorbent surfaces with an additional diffusion layer, such as silica [49] and silane [50,51] coatings on zeolites. Functional groups, such as amine for binding acids [52], has been utilized to modify zeolites. Moreover, the pore openings of adsorbents can be tuned with a thin coating layer on the surface using a combination of molecular and atomic layer deposition methods, such as TiO_2 on zeolite 5A [53].

Self-assembled monolayers (SAMs) are an attractive surface modification technique to tune the properties of materials for applications in CO_2 capture, gas separation, heterogenous catalysis, and sensing. SAMs are thin organic films that form spontaneously on solid surfaces [54]. The SAM structure is represented in Fig. 1.3. A SAM ligand consists of three parts: a head group that chemisorbs on a substrate, a terminal functional group that tunes the properties of the SAM surface, and a spacer group (normally an alkyl chain) that connects the head and terminal functional groups and determines the intermolecular interactions and ordering of the molecules within the monolayer. Various SAMs, such as such as thiols, phosphonic acids, silanes, carboxylic acids, and alcohols, have been investigated for the modification of materials, such as noble metals (gold, silver, palladium, rhodium, etc.), titanium oxides, aluminum oxides, silicon oxides, and mica [55–58]. The SAMs of phosphonic acids bind with surfaces by forming covalent bonds through condensation reactions [55,56], and the coatings have been found to be thermally and chemically stable on the substrates [59,60].

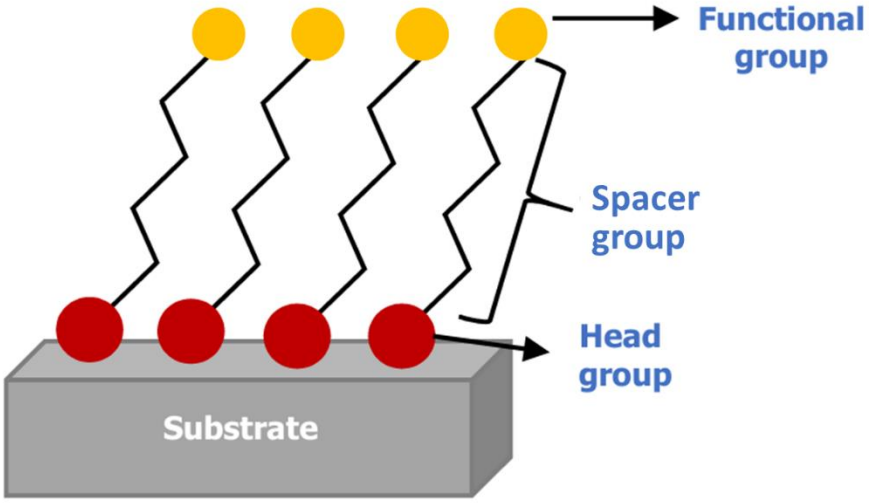

Figure 1.3. Representation of SAM structure. Reproduced from Peng et. al [61].

SAM coating essentially reduces the film thickness to a molecular scale and enables precise control for its structure and applications in different areas. The molecular arrangement of SAMs on the substrate is affected by ligand chain length, coverage (number of molecules per unit of surface area), and functional groups. The ligand chains of SAMs generally have a tilt angle with respect to the substrate [62,63]. Ligands with long chains result in SAMs with a high degree of order due to the strong van der Waals interactions between the long chains, whereas ligands with short chain form less dense, liquid-like structures [64]. The lower grafting density of a coating results in less ordered ligand chains with increased title angle of the molecules axis with the normal to the surface [65,66].

For the terminal functional groups of ligands, nonpolar groups, such as methyl, result in hydrophobic surfaces, being applicable in the field of corrosion protection [67]. Polar groups, such as hydroxyl, carboxyl, and amine, make the surfaces active as adhesion promoters for the attachment of other molecules or surfaces [68].

Particularly, in recent years, amine-containing ligands to modify materials have attracted significant interest in research areas such as CO_2 capture using zeolites, drug delivery, and catalysis. After the modification with amine-containing ligands, the materials, such as hierarchical silica [69], TiO_2 [70], and zeolites [71–75], have exhibited improved CO_2 adsorption capacity. In the field of drug delivery and multimodal theranostic applications, amine-containing phosphonic acids have been used as a covalent linker between magnetic Fe_3O_4 nanoparticles and ß-cyclodextrin to carry and release some drugs [76]. Moreover, biocompatible multi-functional Fe_3O_4 nanoparticles using a mixed monolayer with two phosphonic acids having terminal acetylenic and amine groups have been used to enhance the intracellular transport of *N*-methylated drugs [68]. For catalysis, coating with amino-propyltrimethoxysilane increases the basicity of Na-LTA zeolite catalyst for the Knoevenagel condensation reaction between benzaldehyde and ethyl cyanoacetate [77]. However, amine-containing SAMs have not been reported to modify the pore structure of adsorbents for kinetic adsorptive separation. In the research described in Chapter 4 of this thesis, organic ligands with functional groups (amine and carboxylic acid) were employed to modify zeolites for gas adsorptive separation and the effects of functional groups on coating structure and gas adsorption rates were studied.

Utilizing the steric hindrance property of SAMs, Ellis et. al modified zeolite 5A with organic phosphonic acids (PAs) for gas adsorptive separation. Gas adsorption rates were tuned by changing the alkyl chain length of PAs (shown in Fig. 1.4), and kinetic selectivities were improved with PA coatings [78]. They also found that PAs

with a short alkyl chain having less than four carbons modified the internal zeolite surface, whereas PAs with a long chain such as *n*-octadecylphosphonic acid modified the external surface. However, the mechanism of gas diffusion into PA-coated zeolites has not been well studied. The work described in Chapter 2 focused on understanding the mechanism of selective control for this PA-coated zeolites system.

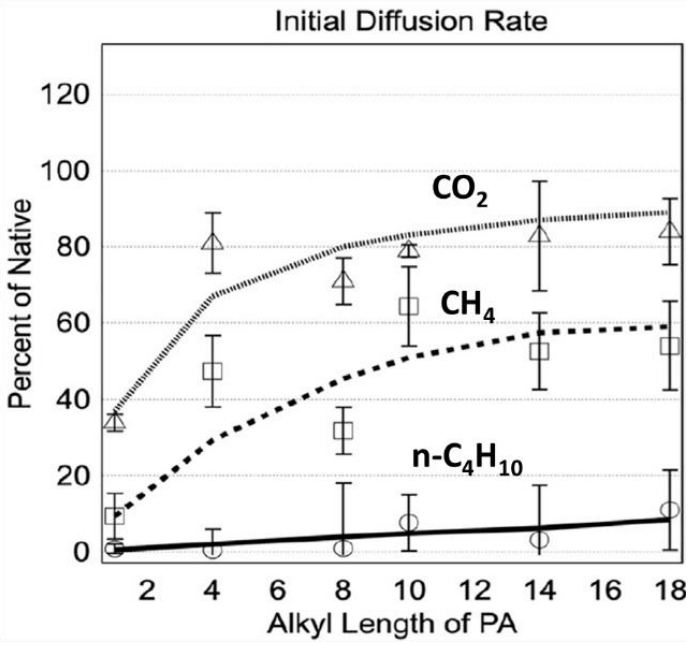

Figure 1.4. Initial diffusion rate of CO_2, CH_4, and *n*-C_4H_{10} as a function of the alkyl tail length of the PA modifier. Interpolations only guide the eye; they do not represent a mathematical function. Error bars, standard error of sample triplicate combined from functionalized and native performances. Reproduced from Ellis et. al [78].

The deposition of PAs is an attractive method for modifying zeolite surfaces. The gas diffusion mechanism in the coating layer and the methods to tune PA structures still need to be studied to enhance the knowledge of the structure-property relationship for PA-coated zeolites for gas adsorptive separation. The work in this thesis attempts to understand the mechanisms of PA-coated zeolites for selective gas adsorption and provide insights for the rational design of high-performance adsorbents.

1.4. Thesis goals

The overall objective of this thesis is to understand the selectivity control of zeolites coated with PAs for gas adsorptive separation, specifically the separation of C_3H_6/C_3H_8. The properties of PA modifiers were tuned by changing ligand chain length, steric configuration, function group, and coating density. Adsorption kinetics and separation performance of adsorbents were investigated by single-gas, pressure-decay adsorption measurements. Competitive adsorption between C_3H_6 and C_3H_8 in mixtures was investigated. The work provided insights for the rational design of adsorbents and adsorptive separation processes.

1.5. Thesis organization

Chapter 2 is adapted from a manuscript published in *Microporous and Mesoporous Materials* [79], entitled "Mechanism of selectivity control for zeolites modified with organic monolayers" with co-authors John L. Falconer and J. Will Medlin. In this project, the PA coatings on zeolite surfaces provide an additional barrier to the diffusion of C_3H_6 and C_3H_8 into zeolites. By varying the properties of PA modifiers, including alkyl chain length and steric configuration, an additional level of control over adsorption selectivity can be achieved. Pressure-decay adsorption measurements of single-component of C_3H_6 and C_3H_8 at 298–423 K were performed on uncoated and PA-coated zeolite 5A to determine the effect of PA on gas diffusion rate and kinetic adsorption selectivity. Moreover, the adsorption curves were fit using

internal diffusion model and surface limitation model to determine the dominant resistance of gas diffusion.

Chapter 3 is adapted from a manuscript published in *Separation and Purification Technology* [80], entitled "Competitive adsorption between propylene and propane on zeolite 5A and the influence of organic phosphonic acid coatings" with co-authors John L. Falconer and J. Will Medlin. In an adsorptive separation process, the difference in interactions of gas components with adsorbent surfaces can affect adsorption selectivity, which may be quite different from ideal selectivity measured by single-gas adsorption. Adsorption measurements with pulse injection for an equimolar and a 90/10 C_3H_6/C_3H_8 mixtures on uncoated and PA-coated zeolite 5A were performed in a fixed bed column, followed by temperature-programmed desorption (TPD) to investigate desorption kinetics. The interactions of gas components with the zeolite were investigated by successive adsorption measurements of pure-component C_3H_6 and C_3H_8. Moreover, the exposure-dependent trends in mixture selectivity were examined.

Chapter 4 contains a manuscript in preparation entitled "Organic-coated zeolites for selective gas adsorption: Effect of functional group identity and coating density" with co-authors John L. Falconer and J. Will Medlin. Inspired by the work developed in chapter 2, we sought to investigate the effects of functional groups (amine and carboxylic acid) of PAs and coating density on gas adsorption rates. Pressure-decay adsorption measurements of single-gas C_3H_6 and C_3H_8 were performed on zeolite 5A coated with 4-phosphonobutyric acid ($COOHC_3PA$) and 3-

aminopropyl phosphonic acid (NH_2C_3PA) and compared with *n*-butylphosphonic acid (BPA) coating with a similar ligand chain length. TPD of *n*-propylamine were performed to investigate the interaction of the amine group with the zeolite surface. Moreover, the density-dependent trends between NH_2C_3PA and ODPA were investigated. At low coating densities, the amine group forms a hydrogen bond with the hydroxyl group on the zeolite surface, resulting in high resistance to gas diffusion.

Finally, chapter 5 summarizes the findings in the previous chapters and concludes with final thoughts on the modification of zeolites with organic monolayers. It also provides perspectives on potential research areas to expand upon this work.

1.6. References

[1] A. Akah, M. Al-Ghrami, Maximizing propylene production via FCC technology, Appl. Petrochem. Res. 5 (2015) 377–392. https://doi.org/10.1007/s13203-015-0104-3.

[2] D.S. Sholl, R.P. Lively, Seven chemical separations to change the world, Nature 532 (2016) 435–437. https://doi.org/10.1038/532435a.

[3] H. Wang, X. Dong, V. Colombo, Q. Wang, Y. Liu, W. Liu, X. Wang, X. Huang, D.M. Proserpio, A. Sironi, Y. Han, J. Li, Tailor-made microporous metal-organic frameworks for the full separation of propane from propylene through selective size exclusion, Adv. Mater. 30 (2018) 1805088. https://doi.org/10.1002/adma.201805088.

[4] R. Faiz, K. Li, Polymeric membranes for light olefin/paraffin separation, Desalination 287 (2012) 82–97. https://doi.org/10.1016/j.desal.2011.11.019.

[5] J.R. Alcántara-Avila, F.I. Gómez-Castro, J.G. Segovia-Hernández, K.I. Sotowa, T. Horikawa, Optimal design of cryogenic distillation columns with side heat pumps for the propylene/propane separation, Chem. Eng. Process.: Process Intensif. 82 (2014) 112–122. https://doi.org/10.1016/j.cep.2014.06.006.

[6] F.A. Da Silva, A.E. Rodrigues, Vacuum swing adsorption for propylene/propane separation with 4A zeolite, Ind. Eng. Chem. Res. 40 (2001) 5758–5774. https://doi.org/10.1021/ie0008732.

[7] H. Maghsoudi, H. Abdi, A. Aidani, Temperature- and pressure-dependent adsorption equilibria and diffusivities of propylene and propane in pure-silica

Si-CHA zeolite, Ind. Eng. Chem. Res. 59 (2020) 1682–1692. https://doi.org/10.1021/acs.iecr.9b05451.
[8] M.H. Weston, Y.J. Colón, Y.S. Bae, S.J. Garibay, R.Q. Snurr, O.K. Farha, J.T. Hupp, S.T. Nguyen, High propylene/propane adsorption selectivity in a copper(catecholate)-decorated porous organic polymer, J. Mater. Chem. A 2 (2014) 299–302. https://doi.org/10.1039/C3TA12999C.
[9] A. Ortiz, L.M. Galán, D. Gorri, A.B. de Haan, I. Ortiz, Reactive ionic liquid media for the separation of propylene/propane gaseous mixtures, Ind. Eng. Chem. Res. 49 (2010) 7227–7233. https://doi.org/10.1021/ie100576r.
[10] G. Yu, L. Deng, A.A. Abdeltawab, S.S. Al-Deyab, X. Chen, J. Zhang, Functional solution composed of Cu(I) salt and ionic liquids to separate propylene from propane, Ind. Eng. Chem. Res. 53 (2014) 13430–13435. https://doi.org/10.1021/ie501522m.
[11] S. Kasahara, E. Kamio, R. Minami, H. Matsuyama, A facilitated transport ion-gel membrane for propylene/propane separation using silver ion as a carrier, J. Membr. Sci. 431 (2013) 121–130. https://doi.org/10.1016/j.memsci.2012.12.026.
[12] M.L. Chng, Y. Xiao, T.S. Chung, M. Toriida, S. Tamai, Enhanced propylene/propane separation by carbonaceous membrane derived from poly (aryl ether ketone)/2,6-bis(4-azidobenzylidene)-4-methyl-cyclohexanone interpenetrating network, Carbon 47 (2009) 1857–1866. https://doi.org/10.1016/j.carbon.2009.03.032.
[13] H.T. Kwon, H.K. Jeong, *In Situ* Synthesis of thin zeolitic-imidazolate framework ZIF-8 membranes exhibiting exceptionally high propylene/propane separation, J. Am. Chem. Soc. 135 (2013) 10763–10768. https://doi.org/10.1021/ja403849c.
[14] S. Shrestha, P.K. Dutta, Modification of a continuous zeolite membrane grown within porous polyethersulfone with Ag(I) cations for enhanced propylene/propane gas separation, Microporous Mesoporous Mater. 279 (2019) 178–185. https://doi.org/10.1016/j.micromeso.2018.12.032.
[15] H. Strathmann, Membranes and membrane separation processes, Ullmann's Encyclopedia of Industrial Chemistry, Wiley-VCH Verlag GmbH & Co. KGaA, Weinheim, Germany. (2005) 16–187. https://doi.org/10.1002/14356007.a16_187.pub2.
[16] R. Bai, X. Song, W. Yan, J. Yu, Low-energy adsorptive separation by zeolites, Natl. Sci. Rev. 9 (2022) nwac064. https://doi.org/10.1093/nsr/nwac064.
[17] M. Thommes, K. Kaneko, A.V. Neimark, J.P. Olivier, F. Rodriguez-Reinoso, J. Rouquerol, K.S.W. Sing, Physisorption of gases, with special reference to the evaluation of surface area and pore size distribution (IUPAC Technical Report), Pure Appl. Chem. 87 (2015) 1051–1069. https://doi.org/10.1515/pac-2014-1117.
[18] Y. Li, L. Li, J. Yu, Applications of zeolites in sustainable chemistry, Chem. 3 (2017) 928–949. https://doi.org/10.1016/j.chempr.2017.10.009.
[19] International Zeolite Association. https://america.iza-structure.org/IZA-SC/ftc_table.php.

[20] W. Zhu, F. Kapteijn, J.A. Moulijn, Shape selectivity in the adsorption of propane/propene on the all-silica DD3R, Chem. Commun. (1999) 2453–2454. https://doi.org/10.1039/a906465f.
[21] M.C. Campo, A.M. Ribeiro, A. Ferreira, J.C. Santos, C. Lutz, J.M. Loureiro, A.E. Rodrigues, New 13X zeolite for propylene/propane separation by vacuum swing adsorption, Sep. Purif. Technol. 103 (2013) 60–70. https://doi.org/10.1016/j.seppur.2012.10.009.
[22] Y. Chai, X. Han, W. Li, S. Liu, S. Yao, C. Wang, W. Shi, I. da-Silva, P. Manuel, Y. Cheng, L.D. Daemen, A.J. Ramirez-Cuesta, C.C. Tang, L. Jiang, S. Yang, N. Guan, L. Li, Control of zeolite pore interior for chemoselective alkyne/olefin separations, Science 368 (2020) 1002–1006. https://doi.org/10.1126/science.aay8447.
[23] H. Abedini, A. Shariati, M.R. Khosravi-Nikou, Separation of propane/propylene mixture using MIL-101(Cr) loaded with cuprous oxide nanoparticles: Adsorption equilibria and kinetics study, Chem. Eng. J. 387 (2020) 124172. https://doi.org/10.1016/j.cej.2020.124172.
[24] D.M. Ruthven, S.C. Reyes, Adsorptive separation of light olefins from paraffins, Microporous Mesoporous Mater. 104 (2007) 59–66. https://doi.org/10.1016/j.micromeso.2007.01.005.
[25] S. Abbasi, M.R. Khosravi-Nikou, A. Shariati, Selective separation of propane from the propylene-propane mixture using pure silica zeolites: A molecular dynamic simulation, Chem. Eng. Process.: Process Intensif. 184 (2023) 109294. https://doi.org/10.1016/j.cep.2023.109294.
[26] C.A. Grande, J. Gascon, F. Kapteijn, A.E. Rodrigues, Propane/propylene separation with Li-exchanged zeolite 13X, Chem. Eng. J. 160 (2010) 207–214. https://doi.org/10.1016/j.cej.2010.03.044.
[27] J.G. Min, K.C. Kemp, K.S. Kencana, R.R. Mukti, S. Bong Hong, Dealuminated Cs-ZK-5 zeolite for propylene/propane separation, Chem. Eng. J. 413 (2021) 127422. https://doi.org/10.1016/j.cej.2020.127422.
[28] C.A. Grande, A. Lind, Ø. Vistad, D. Akporiaye, Olefin-paraffin separation using calcium-ETS-4, Ind. Eng. Chem. Res. 53 (2014) 15522–15530. https://doi.org/10.1021/ie5004703.
[29] A. Anson, C.C.H. Lin, T.M. Kuznicki, S.M. Kuznicki, Separation of ethylene/ethane mixtures by adsorption on small-pored titanosilicate molecular sieves, Chem. Eng. Sci. 65 (2010) 807–811. https://doi.org/10.1016/j.ces.2009.09.033.
[30] Y.S. Bae, C.Y. Lee, K.C. Kim, O.K. Farha, P. Nickias, J.T. Hupp, S.T. Nguyen, R.Q. Snurr, High propene/propane selectivity in isostructural metal-organic frameworks with high densities of open metal sites, Angew. Chem. 124 (2012) 1893–1896. https://doi.org/10.1002/ange.201107534.
[31] E.D. Bloch, W.L. Queen, R. Krishna, J.M. Zadrozny, C.M. Brown, J.R. Long, Hydrocarbon separations in a metal-organic framework with open iron(II) coordination sites, Science 335 (2012) 1606–1610. https://doi.org/10.1126/science.1217544.

[32] C. Krishnaraj, H.S. Jena, K. Leus, H.M. Freeman, L.G. Benning, P. Van Der Voort, An aliphatic hexene-covalent triazine framework for selective acetylene/methane and ethylene/methane separation, J. Mater. Chem. A 7 (2019) 13188–13196. https://doi.org/10.1039/C8TA11722E.
[33] J. Gao, Y. Cai, X. Qian, P. Liu, H. Wu, W. Zhou, D. Liu, L. Li, R. Lin, B. Chen, A microporous hydrogen-bonded organic framework for the efficient capture and purification of propylene, Angew. Chem. 133 (2021) 20563–20569. https://doi.org/10.1002/ange.202106665.
[34] J. Gascon, W. Blom, A. van Miltenburg, A. Ferreira, R. Berger, F. Kapteijn, Accelerated synthesis of all-silica DD3R and its performance in the separation of propylene/propane mixtures, Microporous Mesoporous Mater. 115 (2008) 585–593. https://doi.org/10.1016/j.micromeso.2008.02.038.
[35] M. Khalighi, Y.F. Chen, S. Farooq, I.A. Karimi, J.W. Jiang, Propylene/propane separation using SiCHA, Ind. Eng. Chem. Res. 52 (2013) 3877–3892. https://doi.org/10.1021/ie3026955.
[36] P.J. Bereciartua, Á. Cantín, A. Corma, J.L. Jordá, M. Palomino, F. Rey, S. Valencia, E.W. Corcoran, P. Kortunov, P.I. Ravikovitch, A. Burton, C. Yoon, Y. Wang, C. Paur, J. Guzman, A.R. Bishop, G.L. Casty, Control of zeolite framework flexibility and pore topology for separation of ethane and ethylene, Science 358 (2017) 1068–1071. https://doi.org/10.1126/science.aao0092.
[37] C. Selzer, A. Werner, S. Kaskel, Selective adsorption of propene over propane on hierarchical zeolite ZSM-58, Ind. Eng. Chem. Res. 57 (2018) 6609–6617. https://doi.org/10.1021/acs.iecr.8b00377.
[38] J. Liu, Y. Liu, D.K. Talay, E. Calverley, M. Brayden, M. Martinez, A new carbon molecular sieve for propylene/propane separations, Carbon 85 (2015) 201–211. https://doi.org/10.1016/j.carbon.2014.12.089.
[39] S. Xu, W.C. Li, C. Wang, R. Liu, G.P. Hao, A.H. Lu, Beyond the selectivity-capacity trade-off: Ultrathin carbon nanoplates with easily accessible ultramicropores for high-efficiency propylene/propane separation, Nano Lett. 22 (2022) 6615–6621. https://doi.org/10.1021/acs.nanolett.2c01930.
[40] L. Li, R.B. Lin, X. Wang, W. Zhou, L. Jia, J. Li, B. Chen, Kinetic separation of propylene over propane in a microporous metal-organic framework, Chem. Eng. J. 354 (2018) 977–982. https://doi.org/10.1016/j.cej.2018.08.108.
[41] B.R. Pimentel, R.P. Lively, Propylene enrichment via kinetic vacuum pressure swing adsorption using ZIF-8 fiber sorbents, ACS Appl. Mater. Interfaces 10 (2018) 36323–36331. https://doi.org/10.1021/acsami.8b08983.
[42] Q. Ding, Z. Zhang, P. Zhang, J. Wang, X. Cui, C.H. He, S. Deng, H. Xing, Control of intracrystalline diffusion in a bilayered metal-organic framework for efficient kinetic separation of propylene from propane, Chem. Eng. J. 434 (2022) 134784. https://doi.org/10.1016/j.cej.2022.134784.
[43] J. Padin, S.U. Rege, R.T. Yang, L.S. Cheng, Molecular sieve sorbents for kinetic separation of propane/propylene, Chem. Eng. Sci. 55 (2000) 4525–4535. https://doi.org/10.1016/S0009-2509(00)00099-3.

[44] A. Cadiau, K. Adil, P.M. Bhatt, Y. Belmabkhout, M. Eddaoudi, A metal-organic framework-based splitter for separating propylene from propane, Science 353 (2016) 137–140. https://doi.org/10.1126/science.aaf6323.
[45] H. Zeng, M. Xie, T. Wang, R.J. Wei, X.J. Xie, Y. Zhao, W. Lu, D. Li, Orthogonal-array dynamic molecular sieving of propylene/propane mixtures, Nature 595 (2021) 542–548. https://doi.org/10.1038/s41586-021-03627-8.
[46] Y. Chen, Y. Yang, Y. Wang, Q. Xiong, J. Yang, S. Xiang, L. Li, J. Li, Z. Zhang, B. Chen, Ultramicroporous hydrogen-bonded organic framework material with a thermoregulatory gating effect for record propylene separation, J. Am. Chem. Soc. 144 (2022) 17033–17040. https://doi.org/10.1021/jacs.2c06585.
[47] J. Cui, Z. Zhang, L. Yang, J. Hu, A. Jin, Z. Yang, Y. Zhao, B. Meng, Y. Zhou, J. Wang, Y. Su, J. Wang, X. Cui, H. Xing, A molecular sieve with ultrafast adsorption kinetics for propylene separation, Science (2023) eabn8418. https://doi.org/10.1126/science.abn8418.
[48] J. Shang, G. Li, R. Singh, Q. Gu, K.M. Nairn, T.J. Bastow, N. Medhekar, C.M. Doherty, A.J. Hill, J.Z. Liu, P.A. Webley, Discriminative separation of gases by a "molecular trapdoor" mechanism in chabazite zeolites, J. Am. Chem. Soc. 134 (2012) 19246–19253. https://doi.org/10.1021/ja309274y.
[49] C.D. Chudasama, J. Sebastian, R.V. Jasra, Pore-size engineering of zeolite A for the size/shape selective molecular separation, Ind. Eng. Chem. Res. 44 (2005) 1780–1786. https://doi.org/10.1021/ie049333l.
[50] P. Wei, X. Qu, H. Dong, L. Zhang, H. Chen, C. Gao, Silane-modified NaA zeolite/PAAS hybrid pervaporation membranes for the dehydration of ethanol, J. Appl. Polym. Sci. 128 (2013) 3390–3397. https://doi.org/10.1002/app.38555.
[51] Y. Li, H.M. Guan, T.S. Chung, S. Kulprathipanja, Effects of novel silane modification of zeolite surface on polymer chain rigidification and partial pore blockage in polyethersulfone (PES)–zeolite A mixed matrix membranes, J. Membr. Sci. 275 (2006) 17–28. https://doi.org/10.1016/j.memsci.2005.08.015.
[52] X. Xu, X. Zhao, L. Sun, X. Liu, Adsorption separation of carbon dioxide, methane and nitrogen on monoethanol amine modified ß-zeolite, J. Nat. Gas Chem. 18 (2009) 167–172. https://doi.org/10.1016/S1003-9953(08)60098-5.
[53] Q. Dong, Z. Song, F. Zhou, H. Li, M. Yu, Ultrathin, fine-tuned microporous coating modified 5A zeolite for propane/propylene adsorptive separation, Microporous Mesoporous Mater. 281 (2019) 9–14. https://doi.org/10.1016/j.micromeso.2019.02.038.
[54] A. Ulman, Formation and structure of self-sssembled monolayers, Chem. Rev. 96 (1996) 1533–1554. https://doi.org/10.1021/cr9502357.
[55] E. Hoque, J.A. DeRose, G. Kulik, P. Hoffmann, H.J. Mathieu, B. Bhushan, Alkylphosphonate modified aluminum oxide surfaces, J. Phys. Chem. B 110 (2006) 10855–10861. https://doi.org/10.1021/jp061327a.
[56] T. Hauffman, O. Blajiev, J. Snauwaert, C. Van Haesendonck, A. Hubin, H. Terryn, Study of the self-assembling of *n*-octylphosphonic acid layers on aluminum oxide, Langmuir 24 (2008) 13450–13456. https://doi.org/10.1021/la801978a.

[57] Z. Blanchette, J. Zhang, S. Yazdi, M.B. Griffin, D.K. Schwartz, J.W. Medlin, Investigating deposition sequence during synthesis of Pd/Al_2O_3 catalysts modified with organic monolayers, Catal. Sci. Technol. 12 (2022) 2306–2314. https://doi.org/10.1039/D1CY02131A.
[58] A.H. Jenkins, E.E. Dunphy, M.F. Toney, C.B. Musgrave, J.W. Medlin, Tailoring the near-surface environment of Rh single-atom catalysts for selective CO_2 hydrogenation, ACS Catal. 13 (2023) 15340–15350. https://doi.org/10.1021/acscatal.3c03768.
[59] L.D. Ellis, R.M. Trottier, C.B. Musgrave, D.K. Schwartz, J.W. Medlin, Controlling the surface reactivity of titania via electronic tuning of self-assembled monolayers, ACS Catal. 7 (2017) 8351–8357. https://doi.org/10.1021/acscatal.7b02789.
[60] J. Zhang, L.D. Ellis, B. Wang, M.J. Dzara, C. Sievers, S. Pylypenko, E. Nikolla, J.W. Medlin, Control of interfacial acid-metal catalysis with organic monolayers, Nat. Catal. 1 (2018) 148–155. https://doi.org/10.1038/s41929-017-0019-8.
[61] Y.Y. Peng, S. Srinivas, R. Narain, Modification of polymers, Polymer Science and Nanotechnology, Elsevier. (2020) 95–104. https://doi.org/10.1016/B978-0-12-816806-6.00005-4.
[62] R. Luschtinetz, A.F. Oliveira, H.A. Duarte, G. Seifert, Self-assembled monolayers of alkylphosphonic acids on aluminum oxide surfaces – A theoretical study, Z. Anorg. Allg. Chem. 636 (2010) 1506–1512. https://doi.org/10.1002/zaac.201000016.
[63] P. Gutfreund, O. Bäumchen, R. Fetzer, D. Van Der Grinten, M. Maccarini, K. Jacobs, H. Zabel, M. Wolff, Solid surface structure affects liquid order at the polystyrene-self-assembled-monolayer interface, Phys. Rev. E 87 (2013) 012306. https://doi.org/10.1103/PhysRevE.87.012306.
[64] D.M. Spori, N.V. Venkataraman, S.G.P. Tosatti, F. Durmaz, N.D. Spencer, S. Zürcher, Influence of alkyl chain length on phosphate self-assembled monolayers, Langmuir 23 (2007) 8053–8060. https://doi.org/10.1021/la700474v.
[65] B. Feichtenschlager, C.J. Lomoschitz, G. Kickelbick, Tuning the self-assembled monolayer formation on nanoparticle surfaces with different curvatures: Investigations on spherical silica particles and plane-crystal-shaped zirconia particles, J. Colloid Interface Sci. 360 (2011) 15–25. https://doi.org/10.1016/j.jcis.2011.03.035.
[66] J.M. Castillo, M. Klos, K. Jacobs, M. Horsch, H. Hasse, Characterization of alkylsilane self-assembled monolayers by molecular simulation, Langmuir 31 (2015) 2630–2638. https://doi.org/10.1021/la504178g.
[67] I. Maege, E. Jaehne, A. Henke, H.P. Adler, C. Bram, C. Jung, M. Stratmann, Ultrathin organic layers for corrosion protection, Macromolecular Symposia 126 (1998) 7–24. https://doi.org/10.1002/masy.19981260104.
[68] C. Tudisco, M.T. Cambria, F. Sinatra, F. Bertani, A. Alba, A.E. Giuffrida, S. Saccone, E. Fantechi, C. Innocenti, C. Sangregorio, E. Dalcanale, G.G. Condorelli, Multifunctional magnetic nanoparticles for enhanced intracellular

drug transport, J. Mater. Chem. B 3 (2015) 4134–4145. https://doi.org/10.1039/C5TB00547G.
[69] V. Kulkarni, D. Panda, S.K. Singh, Direct air capture of CO_2 over amine-modified hierarchical silica, Ind. Eng. Chem. Res. 62 (2023) 3800–3811. https://doi.org/10.1021/acs.iecr.2c02268.
[70] C.C. Aquino, G. Richner, M.C. Kimling, D. Chen, G. Puxty, P.H.M. Feron, R.A. Caruso, Amine-functionalized titania-based porous structures for carbon dioxide postcombustion capture, J. Phys. Chem. C 117 (2013) 9747–9757. https://doi.org/10.1021/jp312118e.
[71] S.T. Yang, J.Y. Kim, J. Kim, W.S. Ahn, CO_2 capture over amine-functionalized MCM-22, MCM-36 and ITQ-2, Fuel 97 (2012) 435–442. https://doi.org/10.1016/j.fuel.2012.03.034.
[72] Y. Wang, T. Du, Y. Song, S. Che, X. Fang, L. Zhou, Amine-functionalized mesoporous ZSM-5 zeolite adsorbents for carbon dioxide capture, Solid State Sci. 73 (2017) 27–35. https://doi.org/10.1016/j.solidstatesciences.2017.09.004.
[73] D. Panda, E.A. Kumar, S.K. Singh, Amine Modification of binder-containing zeolite 4A bodies for post-combustion CO_2 capture, Ind. Eng. Chem. Res. 58 (2019) 5301–5313. https://doi.org/10.1021/acs.iecr.8b03958.
[74] V. Tejavath, V. Kasarabada, S. Gonuguntla, V. Perupoga, S.V. Nandury, S. Bojja, U. Pal, Technoeconomic investigation of amine-grafted zeolites and their kinetics for CO_2 capture, ACS Omega 6 (2021) 6153–6162. https://doi.org/10.1021/acsomega.0c05397.
[75] F. Bahmanzadegan, M.A. Pordsari, A. Ghaemi, Improving the efficiency of 4A-zeolite synthesized from kaolin by amine functionalization for CO_2 capture, Sci. Rep. 13 (2023) 12533. https://doi.org/10.1038/s41598-023-39859-z.
[76] C. Tudisco, V. Oliveri, M. Cantarella, G. Vecchio, G.G. Condorelli, Cyclodextrin anchoring on magnetic Fe_3O_4 nanoparticles modified with phosphonic linkers, Eur. J. Inorg. Chem. 2012 (2012) 5323–5331. https://doi.org/10.1002/ejic.201200510.
[77] I.W. Zapelini, D. Cardoso, Amine-grafted Na-LTA zeolite precursors as basic catalysts for Knoevenagel condensation, Microporous Mesoporous Mater. 324 (2021) 111270. https://doi.org/10.1016/j.micromeso.2021.111270.
[78] L.D. Ellis, S.T. Parker, J. Hu, S.F. Zaccarine, M.J. Stellato, H.H. Funke, C. Sievers, S. Pylypenko, J.L. Falconer, J.W. Medlin, Tuning gas adsorption selectivity and diffusion rates in zeolites with phosphonic acid monolayers, Cell Rep. Phys. Sci. 1 (2020) 100036. https://doi.org/10.1016/j.xcrp.2020.100036.
[79] X. Zhou, J.L. Falconer, J.W. Medlin, Mechanism of selectivity control for zeolites modified with organic monolayers, Microporous Mesoporous Mater. 337 (2022) 111913. https://doi.org/10.1016/j.micromeso.2022.111913.
[80] X. Zhou, J.L. Falconer, J.W. Medlin, Competitive adsorption between propylene and propane on zeolite 5A and the influence of organic phosphonic acid coatings, Sep. Purif. Technol. 346 (2024) 127435. https://doi.org/10.1016/j.seppur.2024.127435.

Chapter 2: Mechanism of selectivity control for zeolites modified with organic monolayers

2.1. Abstract

The adsorptive separation of C_3H_6 and C_3H_8 gases using molecular sieves is a challenging process due to the similarity in molecular sizes for the two molecules. In this work, we report that organic phosphonic acid (PA) monolayers on zeolites significantly enhanced the ideal selectivity of C_3H_6/C_3H_8 adsorption by changing the diffusion mechanism based on the properties of the alkyl tail. With an *n*-octadecylphosphonic acid (ODPA) coating on zeolite 5A, the kinetic selectivity of C_3H_6/C_3H_8 was initially >8 at 25 °C, whereas for uncoated 5A, it was limited to ~1.2. Kinetic modelling showed that in ODPA-coated 5A, the diffusion of C_3H_6 and C_3H_8 was limited by the PA monolayer at the external surface of the zeolite. In contrast, for uncoated 5A, it was controlled by the pore channels, so that the enhanced kinetic selectivity from 5A-ODPA was related to a different limiting transport mechanism. The kinetic selectivity was not temperature sensitive in the range of 25–150 °C in 5A-ODPA as the diffusion activation energies of C_3H_6 and C_3H_8 were both small. Modification of 5A with other PAs also increased the kinetic selectivity. Coating with *n*-butylphosphonic acid yielded lower kinetic selectivity than ODPA, ostensibly due to its shorter alkyl tail. Coating with *tert*-butylphosphonic acid, a sterically bulky ligand, decreased kinetic selectivity still further. However, methylphosphonic acid, which partially penetrated the near-surface region of the zeolite, severely lowered the

diffusion rates. The use of organic films may enable rational design of selective adsorbents based on providing gas-specific resistance at the pore entrance.

2.2. Introduction

Propylene is an important feedstock for a wide variety of products, mainly for polypropylene that is used in packaging films, textile fibers, and other applications. The demand for propylene keeps increasing and currently is over 110 million metric tons annually in the world [1]. The main methods to produce propylene are steam cracking, fluid catalytic cracking, and alkane dehydrogenation, which all result in mixtures of propylene and propane. The mixtures need to be separated to obtain "polymer-grade" propylene (minimum purity of 99.5%) for the manufacture of polypropylene. However, traditional separation processes, especially distillation, are energy intensive. Chemical separations have been reported to account for 10%–15% of the total energy consumption in the United States, and distillation consumes about half of the energy [2]. Cryogenic distillation for the separation of propylene and propane with similar boiling points usually requires towers with 150–200 stages, temperatures of 183–233 K, and pressures of 16–20 bar [3].

In the past several decades, many researchers made efforts at finding alternative processes to improve the separation of propylene and propane, such as adsorption [4–7], absorption [8,9], and membrane separation [10–13]. Among these technologies, adsorptive separation is a promising method with low energy consumption and capital cost. Adsorptive separation can be divided into two main

categories: equilibrium separation and kinetic separation. Equilibrium separation is based on the equilibrium loading of one adsorbate being greater than the others, and kinetic separation is by the difference in diffusion rates of adsorbates. Considering the similar kinetic diameters of propylene and propane molecules, rational design of porous adsorbents to achieve high adsorption selectivity is essential for an energy-efficient, kinetic separation process.

Various materials have been studied for the separation of light gases with similar molecular sizes. Carbon molecular sieve fibers with an effective micropore size of 3.4 to 4.9 Å (prepared from pyrolysis of polyvinylidene chloride copolymer) were reported to have propylene/propane (50/50 mixture) adsorptive separation factors of 12–29 [14], but their poor mechanical strength makes them difficult to scale up [3]. Polymeric membranes made from 2,3,5,6-tetra-methyl-1,4-phenylenediamine and 9,10-diisopropyltriptycene-based dianhydride had a propylene/propane ideal selectivity of 16 and a propylene permeability of 817 Barrer [15]. However, polymeric membranes usually cannot simultaneously meet the performance requirements (selectivity 20 and propylene permeability 10 Barrer) [16], and the selectivity usually decreases due to a plasticization effect [3]. Zeolitic imidazolate framework ZIF-8 based membranes have been found to reach propylene/propane selectivity of 100 and propylene permeance $>10^{-8}$ mol Pa^{-1} m^{-2} s^{-1} [17].

Zeolites have been widely investigated for gas separation, owing to their well-defined pores and high chemical, thermal, and mechanical stabilities [18]. There are

more than 200 types of zeolites with different structures. To separate gases with similar molecular sizes, zeolites should have appropriate pore openings and channels.

One method to tune the pore structure of zeolites is to change the composition and bulk framework. Grande et al. [19] synthesized lithium-modified zeolite 13X for propylene/propane separation via vacuum pressure swing adsorption and improved the selectivity compared with Na-13X. Shrestha and Dutta [13] used zeolite membranes grown within porous polyethersulfone supports and coated with a thin layer of polydimethoxysilane for propylene/propane separation and found that Ag^+ cation modification improved propylene/propane selectivity from 2.4 to 4.8 and achieved propylene permeability of 10^3 Barrer. Min et al. [20] found that $CaNH_4$-levyne (Si/Al = 15.5 and Fe/Al = 0.27) had an equilibrium ideal selectivity of 11 for propylene/propane adsorptive separation by the molecular sieve effect of the framework topology and the introduction of Fe to decrease acidity.

For further improving selective adsorption, the external surface of zeolites can be modified with an additional diffusion layer or functional group. Chudasama et al. [21] deposited silica on the external surface of zeolite 4A with tetraethyl orthosilicate and improved the equilibrium ideal selectivity of O_2/N_2 from 0.3 to 2.0 and O_2/Ar from 1.1 to 4.6. Xu et al. [22] deposited monoethanol amine on ß-zeolite and improved the ideal selectivity of CO_2/CH_4 from 4.6 to 7.7 and CO_2/N_2 from 12 to 26 based on a steric effect and adsorbate-adsorbent chemical interaction.

Another method is to tune the pore openings of zeolites to improve adsorption selectivity. Dong et al. [23] coated ultrathin microporous TiO_2 on zeolite 5A by

combining molecular and atomic layer deposition methods to decrease the pore mouth from 0.8 to 0.6 nm, and the diffusivity ratio of propylene to propane were increased from 1 to 75 and a propylene/propane equilibrium ideal selectivity up to 22 was achieved. Ellis et al. [24] deposited methylphosphonic acid (MPA) self-assembled monolayers (SAMs) on zeolite 5A, and both the initial diffusion rate and apparent uptake of *n*-C_4H_{10} were decreased by >90%; the ideal selectivity of propylene/propane reached 59 ± 14 at 46 kPa.

Modification with PAs is a promising method to tune gas diffusion rates and improve the adsorption selectivity. Our research group characterized PA-modified zeolite 5A with various techniques, including X-ray diffraction (XRD), Brunauer-Emmett-Teller (BET) surface area measurement, inductively coupled plasma-mass spectrometry (ICP-MS), scanning transmission electron microscopy (STEM) with energy-dispersive X-ray spectroscopy (EDS), low energy ion scattering (LEIS), and other methods. It was found that the bulk crystalline structure of zeolites did not change after coating with PAs, and MPA (the smallest PA studied) was located at the near-surface region of zeolite 5A. All longer-chain PAs were confined to the external surface [24]. Understanding the diffusion mechanism of gas molecules with PA modification may enable rational design of adsorption materials and separation systems. We hypothesized that PA modifiers deposited at the surface can provide an added barrier to the diffusion of C_3H_6 and C_3H_8 into zeolites, and by tuning the properties of PA modifiers, an additional level of control over adsorption selectivity can be achieved. Here, we modified zeolite 5A with different PAs and measured the

temperature dependence of the kinetic selectivity in the temperature range of 25 to 150 °C. We then investigated the diffusion mechanism using kinetic models based on a rate-limiting step of internal or surface diffusion.

2.3. Experimental

2.3.1. Organic phosphonic acid coating on zeolite and characterization

The SAM coating technique developed previously was employed [24]. Zeolite 5A, $Ca_nNa_{12-2n}[(AlO_2)_{12}(SiO_2)_{12}]$ xH_2O (powder, <10 μm, Sigma-Aldrich 233676), was coated with methylphosphonic acid (MPA, ≥97.5%, Alfa Aesar A12619), *n*-butylphosphonic acid (BPA, ≥88.0%, Sigma-Aldrich 737933), *tert*-butylphosphonic acid (TBPA, ≥97.5%, Acros Organics 321520050), and *n*-octadecylphosphonic acid (ODPA, ≥96.0%, Alfa Aesar 20645), respectively. In detail, zeolite 5A (830 mg) was calcined for 4 h in static air at 400 °C, then cooled down close to room temperature and added to a 200-mL solution (0.01 mol/L) of PA in tetrahydrofuran (THF, high-performance liquid chromatography [HPLC] grade, Fisher Chemical T425-4), then stirred for 16 h, and centrifuged at 8000 rpm for 9 min. The supernatant solvent was decanted, and the remaining precipitant was annealed at 120 °C for 6 h, then cooled to room temperature and rinsed with THF four times to remove physisorbed PA. The powder was dried in a vacuum oven at room temperature. To compare the coverage of PAs on BPA- and TBPA-coated zeolite 5A, LEIS analysis was carried out on a Qtac100 instrument (ION-TOF, Germany) using 6 keV of $^{4+}$He beam. Five to eight spectra were taken from each sample, and the smoothed curve was obtained by taking

the average of these spectra, subtracting a linear background, and smoothing. The element composition from LEIS was determined by integrating the area under the detected peaks.

2.3.2. Pressure-decay adsorption measurement

The pressure-decay measurement was performed on an Autosorb-1 apparatus (Quantachrome Instruments) equipped with a custom LabVIEW-based data acquisition system. Before each measurement, the sample (100 mg) was pretreated for 3 h at 200 °C under vacuum. Three gases, CO_2 (≥99.999%, Airgas), C_3H_6 (≥99.5%, Airgas), and C_3H_8 (≥99.5%, Airgas), were tested separately at a manifold pressure of 40 kPa and room temperature for uncoated zeolite 5A and the zeolites coated with MPA, BPA, TBPA, and ODPA, respectively. Based on the pressure drop during adsorption, the amount of adsorbed gas and ideal selectivity (ratio of C_3H_6 uptake to C_3H_8 uptake at the same adsorption time and temperature) were calculated. To investigate the effect of temperature on the ideal selectivity of C_3H_6/C_3H_8, the adsorption was measured in the temperature range of 25 to 150 °C.

2.3.3. Diffusion models

Kinetic models describing uptake limited by internal or surface diffusion were used to simulate adsorption process of porous adsorbents under the assumptions of uniform particle size, spherical particle shape, and constant adsorbate concentration on the surface of adsorbent. In the internal diffusion model, the uptake is controlled entirely by internal diffusion, and the surface resistance is assumed to be negligible. The equation is expressed as the following [25].

$$\frac{m_t}{m_\infty} = 1 - \frac{6}{\pi^2}\sum_{n=1}^{\infty}\frac{1}{n^2}e^{-n^2\pi^2 t(D/R^2)} \quad (1)$$

In the surface limitation model, the uptake is assumed to be controlled entirely by surface resistance. The equation is expressed as the following [26].

$$\frac{m_t}{m_\infty} = 1 - e^{-3t(k/R)} \quad (2)$$

In Eq. (1) and (2), m_t/m_∞ is the ratio of mass adsorbed at time t to that at infinite time, R is equivalent radius of pores in adsorbent, D is intrapore diffusivity, and k is surface rate coefficient. We carried out nonlinear regression (minimizing the residual sum of squares) for full experimental data of m_t versus t (120 min for C_3H_6 and C_3H_8 adsorption on ODPA-coated 5A and C_3H_6 adsorption on MPA-coated 5A, and 10 min for the others) to find the model parameters (D/R^2 in internal diffusion and k/R in surface limitation model) and the loadings at infinite adsorption time. To investigate the sensitivity of the fits to the time used for fitting, the loadings at long times from use of the entire experimental time for the fits was used to calculate the fractional uptakes m_t/m_∞, then m_t/m_∞ versus t was fit for various time spans.

The diffusion rate constants evaluated at different temperatures were used to calculate activation energies. Plots of ln K versus $1/T$ were employed to determine the apparent activation energies E_a of gas adsorption, in which K is the diffusion rate constant (D/R^2 for internal diffusion model and k/R for surface limitation model), and T is the absolute temperature.

2.3.4. Thermodynamic calculations

Plots of ln $[((p_i - p_e)/p^0)/(p_e/p^0)]$ versus $1/T$ based on the van't Hoff equation were used to determine the standard enthalpy changes ΔH^0 and standard entropy changes ΔS^0 of gas adsorption in our system, in which p_i is the initial pressure of the system, p_e is the equilibrium pressure of the system, p^0 is the standard pressure (100 kPa), and T is the absolute temperature.

2.4. Results and discussion

2.4.1. Organic phosphonic acids tune gas adsorption rates in zeolite 5A

Single-gas, pressure-decay adsorption measurements of CO_2, C_3H_6, and C_3H_8 on uncoated zeolite 5A and the 5A coated with PAs (TBPA, BPA, ODPA, and MPA) at 25 °C were performed. On uncoated 5A, the adsorption equilibrium loadings of these three gases measured from highest to lowest were: CO_2 (2.40 mmol/g) > C_3H_6 (1.85 mmol/g) > C_3H_8 (1.48 mmol/g) (Figs. 2.1A). The highest loading of CO_2 could be attributed to its small molecular kinetic diameter (where the kinetic diameters were reported as 3.3 Å for CO_2 [27], 4.31 Å for C_3H_6 [28], and 4.46 Å for C_3H_8 [28]), linear geometry, and strong interaction forces [29, 30]. The lowest loading of C_3H_8 was mainly ascribed to its molecular size [30].

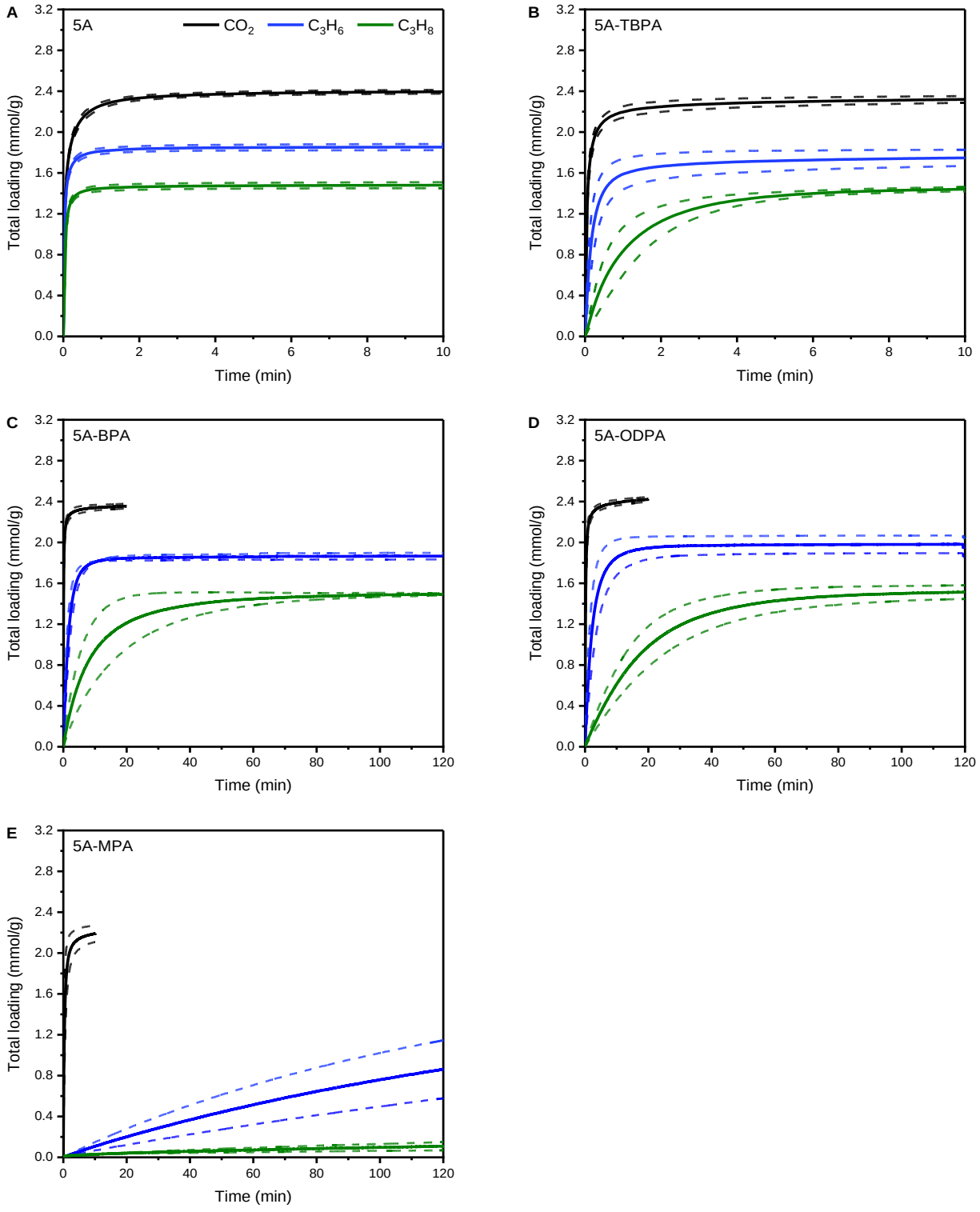

Figure 2.1. CO_2, C_3H_6, and C_3H_8 adsorption on (A) uncoated, (B) TBPA-, (C) BPA-, (D) ODPA-, and (E) MPA-coated 5A at 25 °C. Uncertainty bounds are based on standard deviations of triplicate measurements for separately prepared samples, with the exception of C_3H_6 and C_3H_8 adsorption on 5A-MPA, where the dashed curves represent the span of duplicate measurements with separate samples.

The PAs had minimal effect on CO_2 adsorption, but they increased the adsorption time of C_3H_6 and C_3H_8 to reach equilibrium (Figs. 2.1 and A.1). For C_3H_6, the approximate time to reach equilibrium loading was 1 min on uncoated 5A, 2 min on TBPA-coated 5A, 10 min on BPA-coated 5A, 20 min on ODPA-coated 5A, and >120 min on MPA-coated 5A. With PA coatings, the adsorption time of C_3H_8 to reach equilibrium increased even more; it was 1 min on uncoated 5A, 8 min on TBPA-coated 5A, 80 min on BPA-coated 5A, 100 min on ODPA-coated 5A, and >>120 min on MPA-coated 5A.

The chain length and steric configuration of PA modifiers affected the diffusion rates of both C_3H_6 and C_3H_8. The adsorption from fastest to slowest for both C_3H_6 and C_3H_8 was: 5A > 5A-TBPA > 5A-BPA > 5A-ODPA >> 5A-MPA (Fig. 2.2). Deposition of MPA, which partially penetrated the near-surface region of zeolite based on the elemental analysis on different regions of the particle with EDS and surface element detection with LEIS [24], severely lowered the diffusion rates. The PAs with longer alkyl chains, BPA and ODPA, which were confined to a monolayer on the external surface of zeolite [24], had less resistance to gas diffusion than MPA, and ODPA (with a longer alkyl chain) slowed diffusion more than BPA. Moreover, TBPA, a sterically bulkier modifier, had lower PA coverage than BPA (with a linear alkyl chain) on the surface of zeolite 5A particles based on LEIS analysis (Fig. A.2 and Table A.1), and it had less effect on diffusion rates than BPA. Ellis et al. [24] also found that PA chain length had a similar effect on initial diffusion rates of gases, where CO_2, CH_4, and *n*-

C_4H_{10} adsorption were measured; however, sterically bulky modifiers were not investigated.

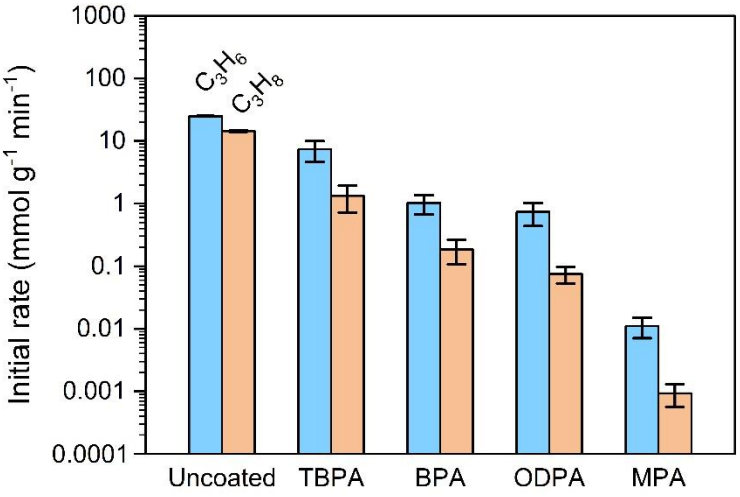

Figure 2.2. Initial rates of C_3H_6 and C_3H_8 adsorption on uncoated, TBPA-, BPA-, ODPA-, and MPA-coated 5A at 25 °C.

The effect of PA coatings on ideal selectivity of C_3H_6/C_3H_8 adsorption at 25 °C is shown in Fig. 2.3. Before adsorption reached equilibrium, the kinetic selectivities of C_3H_6/C_3H_8 on TBPA-, BPA-, and ODPA-coated 5A were higher than uncoated 5A, and the kinetic selectivities for the coatings from highest to lowest were: ODPA > BPA > TBPA. The adsorbents with higher kinetic selectivities took longer time to reach equilibrium selectivity. For ODPA-coated 5A, the kinetic selectivity was initially >8, and it reached stability after 80 min. For MPA-coated 5A, the kinetic selectivity was about 7 after ~60 min (data before 30 min were error-prone due to the low uptakes of C_3H_6 and C_3H_8), but C_3H_6 loading was low (0.86 mmol/g at 120 min). The high kinetic selectivity of C_3H_6/C_3H_8 adsorption from PA-coated 5A at short times could potentially be used for kinetic separation of C_3H_6 and C_3H_8, especially in the

case of ODPA-coated 5A, which had an initial ideal selectivity >8 under the reported experimental conditions.

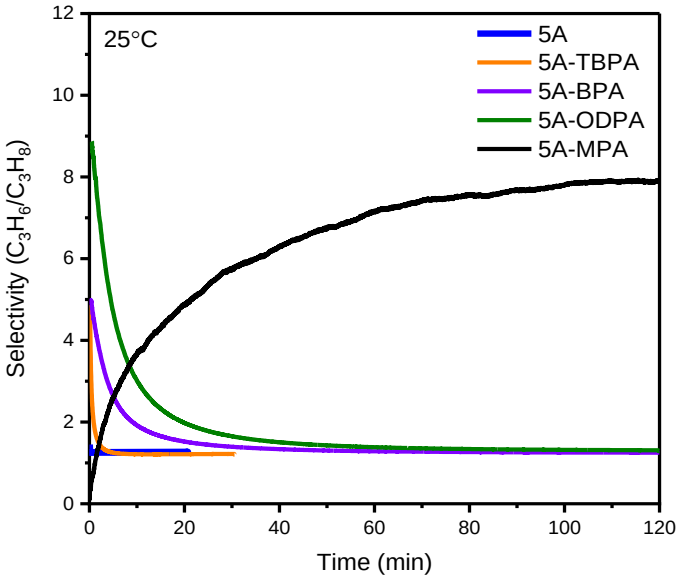

Figure 2.3. C_3H_6/C_3H_8 ideal selectivities as a function of adsorption time on uncoated, TBPA-, BPA-, ODPA-, and MPA-coated 5A at 25 °C.

2.4.2. Temperature dependence of equilibrium and kinetic adsorption on PA-coated 5A

The temperature dependence of C_3H_6, C_3H_8, and CO_2 adsorption in the temperature range of 25 to 150 °C on uncoated, ODPA-coated, and MPA-coated 5A is shown in Figs. 2.4 and A.3. We selected ODPA and MPA coatings for these variable temperature studies to probe the effects of surface-confined and surface-penetrating coatings, respectively. At higher temperatures, C_3H_6, C_3H_8, and CO_2 had lower equilibrium loadings on all adsorbents, as expected for exothermic adsorption processes, and C_3H_8 had a greater decrease in equilibrium loading than C_3H_6. With the increase of temperature, the gases required less time to reach adsorption equilibrium on uncoated and ODPA-coated 5A. For MPA-coated 5A, C_3H_6 and C_3H_8 still had not reached equilibrium after 120 min at 150 °C.

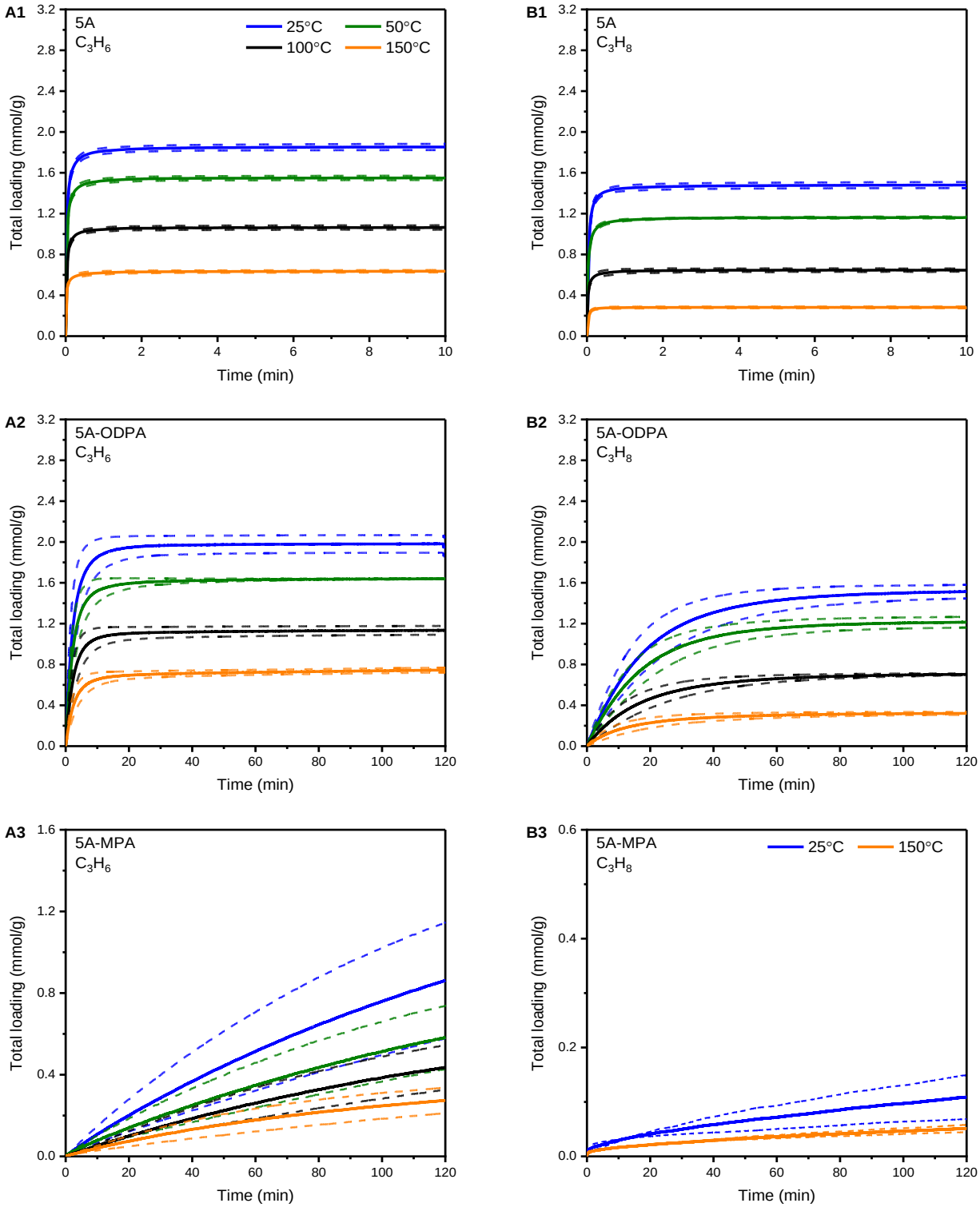

Figure 2.4. Temperature dependence (25–150 °C) of C_3H_6 (A1, A2, and A3) and C_3H_8 (B1, B2, and B3) adsorption on uncoated, ODPA-, and MPA-coated 5A. Uncertainty bounds are generally based on standard deviations of triplicates for separately prepared samples, with the exception of C_3H_6 and C_3H_8 adsorption on 5A-MPA, where the dashed curves represent the span of duplicates.

The equilibrium selectivity of C_3H_6/C_3H_8 adsorption increased as the temperature increased from 25 to 150 °C on both uncoated and ODPA-coated 5A, as shown in Fig. 2.5. For uncoated 5A, selectivity was nearly constant with time at all temperatures, and the equilibrium selectivity was below 2.4 even at 150 °C (Fig. 2.5A). For ODPA-coated 5A, the kinetic selectivity was initially >8 and then decreased with time at all temperatures (Fig. 2.5B). After the adsorption approached equilibrium, the equilibrium selectivity was similar to that for uncoated 5A at the same temperature. The temperature influence on the initial selectivity was not strong, so that kinetic selectivity was less sensitive to temperature than equilibrium selectivity.

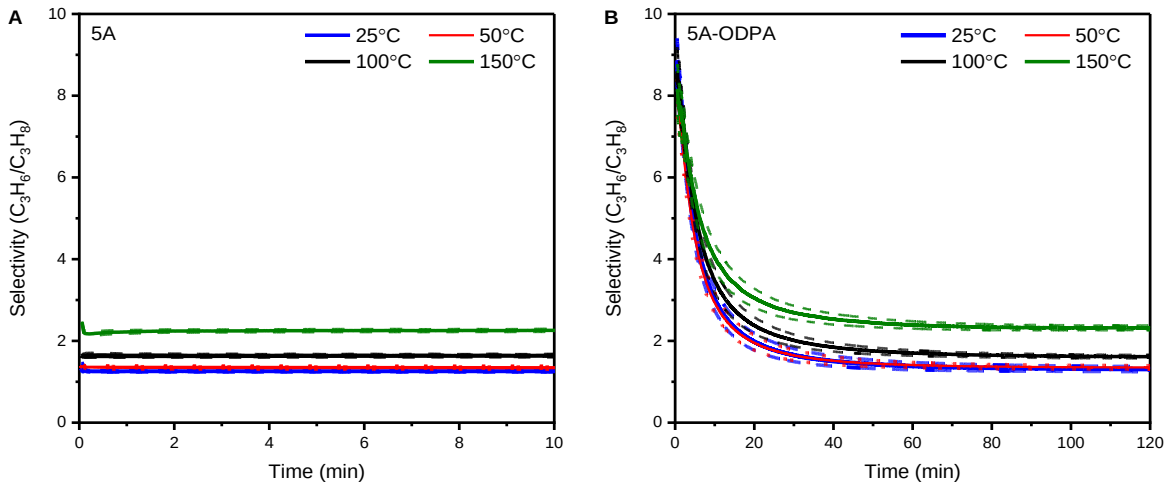

Figure 2.5. C_3H_6/C_3H_8 ideal selectivities as a function of temperature and time on (A) uncoated and (B) ODPA-coated 5A. The dashed curves represent the uncertainty bounds based on standard deviations of triplicates for separately prepared samples.

Based on the temperature-dependent equilibrium loading data, the standard enthalpy changes ΔH^0 and standard entropy changes ΔS^0 of C_3H_6, C_3H_8 and CO_2 adsorption on zeolite 5A were calculated (Table 2.1) from plots of ln $[((p_i - p_e)/p^0)/(p_e/p^0)]$ versus $1/T$ (Fig. A.4). The enthalpy changes ΔH^0 of adsorption was more negative for C_3H_8 than C_3H_6, with a difference ($\Delta H^0_{C3H8} - \Delta H^0_{C3H6}$) of -4.1 kJ/mol, so

rising temperature was found to disfavor the adsorption of C_3H_8 and result in higher equilibrium selectivity (Fig. 2.5A). Adsorption of CO_2 had a more negative enthalpy than C_3H_6 and C_3H_8, so its equilibrium loading was more sensitive to temperature, as shown in Figs. A.3, 2.4A1, and 2.4B1. The small enthalpy changes for C_3H_6, C_3H_8 and CO_2 adsorption on zeolite 5A are in favor of energy management of the process and the regeneration of adsorbent.

Table 2.1 Standard enthalpy changes ΔH^0 and standard entropy changes ΔS^0 of C_3H_6, C_3H_8, and CO_2 adsorption on uncoated zeolite 5A.

5A	C_3H_6	C_3H_8	CO_2
ΔH^0 (kJ/mol)	-12.1 ± 0.5	-16.2 ± 0.5	-29.5 ± 1.0
ΔS^0 (J/mol·K)	-35.1 ± 1.4	-52.9 ± 1.6	-85.5 ± 2.7

2.4.3. Diffusion modeling of kinetic adsorption

To determine the rate-limiting resistance of gas diffusion into zeolite 5A coated with PAs, gas adsorption measured in the temperature range of 25–150 °C was simulated using an internal diffusion model and a surface limitation model. The fitting was appraised using the adjusted R^2, where the model with a higher adjusted R^2 would be a better fit. For instance, C_3H_6 adsorption on MPA-coated 5A in the temperature range of 25–150 °C had adjusted R^2 in the range of 0.86–0.88 from internal diffusion model while they were all nearly 1 from surface limitation model (Table A.10). Therefore, the surface limitation model was a better fit than the internal diffusion model in this case. On uncoated 5A for CO_2, C_3H_6, and C_3H_8 adsorption, the internal diffusion model resulted in higher adjusted R^2 values and so fit better than the surface limitation model (Figs. 2.6A and A.6–A.8, Tables A.3–A.5). For ODPA- and MPA-coated 5A, the internal diffusion model still provided a better fit for CO_2

adsorption, but the surface limitation model was a much better fit for C_3H_6 adsorption on 5A-ODPA and 5A-MPA and also for C_3H_8 adsorption on 5A-ODPA (Figs. 2.6B and A.9–A.13, Tables A.6–A.10). The simulation of C_3H_8 adsorption on 5A-MPA was not conducted since the uptake was low, only 0.15 mmol/g after 120 min, so that it had a big relative error. The observation of surface limitation in the case of the PA-modified zeolites was intuitive given that: (1) previous work had shown that PAs were confined to the surface of the zeolites [24]; and (2) the observations in the current work showed that PAs drastically changed adsorption rates and selectivities. In addition, for adsorption with relatively fast diffusion rates, including C_3H_6 and C_3H_8 adsorption on uncoated 5A and CO_2 adsorption on uncoated 5A and PA-coated 5A, the fitting curves from both models deviated from experimental data at the inflection points of the curves, especially for CO_2 adsorption on uncoated 5A. We tested the effect of using different time scales for the fits; here, longer times provide more emphasis to the final equilibration process, whereas shorter times emphasize the initial rise in uptake to a greater extent. In particular, models for adsorption times near the inflection points (0.2, 0.5, and 1 min) were studied; although the fits in all cases showed some deviation from experiment, the internal diffusion model was always superior to surface limitation model for CO_2 adsorption on uncoated 5A (Table A.11).

With PA modification, the dominant diffusion resistance for C_3H_6 and C_3H_8 changed such that the surface penetration model clearly provided the better fit. We proposed that PAs functioned as “gate-keepers” by adding an additional diffusion barrier to gas adsorption (through the presence of an organic film that restricted

access to the pore opening) and decreasing the diffusion rate more for C_3H_8 than C_3H_6. The PA modifiers decreased the diffusion rates of C_3H_6 and C_3H_8, and MPA had more influence than ODPA. According to the diffusion models, the notion that the effects of ODPA, BPA, and TBPA modification would improve kinetic selectivity through adding a surface resistance layer was also consistent with the similar equilibrium selectivity observed for those coatings and the uncoated zeolite.

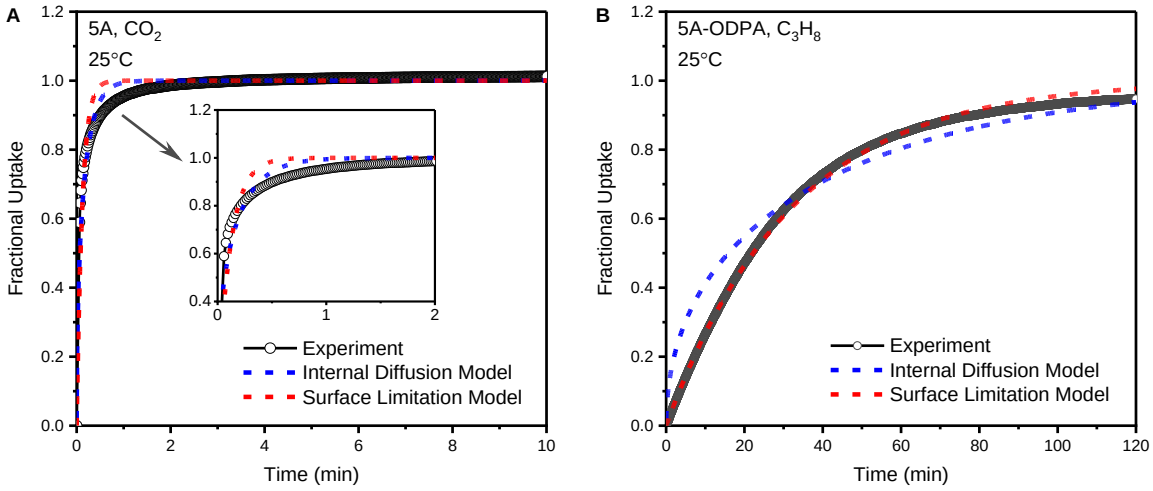

Figure 2.6. Modeling of uptake curves for (A) CO_2 on uncoated and (B) C_3H_8 on ODPA-coated 5A at 25 °C.

Based on the diffusion rate constants K in the temperature range of 25–150 °C, plots of ln K versus $1/T$ (Fig. A.5) were generated, and the apparent activation energies E_a of C_3H_6, C_3H_8 and CO_2 were determined as listed in Table 2.2. The activation energy is related to the enthalpy barrier for gas molecules to diffuse into zeolites in the adsorption process. In uncoated, ODPA-, and MPA-coated 5A, the diffusion enthalpy barrier for CO_2 was higher than C_3H_6, i.e. CO_2 diffusion was more sensitive to temperature despite being a smaller molecule. In ODPA-coated 5A, the apparent activation energies of C_3H_6 and C_3H_8 were small and of a similar magnitude,

so that the initial selectivity was essentially temperature insensitive (Fig. 2.5B). The standard deviation of activation energy for CO_2 adsorption was greater, which was ascribed to the CO_2 adsorption rate being fast, such that fewer data points could be obtained before equilibration. Though, the activation energy of CO_2 adsorption on uncoated 5A was not significantly affected by the time span employed for the modelling (Table A.11).

Table 2.2 Apparent activation energies (determined by Arrhenius analysis of fitted rate parameters) of C_3H_6, C_3H_8, and CO_2 adsorption on uncoated, ODPA-, and MPA-coated 5A.

Adsorbate	E_a (kJ/mol)		
	5A	5A-ODPA	5A-MPA
C_3H_6	1.8 ± 0.4	1.0 ± 0.2	0.5 ± 0.1 [a]
C_3H_8	3.6 ± 0.2	2.2 ± 0.2	/ [b]
CO_2	9.8 ± 1.1	9.7 ± 1.8	7.4 ± 1.0

* The surface limitation model was employed for C_3H_6 and C_3H_8 adsorption on PA-coated 5A, and the internal diffusion model for the others.
[a] From duplicate measurement, and the others from triplicates.
[b] The loadings of C_3H_8 on MPA-coated 5A at 25 and 150 °C were both small, and consequently its activation energy was not determined.

Although we can conclude long-chain PA coatings function by adding a diffusion resistance that differs for different gases, the precise mechanism for selective suppression of C_3H_8 diffusion is not clear. Based on the higher diffusion rates for both C_3H_6 and C_3H_8 on the BPA-coated zeolite than the ODPA-coated, we proposed that diffusion was controlled in part by the thickness of the organic layer. Interestingly, the difference in diffusion rates for C_3H_6 and C_3H_8 in ODPA-coated 5A appeared to be largely entropically driven, i.e. there was a significant difference in pre-exponential factors (Table A.2) rather than activation energies in the Arrhenius analysis. Thus, the more rapid diffusion of C_3H_6 through ODPA might be driven by a

larger number of available configurations in the closely packed monolayer film. Molecular dynamics simulations may be needed to provide molecular insights into the diffusion pathways available for different gases in these organic films.

Coatings of PAs on the surface of zeolites changed the dominant diffusion barrier for gas molecules from pore channels to coating layers, thereby improving the kinetic selectivity of C_3H_6 over C_3H_8 by preferentially decreasing the diffusion rate of C_3H_8. Moreover, the diffusion rates (and thus kinetic selectivities) of gases can apparently be controlled by varying the structure of PAs, including parameters such as alkyl chain length and steric configuration. Other structural variations (e.g., incorporation of unsaturated groups or heteroatoms) could lead to further ability to tune kinetic adsorption rates. The ideal selectivity of C_3H_6/C_3H_8 adsorption was investigated in this work, but further measurements are needed for gas mixture separation with PA-coated zeolites for practical application. Compared with the approaches to modify the bulk structure of zeolites for gas separation, this approach has potential to provide another lever to tune the diffusion rates of gases by choosing suitable PAs and zeolites. Such an approach may be broadly applicable to diverse adsorbents, i.e., a kinetically selective coating can enhance performance for an underlying equilibrium-selective material.

2.5. Conclusions

Modification of zeolite 5A with PAs was shown to increase the diffusion resistance of C_3H_6 and C_3H_8, which changed the rate-limiting step from internal

diffusion to surface penetration and provided a basis for kinetic separation. For both uncoated and ODPA-coated 5A, the equilibrium selectivity of C_3H_6/C_3H_8 adsorption increased when rising temperature, and the kinetic selectivity was less sensitive to temperature than equilibrium selectivity. The modifier ODPA (with a longer alkyl chain) decreased the diffusion rates of C_3H_6 and C_3H_8 more than BPA (with a shorter alkyl chain), and TBPA (with a sterically bulkier configuration) had the least effect on diffusion rates. The zeolite 5A coated with ODPA had an initial ideal selectivity of C_3H_6/C_3H_8 adsorption >8, and it had higher kinetic selectivity than uncoated 5A within 80 min, making it potentially attractive for efficient adsorptive separation of C_3H_6 and C_3H_8.

2.6. References

[1] A. Akah, M. Al-Ghrami, Maximizing propylene production via FCC technology, Appl. Petrochem. Res. 5 (2015) 377–392. https://doi.org/10.1007/s13203-015-0104-3.

[2] D.S. Sholl, R.P. Lively, Seven chemical separations to change the world, Nature 532 (2016) 435–437. https://doi.org/10.1038/532435a.

[3] R. Faiz, K. Li, Polymeric membranes for light olefin/paraffin separation, Desalination. 287 (2012) 82–97. https://doi.org/10.1016/j.desal.2011.11.019.

[4] F.A. Da Silva, A.E. Rodrigues, Vacuum swing adsorption for propylene/propane separation with 4A zeolite, Ind. Eng. Chem. Res. 40 (2001) 5758–5774. https://doi.org/10.1021/ie0008732.

[5] H. Maghsoudi, H. Abdi, A. Aidani, Temperature- and pressure-dependent adsorption equilibria and diffusivities of propylene and propane in pure-silica Si-CHA zeolite, Ind. Eng. Chem. Res. 59 (2020) 1682–1692. https://doi.org/10.1021/acs.iecr.9b05451.

[6] L. Li, R.B. Lin, R. Krishna, X. Wang, B. Li, H. Wu, J. Li, W. Zhou, B. Chen, Flexible-robust metal-organic framework for efficient removal of propyne from propylene, J. Am. Chem. Soc. 139 (2017) 7733–7736. https://doi.org/10.1021/jacs.7b04268.

[7] M.H. Weston, Y.J. Colón, Y.S. Bae, S.J. Garibay, R.Q. Snurr, O.K. Farha, J.T. Hupp, S.T. Nguyen, High propylene/propane adsorption selectivity in a

copper(catecholate)-decorated porous organic polymer, J. Mater. Chem. A. 2 (2014) 299–302. https://doi.org/10.1039/C3TA12999C.
[8] A. Ortiz, L.M. Galán, D. Gorri, A.B. de Haan, I. Ortiz, Reactive ionic liquid media for the separation of propylene/propane gaseous mixtures, Ind. Eng. Chem. Res. 49 (2010) 7227–7233. https://doi.org/10.1021/ie100576r.
[9] G. Yu, L. Deng, A.A. Abdeltawab, S.S. Al-Deyab, X. Chen, J. Zhang, Functional solution composed of Cu(I) salt and ionic liquids to separate propylene from propane, Ind. Eng. Chem. Res. 53 (2014) 13430–13435. https://doi.org/10.1021/ie501522m.
[10] S. Kasahara, E. Kamio, R. Minami, H. Matsuyama, A facilitated transport ion-gel membrane for propylene/propane separation using silver ion as a carrier, J. Membr. Sci. 431 (2013) 121–130. https://doi.org/10.1016/j.memsci.2012.12.026.
[11] M.L. Chng, Y. Xiao, T.S. Chung, M. Toriida, S. Tamai, Enhanced propylene/propane separation by carbonaceous membrane derived from poly (aryl ether ketone)/2,6-bis(4-azidobenzylidene)-4-methyl-cyclohexanone interpenetrating network, Carbon 47 (2009) 1857–1866. https://doi.org/10.1016/j.carbon.2009.03.032.
[12] Y. Pan, T. Li, G. Lestari, Z. Lai, Effective separation of propylene/propane binary mixtures by ZIF-8 membranes, J. Membr. Sci. 390–391 (2012) 93–98. https://doi.org/10.1016/j.memsci.2011.11.024.
[13] S. Shrestha, P.K. Dutta, Modification of a continuous zeolite membrane grown within porous polyethersulfone with Ag(I) cations for enhanced propylene/propane gas separation, Microporous Mesoporous Mater. 279 (2019) 178–185. https://doi.org/10.1016/j.micromeso.2018.12.032.
[14] J. Liu, J. Goss, T. Calverley, Y. Liu, C. Broomall, J. Kang, R. Golombeski, D. Anaya, B. Moe, K. Mabe, G. Watson, A. Wetzel, Carbon molecular sieve fiber with 3.4–4.9 angstrom effective micropores for propylene/propane and other gas separations, Microporous Mesoporous Mater. 305 (2020) 110341. https://doi.org/10.1016/j.micromeso.2020.110341.
[15] R.J. Swaidan, B. Ghanem, R. Swaidan, E. Litwiller, I. Pinnau, Pure- and mixed-gas propylene/propane permeation properties of spiro- and triptycene-based microporous polyimides, J. Membr. Sci. 492 (2015) 116–122. https://doi.org/10.1016/j.memsci.2015.05.044.
[16] M. Guo, M. Kanezashi, Recent progress in a membrane-based technique for propylene/propane separation, Membranes. 11 (2021) 310. https://doi.org/10.3390/membranes11050310.
[17] X. Ma, P. Kumar, N. Mittal, A. Khlyustova, P. Daoutidis, K.A. Mkhoyan, M. Tsapatsis, Zeolitic imidazolate framework membranes made by ligand-induced permselectivation, Science 361 (2018) 1008–1011. https://doi.org/10.1126/science.aat4123.
[18] Y. Li, L. Li, J. Yu, Applications of zeolites in sustainable chemistry, Chem. 3 (2017) 928–949. https://doi.org/10.1016/j.chempr.2017.10.009.

[19] C.A. Grande, J. Gascon, F. Kapteijn, A.E. Rodrigues, Propane/propylene separation with Li-exchanged zeolite 13X, Chem. Eng. J. 160 (2010) 207–214. https://doi.org/10.1016/j.cej.2010.03.044.
[20] J.G. Min, K.C. Kemp, S.B. Hong, Propylene/propane separation on a ferroaluminosilicate levyne zeolite, Microporous Mesoporous Mater. 294 (2020) 109833. https://doi.org/10.1016/j.micromeso.2019.109833.
[21] C.D. Chudasama, J. Sebastian, R.V. Jasra, Pore-size engineering of zeolite A for the size/shape selective molecular separation, Ind. Eng. Chem. Res. 44 (2005) 1780–1786. https://doi.org/10.1021/ie049333l.
[22] X. Xu, X. Zhao, L. Sun, X. Liu, Adsorption separation of carbon dioxide, methane and nitrogen on monoethanol amine modified ß-zeolite, J. Nat. Gas Chem. 18 (2009) 167–172. https://doi.org/10.1016/S1003-9953(08)60098-5.
[23] Q. Dong, Z. Song, F. Zhou, H. Li, M. Yu, Ultrathin, fine-tuned microporous coating modified 5A zeolite for propane/propylene adsorptive separation, Microporous Mesoporous Mater. 281 (2019) 9–14. https://doi.org/10.1016/j.micromeso.2019.02.038.
[24] L.D. Ellis, S.T. Parker, J. Hu, S.F. Zaccarine, M.J. Stellato, H.H. Funke, C. Sievers, S. Pylypenko, J.L. Falconer, J.W. Medlin, Tuning gas adsorption selectivity and diffusion rates in zeolites with phosphonic acid monolayers, Cell Rep. Phys. Sci. 1 (2020) 100036. https://doi.org/10.1016/j.xcrp.2020.100036.
[25] H. Abdi, H. Maghsoudi, All-silica DD3R zeolite for adsorptive separation of propylene from propane: Equilibrium and kinetic data, Microporous Mesoporous Mater. 307 (2020) 110513. https://doi.org/10.1016/j.micromeso.2020.110513.
[26] D.M. Ruthven, Diffusion in type A zeolites: New insights from old data, Microporous Mesoporous Mater. 162 (2012) 69–79. https://doi.org/10.1016/j.micromeso.2011.12.025.
[27] O. Cheung, N. Hedin, Zeolites and related sorbents with narrow pores for CO_2 separation from flue gas, RSC Adv. 4 (2014) 14480–14494. https://doi.org/10.1039/C3RA48052F.
[28] W. Zhu, F. Kapteijn, J.A. Moulijn, Shape selectivity in the adsorption of propane/propene on the all-silica DD3R, Chem. Commun. (1999) 2453–2454. https://doi.org/10.1039/a906465f.
[29] M. Gehre, Z. Guo, G. Rothenberg, S. Tanase, Sustainable separations of C_4-hydrocarbons by using microporous materials, ChemSusChem. 10 (2017) 3947–3963. https://doi.org/10.1002/cssc.201700657.
[30] T.D. Pham, R.F. Lobo, Adsorption equilibria of CO_2 and small hydrocarbons in AEI-, CHA-, STT-, and RRO-type siliceous zeolites, Microporous Mesoporous Mater. 236 (2016) 100–108. http://dx.doi.org/10.1016/j.micromeso.2016.08.025.

Chapter 3: Competitive adsorption between propylene and propane on zeolite 5A and the influence of organic phosphonic acid coatings

3.1. Abstract

Understanding competitive adsorption between propylene (C_3H_6) and propane (C_3H_8) in mixtures is essential for the development of an adsorptive separation process, a promising alternative to energy-intensive distillation, to produce polymer-grade propylene. This work investigated the selective adsorption of C_3H_6 over C_3H_8 on zeolite 5A using a pulse injection method, followed by temperature-programmed desorption (TPD) to investigate desorption kinetics. In mixture adsorption on uncoated 5A, C_3H_6/C_3H_8 selectivity increased markedly with cumulative gas exposure, such that it reached ~26 from an equimolar mixture at high exposures; in contrast, the ideal selectivity measured from single-gas adsorption was only ~1.6. TPD experiments indicated that mixture selectivity was higher than ideal selectivity because C_3H_6, having a stronger affinity for the zeolite, hindered C_3H_8 adsorption and displaced pre-adsorbed C_3H_8. To gain further insights into the roles of pore diffusion versus surface penetration in the separation mechanism, zeolite 5A was also modified with *tert*-butylphosphonic acid (TBPA) or *n*-octadecylphosphonic acid (ODPA). These coatings imposed an additional diffusion barrier that hindered C_3H_8 transport more substantially than C_3H_6, with highly dense ODPA having more effect than sterically bulky TBPA. While the coatings were selective to C_3H_6 transport, their effect on overall selectivity in mixture adsorption was complex: initial selectivity was higher than on uncoated 5A, but the selectivity on PA-coated zeolites did not improve as

rapidly with exposure time. Thus, design of optimal composite materials for selective adsorption must account for both barriers to gas diffusion and competition for adsorption sites between adsorbates.

3.2. Introduction

The separation of propylene/propane (C_3H_6/C_3H_8) mixtures to produce polymer-grade propylene (desired purity ≥99.5%), mainly used for the manufacture of polypropylene, is of great importance [1,2]. The C_3H_6/C_3H_8 mixtures are mainly produced by steam cracking of naphtha and during fluid catalytic cracking of gas oils in refineries, with C_3H_6 purities of 50–60% and 80–87%, respectively [3]. Due to the low and similar boiling points of C_3H_6 and C_3H_8 (225.6 K and 231.2 K, respectively), the distillation separation process is energy-intensive, requiring sub-ambient temperature of 183–233 K, high pressure of 16–20 bar, and towers with 150–200 stages [4,5]. A promising energy-efficient alternative is adsorptive separation based on equilibrium uptakes (equilibrium separation), molecular sieving effect (steric separation), or adsorption rates (kinetic separation) [6–8].

In equilibrium separation for olefin/paraffin, the adsorbents generally have strong affinity towards olefin compared to paraffin. The materials which can form π-complexation with olefins are usually used, such as zeolites modified with metal cations Li-13X [9], Ag-X [10], and Cs-ZK-5 [11], metal organic frameworks (MOFs) with open metal sites Co-MOF-74 [12], Fe_2(dobdc) [13], and Cu@MIL-101(Cr) [14], and covalent organic framework (COF) hexene-covalent triazine framework (CTF)

[15]. Moreover, hydrogen-bonded organic framework (HOF) HOF-16 with free -COOH sites and suitable pore confinement can selectively adsorb olefins, and its regeneration is easy due to the weak binding with olefins [16].

To utilize the sieving effect for the separation of C_3H_6 and C_3H_8, adsorbents with precisely controlled pore structures have been used, such as zeolites 4A and SAPO-14 [17], MOF materials KAUST-7 [18] and Y-abtc [3]. The MOF material JNU-3a realized high C_3H_6/C_3H_8 selectivity by featuring dynamic molecular pockets opening to one-dimension diffusion channels [19]. It was recently reported that the local sieving channels of ZU-609 enabled high selectivity and gas diffusion rates [20]. Moreover, HOF material HOF-FJU-1 achieved high selectivity and gas capacity benefited from highly discriminating gating effect under elevated temperatures [21].

In kinetic separation, porous materials with suitable aperture windows or pore channels have been utilized, such as zeolites DD3R [22], SiCHA [23], ITQ-55 [24], and ZSM-58 [25], carbon materials CMS [26] and CNP [27], and MOF materials ELM-12 [6], ZIF-8 [28], and Zn-ATA [29]. The kinetic separation process is generally more energy-efficient than equilibrium separation for recovering C_3H_6 from adsorbents due to the absence of strong interactions, and it has less serious problems of gas diffusion and adsorbent regeneration in steric separation with strong restriction of the pore structures [6]. The adsorption selectivity of kinetic separation can be improved by tuning the pore structures of adsorbents, e.g. by functionalizing the external surfaces of adsorbents with additional diffusion layers or functional groups [30,31] or by tuning the pore openings with deposition of coatings on adsorbent surfaces [32].

Modification with self-assembled monolayers of organic phosphonic acids (PAs) is a promising method to tune the properties of metal oxide surfaces, in which covalent bonds are formed between PA and hydroxyl surface through condensation reactions [33,34]. As discussed in Chapter 2, the PA coatings on zeolite surfaces can control the relative adsorption rates of pure-component C_3H_6 and C_3H_8 by varying the molecular structure of the PAs, such as changing the alkyl chain length and steric configuration of the PAs [35,36]. Single-gas, pressure-decay adsorption measurements revealed that PA monolayers on zeolite 5A significantly enhanced the kinetic selectivity of C_3H_6/C_3H_8, and the kinetic modeling with an internal diffusion model and a surface limitation model showed that PA coatings changed the diffusion rate-limiting step from zeolite pore channels to the PA coating layers at the external surfaces of the zeolites [36]. However, this previous study focused on the effect of PA coatings on single-gas diffusion and ideal selectivity. Further measurements, such as breakthrough and mixture adsorption selectivity, are needed to examine the performance of PA-coated zeolites as potential adsorbents for the adsorptive separation of C_3H_6/C_3H_8 in mixtures.

In an adsorptive separation process, the difference in interactions of gas components with adsorbent surfaces can affect mixture adsorption selectivity, which may be quite different from ideal selectivity measured with single-gas adsorption. Campo et al. [37] reported that the displacement of pre-adsorbed C_3H_8 by C_3H_6 on zeolite 13X was observed in the breakthrough curve for a 75/25 (molar ratio) C_3H_6/C_3H_8 mixture, and the authors attributed this displacement to stronger

adsorption of C_3H_6 than C_3H_8 on zeolite 13X. Chai et al. [38] found that in the adsorption of an equimolar mixture of acetylene (C_2H_2) and ethylene (C_2H_4) on zeolite Ni@FAU, little C_2H_4 adsorbed, and the dynamic separation selectivity of C_2H_2/C_2H_4 was up to 100, whereas the ideal selectivity was only 1.5. Their successive adsorption experiments showed that C_2H_2 displaced pre-adsorbed C_2H_4 on Ni@FAU, and they ascribed this to strong binding of C_2H_2 with the zeolite; this was confirmed by differential scanning calorimetry and in situ Fourier transform infrared spectroscopy. Abedini et al. [39] reported that the mole fraction of C_3H_8 in the effluent from a 30/30/40 (molar ratio) C_3H_6/C_3H_8/Ar feed mixture was as high as 0.59 in a breakthrough measurement on Cu-MOF-74, which was higher than expected if no C_3H_6 was in the effluent. The excess C_3H_8 in the effluent was ascribed to the displacement of pre-adsorbed C_3H_8 by C_3H_6 due to the stronger affinity of adsorbent towards C_3H_6; this was confirmed by the higher heat of adsorption for C_3H_6 than C_3H_8. Similar displacement phenomenon in mixture adsorption was observed in systems using zeolite ITQ-55 [24], MOF material ZU-36-Ni [40], and HOF material HOF-FJU-1 [21].

In this chapter, the adsorptive separation performance of uncoated zeolite 5A and the same material coated with PAs was measured for C_3H_6/C_3H_8 mixtures and compared with single-gas adsorption measurements. We found that mixture adsorption yielded surprising improvements in selectivity, which were not apparent from prior single-gas measurements. To understand the origins of the improved selectivity, we investigated the interactions of gas components with the zeolite as a

function of gas exposure by means of successive adsorption of pure-component C_3H_6 and C_3H_8 and by mixture adsorption on uncoated and PA-coated zeolite 5A. Adsorption experiments were followed by temperature-programmed desorption (TPD) to quantify gas desorption kinetics. To control the surface barriers to gas diffusion, we studied a sterically bulkier PA (*tert*-butylphosphonic acid, TBPA) and a long, linear chain PA (*n*-octadecylphosphonic acid, ODPA) on the zeolite surfaces. We found that C_3H_6/C_3H_8 selectivity was related to cumulative gas exposure and diffusion resistance through the PA coating layers on the zeolite surfaces, which may provide support for the design of adsorbents and adsorptive separation processes.

3.3. Experimental

3.3.1. Materials and characterization

The PA-coated zeolite 5A used in this work was synthesized based on the procedures reported previously [35,36]. For the synthesis, 830 mg of zeolite 5A calcined at 673 K in air for 4 h was added to 200-mL solution (0.01 mol/L) of PA in tetrahydrofuran (THF), then stirred for 16 h, and centrifuged at 8000 rpm for 9 min. The solvent was decanted, and the solid was annealed at 393 K for 6 h, then rinsed with THF for four times, and dried in a vacuum oven at room temperature. Zeolite 5A (LTA type), $Ca_nNa_{12-2n}[(AlO_2)_{12}(SiO_2)_{12}]$ xH_2O (powder, <10 μm, Sigma-Aldrich 233676), *tert*-butylphosphonic acid (TBPA, ≥97.5%, Acros Organics 321520050), *n*-octadecylphosphonic acid (ODPA, ≥96.0%, Alfa Aesar 20645), and THF (high-performance liquid chromatography grade, Fisher Chemical T425-4) were used as

received. The uncoated zeolite 5A in the result section was zeolite 5A calcined at 673 K in air for 4 h, cooled, then put through deposition process in THF solvent without a PA modifier.

The crystal structures of the materials were characterized on an X-ray diffractometer (XRD), Rigaku Smartlab model, with a Cu K_α radiation source, using standard 2D detection from 7 to 40° (angle 2θ) with a step of 0.01° and a scan rate of 2°/min. The porosities were determined by nitrogen (≥99.999%, Airgas) adsorption isotherms at 77 K measured on a surface characterization analyzer, 3Flex model (Micromeritics Instruments). Based on the N_2 adsorption isotherms, the total surface areas were determined with the Brunauer-Emmett-Teller (BET) multi-point method [41] using relative pressure p/p^0 in the range of 10^{-7}–0.05. The external surface areas (pore size >2.5 nm) were determined with the t-plot method [42] using p/p^0 in the range of 0.20–0.40. The micropore size distributions were determined with the Horvath-Kawazoe (HK) method [43]. Besides the N_2 adsorption isotherms, the adsorption capacities of the materials were measured by pressure-decay adsorption using probe molecule CO_2 (≥99.999%, Airgas) at room temperature under manifold pressure of 40 kPa and by CO_2 isotherms at 300 K in the pressure range of 2–800 mmHg on an Autosorb-1 apparatus (Quantachrome Instruments) equipped with a custom LabVIEW-based data acquisition system. The thermal stability of PA modifiers was tested by TPD from 298 to 823 K with a heating rate of 8 K/min under 20 SCCM of helium carrier gas, and the gas composition from desorption was analyzed on a quadrupole mass spectrometer (MS, Balzers Prisma QME 200)

interfaced to the flow system via a capillary line.

3.3.2. Adsorption and desorption measurements

High purity C_3H_6 gas (≥99.5%, Airgas) and C_3H_8 gas (≥99.5%, Airgas) were used for adsorption. In the apparatus as shown in Fig. B.1, the gases were adsorbed with pulse injection over a 200-mg fixed bed (10 mm in diameter and 5 mm in height) of uncoated or PA-coated zeolite 5A under helium carrier gas. An equimolar C_3H_6/C_3H_8 mixture was prepared by mixing 0.5 mL of each gas in a 1-mL syringe, and a 90/10 C_3H_6/C_3H_8 mixture was prepared by mixing 0.9 mL C_3H_6 with 0.1 mL C_3H_8. The cumulative gas exposure was controlled by changing the number of injections (1.0 mL per dose), and the time interval between injections was 3.6 min. The flow rate of the helium carrier gas was adjusted using a mass flow controller, in which the space time was 1.2 s for the gas passing through the bed when 20 SCCM of gas flow was used. Before adsorption measurements, the uncoated and PA-coated zeolite 5A were pretreated at 523 K for 2 h under 20 SCCM of helium carrier gas. Adsorption of pure-component C_3H_6 and C_3H_8, an equimolar C_3H_6/C_3H_8 mixture, and a 90/10 C_3H_6/C_3H_8 mixture was carried out at 298 K under atmospheric pressure. After gas adsorption, desorption rates and yields were measured by TPD from 298 to 523 K with a heating rate of 8 K/min under helium carrier gas with the same flow rate as in adsorption.

Gas composition was analyzed using a mass spectrometer (Balzers Prisma QME 200). In the mass spectrometer fragmentation pattern for C_3H_8, the highest-intensity signal is from the mass/charge (m/z) 29 fragment, which is specific to C_3H_8

since C_3H_6 does not produce m/z 29. The highest-intensity signal for C_3H_6 is from m/z 41, but C_3H_8 also produces m/z 41 with weak intensity. The intensity ratio of m/z 41 to m/z 29 for C_3H_8 was determined with pure C_3H_8. For gas adsorption and desorption, the area under the signal curve for a mass fragment is proportional to the gas concentration at the bed outlet, and the gas amount was determined by calibration using 1.0 mL C_3H_6 and 1.0 mL C_3H_8, separately, without adsorbents in the bed. The selectivity (loading ratio of C_3H_6 to C_3H_8 at the same adsorption time divided by the ratio of components in the feed) was determined for single-gas adsorption measurement (ideal selectivity) and C_3H_6/C_3H_8 mixture adsorption (mixture selectivity). The relative concentration C/C_0 (gas concentration of a species in the effluent relative to that in the feed) in adsorption and the gas purity (gas concentration of a species relative to the total in the effluent) in sorption were determined.

3.3.3. TPD profile analysis

The desorption rates from TPD profiles were fit with a first-order model [44,45]. The desorption activation energy E_a and the rate constant pre-exponential factor ν were determined by non-linear regression fitting of the desorption rates $-d\theta/dt$ versus temperature, where t is the desorption time, and θ is the fractional gas coverage on the zeolite (the ratio of gas loading at desorption time t to the maximum loading in adsorption). The coefficient of determination indicated the goodness of fit with experimental data.

3.4. Results

3.4.1. Material structure

The deposition of TBPA and ODPA did not change the bulk crystalline structure of the zeolite, as shown by XRD (Fig. B.2). For the uncoated and TBPA coated zeolite 5A, the N_2 adsorption isotherms exhibited reversible type I(a) behavior according to the IUPAC classification (Fig. B.3A and B), which indicated microporous structures of the adsorbents; the micropores dominated the total surface areas (Table B.1), and the micropore size distributions were narrow with median pore width 5.8 Å (Fig. B.4). The diffusion barrier of N_2 into the ODPA-coated zeolite at 77 K was found to be extremely high (at relative pressure 0.05, only 0.12 mmol/g of N_2 adsorbed on the ODPA-coated 5A, whereas 7.6 mmol/g adsorbed on the uncoated 5A) (Fig. B.3C), similar to molecular sieve ZU-609 [20], making the determination of surface area via the BET method problematic. This diffusion barrier is consistent with the expectation that the ODPA coating was highly crystalline, with a low degree of chain mobility, at the low temperature of the measurement. As an alternative to estimate the effect of the coatings on adsorption site availability, the adsorption capacities of the materials were measured using CO_2. The equilibrium uptake of CO_2 on PA-coated 5A was similar to that on the uncoated zeolite, which indicated that PA coatings did not cover the adsorption sites in the zeolites (Figs. B.5 and B.6). Additionally, the PA coatings on zeolite 5A were thermally stable up to 570 K as confirmed by TPD (Fig. B.7), similar to prior measured stabilities on TiO_2 [46].

3.4.2. Single-gas measurements

Single-gas adsorption was measured for C_3H_6 and C_3H_8 using pulse injections at 298 K, and after a series of injections, TPD measured gas desorption (Fig. B.8). On uncoated 5A, the C_3H_6 loading was higher than C_3H_8 with 30 doses (1.0 mL for each dose), 2.44 ± 0.08 and 1.50 ± 0.20 mmol/g, respectively (Fig. 3.1A1). The TBPA coating did not detectably affect C_3H_6 adsorption, but it decreased the initial adsorption rate of C_3H_8 to 87% of the initial rate on uncoated 5A (Figs. 3.1B1, B.9, B.10, and Table B.2). On ODPA-coated 5A, the initial adsorption rates of C_3H_6 and C_3H_8 were 54% and 12%, respectively, of those on uncoated 5A (Figs. 3.1C1, B.9, B.10, and Table B.2). C_3H_8 adsorption on ODPA-coated 5A did not reach equilibrium after 30 doses; the slow adsorption in the pulse injection compared with pressure-decay measurement in Chapter 2 was due to the lower C_3H_8 partial pressure (1.4 kPa). It is expected that ODPA-coated 5A has similar gas equilibrium loadings as the uncoated zeolite, since PA coatings do not cover the adsorption sites in the zeolites as discussed in Section 3.4.1 above. By slowing C_3H_8 diffusion more significantly, the ODPA coating increased C_3H_6/C_3H_8 ideal selectivity to ~4 at low gas exposures, whereas on uncoated 5A, it was only ~1.6 (Fig. B.11). The effect of PA coatings on gas adsorption rates and ideal selectivity from pulse injection measurements was in agreement with the pressure-decay measurements for single-gas as discussed in Chapter 2; the PA coatings added an adsorption barrier on the zeolite surfaces [36]. We proposed that the differences in diffusion rates of C_3H_6 and C_3H_8 in ODPA coating layer were

entropically driven, where C_3H_6 had more available configurations, resulting in faster diffusion rate and higher selectivity than C_3H_8 [36].

For uncoated 5A, C_3H_6 breakthrough in single-gas adsorption took place after 8 injections, whereas C_3H_8 was detected at the outlet of the bed from the first injection (Fig. 3.1A2). The longer breakthrough time for C_3H_6 was ascribed to its stronger affinity for the zeolite. The TBPA coating did not measurably affect the C_3H_6 breakthrough time, and it did not strongly affect the C_3H_8 breakthrough, though a small increase in relative concentration C/C_0 of approximately 0.1 compared with the uncoated 5A was observed during the first ~6 injections of C_3H_8 (Fig. 3.1B2), consistent with a slightly smaller adsorption rate of C_3H_8 on TBPA-coated 5A. For ODPA-coated 5A, both C_3H_6 and C_3H_8 were detected in high concentrations at the outlet of the bed from the first injection (Fig. 3.1C2), indicating a significant barrier for adsorbate penetration.

After the breakthrough measurements, desorption was carried out using TPD. The gas amount from desorption was consistent with the uptake in adsorption (Table B.3). The TPD profiles (Fig. 3.2) showed that on uncoated 5A, the peak desorption temperature of C_3H_6 (380 K) was higher than C_3H_8 (345 K), which indicated that C_3H_6 had higher affinity for the zeolite. With a TBPA coating, the C_3H_8 desorption peak shifted to the right and broadened, with a peak temperature that increased by 6 K compared with uncoated 5A, which suggested that TBPA added a small diffusion barrier for C_3H_8 desorption, whereas it had no detectable effect on C_3H_6. On ODPA-coated 5A, the C_3H_6 peak temperature increased by 34 K compared with the uncoated

zeolite, whereas the C_3H_8 peak temperature increased by 90 K, so that C_3H_8 desorbed at a higher peak temperature than C_3H_6. This indicated that diffusion in the coating layer controlled the appearance of gases from desorption, and the diffusion barrier was higher for C_3H_8 than C_3H_6.

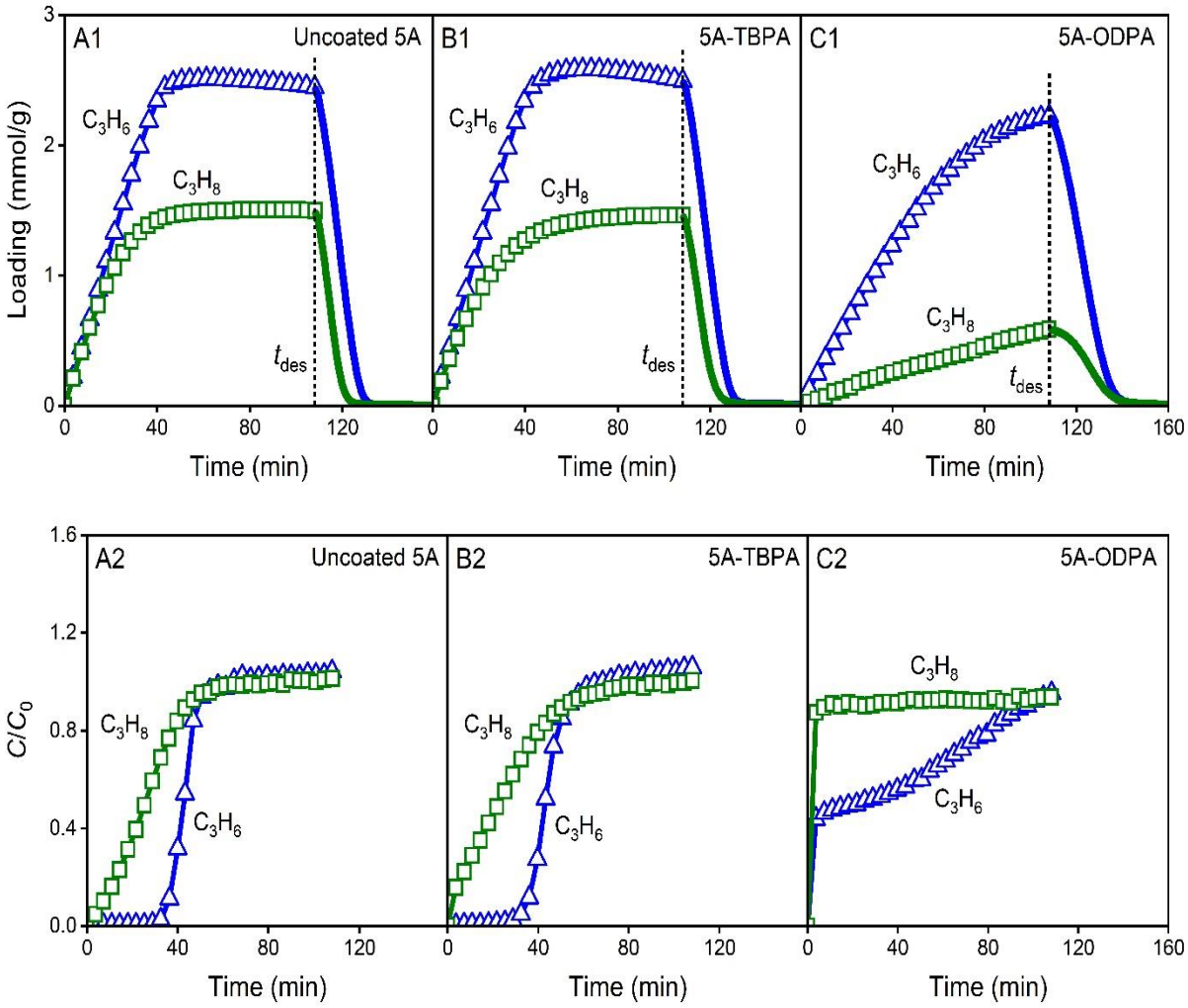

Figure 3.1. Loadings of C_3H_6 and C_3H_8 in single-gas adsorption with 30 doses (1.0 mL per dose) for each gas at 298 K, followed by TPD (start at time t_{des}), under 20 SCCM of helium, and relative concentrations C/C_0 in adsorption on (A1, A2) uncoated, (B1, B2) TBPA-, and (C1, C2) ODPA-coated zeolite 5A.

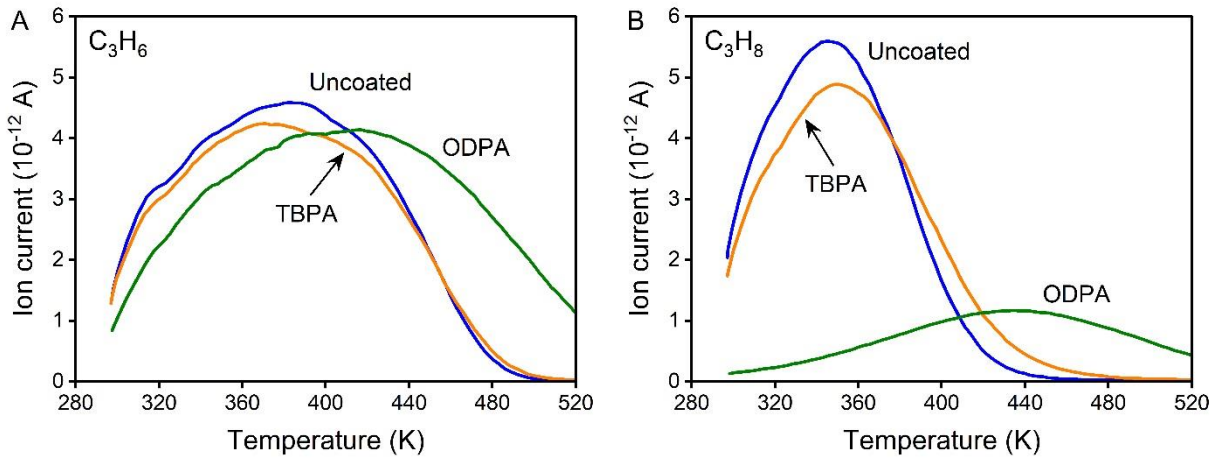

Figure 3.2. TPD curves of (A) C_3H_6 and (B) C_3H_8 from uncoated, TBPA-, and ODPA-coated zeolite 5A after single-gas adsorption with 30 doses (1.0 mL per dose) for each gas at 298 K under 20 SCCM of helium.

The TPD data for uncoated and ODPA-coated zeolite 5A after single-gas adsorption with 5 doses of C_3H_6 and C_3H_8 were fit with a first-order model (Fig. 3.3 and Table 3.1) to evaluate the trends in desorption kinetics at low loadings. On uncoated 5A, the calculated apparent activation energy of C_3H_6 desorption (41.3 ± 2.2 kJ/mol) was higher than C_3H_8 (29.9 ± 1.1 kJ/mol). With an ODPA coating, the apparent activation energies for both C_3H_6 and C_3H_8 desorption into the vapor phase were smaller than uncoated 5A, which seems surprising since the peak temperatures were higher on 5A-ODPA than uncoated 5A; for processes occurring through the same rate-limiting step, higher activation energies are expected to correlate with increased TPD peak temperatures. Interestingly, we found that the pre-exponential factors of the desorption rate constants for both gases were also much smaller on 5A-ODPA.

We proposed that ODPA modification changed the rate-limiting step of the desorption process from gas molecules leaving adsorption sites within the zeolite to their transport through the ODPA monolayer film [36]. The activation barrier

measured for the ODPA-coated 5A corresponds to a different elementary step, diffusion through the added ODPA layer, and we proposed that the interaction enthalpies of gas molecules with PA chains were lower than with adsorption sites at zeolite internal surfaces, accounting for the small apparent activation energies of C_3H_6 and C_3H_8 desorption from 5A-ODPA. Moreover, we speculated that desorbing gas molecules experienced a large entropic penalty to diffuse through the dense ODPA coating layer, accounting for the small pre-exponential factors of desorption rate constants.

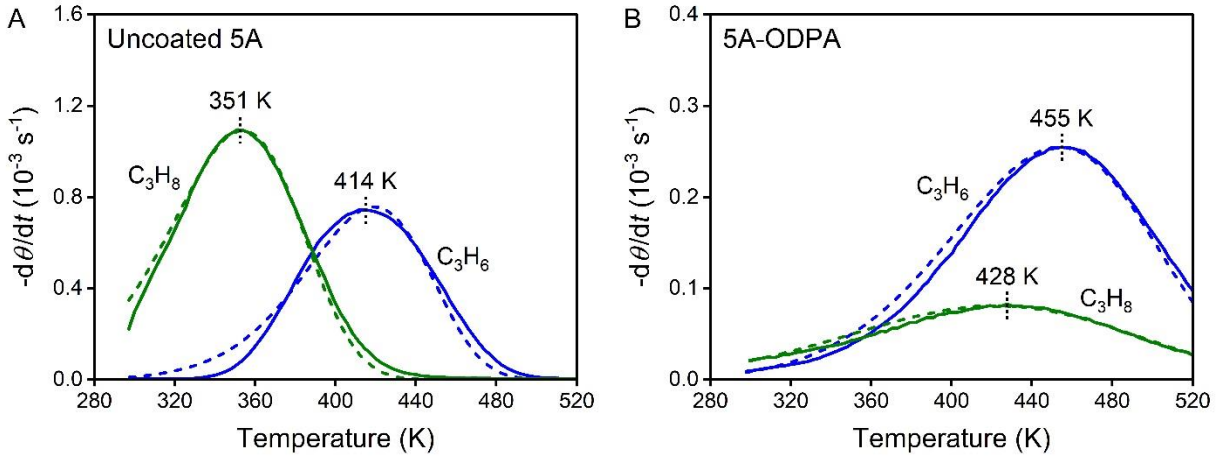

Figure 3.3. Experimental (solid curves) and simulated (dashed curves) desorption rates -dθ/dt versus temperature of C_3H_6 and C_3H_8 from (A) uncoated and (B) ODPA-coated zeolite 5A after single-gas adsorption with 5 doses (1.0 mL per dose) for each gas at 298 K under 20 SCCM of helium.

Table 3.1 Kinetic parameters from first-order modeling of C_3H_6 and C_3H_8 TPD data after single-gas adsorption on uncoated and ODPA-coated zeolite 5A.

Adsorbent	Adsorbate	E_a (kJ/mol)	ν (s^{-1})	Coefficient of determination
Uncoated 5A	C_3H_6	41.3 ± 2.2	(7.0 ± 3.3)×10^2	0.99 ± 0.01
	C_3H_8	29.9 ± 1.1	(1.3 ± 0.6)×10^2	1.00 ± 0.00
5A-ODPA	C_3H_6	30.4 ± 0.6	6.3 ± 1.4	1.00 ± 0.00
	C_3H_8	17.1 ± 0.5	0.2 ± 0.1	0.99 ± 0.01

* The standard deviations of kinetic parameters were determined from triplicate measurements.

3.4.3. Competitive adsorption on uncoated zeolite 5A

Successive adsorption measurements were performed to investigate competitive adsorption between C_3H_6 and C_3H_8 on uncoated zeolite 5A. In the "C_3H_6-first" measurement, 10 doses of C_3H_6 were injected and 2.22 mmol/g C_3H_6 adsorbed, and then 10 doses of C_3H_8 were injected and 0.46 mmol/g C_3H_8 adsorbed. The C_3H_8 displaced 0.34 mmol/g pre-adsorbed C_3H_6; that is, 15% of the C_3H_6 was displaced (Fig. 3.4A and Fig. B.12A). In contrast, when the dosing order was switched ("C_3H_8-first" measurement), C_3H_6 displaced 87% of pre-adsorbed C_3H_8 (Fig. 3.4B and Fig. B.12B). Significant displacement of pre-adsorbed C_3H_8 by C_3H_6 confirmed that C_3H_6 adsorbed more strongly on uncoated 5A.

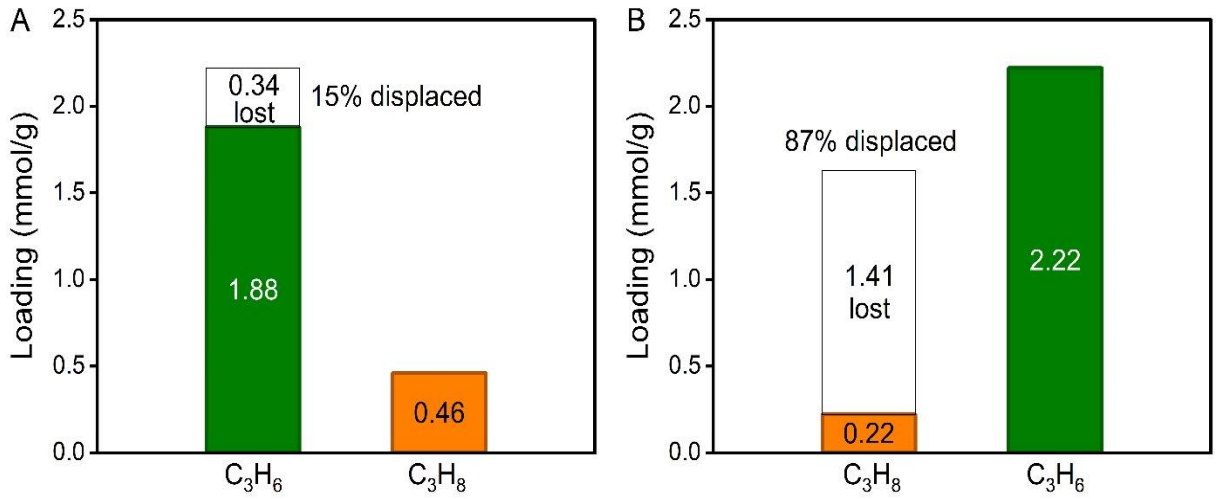

Figure 3.4. Gas loadings in successive adsorption on uncoated zeolite 5A with (A) 10 doses of C_3H_6 then 10 doses of C_3H_8 ("C_3H_6-first") and (B) 10 doses of C_3H_8 then 10 doses of C_3H_6 ("C_3H_8-first") at 298 K under 10 SCCM of helium. In "C_3H_6-first", C_3H_8 displaced 15% pre-adsorbed C_3H_6, and in "C_3H_8-first", C_3H_6 displaced 87% pre-adsorbed C_3H_8.

Mixture adsorption measurements of equimolar and 90/10 (molar ratio) C_3H_6/C_3H_8 were conducted to examine the performance of zeolite 5A under competitive adsorption conditions. For equimolar mixture adsorption on uncoated 5A,

as the number of mixture injections increased, the loadings of both C_3H_6 and C_3H_8 increased significantly at low numbers of injections; after 10 injections, the loading of C_3H_6 kept increasing, whereas that of C_3H_8 decreased, which indicated that C_3H_6 displaced pre-adsorbed C_3H_8 (Fig. 3.5A1). The concentration of C_3H_8 in the effluent relative to the feed gradually increased and was over 1.0 after 10 injections (Fig. 3.5A2); the excess C_3H_8 was from the displacement by C_3H_6. For a 90/10 C_3H_6/C_3H_8 mixture, C_3H_6 adsorption reached equilibrium faster than that from an equimolar mixture due to the high C_3H_6 concentration in the feed (Fig. 3.5B1). The adsorption selectivity from a 90/10 C_3H_6/C_3H_8 mixture was up to 23, whereas it was 12 from an equimolar mixture (Fig. 3.6). In the effluent, the C_3H_8 C/C_0 peak reached 1.8 in 90/10 C_3H_6/C_3H_8 mixture adsorption, indicating significant displacement of pre-adsorbed C_3H_8 by C_3H_6 (Fig. 3.5B2). Noticeably, following the adsorption of a 90/10 C_3H_6/C_3H_8 mixture, C_3H_6 gas with 99.5% purity was obtained during desorption in the collecting time represented by the interval t_i to t_f (Fig. 3.5B3), during which 79.1% of the desorbed C_3H_6 was collected (Fig. B.13), whereas for an equimolar mixture, 46.4% of the desorbed C_3H_6 with 99.0% purity was obtained (Figs. 3.5A3 and B.13). Overall, as indicated by Fig. 3.6, the exposure-dependent trends in C_3H_6 selectivity were similar across the equimolar and C_3H_6-rich feed, with a large enhancement in both cases.

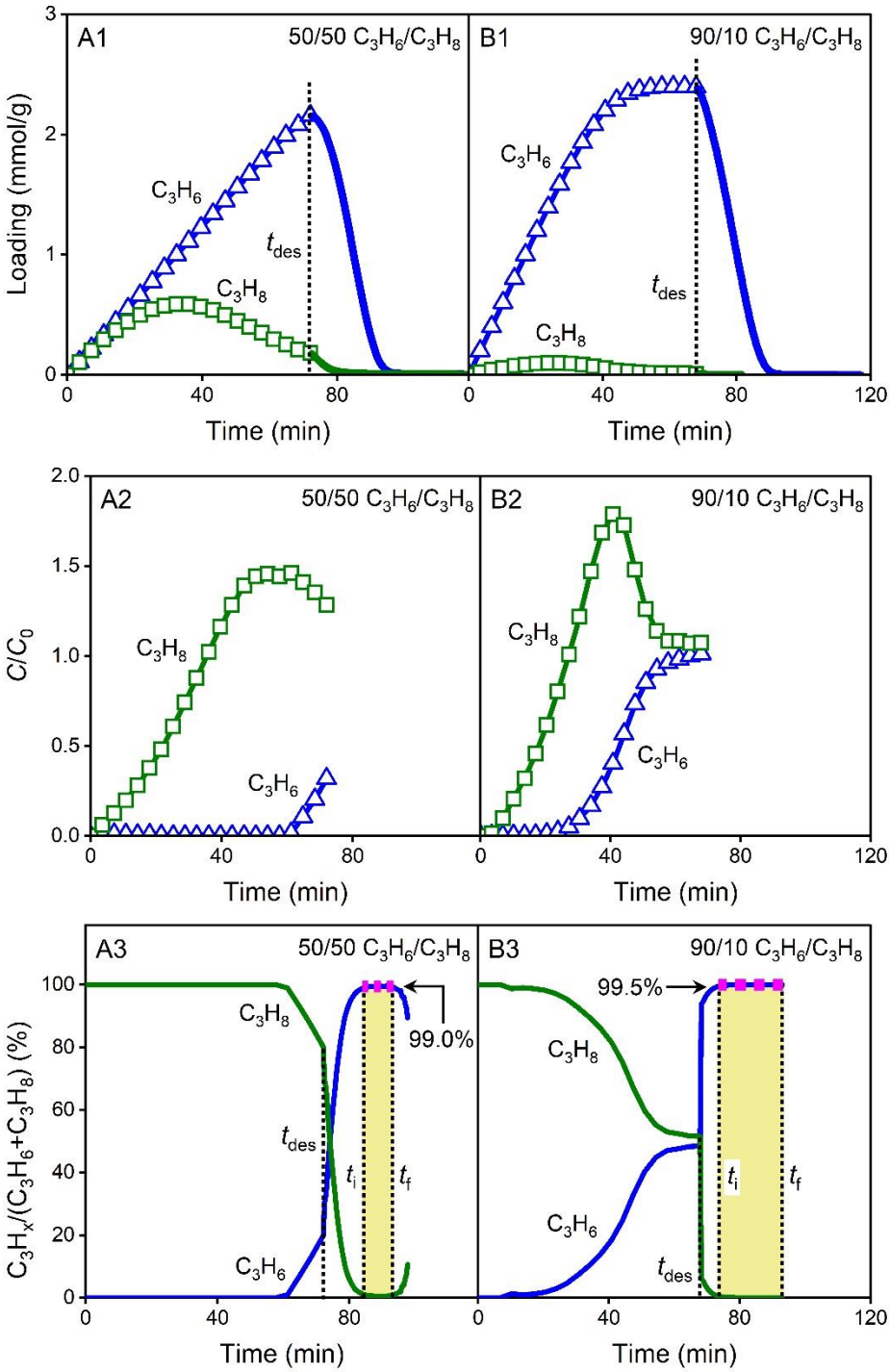

Figure 3.5. Loadings of C_3H_6 and C_3H_8 in adsorption on uncoated zeolite 5A with 20 doses (1.0 mL per dose) at 298 K, followed by TPD (start at time t_{des}), under 20 SCCM of helium, relative concentrations C/C_0 in adsorption, and gas purities in ad/desorption (dashed pink line highlighted C_3H_6 purity collected from time t_i to t_f in desorption) from (A1, A2, A3) an equimolar mixture and (B1, B2, B3) a 90/10 C_3H_6/C_3H_8 mixture.

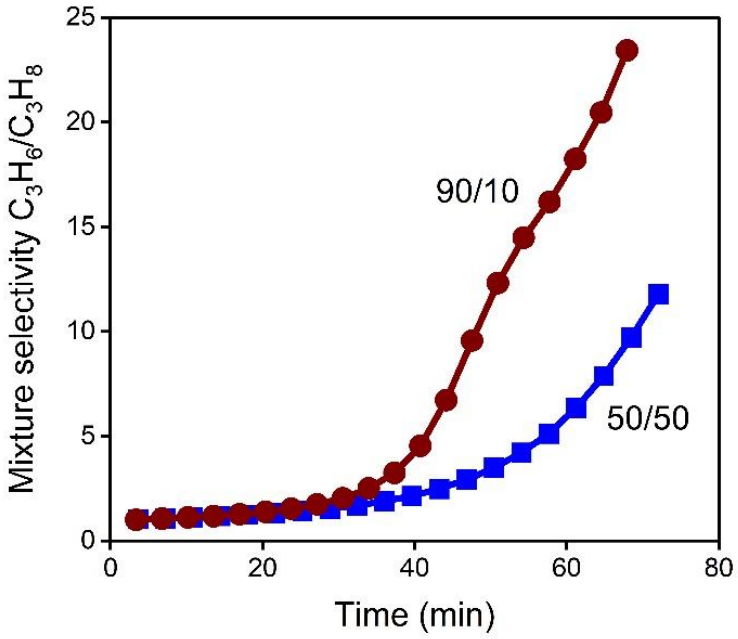

Figure 3.6. Adsorption selectivities with 20 doses (1.0 mL for each dose) of equimolar C_3H_6/C_3H_8 mixture and 90/10 C_3H_6/C_3H_8 mixture on uncoated zeolite 5A at 298 K.

The effect of flow rate of helium carrier gas on equimolar C_3H_6/C_3H_8 mixture adsorption on the uncoated zeolite 5A was investigated. With the same gas exposures, the C_3H_6 and C_3H_8 loadings under 40 SCCM of helium were lower than 10 and 20 SCCM of helium due to the lower concentrations of gases in the feed (Fig. B.14A1, B1, and C1). The C_3H_6 breakthrough time was reduced with the increase of helium flow rate (Fig. B.14A2, B2, and C2). Under 40 SCCM of helium, the gas concentration was low (Fig. B.14C3), resulting in weak mass spectrometer signals. At a given C_3H_6 loading, a higher gas flow rate resulted in increased mixture selectivity (Fig. B.15). The TPD peak of C_3H_6 shifted to low temperature and narrowed under high gas flow rate, though there was no significant difference in the C_3H_8 peak temperatures across various flow rates (Fig. B.16). Considering the TPD peak shape and the intensity of

mass spectrometer signals, 20 SCCM of gas flow rate was selected for the following adsorption and desorption measurements.

3.4.4. Influence of PA coatings on competitive adsorption

For equimolar C_3H_6/C_3H_8 mixture adsorption, similar to the uncoated 5A (Fig. 3.7A1 and A2), displacement behavior (with a smaller peak in C_3H_8 C/C_0) was observed for TBPA-coated 5A (Fig. 3.7B1 and B2), but it was not noticeable for ODPA-coated 5A within 30 doses (Fig. 3.7C1 and C2), perhaps because of the lower gas loadings in the ODPA-coated samples at any given number of doses. The strong competitivity of C_3H_6 adsorption was apparent even before displacement took place on any of the zeolite 5A samples: the loading of C_3H_8 in mixture adsorption was lower than that from single-gas adsorption at the same volume of C_3H_8 injected into the system, and the hindrance to C_3H_8 adsorption became more significant at higher gas exposures (Fig. 3.8). In desorption, the purity of C_3H_6 in the initial effluent before time point t_i was low. After most of the C_3H_8 had desorbed, C_3H_6 gas with high purity was obtained (99.5% from uncoated zeolite 5A, 98.8% from TBPA-coated 5A, and 91.3% from ODPA-coated 5A) in collecting time represented by the interval t_i to t_f (Fig. 3.7A3, B3, and C3), during which 41.3%, 41.9%, and 34.2% of the desorbed C_3H_6 were collected from those three materials, respectively (Fig. B.17). The gas mixtures with C_3H_6 purity lower than polymer-grade (99.5%) need more cycles of separation [3].

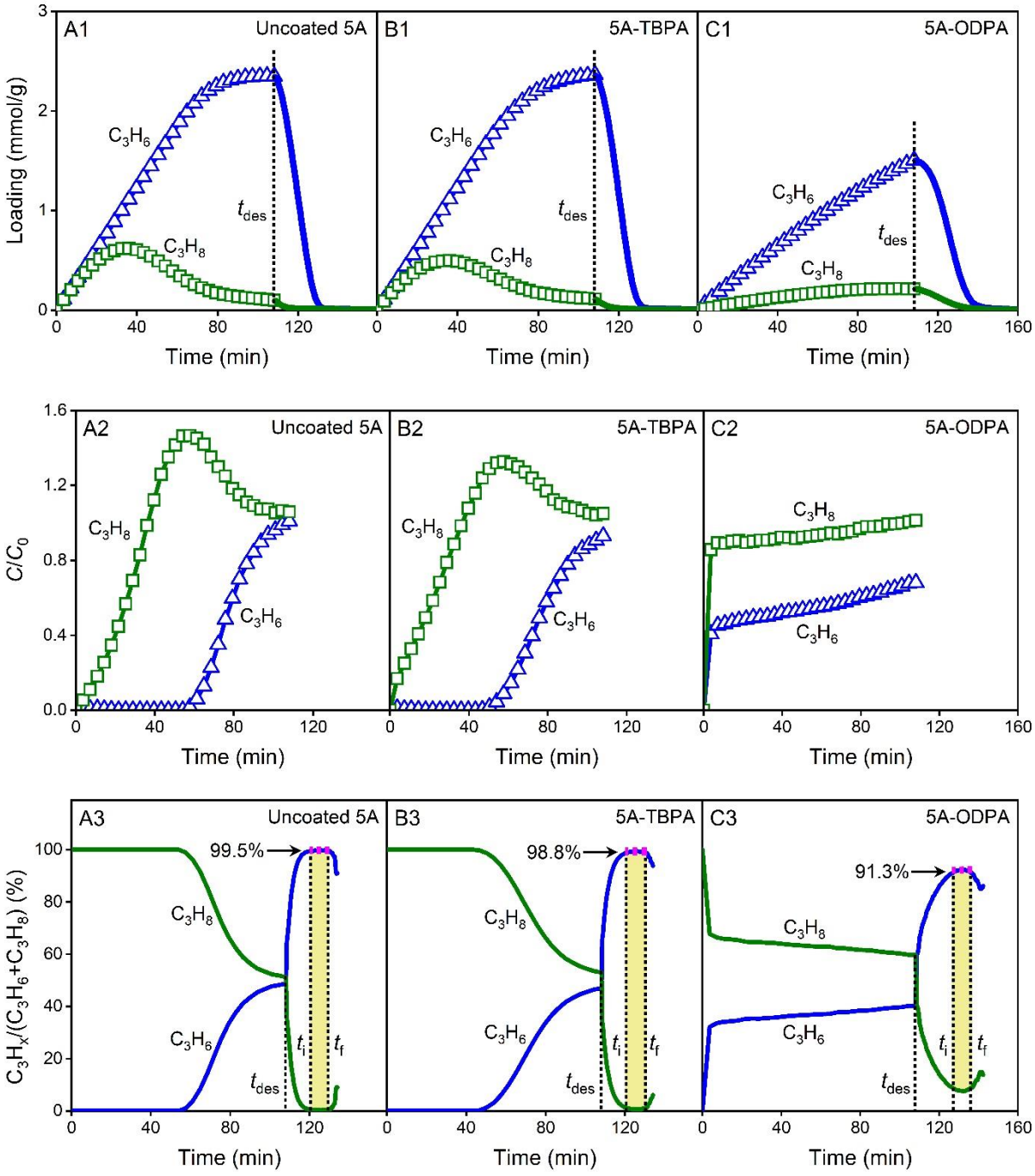

Figure 3.7. Loadings of C_3H_6 and C_3H_8 in adsorption with 30 doses (1.0 mL per dose) of equimolar C_3H_6/C_3H_8 mixture at 298 K, followed by TPD (start at time t_{des}), under 20 SCCM of helium, relative concentrations C/C_0 in adsorption, and gas purities in ad/desorption (dashed pink line highlighted C_3H_6 purity collected from time t_i to t_f in desorption) on (A1, A2, A3) uncoated, (B1, B2, B3) TBPA-, and (C1, C2, C3) ODPA-coated zeolite 5A.

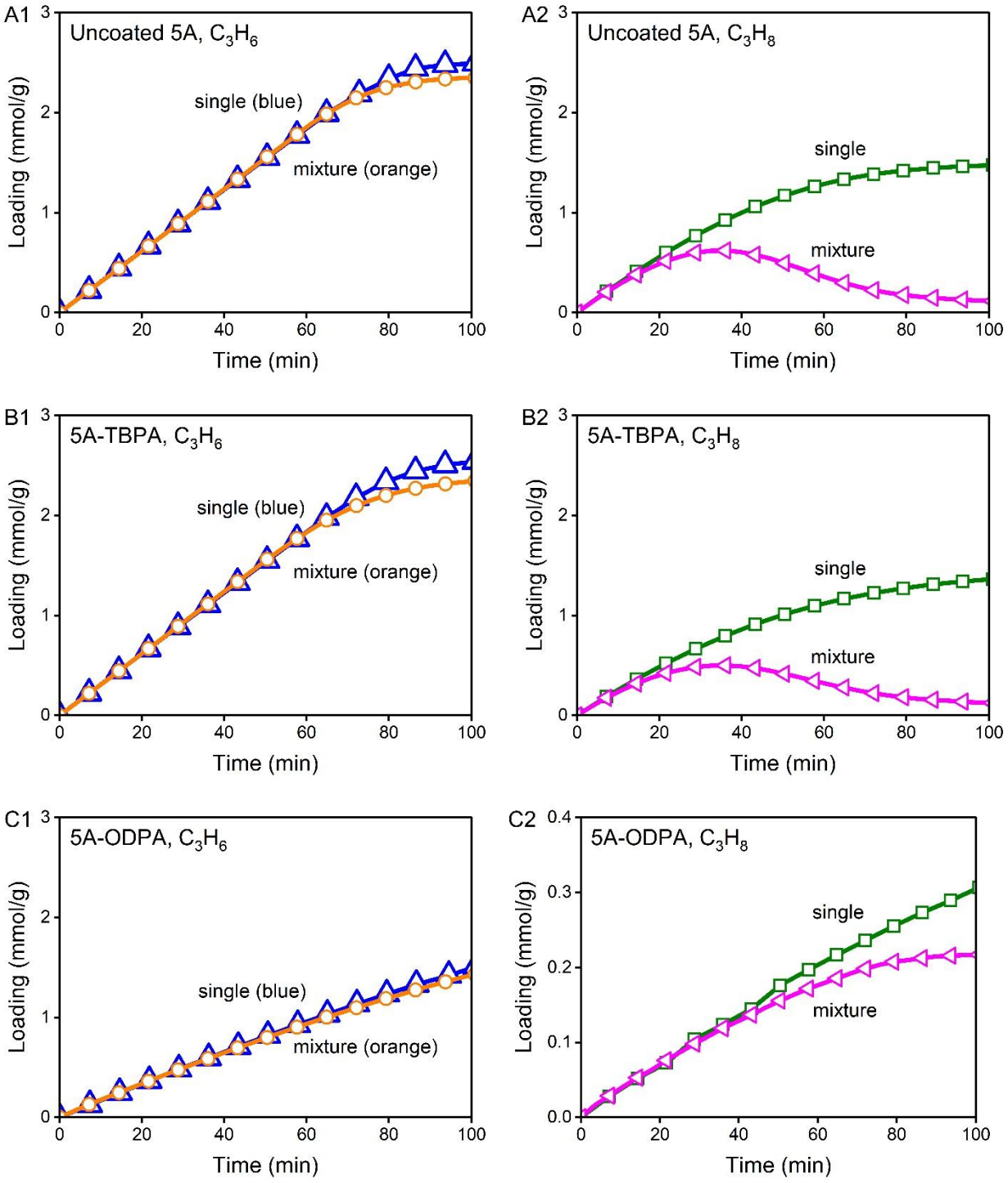

Figure 3.8. Comparison of loadings between single-gas adsorption and equimolar C_3H_6/C_3H_6 mixture adsorption at 298 K under 20 SCCM of helium with the same volume of species injected into the system on (A1, A2) uncoated, (B1, B2) TBPA-coated, and (C1, C2) ODPA-coated 5A.

The mixture selectivities of C_3H_6/C_3H_8 from equimolar mixture adsorption on uncoated, TBPA-, and ODPA-coated zeolite 5A increased as more doses of the gas mixture were injected into the system (Fig. 3.9A), indicating that C_3H_6 hindered C_3H_8 adsorption and displaced pre-adsorbed C_3H_8. At low gas exposures, the mixture selectivity from highest to lowest was: 5A-ODPA > 5A-TBPA > uncoated 5A, whereas at high gas exposures, uncoated 5A had higher mixture selectivity than TBPA- and ODPA-coated 5A. On uncoated 5A, the mixture selectivity was up to 26 ± 2 with 30 doses of the gas mixture (Fig. 3.9A), whereas the ideal selectivity was only 1.6 ± 0.2 (Fig. B.11). The high selectivity for the uncoated zeolite at higher gas exposures was attributed to the faster filling of the zeolite; i.e., C_3H_6 and C_3H_8 adsorbed more rapidly into the uncoated zeolite, so that a regime in which C_3H_6 displaced pre-adsorbed C_3H_8 was reached earlier in time. At a given C_3H_6 loading, 5A-ODPA had a higher mixture selectivity than the uncoated zeolite (Fig. 3.9B), because the ODPA coating had a larger diffusion resistance for C_3H_8 than C_3H_6. For the adsorptive separation of an equimolar mixture, the ODPA-coated zeolite 5A (C_3H_6 loading of 1.5 mmol/g, C_3H_6/C_3H_8 mixture adsorption selectivity of 8.3) and the uncoated 5A (2.3 mmol/g, 26.4) are comparable to the state-of-the-art adsorbents, such as Co-MOF-74 (6.8 mmol/g, 6.5) [12], Y-abtc (1.3 mmol/g, 8.3) [3], ZU-36-Ni (1.4 mmol/g, 19) [40], and KAUST-7 (1.3 mmol/g, 26.6) [21], at 298 K. They are also comparable to values measured for HOF-FJU-1 (2.1 mmol/g, 56.3) and JNU-3 (1.2 mmol/g, 5.9), two dynamic molecular sieving materials with a thermoregulatory gating effect, at 333 K [21]. (See Fig. 3.9C).

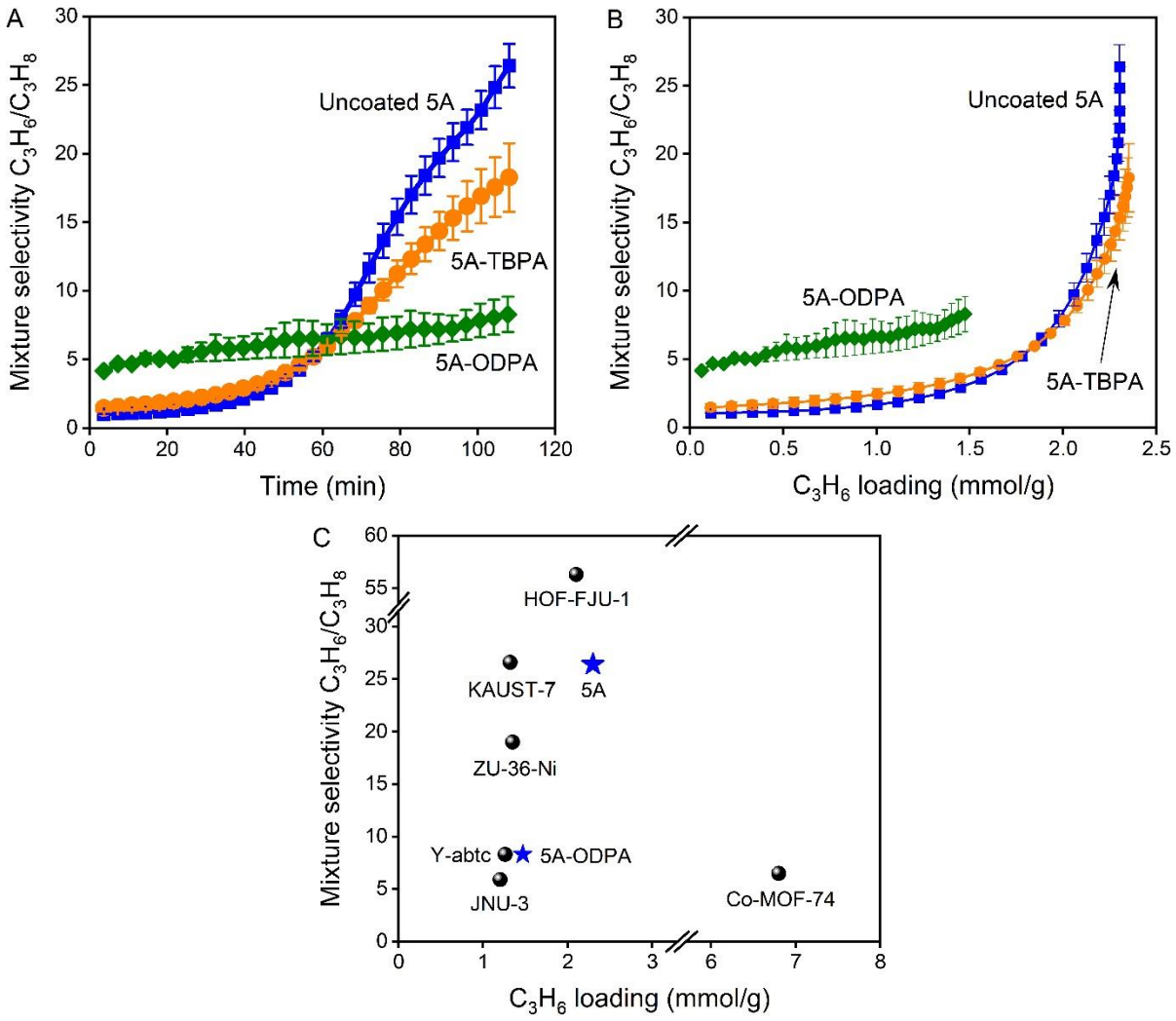

Figure 3.9. Mixture adsorption selectivity versus (A) time and (B) C_3H_6 loading with 30 doses (1.0 mL for each dose) of equimolar C_3H_6/C_3H_8 at 298 K on uncoated, TBPA-, and ODPA-coated zeolite 5A. (C) Mixture selectivity against C_3H_6 loading from equimolar C_3H_6/C_3H_8 adsorption compared with state-of-the-art adsorbents (HOF-FJU-1 and JNU-3 at 333 K, and the others at 298 K).

3.4.5. TPD profiles of zeolite 5A with different coverages

To understand the difference in the affinity of C_3H_6 and C_3H_8 for zeolite 5A, the exposure-dependent desorption following single-gas adsorption was considered. As shown in Fig. 3.10A and Table B.4, on the uncoated zeolite 5A, the TPD peak temperature of C_3H_6 decreased from 414 to 380 K as the fractional coverage increased from 0.45 to 1.0, which was ascribed to the population of more weakly binding sites

at higher coverages on the zeolite surfaces. In contrast, the peak temperature of C_3H_8 hardly changed with coverage, from approximately 351 to 345 K (Fig. 3.10B and Table B.5), indicating a smaller degree of heterogeneity in the (weaker) binding sites for C_3H_8.

Competitive adsorption effects in equimolar C_3H_6/C_3H_8 mixtures were also supported by TPD experiments. Similar to C_3H_6 TPD curves measured after single-gas adsorption, the C_3H_6 peak desorption temperature after mixture adsorption on the uncoated zeolite 5A decreased with increased coverage, from approximately 429 to 385 K (Fig. 3.10C, and Table B.6). For C_3H_8, the peak temperature decreased from 351 to 309 K as the gas exposure increased in mixture adsorption (Fig. 3.10D and Table B.7), whereas it had almost no change with coverage in C_3H_8 single-gas measurement (Fig. 3.10B and Table B.5). We proposed that the reason for the peak temperature decrease of C_3H_8 desorption with increased gas exposure was that C_3H_6 with strong affinity for the zeolite repulsed C_3H_8 molecules on the zeolite surfaces, and the repulsion to C_3H_8 was more significant at higher gas exposures so that C_3H_8 molecules became easier to desorb from the zeolite surfaces. In other words, it appeared that even relatively weakly-binding sites in the zeolite had a significant preference for adsorption of C_3H_6. The C_3H_8 coverage calculated from TPD curves decreased as the gas exposure increased (Table B.7), which was consistent with the competitive adsorption that C_3H_6 displaced pre-adsorbed C_3H_8 at high gas exposures (Fig. 3.7A1).

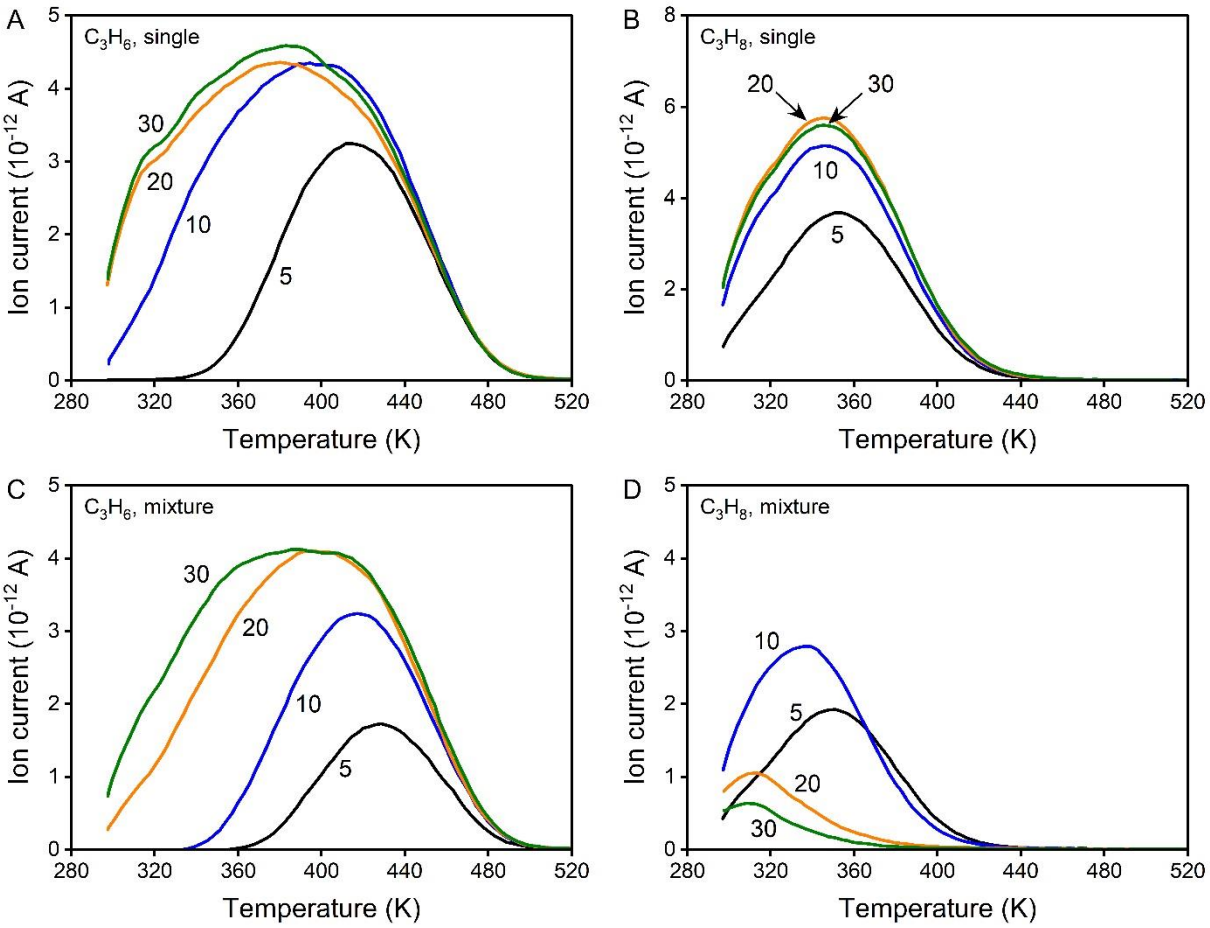

Figure 3.10. TPD curves of uncoated zeolite 5A after adsorption at 298 K under 20 SCCM of helium with 5, 10, 20, 30 doses (1.0 mL per dose) of single gases: (A) C_3H_6, (B) C_3H_8, and equimolar C_3H_6/C_3H_8 mixture: (C) C_3H_6, (D) C_3H_8.

For the same TPD experiments after adsorption on ODPA-coated 5A, the peak desorption temperatures of C_3H_6 and C_3H_8 from both single-gas and mixture adsorption were higher than those on uncoated 5A (Fig. 3.11); the ODPA coating layers on the zeolite surfaces added resistance for diffusion of gas molecules from desorption and therefore lowered the initial desorption rate. On ODPA-coated 5A after mixture adsorption, the TPD peak temperature of C_3H_6 decreased as coverage increased (Fig. 3.11C and Table B.10), similar to the trend for C_3H_6 single-gas measurements (Fig. 3.11A and Table B.8). For C_3H_8 after mixture adsorption, the

peak desorption temperature decreased from 438 to 394 K (Fig. 3.11D and Table B.11), such that there was some effective "repulsion" from C_3H_6 molecules on the zeolite surfaces, especially at high coverage. In contrast, the C_3H_8 peak temperature from single-gas measurements showed no apparent change with coverage (Fig. 3.11B and Table B.9). Different from uncoated 5A, the displacement phenomenon on 5A-ODPA was not observed until 30 doses of mixture, and C_3H_8 loading kept increasing as the gas exposure increased (Table B.11).

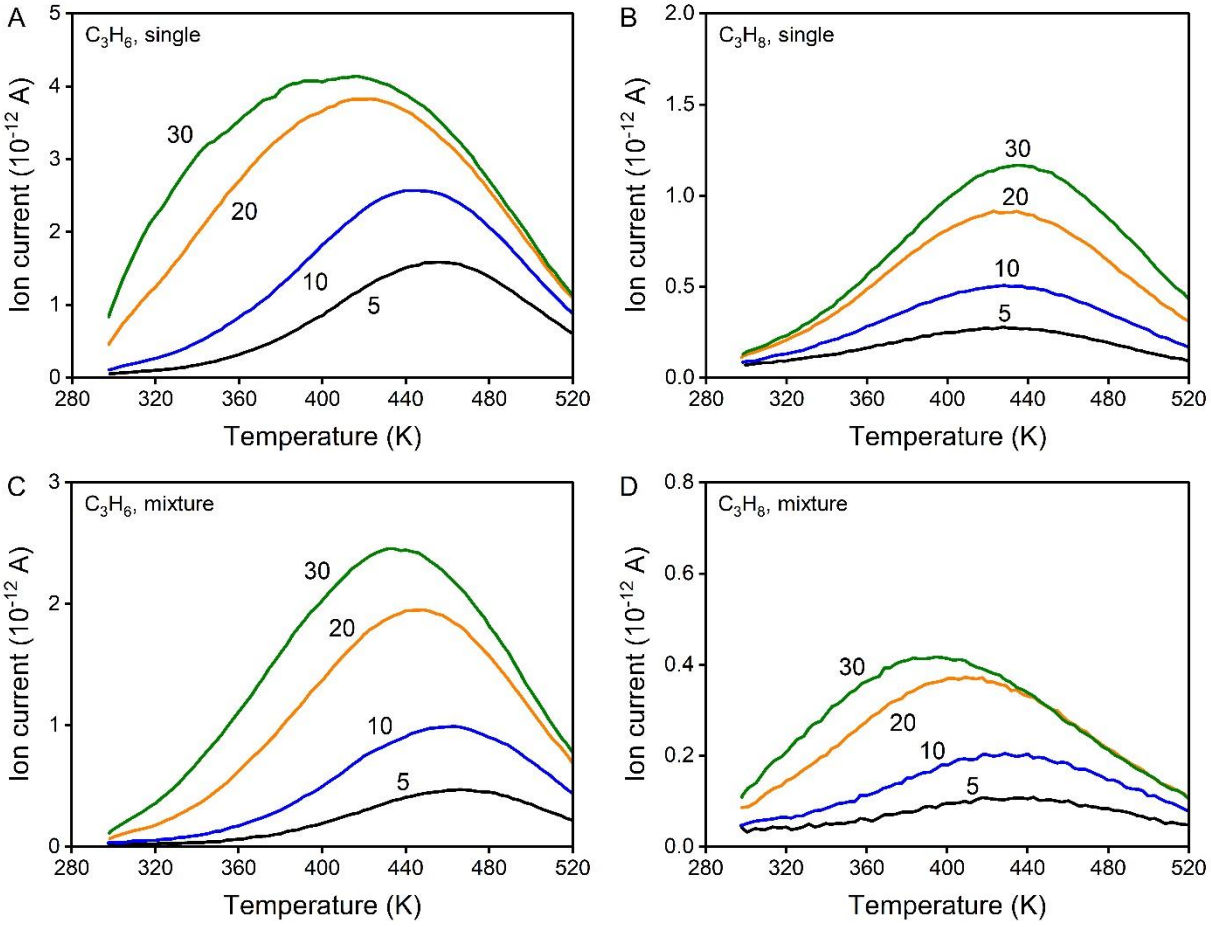

Figure 3.11. TPD curves of ODPA-coated zeolite 5A after adsorption at 298 K under 20 SCCM of helium with 5, 10, 20, 30 doses (1.0 mL per dose) of single gases: (A) C_3H_6, (B) C_3H_8, and equimolar C_3H_6/C_3H_8 mixture: (C) C_3H_6, (D) C_3H_8.

In mixture adsorption, the ODPA coating enhanced the kinetic selectivity of C_3H_6/C_3H_8 by adding an additional diffusion barrier on the zeolite surfaces, but the ODPA coating lowered adsorption rates. The uncoated 5A had low initial mixture selectivity, but it had much higher mixture selectivity at high gas exposures because C_3H_6 displaced pre-adsorbed C_3H_8. The ODPA coating favored adsorption selectivity of C_3H_6/C_3H_8 at low gas exposures, whereas uncoated zeolite 5A is a potential adsorbent for the separation at high gas exposures. Essentially, uncoated zeolite 5A allowed for high gas loadings to be achieved at earlier times, providing a thermodynamic driver for high selectivity based on the favorable adsorption of C_3H_6. Moreover, the properties of the coating played a major role in dictating the overall separation performance: whereas ODPA dramatically improved initial selectivity and suppressed adsorption rates, TBPA had much more muted effects on both parameters. Therefore, in gas separation process, there is a tradeoff between adsorption rate and selectivity for the selection of adsorbent. In addition, the operating parameters need to be optimized to improve the adsorption kinetics for industrial application, and competitive adsorption needs to be considered for the determination of operating conditions.

3.5. Conclusions

The performance of zeolite 5A for C_3H_6/C_3H_8 separation and the influence of PA coatings were evaluated by both single-gas and mixture adsorption using pulse injections, following by temperature-programmed desorption. In gas adsorption, C_3H_6

preferentially adsorbed on uncoated and PA-coated 5A because of the higher diffusion rate of C_3H_6 and its stronger affinity for the zeolite. The PA coatings added additional diffusion barriers on the zeolite surfaces and resulted in high mixture selectivity of C_3H_6/C_3H_8 at low gas exposures. The sterically bulkier TBPA created lower density coating layers on the zeolite surface, and it had less effect on adsorption than ODPA with a long, linear chain. While the selectivity effects of coatings on single-gas adsorption were relatively straightforward, mixed gas adsorption revealed more complex behavior. On uncoated 5A, C_3H_6 displaced pre-adsorbed C_3H_8 and resulted in high mixture selectivity, up to ~26 from an equimolar C_3H_6/C_3H_8 mixture at high gas exposures, whereas the ideal selectivity was only ~1.6. A C_3H_6-rich mixture promoted the displacement and resulted in higher selectivity than an equimolar mixture at the same gas exposure. For both uncoated and ODPA-coated 5A, the C_3H_8 peak desorption temperature decreased significantly after mixture adsorption compared with that after C_3H_8 single-gas adsorption, indicating that C_3H_8 desorption was promoted by the repulsion from C_3H_6 on the zeolite surfaces. Moreover, experiments in which the adsorption sequence of pure-component C_3H_6 and C_3H_8 was switched further confirmed the preferential adsorption of C_3H_6 over C_3H_8, with C_3H_6 displacing far more C_3H_8 than vice versa. The findings demonstrate the importance of competitive adsorption in dictating mixture selectivity. Comparison of the mixture adsorption performance of the ODPA-coated and uncoated zeolites revealed that use of materials having faster adsorption is not only attractive from the perspective of

more rapid uptake but also, unexpectedly, can improve selectivity by enabling a faster rate of displacement of one adsorbate (propane) by another (propylene).

3.6. References

[1] A. Akah, M. Al-Ghrami, Maximizing propylene production via FCC technology, Appl. Petrochem. Res. 5 (2015) 377–392. https://doi.org/10.1007/s13203-015-0104-3.

[2] D.S. Sholl, R.P. Lively, Seven chemical separations to change the world, Nature 532 (2016) 435–437. https://doi.org/10.1038/532435a.

[3] H. Wang, X. Dong, V. Colombo, Q. Wang, Y. Liu, W. Liu, X. Wang, X. Huang, D.M. Proserpio, A. Sironi, Y. Han, J. Li, Tailor - made microporous metal-organic frameworks for the full separation of propane from propylene through selective size exclusion, Adv. Mater. 30 (2018) 1805088. https://doi.org/10.1002/adma.201805088.

[4] R. Faiz, K. Li, Polymeric membranes for light olefin/paraffin separation, Desalination. 287 (2012) 82–97. https://doi.org/10.1016/j.desal.2011.11.019.

[5] J.R. Alcántara-Avila, F.I. Gómez-Castro, J.G. Segovia-Hernández, K.I. Sotowa, T. Horikawa, Optimal design of cryogenic distillation columns with side heat pumps for the propylene/propane separation, Chem. Eng. Process.: Process Intensif. 82 (2014) 112–122. https://doi.org/10.1016/j.cep.2014.06.006.

[6] L. Li, R.B. Lin, X. Wang, W. Zhou, L. Jia, J. Li, B. Chen, Kinetic separation of propylene over propane in a microporous metal-organic framework, Chem. Eng. J. 354 (2018) 977–982. https://doi.org/10.1016/j.cej.2018.08.108.

[7] D.M. Ruthven, S.C. Reyes, Adsorptive separation of light olefins from paraffins, Microporous Mesoporous Mater. 104 (2007) 59–66. https://doi.org/10.1016/j.micromeso.2007.01.005.

[8] S. Abbasi, M.R. Khosravi-Nikou, A. Shariati, Selective separation of propane from the propylene-propane mixture using pure silica zeolites: A molecular dynamic simulation, Chem. Eng. Process.: Process Intensif. 184 (2023) 109294. https://doi.org/10.1016/j.cep.2023.109294.

[9] C.A. Grande, J. Gascon, F. Kapteijn, A.E. Rodrigues, Propane/propylene separation with Li-exchanged zeolite 13X, Chem. Eng. J. 160 (2010) 207–214. https://doi.org/10.1016/j.cej.2010.03.044.

[10] M. Sakai, N. Fujimaki, Y. Sasaki, N. Yasuda, M. Seshimo, M. Matsukata, Preferential adsorption of propylene over propane on a Ag-exchanged X-type zeolite membrane, ACS Appl. Mater. Interfaces. 12 (2020) 24086–24092. https://doi.org/10.1021/acsami.0c01461.

[11] J.G. Min, K.C. Kemp, K.S. Kencana, R.R. Mukti, S.B. Hong, Dealuminated Cs-ZK-5 zeolite for propylene/propane separation, Chem. Eng. J. 413 (2021) 127422. https://doi.org/10.1016/j.cej.2020.127422.

[12] Y.S. Bae, C.Y. Lee, K.C. Kim, O.K. Farha, P. Nickias, J.T. Hupp, S.T. Nguyen, R.Q. Snurr, High propene/propane selectivity in isostructural metal-organic frameworks with high densities of open metal sites, Angew. Chem. 124 (2012) 1893–1896. https://doi.org/10.1002/ange.201107534.
[13] E.D. Bloch, W.L. Queen, R. Krishna, J.M. Zadrozny, C.M. Brown, J.R. Long, Hydrocarbon separations in a metal-organic framework with open iron(II) coordination sites, Science 335 (2012) 1606–1610. https://doi.org/10.1126/science.1217544.
[14] H. Abedini, A. Shariati, M.R. Khosravi-Nikou, Separation of propane/propylene mixture using MIL-101(Cr) loaded with cuprous oxide nanoparticles: Adsorption equilibria and kinetics study, Chem. Eng. J. 387 (2020) 124172. https://doi.org/10.1016/j.cej.2020.124172.
[15] C. Krishnaraj, H.S. Jena, K. Leus, H.M. Freeman, L.G. Benning, P. van der Voort, An aliphatic hexene-covalent triazine framework for selective acetylene/methane and ethylene/methane separation, J. Mater. Chem. A. 7 (2019) 13188–13196. https://doi.org/10.1039/C8TA11722E.
[16] J. Gao, Y. Cai, X. Qian, P. Liu, H. Wu, W. Zhou, D. Liu, L. Li, R. Lin, B. Chen, A Microporous hydrogen - bonded organic framework for the efficient capture and purification of propylene, Angew. Chem. 133 (2021) 20563–20569. https://doi.org/10.1002/ange.202106665.
[17] J. Padin, S.U. Rege, R.T. Yang, L.S. Cheng, Molecular sieve sorbents for kinetic separation of propane/propylene, Chem. Eng. Sci. 55 (2000) 4525–4535. https://doi.org/10.1016/S0009-2509(00)00099-3.
[18] A. Cadiau, K. Adil, P.M. Bhatt, Y. Belmabkhout, M. Eddaoudi, A metal-organic framework-based splitter for separating propylene from propane, Science 353 (2016) 137–140. https://doi.org/10.1126/science.aaf6323.
[19] H. Zeng, M. Xie, T. Wang, R.J. Wei, X.J. Xie, Y. Zhao, W. Lu, D. Li, Orthogonal-array dynamic molecular sieving of propylene/propane mixtures, Nature 595 (2021) 542–548. https://doi.org/10.1038/s41586-021-03627-8.
[20] J. Cui, Z. Zhang, L. Yang, J. Hu, A. Jin, Z. Yang, Y. Zhao, B. Meng, Y. Zhou, J. Wang, Y. Su, J. Wang, X. Cui, H. Xing, A molecular sieve with ultrafast adsorption kinetics for propylene separation, Science (2023) eabn8418. https://doi.org/10.1126/science.abn8418.
[21] Y. Chen, Y. Yang, Y. Wang, Q. Xiong, J. Yang, S. Xiang, L. Li, J. Li, Z. Zhang, B. Chen, Ultramicroporous hydrogen-bonded organic framework material with a thermoregulatory gating effect for record propylene separation, J. Am. Chem. Soc. 144 (2022) 17033–17040. https://doi.org/10.1021/jacs.2c06585.
[22] J. Gascon, W. Blom, A. van Miltenburg, A. Ferreira, R. Berger, F. Kapteijn, Accelerated synthesis of all-silica DD3R and its performance in the separation of propylene/propane mixtures, Microporous Mesoporous Mater. 115 (2008) 585–593. https://doi.org/10.1016/j.micromeso.2008.02.038.
[23] M. Khalighi, Y.F. Chen, S. Farooq, I.A. Karimi, J.W. Jiang, Propylene/propane separation using SiCHA, Ind. Eng. Chem. Res. 52 (2013) 3877–3892. https://doi.org/10.1021/ie3026955.

[24] P.J. Bereciartua, Á. Cantín, A. Corma, J.L. Jordá, M. Palomino, F. Rey, S. Valencia, E.W. Corcoran, P. Kortunov, P.I. Ravikovitch, A. Burton, C. Yoon, Y. Wang, C. Paur, J. Guzman, A.R. Bishop, G.L. Casty, Control of zeolite framework flexibility and pore topology for separation of ethane and ethylene, Science 358 (2017) 1068–1071. https://doi.org/10.1126/science.aao0092.
[25] C. Selzer, A. Werner, S. Kaskel, Selective adsorption of propene over propane on hierarchical zeolite ZSM-58, Ind. Eng. Chem. Res. 57 (2018) 6609–6617. https://doi.org/10.1021/acs.iecr.8b00377.
[26] J. Liu, Y. Liu, D.K. Talay, E. Calverley, M. Brayden, M. Martinez, A new carbon molecular sieve for propylene/propane separations, Carbon 85 (2015) 201–211. https://doi.org/10.1016/j.carbon.2014.12.089.
[27] S. Xu, W.C. Li, C. Wang, R. Liu, G.P. Hao, A.H. Lu, Beyond the selectivity-capacity trade-off: Ultrathin carbon nanoplates with easily accessible ultramicropores for high-efficiency propylene/propane separation, Nano Lett. 22 (2022) 6615–6621. https://doi.org/10.1021/acs.nanolett.2c01930.
[28] B.R. Pimentel, R.P. Lively, Propylene enrichment via kinetic vacuum pressure swing adsorption using ZIF-8 fiber sorbents, ACS Appl. Mater. Interfaces. 10 (2018) 36323–36331. https://doi.org/10.1021/acsami.8b08983.
[29] Q. Ding, Z. Zhang, P. Zhang, J. Wang, X. Cui, C.H. He, S. Deng, H. Xing, Control of intracrystalline diffusion in a bilayered metal-organic framework for efficient kinetic separation of propylene from propane, Chem. Eng. J. 434 (2022) 134784. https://doi.org/10.1016/j.cej.2022.134784.
[30] C.D. Chudasama, J. Sebastian, R.V. Jasra, Pore-size engineering of zeolite A for the size/shape selective molecular separation, Ind. Eng. Chem. Res. 44 (2005) 1780–1786. https://doi.org/10.1021/ie049333l.
[31] X. Xu, X. Zhao, L. Sun, X. Liu, Adsorption separation of carbon dioxide, methane and nitrogen on monoethanol amine modified ß-zeolite, J. Nat. Gas Chem. 18 (2009) 167–172. https://doi.org/10.1016/S1003-9953(08)60098-5.
[32] Q. Dong, Z. Song, F. Zhou, H. Li, M. Yu, Ultrathin, fine-tuned microporous coating modified 5A zeolite for propane/propylene adsorptive separation, Microporous Mesoporous Mater. 281 (2019) 9–14. https://doi.org/10.1016/j.micromeso.2019.02.038.
[33] E. Hoque, J.A. DeRose, G. Kulik, P. Hoffmann, H.J. Mathieu, B. Bhushan, Alkylphosphonate modified aluminum oxide surfaces, J. Phys. Chem. B. 110 (2006) 10855–10861. https://doi.org/10.1021/jp061327a.
[34] T. Hauffman, O. Blajiev, J. Snauwaert, C. van Haesendonck, A. Hubin, H. Terryn, Study of the self-assembling of *n*-octylphosphonic acid layers on aluminum oxide, Langmuir. 24 (2008) 13450–13456. https://doi.org/10.1021/la801978a.
[35] L.D. Ellis, S.T. Parker, J. Hu, S.F. Zaccarine, M.J. Stellato, H.H. Funke, C. Sievers, S. Pylypenko, J.L. Falconer, J.W. Medlin, Tuning gas adsorption selectivity and diffusion rates in zeolites with phosphonic acid monolayers, Cell Rep. Phys. Sci. 1 (2020) 100036. https://doi.org/10.1016/j.xcrp.2020.100036.

[36] X. Zhou, J.L. Falconer, J.W. Medlin, Mechanism of selectivity control for zeolites modified with organic monolayers, Microporous Mesoporous Mater. 337 (2022) 111913. https://doi.org/10.1016/j.micromeso.2022.111913.
[37] M.C. Campo, A.M. Ribeiro, A. Ferreira, J.C. Santos, C. Lutz, J.M. Loureiro, A.E. Rodrigues, New 13X zeolite for propylene/propane separation by vacuum swing adsorption, Sep. Purif. Technol. 103 (2013) 60–70. https://doi.org/10.1016/j.seppur.2012.10.009.
[38] Y. Chai, X. Han, W. Li, S. Liu, S. Yao, C. Wang, W. Shi, I. da-Silva, P. Manuel, Y. Cheng, L.D. Daemen, A.J. Ramirez-Cuesta, C.C. Tang, L. Jiang, S. Yang, N. Guan, L. Li, Control of zeolite pore interior for chemoselective alkyne/olefin separations, Science 368 (2020) 1002–1006. https://doi.org/10.1126/science.aay8447.
[39] H. Abedini, M. Asgari, M. Watt Coull, A. Shariati, M.R. Khosravi-Nikou, Efficient production of polymer-grade propylene from the propane/propylene binary mixture using Cu-MOF-74 framework, Sep. Purif. Technol. 276 (2021) 119172. https://doi.org/10.1016/j.seppur.2021.119172.
[40] Z. Zhang, Q. Ding, X. Cui, X.M. Jiang, H. Xing, Fine-tuning and selective-binding within an anion-functionalized ultramicroporous metal-organic framework for efficient olefin/paraffin separation, ACS Appl. Mater. Interfaces. 12 (2020) 40229–40235. https://doi.org/10.1021/acsami.0c07800.
[41] S. Brunauer, P.H. Emmett, E. Teller, Adsorption of gases in multimolecular layers, J. Am. Chem. Soc. 60 (1938) 309–319. https://doi.org/10.1021/ja01269a023.
[42] J.H. de Boer, B.C. Lippens, B.G. Linsen, J.C.P. Broekhoff, A. van den Heuvel, Th.J. Osinga, The t-curve of multimolecular N_2-adsorption, J. Colloid Interface Sci. 21 (1966) 405–414. https://doi.org/10.1016/0095-8522(66)90006-7.
[43] G. Horváth, K. Kawazoe, Method for the calculation of effective pore size distribution in molecular sieve carbon, J. Chem. Eng. Japan. 16 (1983) 470–475. https://doi.org/10.1252/jcej.16.470.
[44] J.L. Falconer, J.A. Schwarz, Temperature-programmed desorption and reaction: applications to supported catalysts, Catal. Rev. 25 (1983) 141–227. https://doi.org/10.1080/01614948308079666.
[45] P.A. Redhead, Thermal desorption of gases, Vaccum. 12 (1962) 203–211. https://doi.org/10.1016/0042-207X(62)90978-8.
[46] L.D. Ellis, R.M. Trottier, C.B. Musgrave, D.K. Schwartz, J.W. Medlin, Controlling the surface reactivity of titania via electronic tuning of self-assembled monolayers, ACS Catal. 7 (2017) 8351–8357. https://doi.org/10.1021/acscatal.7b02789.

Chapter 4: Organic-coated zeolites for selective gas adsorption: Effect of functional group identity and coating density

4.1. Abstract

Adsorptive separation of propylene (C_3H_6) and propane (C_3H_8) is an alternative to energy-intensive distillation, but improving kinetic separation selectivity via tuning sorbent pore structure is challenging for molecules with similar sizes. Composite materials consisting of a barrier monolayer film deposited on the external surface of a zeolite have shown promise for enabling higher selectivity; however, structure-function relationships for these materials are currently lacking. Here, gas adsorption rates on zeolite 5A were controlled by varying the terminal functional group (amine or carboxylic acid) and coating density of organic phosphonic acid (PA) modifiers. Single-gas pressure decay adsorption measurements showed that with a 4-phosphonobutyric acid ($COOHC_3PA$) coating, the kinetic selectivity of C_3H_6/C_3H_8 increased with time and reached 15 at 60 min. For *n*-butylphosphonic acid, with a chain length comparable to $COOHC_3PA$ but lacking a functional group, the initial selectivity was greater than 5, whereas the selectivity was ~1.2 for uncoated 5A. Coating with 3-aminopropyl phosphonic acid (NH_2C_3PA) resulted in high resistance to gas diffusion such that both C_3H_6 and C_3H_8 loadings were <0.02 mmol/g, even after 60 min. To investigate whether the slow adsorption was attributable to excessive NH_2C_3PA, the coating density was tuned by varying PA concentration for deposition. As the coating density decreased, the initial adsorption rates of both C_3H_6 and C_3H_8 increased, but the density-dependent trends varied drastically between NH_2C_3PA

and *n*-octadecylphosphonic acid. With a 0.1 monolayer coverage of NH_2C_3PA, the kinetic selectivity of C_3H_6/C_3H_8 was >15 for 60 min. Temperature-programmed desorption of *n*-propylamine ($C_3H_7NH_2$) suggested that the strong blocking and improved selectivity of NH_2C_3PA may be associated with the affinity of the amine group for the zeolite surface. The results show that gas adsorption rates and selectivities in zeolites are highly sensitive to the composition and density of monolayer films on the external surface.

4.2. Introduction

The strategy of surface coating on materials has attracted significant attention for applications in CO_2 capture, gas separation, heterogenous catalysis, pollutant elimination, and sensing. A self-assembled monolayer (SAM) coating essentially reduces the film thickness to a molecular scale and enables precise control over the functional group in the coating. Various SAMs, such as thiols, phosphonic acids, silanes, carboxylic acids, and alcohols, have been investigated for the modification of materials, such as noble metals (Au, Pd, Pt, Rh, etc.), TiO_2, Al_2O_3, SiO_2, and MnO_2. These coatings have been found to be thermally and chemically stable [1–4].

Organic phosphonic acids (PAs) were utilized to modify zeolite 5A for the adsorptive separation of C_3H_6 and C_3H_8, and the adsorption rates were tuned by changing the alkyl chain length and steric configuration of the PAs [5–7], as discussed in Chapters 2 and 3. The kinetic selectivity of C_3H_6/C_3H_8 was increased by changing the diffusion rate-limiting step from zeolite pore channels to the PA coating layers on

the external surfaces of zeolites [6]. To date, however, only alkyl PAs have been employed to control kinetic selectivity; the dependence of performance on more strongly interacting functional groups in the SAMs has not previously been tested.

The molecular arrangement of SAMs on the substrate is affected by ligand chain length, coverage (number of molecules per unit of surface area), and functional groups. Spori et al. [8] reported that for alkyl phosphate SAM-modified TiO_2, ligands with chain lengths of C_{10} to C_{13} assembled into less dense, liquid-like structures, and those with alkyl chain lengths exceeding 15 carbon atoms formed more crystalline, all-*trans* structures due to the strong van der Waals interactions between the long chains. Kickelbick et al. [9] decreased the concentration of dodecylphosphonic acid for ZrO_2 modification and obtained low grafting density with less ordered alkyl chains, indicated by a blueshift of methylene groups in infrared (IR) spectra. Castillo et al. [10] studied SAMs of octadecyltrichlorosilane on silica by molecular dynamics simulations and varied the coverage of alkylsilane molecules from 1.0 to 5.5 nm^{-2}. As the coverage increased, the silane coating layer thickness increased and the tilt angle of the molecular axis with the normal to the surface decreased; the tilt angle was lower than 20° for coverages higher than 4.0 nm^{-2}. Gys et al. [11] reported that the coating coverages from 3-aminopropylphosphonic acid were lower than propylphosphonic acid on mesoporous TiO_2 at 363 K and high concentrations (75 and 150 mmol/L) of modifiers. Moreover, their density functional theory (DFT) calculations showed that the amine groups formed hydrogen bonds within single ligands, between neighboring ligands, and between ligands and the material surface.

In recent years, modification of materials using organic ligands with terminal functional groups has attracted significant interest. Carboxylic acid terminated monolayers have been applied in protein immobilization [12], sensing [13], electronic devices [14], and catalysis [15]. Amine-containing ligands have been widely used to modify materials, such as hierarchical silica [16,17], and zeolites 13X [18], 4A [19], and ITQ-2 [20] and SBA-15 [21], and metal-oragic framworks (MOFs) MIL-100(Cr) [22] and the materials exhibited improved CO_2 adsorption capacity. In the field of drug delivery and multimodal theranostic applications, Tudisco et al. [23] used 3-aminopropylphosphonic acid as a covalent linker between magnetic Fe_3O_4 nanoparticles and ß-cyclodextrin to carry and release some drugs. Moreover, they prepared biocompatible multi-functional Fe_3O_4 nanoparticles using a mixed monolayer with two phosphonic acids having terminal acetylenic and amine groups to enhance the intracellular transport of *N*-methylated drugs [24]. For catalysis, Zapelini et al. [25] used amino-propyltrimethoxysilane coating to increase the basicity of Na-LTA zeolite catalyst for the Knoevenagel condensation reaction between benzaldehyde and ethyl cyanoacetate. However, amine-containing SAMs have not been reported to modify the pore structure of adsorbents for kinetic adsorptive separation.

In this chapter, as part of a continuing effort to understand the role of PA coating structure on selective gas adsorption, PAs with functional groups (amine or carboxylic acid) were coated on zeolites and their effects on gas adsorption rates were investigated. While amines and carboxylic acids are not expected to exhibit strong

interactions with hydrocarbons like C_3H_6 and C_3H_8, we hypothesized that interactions between functional groups on the ligands, or between those groups and the zeolite surface, would lead to more substantial (and potentially tunable) diffusion barriers near the zeolite pore entrances. Pressure-decay adsorption measurements were performed to examine the performance of the materials for C_3H_6 and C_3H_8 separation. Moreover, to further investigate the structure-function relationships of PA coatings, the coating density was adjusted by varying the concentration of PAs for deposition. The findings may provide insights for the design of efficient adsorbents and adsorptive separation processes.

4.3. Experimental

4.3.1. Materials and characterization

The deposition of organic phosphonic acids (PAs) onto zeolite 5A was based on the procedures reported previously [5,6]. First, 830 mg of zeolite 5A was calcined at 673 K in air for 4 h. Then, the calcined zeolite was added to a 200-mL solution of PA (10 mmol/L for full monolayer) in tetrahydrofuran (THF) and stirred at ambient conditions for 16 h. The amount of PA added to the solution was twelve times the theoretical amount needed (0.83 mmol/L) to form a full monolayer based on the assumption of a surface coverage of 4 PA molecules per nm^2 on the zeolite 5A surface [26,27] and a measured external surface area of 33 m^2/g from the nitrogen adsorption isotherm (see below, Section 4.4.1). After the solution was stirred, the solid was separated from it via centrifugation at 8000 rpm for 9 min, annealed at 393 K for 6 h,

then rinsed with THF four times, and dried in a vacuum oven overnight at room temperature. Zeolite 5A (LTA type), $Ca_nNa_{12-2n}[(AlO_2)_{12}(SiO_2)_{12}]$ xH_2O (powder, <10 μm, Sigma-Aldrich 233676), *n*-butylphosphonic acid (BPA, ≥88.0%, Sigma-Aldrich 737933), 4-phosphonobutyric acid ($COOHC_3PA$, ≥98.0%, TCI P2349), 3-aminopropylphosphonic acid (NH_2C_3PA, ≥98.0%, AmBeed A172849), *n*-octadecylphosphonic acid (ODPA, ≥96.0%, Alfa Aesar 20645), and THF (high-performance liquid chromatography grade, Fisher Chemical T425-4) were used as received. For control experiments, the uncoated zeolite 5A was zeolite 5A calcined at 673 K in air for 4 h, cooled, and then put through deposition process in THF solvent but without a PA modifier.

To prepare low coating densities of PAs on zeolite 5A, 200-mL solutions of PAs with low concentrations in THF were used (Table C.1 and Table C.2), following the same PA deposition procedures as for the full monolayer. The monolayer fraction for low-density coating is a nominal number, representing the ratio of PA concentration used for the deposition to the theoretical concentration (0.83 mmol/L) needed to form a full monolayer. Because not all of the PAs in solution deposit on the substrate, the reported monolayer fraction should be an upper bound on the actual coating density.

The crystal structure of the materials was characterized on an X-ray diffractometer (XRD), Rigaku Smartlab model, with a Cu K_α radiation source, using standard 2D detection from 2 to 50° (angle 2θ) with a step of 0.01° and a scan rate of 2°/min. Nitrogen (≥99.999%, Airgas) ad/desorption isotherms at liquid nitrogen temperature on the uncoated zeolite 5A were measured on a surface characterization

analyzer, 3Flex model (Micromeritics Instruments). Prior to adsorption measurements, the sample was pretreated at 473 K under vacuum for 6 h. Based on the N_2 adsorption isotherm, the total surface area was determined with the Brunauer-Emmett-Teller (BET) multi-point method [28] using relative pressure p/p^0 in the range of 10^{-7}–0.05. The external surface area (pore size >2.5 nm) was determined with the t-plot method [29] using p/p^0 in the range of 0.20–0.40. The micropore size distribution was determined with the Horvath-Kawazoe (HK) method [30]. The zeolite particles were observed using a scanning electron microscope (SEM), Hitachi SU3500 VP model, with gold sputter coating for the zeolite sample on a sputter coater, Leica EM ACE600 model, and the elemental composition was obtained by energy dispersive spectroscopy (EDS). The thermal stability of PA modifiers was tested by temperature programmed desorption (TPD) from 298 to 823 K with a heating rate of 8 K/min under 20 SCCM of helium carrier gas, and the gas composition from desorption was analyzed on a quadrupole mass spectrometer (MS, Balzers Prisma QME 200) interfaced to the flow system via a capillary line. Thermogravimetric analysis (TGA) was performed for uncoated and PA-coated samples with a nitrogen purge of 60 mL/min and temperature ramp from room temperature to 960 K with a heating rate of 20 K/min. The loading of PA on the zeolite was calculated based on the weight lost from 300 to 960 K using the uncoated zeolite as the reference and assuming that during the heating in nitrogen, the PA tail was released after decomposition and the head group phosphonate still bound with the zeolite surface [31–33].

4.3.2. Pressure-decay adsorption measurement

The single-gas, pressure-decay adsorption measurements were performed on an Autosorb-1 apparatus (Quantachrome Instruments) equipped with a custom LabVIEW-based data acquisition system. Before an adsorption measurement, the sample (100 mg) was pretreated for 3 h at 473 K under vacuum. Three gases, CO_2 (≥99.999%, Airgas), C_3H_6 (≥99.5%, Airgas), and C_3H_8 (≥99.5%, Airgas), were tested separately at 298 K under a manifold pressure of 40 kPa for uncoated zeolite 5A and the zeolites coated with BPA, $COOHC_3PA$, NH_2C_3PA, and ODPA, respectively. The amount of gas adsorbed in a given time period was calculated based on the pressure drop during adsorption. The initial gas adsorption rate was calculated from the slope of a linear fit of the adsorption data at early adsorption times. The ideal selectivity was determined by the loading ratio of C_3H_6 to C_3H_8 at the same adsorption time in single-gas measurements.

4.3.3. n-Propylamine TPD measurement

We carried out TPD experiments after exposing various materials to *n*-propylamine. In the apparatus, shown in Fig. C.1, 0.5 g of zeolite 5A or PA-coated zeolite 5A was pretreated in a fixed bed at 523 K for 2 h under 20 SCCM of helium carrier gas. Then, *n*-propylamine was adsorbed on the zeolite at 298 K for 1 h by introducing liquid *n*-propylamine into the helium carrier gas at room temperature and atmospheric pressure from a glass bubbler using 5 SCCM of helium. The vapor exiting the bubbler was diluted by 100 SCCM of helium, resulting in *n*-propylamine partial pressure of 0.038 bar. After gas adsorption, the sample was purged with 105

SCCM helium at 298 K for 8 h to remove weakly adsorbed *n*-propylamine. Then, TPD from 298 to 873 K was carried out with a heating rate of 10 K/min under 105 SCCM of helium. The gases in the effluent were analyzed using a mass spectrometer (Balzers Prisma QME 200). The signals in the mass spectra corresponded to *n*-propylamine (mass/charge m/z = 30, 17, and 41), propylene (m/z 41), and ammonia (m/z 17). For PA-coated 5A, decomposition of PAs at temperatures >573 K also generates mass fragments that overlap with *n*-propylamine and propylene. To account for this, we carried out the same TPD procedure using PA-coated 5A TPD but without dosing *n*-propylamine. The intensity of m/z 41 from propylene was determined by subtracting the intensity contributed by *n*-propylamine and PA decompositions from the total intensity of m/z 41. The amounts of propylene and *n*-propylamine from TPD were determined by calibration separately using 1 mL of propylene gas and 1 μL of *n*-propylamine liquid in a helium carrier gas.

4.4. Results and discussion

4.4.1. Material structure

We coated zeolite 5A with various PA monolayers, including *n*-butylphosphonic acid (BPA), 4-phosphonobutyric acid ($COOHC_3PA$), and 3-aminopropyl phosphonic acid (NH_2C_3PA) as a series of monolayers containing methyl, carboxylic acid, and amine terminal functional groups, respectively. However, it is important to note that NH_2C_3PA deposition was challenged by the limited solubility of NH_2C_3PA in THF. We observed the existence of crystals of solid PA in solutions containing even low

concentrations of NH_2C_3PA; for example, some crystals were detected even for a solution concentration low enough (0.14 mmol/L) to only deposit a maximum of ~0.2 monolayer (ML) of the modifier, as shown in XRD (Fig. C.2). Our approach in such cases was to use variable loadings of NH_2C_3PA despite the solubility limitations, rationalizing that undissolved PAs could still serve as a source for maintaining sufficient local chemical potential during deposition. Indeed, as discussed below, we did observe a significant effect of using higher loadings of NH_2C_3PA even beyond the apparent solubility limits. The bulk crystalline structure of the zeolite 5A did not change after coating with PAs, as shown by XRD (Fig. 4.1). For the zeolite coated with BPA and $COOHC_3PA$, no diffraction peaks from PAs were noticed since these two PAs dissolved well in THF.

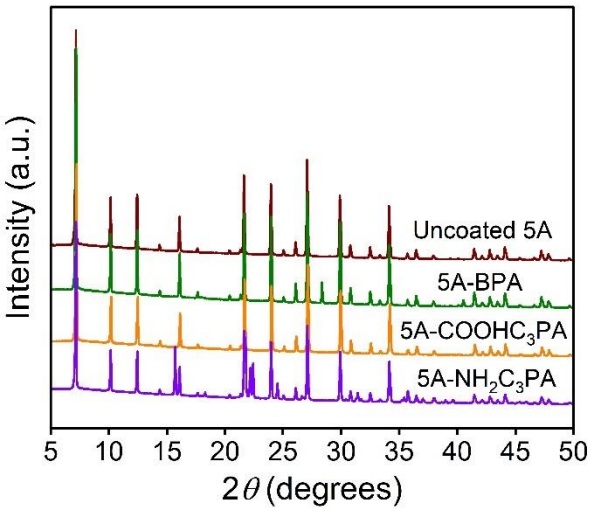

Figure 4.1. XRD patterns of uncoated, BPA-, $COOHC_3PA$-, and NH_2C_3PA-coated 5A.

Nitrogen adsorption at liquid nitrogen temperature on uncoated zeolite 5A exhibited a reversible type I(a) isotherm according to the International Union of Pure and Applied Chemistry (IUPAC) classification (Fig. C.3), indicating that the zeolite had a microporous structure. The measured total surface area of the zeolite was 715

± 11 m^2/g, and the external surface area was 33 ± 2 m^2/g (equivalent to a particle size of 120 nm) as determined by the t-plot method. The median width of the micropores was 5.8 Å (Fig. C.4). Under SEM observation, zeolite particles with a cubic geometry and sizes as high as ~4 µm were observed. However, the particle size distribution appeared broad, and small particles of <100 nm sizes were also evident (Fig. C.5); the variety of particles and poor contrast between them made it difficult to determine the average particle size and calculate external surface area from SEM images. Instead, we relied on the external area determined from nitrogen adsorption isotherms as described above. From SEM-EDS, the Si/Al atomic ratio of the zeolite 5A was ~1, and the Ca/Na atomic ratio was ~2 (Table C.3).

The PA coatings on the zeolite were found to be thermally stable up to 570 K as confirmed by TPD (Fig. C.6), similar to prior reported stabilities on TiO_2 [34]. The signal intensities from decomposition of 5A-NH_2C_3PA were much higher than those from the other PAs (Fig. C.6), since the sample contained a large amount of undissolved NH_2C_3PA crystals, as indicated by the XRD peaks (Fig. 4.1). Based on TGA measurements, for the zeolites coated with a full monolayer of BPA or $COOHC_3PA$ (using 10 mmol/L PA for the deposition), the PA loadings were calculated to be <3 wt% based on the weight loss of <1 wt% compared with the uncoated 5A (Fig. C.7A–C). The weight loss of zeolite 5A coated with a full monolayer of NH_2C_3PA was 10.5 wt% (Fig. C.7D); the value was higher than the theoretical quantity for a full monolayer (~3 wt%) because undissolved NH_2C_3PA was left in the sample, and thereby the weight loss cannot be used to calculate the deposited amount of NH_2C_3PA.

4.4.2. Effect of functional group of phosphonic acid on gas adsorption

To investigate the effect of the functional group (amine or carboxylic acid group) of the PA ligand on gas adsorption rates, single-gas, pressure-decay adsorption at 298 K was measured for CO_2, C_3H_6, and C_3H_8 separately on zeolite 5A coated with $COOHC_3PA$ and NH_2C_3PA and compared with the zeolite coated with alkyl BPA, which has a similar ligand chain length. For $COOHC_3PA$-coated zeolite 5A, it had minimal effect on CO_2 adsorption, but the adsorption rates of both C_3H_6 and C_3H_8 were lower than on BPA-coated 5A (Fig. 4.2B and C), indicating higher gas diffusion resistance from the $COOHC_3PA$ coating layer. The C_3H_6 molecules slowly diffused into the pores with a loading of ~0.5 mmol/g at 60 min, whereas the C_3H_8 loading was <0.03 mmol/g, even after 60 min (Fig. 4.2C). The ideal kinetic selectivity of C_3H_6/C_3H_8 reached 15 at 60 min. In contrast, the kinetic selectivity on BPA-coated 5A was initially 5. As expected for these selectivities based on single-gas measurements, the selectivity decreased at longer times and eventually approached the equilibrium selectivity (1.2) observed on the uncoated 5A (Fig. C.8). The $COOHC_3PA$-coated 5A could be a potential adsorbent for C_3H_6/C_3H_8 separation because of its higher kinetic selectivity and a substantial amount of C_3H_6 loading.

For $COOHC_3PA$, it is expected that a monolayer of carboxylic acid terminated chains forms on the material surface since the phosphonic acid group binds more strongly than the carboxylic acid group [15,35]. Previous work has also suggested that hydrogen bonds form between carboxylic acid groups at the end of the tails resulting in lower flexibility of PA ligands than the PAs without terminal function groups [35].

The temperature dependence of gas adsorption on zeolite coated with $COOHC_3PA$ was investigated and compared with ODPA to probe the effects of the carboxylic acid terminal group, since both coatings have significant resistance to gas diffusion but achieve high gas loadings. On the zeolite 5A coated with a monolayer of ODPA, the C_3H_6 adsorption at 298–423 K reached equilibrium in ~20 min, and with the increase of adsorption temperature, the equilibrium loading decreased (Fig. 4.3A1); however, the rate to approach equilibrium was not temperature sensitive (Fig. 4.3A2 and Table C.4). On the zeolite 5A coated with $COOHC_3PA$, the C_3H_6 adsorption did not reach equilibrium after 60 min at 298–423 K (Fig. 4.3B1); with the increase of temperature, the initial rate increased (the initial rate at 423 K was 2.6 times higher than the rate at 298 K) (Fig. 4.3B2 and Table C.4), which was attributed to the temperature sensitivity of hydrogen bonding between the carboxylic acid groups on the zeolite surface [36].

The NH_2C_3PA coating layer exhibited high gas diffusion resistance, such that the loadings of both C_3H_6 and C_3H_8 were <0.02 mmol/g even after 60 min, and the adsorption rate of CO_2 also decreased markedly (Fig. 4.2D), which had not been observed for the other PA coatings [6]. The resistance to gas diffusion from the NH_2C_3PA coating was higher than $COOHC_3PA$ coating. We proposed that hydrogen bonds form between amine groups at the end of the tails, similar to carboxylic acid groups; however, the distance between amine groups is shorter than that between carboxylic acid groups, resulting in a denser structure and higher gas diffusion resistance. Due to the low gas uptakes, zeolite 5A coated with NH_2C_3PA from

saturating deposition of monolayer is not an efficient adsorbent for C_3H_6/C_3H_8 separation.

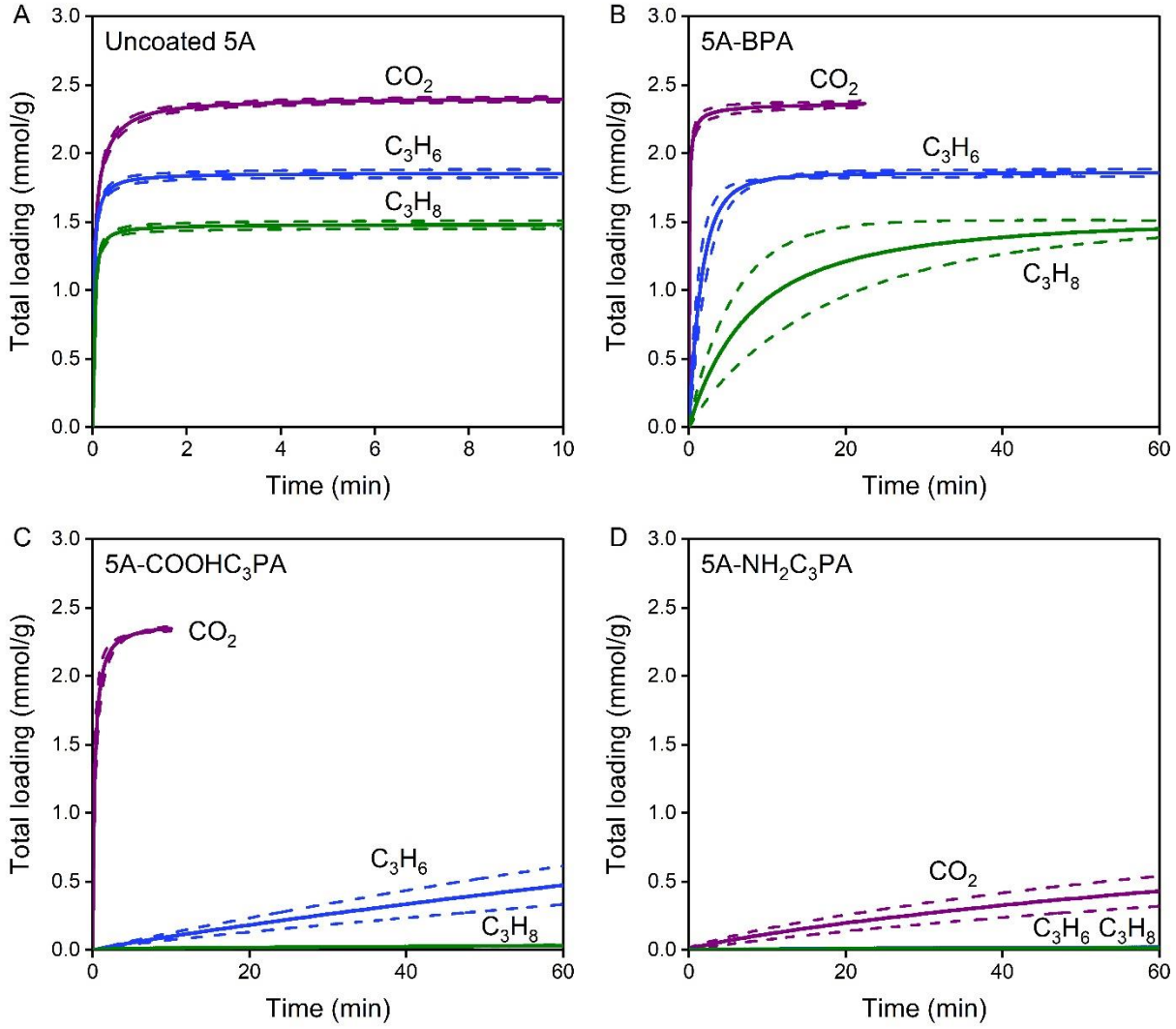

Figure 4.2. Loadings of CO_2, C_3H_6, and C_3H_8 in single-gas pressure-decay adsorption at 298 K on (A) uncoated, (B) BPA, (C) $COOHC_3PA$, and (D) NH_2C_3PA-coated zeolite 5A. The PA coatings were from saturating depositions of monolayers. The dashed curves represent the uncertainty bounds based on standard deviations of triplicate measurements.

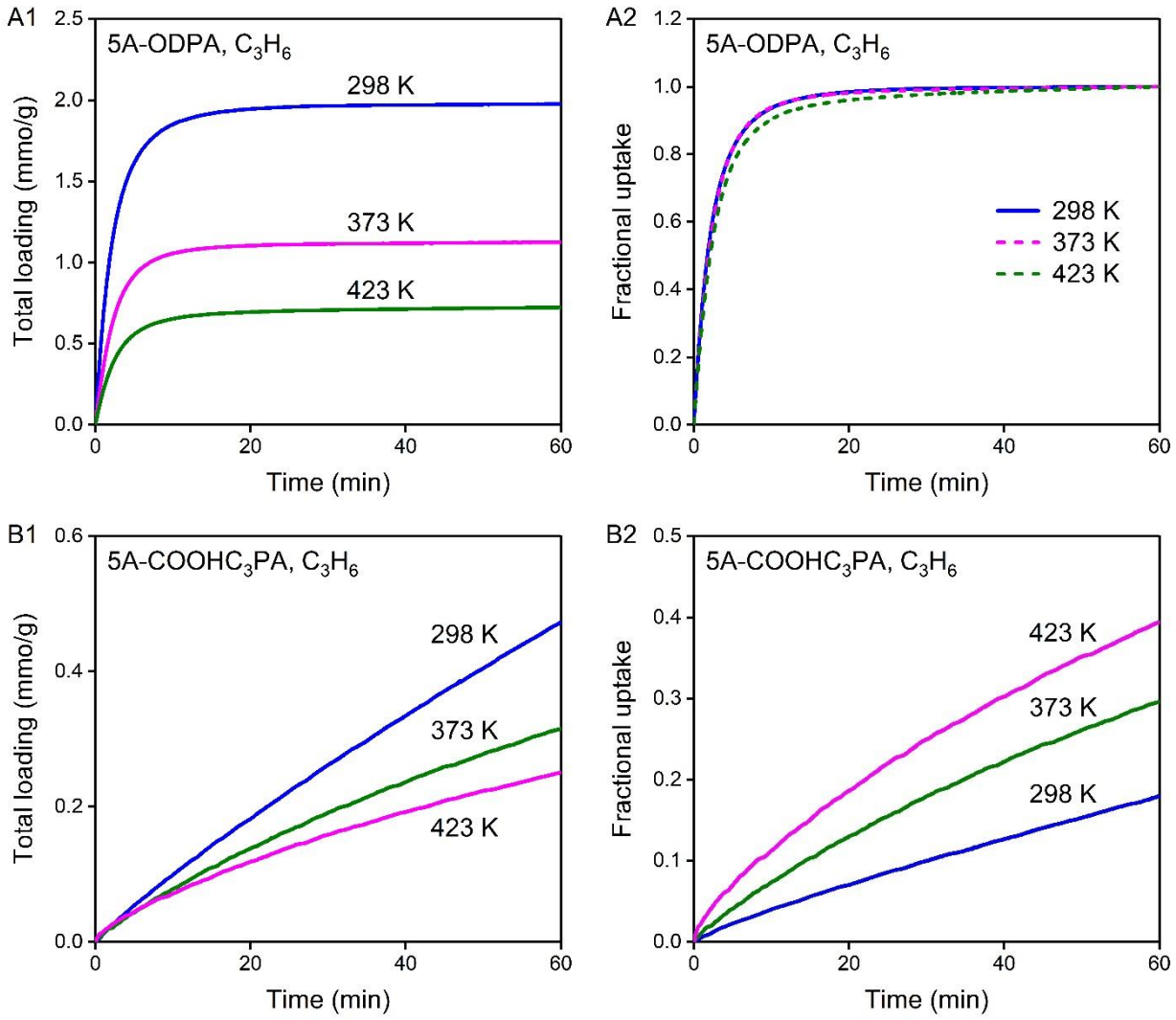

Figure 4.3. Temperature dependence (298–423 K) of C_3H_6 adsorption on zeolite 5A coated with (A1 and A2) ODPA and (B1 and B2) $COOHC_3PA$. The PA coatings were from saturating depositions of monolayers.

4.4.3. Effect of coating density on gas adsorption

A full monolayer of NH_2C_3PA on zeolite 5A had high diffusion resistance to all test molecules, with low gas uptakes after even one hour. To test whether lower coating densities could enable faster adsorption, low densities of NH_2C_3PA were investigated. Moreover, a full monolayer of ODPA also had significant resistance for gas diffusion and the mechanism of alkyl PA system was relatively well understood

[6,7]. We therefore initially studied low densities of ODPA to understand density effects for simple alkyl ligands, and subsequently compared those trends with similar coverage-dependent trends for NH_2C_3PA.

For the ODPA coating, the initial adsorption rates increased by an order of magnitude from a full monolayer to 0.9 ML (Fig. 4.4A1 and A2, Fig. 4.5), which was ascribed to the lower degree of ODPA ordering at submonolayer coverages and the fast penetration of gas molecules through the structural defects. A monolayer of ODPA on zeolite 5A was obtained using 3x the theoretical amount of ODPA needed since similar adsorption rates were obtained using 12x the amount of ODPA (Fig. C.9), indicating that supersaturating amounts of ODPA did not affect sorption properties. Varying ODPA coating density between 0.2 and 0.9 ML did not noticeably affect the initial rates of C_3H_6 and C_3H_8 adsorption (Fig. 4.4A1 and A2, Fig. 4.5). The kinetic selectivity of C_3H_6/C_3H_8 on the zeolite coated with a monolayer of ODPA was 24 initially and decreased below 3 within 40 min. With coating densities of 0.2–0.9 ML, the initial selectivities were ~5 (similar to the shorter-chain alkyl BPA) and then decreased to the equilibrium selectivity in about 2 min (Fig. 4.6A). This weak sensitivity across most of the coverage range indicated that the presence of a relatively low density of vacancies/defects lead to rapid diffusion of gas molecules into the zeolite and loss of kinetic selectivity.

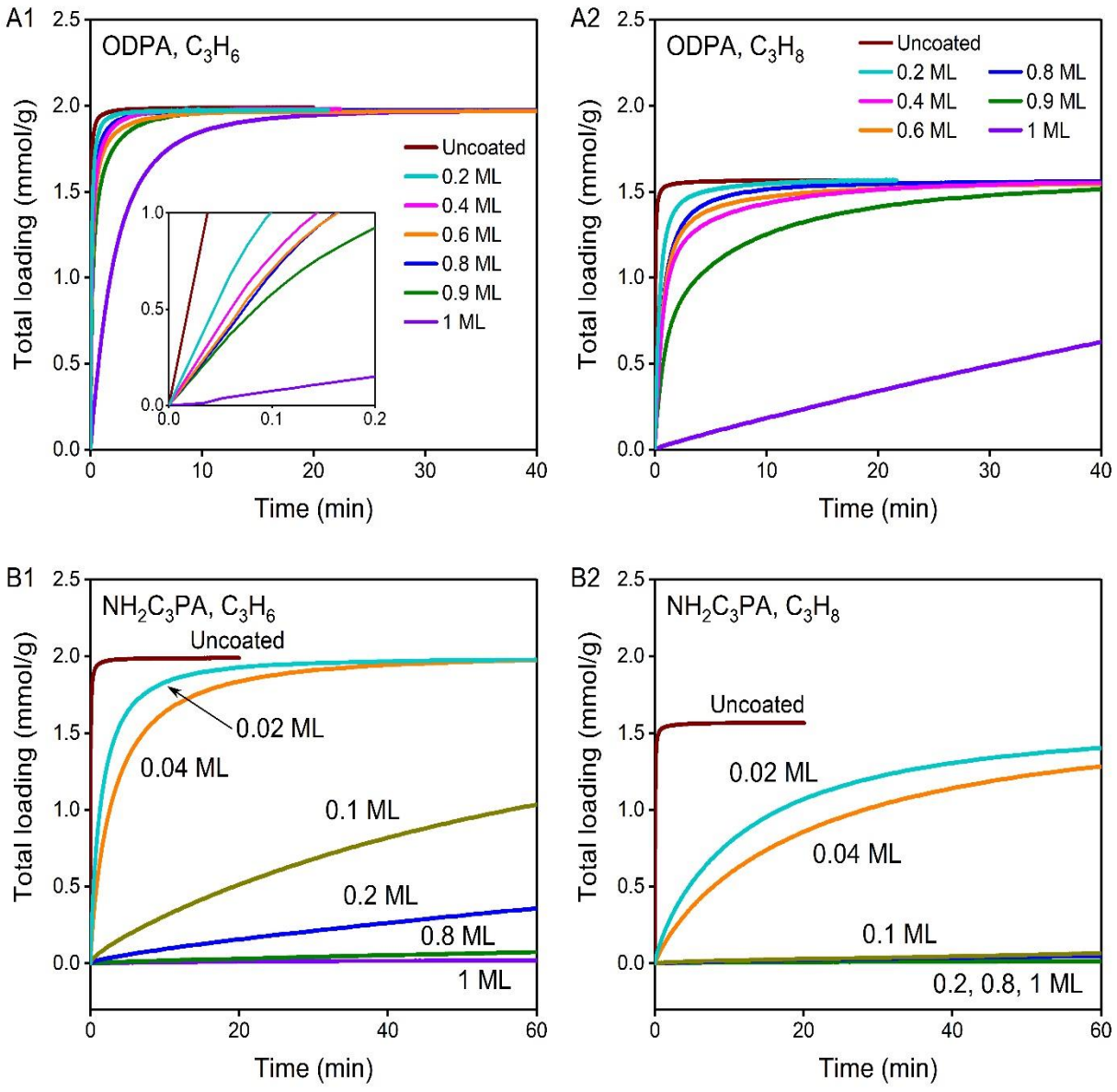

Figure 4.4. Loadings of C_3H_6 and C_3H_8 in single-gas pressure-decay adsorption at 298 K on zeolite 5A coated with different coverages of (A1 and A2) ODPA and (B1 and B2) NH_2C_3PA.

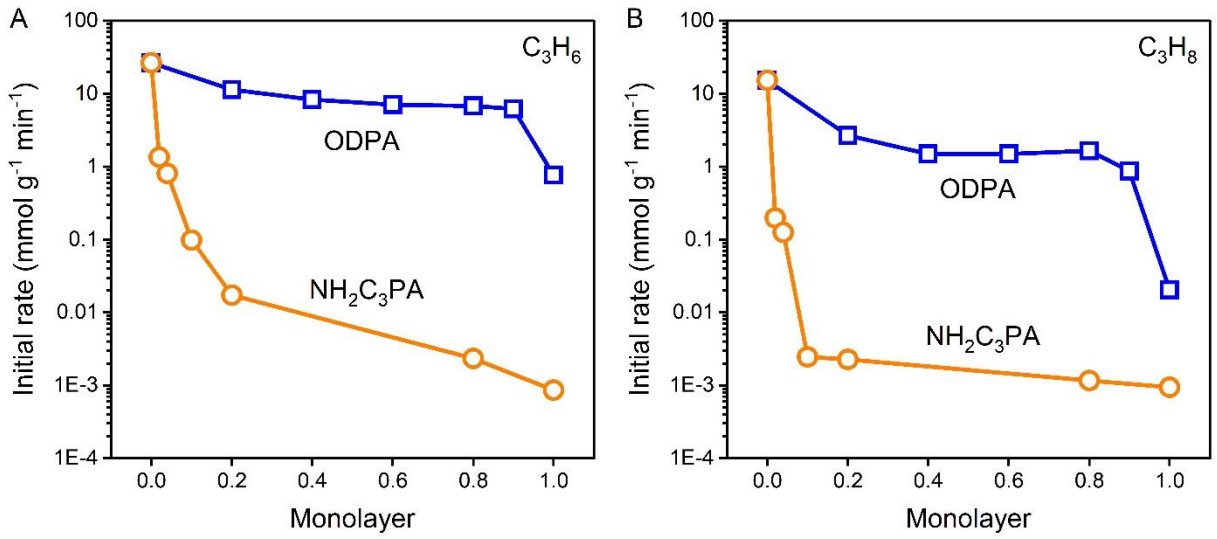

Figure 4.5. Initial adsorption rates of (A) C_3H_6 and (B) C_3H_8 as a function of PA loading of ODPA and NH_2C_3PA on zeolite 5A.

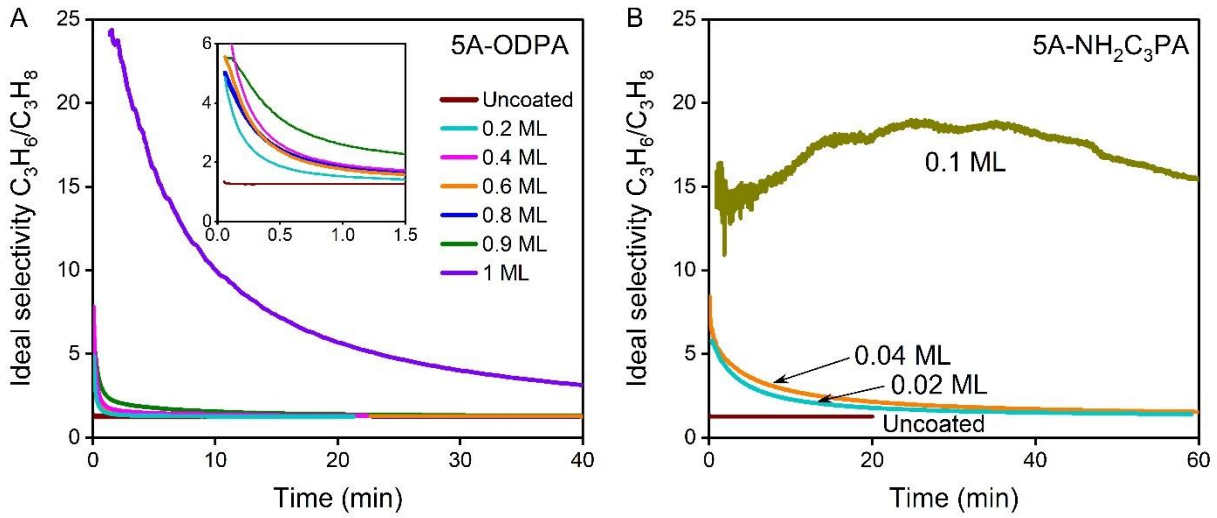

Figure 4.6. Ideal selectivities of C_3H_6/C_3H_8 on zeolite 5A coated with (A) ODPA and (B) NH_2C_3PA with different PA coating density.

Different from ODPA coating, for NH_2C_3PA-coated zeolite 5A, both C_3H_6 and C_3H_8 loadings increased as the coating density decreased (Fig. 4.4B1 and B2). Interestingly, with a coating density >0.2 ML, the initial rate of C_3H_6 adsorption into the NH_2C_3PA-coated zeolite was approximately a factor of 10^3 times lower than ODPA-coated 5A (Fig. 4.5). The zeolite coated with only 0.04 ML of NH_2C_3PA had

about the same initial C_3H_6 adsorption rate as the zeolite fully coated with ODPA. One possible explanation for this behavior is at low coating densities of NH_2C_3PA, the amine group of the PA ligand binds to the zeolite surface and results in high gas diffusion resistance. It is well-known that at partial coverages of self-assembled monolayers, ligands with amine and other functional groups tend to bind through both the head and tail groups, producing flat-lying or bridging structures [37,38]. Interestingly, the 0.1 ML NH_2C_3PA coating yielded a C_3H_6/C_3H_8 selectivity over 15 and a C_3H_6 loading of 1.0 mmol/g after 60 min (Fig. 4.6B), though it must be noted that diffusion was still slow compared to typically used sorbents.

4.4.4. Interaction between amine group and zeolite surface

The NH_2C_3PA coating on zeolite 5A created much higher gas diffusion resistance than BPA and ODPA, and the resistance was significant even at low coating densities. To investigate whether the amine group could interact strongly with the zeolite surface at low coating density, hypothetically via the hydroxyl groups on the external surface, *n*-propylamine TPD was performed. Propylamine was selected for the measurement since it has an amine group and a chain length similar to NH_2C_3PA but lacks the phosphonic acid head. In the TPD after *n*-propylamine adsorption on zeolite 5A without PA coatings, only unreacted *n*-propylamine desorbed from the zeolite below 650 K (Fig. 4.7A), with a quantity of 324 ± 37 µmol/g calculated from the peak area. Two *n*-propylamine desorption peaks were observed at 430 and 627 K, indicating two types of adsorption sites on zeolite 5A. Above 650 K, propylene desorption with a peak temperature of 770 K was observed, (Fig. 4.7B) with a

production amount of 132 ± 21 µmol/g. Adsorbed *n*-propylamine converts to propylene and ammonia on Brønsted sites of zeolites above 650 K through a reaction similar to the Hofmann elimination reaction [39,40]. In this work, the zeolite 5A contains Ca^{2+} and Na^{+} and is not expected to have typical Brønsted sites with protons combining with bridge oxygen atoms between aluminum and silicon atoms on the internal zeolite surface. However, the hydroxyl groups bonded to Al atoms (Al-OH) on the external surface provide sites for *n*-propylamine adsorption, similar to Brønsted sites, and *n*-propylamine is expected to convert to propylene and ammonia on these sites. The concentration of Al-OH sites on the external surface was assumed to be equal to the concentration of sites causing the production of propylene, 132 µmol/g, corresponding to 2.4 sites per nm^2 based on an external surface area of 33 m^2/g; this is about one site per surface Al atom, similar to that reported in the literature [39]. The measured Al-OH site concentration is close to the theoretical value of 145 µmol/g calculated from the zeolite external surface area.

For the BPA-coated zeolite 5A, the amount of *n*-propylamine desorbed in TPD was 1.2 µmol/g (Fig. 4.7A), much lower than that from uncoated 5A, likely because of blocking of adsorption sites at the external surface by the PAs. PAs also consume the hydroxyl groups on the external surfaces of the zeolites, thus decreasing surface -OH density, consistent with the low yield of propylene (24 µmol/g) (Fig. 4.7B). Moreover, for zeolite 5A coated with 0.1 ML of NH_2C_3PA, the amounts of *n*-propylamine desorbed and propylene yield were both <1 µmol/g (Fig. 4.7). This suggests that even a low loading of the NH_2C_3PA is sufficient to completely consume or block access to

the hydroxyl groups, with a bridged-shaped ligand structure perhaps playing a role. The density of 0.1 ML may correspond to a situation in which NH_2C_3PA occludes nearly all the pore windows, approximately one PA ligand per pore window, based on 6 PA ligands per pore window (4 PA per nm^2) for a monolayer (Fig. 4.8).

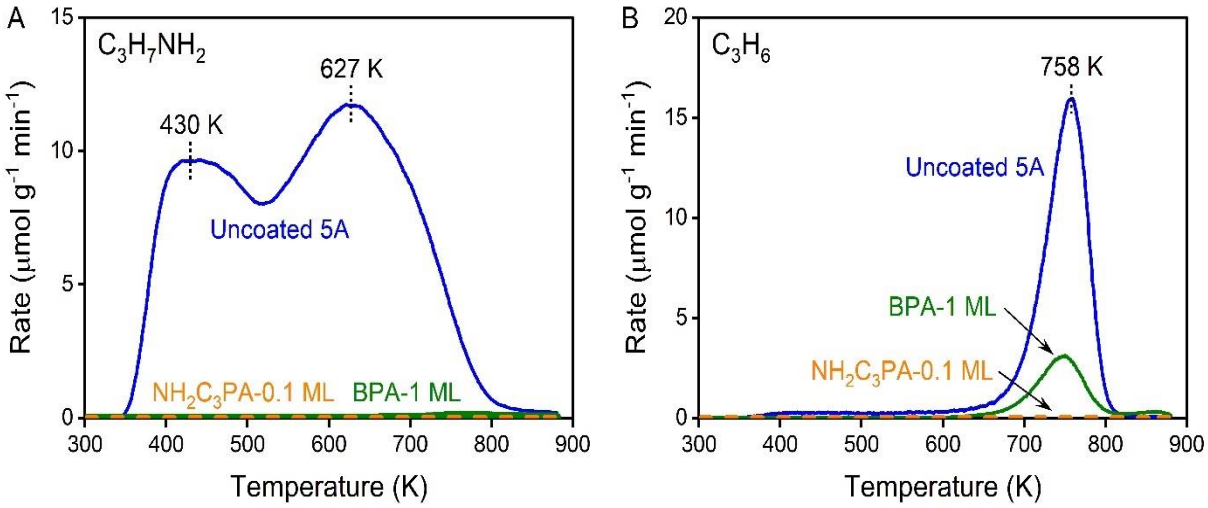

Figure 4.7. Rates of (A) n-propylamine desorption and (B) propylene production in TPD for uncoated, 1 ML BPA-, and 0.1 ML NH_2C_3PA coated zeolite 5A after n-propylamine exposure at 298 K for 1 h and following helium purge for 8 h.

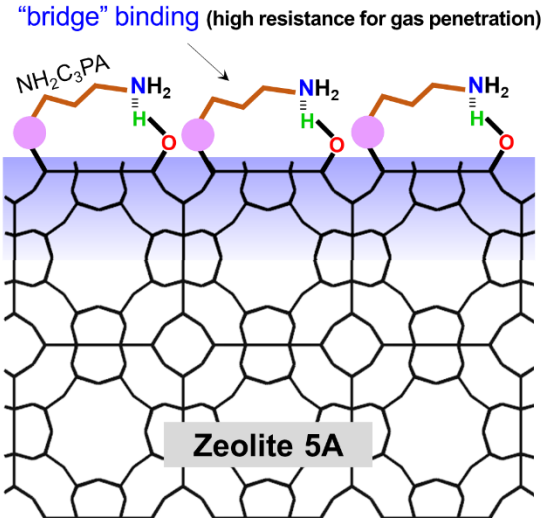

Figure 4.8. Schematic illustration of NH_2C_3PA-coated (0.1 ML) zeolite 5A with one ligand per pore window. Hydrogen bond formed between the amine group and the hydroxyl group on zeolite surface.

The temperature dependence of gas adsorption on zeolite coated with 0.1 ML NH_2C_3PA was investigated. The C_3H_6 adsorption was still far from equilibrium after 60 min at 298 K, but it almost reached equilibrium after 60 min at 343 and 373 K (Fig. 4.9A); with the increase of temperature, the rate to approach equilibrium increased (the initial fractional rate at 373 K was three times higher than the rate at 298 K) (Fig. 4.9B and Table C.5), indicating that C_3H_6 adsorption rate was temperature sensitive, consistent with an energy barrier for disruption of hydrogen bonding between the amine group and hydroxyl group on the zeolite surface.

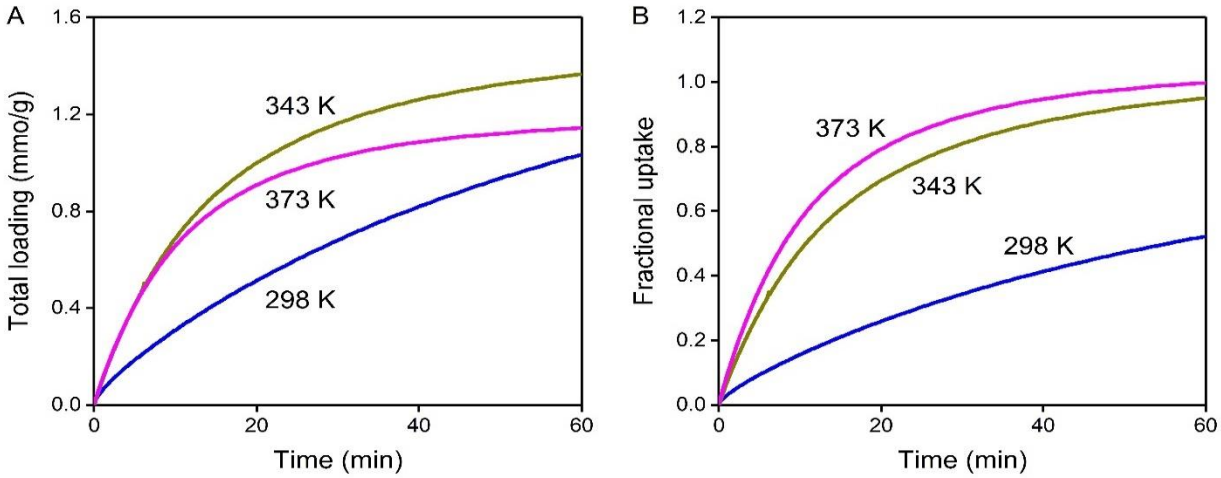

Figure 4.9. C_3H_6 adsorption (A) loading and (B) fractional uptake at different temperatures (298–373 K) on zeolite 5A coated with 0.1 ML NH_2C_3PA.

4.5. Conclusions

Amine and carboxylic acid terminal functional groups of PAs influenced the interaction of ligands with the surfaces of zeolite 5A and thus the arrangement of PA molecules, and they were employed to tune gas adsorption rates of C_3H_6 and C_3H_8 . With similar ligand chain lengths, the $COOHC_3PA$ coating layer had higher resistance to gas diffusion than BPA, and the gas diffusion resistance was even higher for the NH_2C_3PA coating so that even CO_2 diffused slowly into the pores. The PA

coating density on zeolite surfaces was adjusted by varying the concentration of PAs during deposition. As the PA coating density decreased, the initial adsorption rates of both C_3H_6 and C_3H_8 increased; however, the density-dependent trend for NH_2C_3PA was far more pronounced than that for ODPA. The zeolite coated with only 0.04 ML of NH_2C_3PA had about the same resistance for C_3H_6 diffusion as the zeolite fully coated with ODPA. With a 0.1 ML coating of NH_2C_3PA on zeolite 5A, the kinetic ideal selectivity was 15 for 60 min. We found that a probe molecule, *n*-propylamine, adsorbed strongly to hydroxyl groups on the external surface of the zeolite, suggesting that at low coating densities of NH_2C_3PA, a bridge-shaped structure may form across the zeolite pore window to create high gas diffusion resistance. Varying the functional group of PA and coating density allows gas adsorption rates and kinetic adsorption selectivities to be tuned, which provides insights for the rational design of adsorbent for gas adsorptive separation.

4.6. References

[1] E. Hoque, J.A. DeRose, G. Kulik, P. Hoffmann, H.J. Mathieu, B. Bhushan, Alkylphosphonate modified aluminum oxide surfaces, J. Phys. Chem. B 110 (2006) 10855–10861. https://doi.org/10.1021/jp061327a.

[2] T. Hauffman, O. Blajiev, J. Snauwaert, C. Van Haesendonck, A. Hubin, H. Terryn, Study of the self-assembling of *n*-octylphosphonic acid layers on aluminum oxide, Langmuir 24 (2008) 13450–13456. https://doi.org/10.1021/la801978a.

[3] Z. Blanchette, J. Zhang, S. Yazdi, M.B. Griffin, D.K. Schwartz, J.W. Medlin, Investigating deposition sequence during synthesis of Pd/Al_2O_3 catalysts modified with organic monolayers, Catal. Sci. Technol. 12 (2022) 2306–2314. https://doi.org/10.1039/D1CY02131A.

[4] A.H. Jenkins, E.E. Dunphy, M.F. Toney, C.B. Musgrave, J.W. Medlin, Tailoring the near-surface environment of Rh single-atom catalysts for selective CO_2 hydrogenation, ACS Catal. 13 (2023) 15340–15350.

https://doi.org/10.1021/acscatal.3c03768.
[5] L.D. Ellis, S.T. Parker, J. Hu, S.F. Zaccarine, M.J. Stellato, H.H. Funke, C. Sievers, S. Pylypenko, J.L. Falconer, J.W. Medlin, Tuning gas adsorption selectivity and diffusion rates in zeolites with phosphonic acid monolayers, Cell Rep. Phys. Sci. 1 (2020) 100036. https://doi.org/10.1016/j.xcrp.2020.100036.
[6] X. Zhou, J.L. Falconer, J.W. Medlin, Mechanism of selectivity control for zeolites modified with organic monolayers, Microporous Mesoporous Mater. 337 (2022) 111913. https://doi.org/10.1016/j.micromeso.2022.111913.
[7] X. Zhou, J.L. Falconer, J.W. Medlin, Competitive adsorption between propylene and propane on zeolite 5A and the influence of organic phosphonic acid coatings, Sep. Purif. Technol. 346 (2024) 127435. https://doi.org/10.1016/j.seppur.2024.127435.
[8] D.M. Spori, N.V. Venkataraman, S.G.P. Tosatti, F. Durmaz, N.D. Spencer, S. Zürcher, Influence of alkyl chain length on phosphate self-assembled monolayers, Langmuir 23 (2007) 8053–8060. https://doi.org/10.1021/la700474v.
[9] B. Feichtenschlager, C.J. Lomoschitz, G. Kickelbick, Tuning the self-assembled monolayer formation on nanoparticle surfaces with different curvatures: Investigations on spherical silica particles and plane-crystal-shaped zirconia particles, J. Colloid Interface Sci. 360 (2011) 15–25. https://doi.org/10.1016/j.jcis.2011.03.035.
[10] J.M. Castillo, M. Klos, K. Jacobs, M. Horsch, H. Hasse, Characterization of alkylsilane self-assembled monolayers by molecular simulation, Langmuir 31 (2015) 2630–2638. https://doi.org/10.1021/la504178g.
[11] N. Gys, L. Siemons, B. Pawlak, K. Wyns, K. Baert, T. Hauffman, P. Adriaensens, F. Blockhuys, B. Michielsen, S. Mullens, V. Meynen, Experimental and computational insights into the aminopropylphosphonic acid modification of mesoporous TiO_2 powder: The role of the amine functionality on the surface interaction and coordination, Appl. Surf. Sci. 566 (2021) 150625. https://doi.org/10.1016/j.apsusc.2021.150625.
[12] M. Gnauck, E. Jaehne, T. Blaettler, S. Tosatti, M. Textor, H.-J.P. Adler, Carboxy-terminated oligo(ethylene glycol)-alkane phosphate: Synthesis and self-Assembly on titanium oxide surfaces, Langmuir 23 (2007) 377–381. https://doi.org/10.1021/la0606648.
[13] D.K. Jacquelín, M.A. Pérez, E.M. Euti, N. Arisnabarreta, F.P. Cometto, P. Paredes-Olivera, E.M. Patrito, A pH-sensitive supramolecular switch based on mixed carboxylic acid terminated self-assembled monolayers on Au(111), Langmuir 32 (2016) 947–953. https://doi.org/10.1021/acs.langmuir.5b03807.
[14] S. Pookpanratana, J.W.F. Robertson, C. Jaye, D.A. Fischer, C.A. Richter, C.A. Hacker, Electrical and physical characterization of bilayer carboxylic acid-functionalized molecular layers, Langmuir 29 (2013) 2083–2091. https://doi.org/10.1021/la304225m.
[15] P.D. Coan, L.D. Ellis, M.B. Griffin, D.K. Schwartz, J.W. Medlin, Enhancing cooperativity in bifunctional acid-Pd catalysts with carboxylic acid-functionalized organic monolayers, J. Phys. Chem. C 122 (2018) 6637–6647.

https://doi.org/10.1021/acs.jpcc.7b12442.
[16] V. Kulkarni, D. Panda, S.K. Singh, Direct air capture of CO_2 over amine-modified hierarchical silica, Ind. Eng. Chem. Res. 62 (2023) 3800–3811. https://doi.org/10.1021/acs.iecr.2c02268.
[17] H. Chen, F. Yan, X. Jiao, H. Wu, X. Liang, X. Shen, H. Fan, Z. Zhang, Facile and efficient amine@AD-SiO_2 adsorbents from coal fly ash: Comparison of various amines for CO_2 adsorption capacity and cyclic stability, Sep. Purif. Technol. 346 (2024) 127469. https://doi.org/10.1016/j.seppur.2024.127469.
[18] V. Tejavath, V. Kasarabada, S. Gonuguntla, V. Perupoga, S.V. Nandury, S. Bojja, U. Pal, Technoeconomic investigation of amine-grafted zeolites and their kinetics for CO_2 capture, ACS Omega 6 (2021) 6153–6162. https://doi.org/10.1021/acsomega.0c05397.
[19] F. Bahmanzadegan, M.A. Pordsari, A. Ghaemi, Improving the efficiency of 4A-zeolite synthesized from kaolin by amine functionalization for CO_2 capture, Sci Rep 13 (2023) 12533. https://doi.org/10.1038/s41598-023-39859-z.
[20] S.T. Yang, J.Y. Kim, J. Kim, W.S. Ahn, CO_2 capture over amine-functionalized MCM-22, MCM-36 and ITQ-2, Fuel 97 (2012) 435–442. https://doi.org/10.1016/j.fuel.2012.03.034.
[21] L. Lin, S. Han, F. Meng, J. Li, K. Chen, E. Hu, J. Jiang, The influence of pore size and pore structure of silica-based material on the amine-modified adsorbent for CO_2 capture, Sep. Purif. Technol. 340 (2024) 126735. https://doi.org/10.1016/j.seppur.2024.126735.
[22] T. Wang, F. Liu, W. Tang, S. Xu, H. Dong, Z. Chen, X. Gao, Ultra-highly efficient adsorbent for CO_2 capture from air by directional deprotonation regulation of MOFs-based amine grafting, Chem. Eng. J. 490 (2024) 151426. https://doi.org/10.1016/j.cej.2024.151426.
[23] C. Tudisco, V. Oliveri, M. Cantarella, G. Vecchio, G.G. Condorelli, Cyclodextrin anchoring on magnetic Fe_3O_4 nanoparticles modified with phosphonic linkers, Eur. J. Inorg. Chem. 2012 (2012) 5323–5331. https://doi.org/10.1002/ejic.201200510.
[24] C. Tudisco, M.T. Cambria, F. Sinatra, F. Bertani, A. Alba, A.E. Giuffrida, S. Saccone, E. Fantechi, C. Innocenti, C. Sangregorio, E. Dalcanale, G.G. Condorelli, Multifunctional magnetic nanoparticles for enhanced intracellular drug transport, J. Mater. Chem. B 3 (2015) 4134–4145. https://doi.org/10.1039/C5TB00547G.
[25] I.W. Zapelini, D. Cardoso, Amine-grafted Na-LTA zeolite precursors as basic catalysts for Knoevenagel condensation, Microporous Mesoporous Mater. 324 (2021) 111270. https://doi.org/10.1016/j.micromeso.2021.111270.
[26] R. Helmy, A.Y. Fadeev, Self-Assembled monolayers supported on TiO_2 : Comparison of $C_{18}H_{37}SiX_3$ (X = H, Cl, OCH_3), $C_{18}H_{37}Si(CH_3)_2Cl$, and $C_{18}H_{37}PO(OH)_2$, Langmuir 18 (2002) 8924–8928. https://doi.org/10.1021/la0262506.
[27] P.D. Coan, M.B. Griffin, P.N. Ciesielski, J.W. Medlin, Phosphonic acid modifiers for enhancing selective hydrodeoxygenation over Pt catalysts: The

role of the catalyst support, J. Catal. 372 (2019) 311–320. https://doi.org/10.1016/j.jcat.2019.03.011.
[28] S. Brunauer, P.H. Emmett, E. Teller, Adsorption of gases in multimolecular layers, J. Am. Chem. Soc. 60 (1938) 309–319. https://doi.org/10.1021/ja01269a023.
[29] J.H. de Boer, B.C. Lippens, B.G. Linsen, J.C.P. Broekhoff, A. Van Den Heuvel, Th.J. Osinga, The t-curve of multimolecular N_2-adsorption, J. Colloid Interface Sci. 21 (1966) 405–414. https://doi.org/10.1016/0095-8522(66)90006-7.
[30] G. Horváth, K. Kawazoe, Method for the calculation of effective pore size distribution in molecular sieve carbon., J. Chem. Eng. Japan 16 (1983) 470–475. https://doi.org/10.1252/jcej.16.470.
[31] G.J. Kluth, M.M. Sung, R. Maboudian, Thermal behavior of alkylsiloxane self-assembled monolayers on the oxidized Si(100) surface, Langmuir 13 (1997) 3775–3780. https://doi.org/10.1021/la970135r.
[32] Y. Kim, Thermal decomposition of octanethiolate self-assembled monolayers on Cu(111) in UHV, Bull. Korean Chem. Soc. 24 (2003) 610–612. https://doi.org/10.5012/BKCS.2003.24.5.610.
[33] X. Wan, I. Lieberman, A. Asyuda, S. Resch, H. Seim, P. Kirsch, M. Zharnikov, Thermal stability of phosphonic acid self-assembled monolayers on alumina substrates, J. Phys. Chem. C 124 (2020) 2531–2542. https://doi.org/10.1021/acs.jpcc.9b10628.
[34] L.D. Ellis, R.M. Trottier, C.B. Musgrave, D.K. Schwartz, J.W. Medlin, Controlling the surface reactivity of titania via electronic tuning of self-assembled monolayers, ACS Catal. 7 (2017) 8351–8357. https://doi.org/10.1021/acscatal.7b02789.
[35] S. Pawsey, K. Yach, L. Reven, Self-assembly of carboxyalkylphosphonic acids on metal oxide powders, Langmuir 18 (2002) 5205–5212. https://doi.org/10.1021/la015749h.
[36] M. Huelsekopf, R. Ludwig, Temperature dependence of hydrogen bonding in alcohols, J. Mol. Liq. 85 (2000) 105–125. https://doi.org/10.1016/S0167-7322(99)00168-3.
[37] D.K. Schwartz, Mechanisms and kinetics of self-assembled monolayer formation, Annu. Rev. Phys. Chem. 52 (2001) 107–137. https://doi.org/10.1146/annurev.physchem.52.1.107.
[38] J. Lahann, S. Mitragotri, T.N. Tran, H. Kaido, J. Sundaram, I.S. Choi, S. Hoffer, G.A. Somorjai, R. Langer, A reversibly switching surface, Science 299 (2003) 371–374. https://doi.org/10.1126/science.1078933.
[39] O. Kresnawahjuesa, R. Heussner, C.C. Lee, G. Kuehl, R.J. Gorte, An examination of acid sites in H-LTA zeolites, Appl. Catal. A: General 199 (2000) 53–60. https://doi.org/10.1016/S0926-860X(99)00549-9.
[40] A.I. Biaglow, D.J. Parrillo, R.J. Gorte, Characterization of H,Na-Y using amine desorption, J. Catal. 144 (1993) 193–201. https://doi.org/10.1006/jcat.1993.1323.

Chapter 5: Conclusions and future directions

5.1. Summary

Adsorptive separation is an energy-efficient alternative method to traditional distillation for gas separation. Kinetic separation of C_3H_6 and C_3H_8 is challenging due to the similar molecular sizes for the two molecules. Zeolites are widely used as adsorbents for gas adsorptive separation. Surface coating modification for zeolites is an effective method to improve kinetic selectivity. In this thesis, organic phosphonic acids (PAs) were used to modify zeolite surfaces for the adsorptive separation of C_3H_6 and C_3H_8. The gas diffusion rates were controlled by changing the properties of PA coatings, such as varying the ligand chain length, steric configuration, functional group, and coating density. The role of displacement of one adsorbate by another on mixture adsorption selectivity was studied. The aim of this work is not only to develop efficient adsorbents but also to provide insights on the structure-function relationships of zeolites coated with PAs and understand the mechanism of selectivity control for the adsorbents in gas separation.

The PA coatings have been used to modify zeolite surfaces to tune gas adsorption rates. It is important to understand the mechanism of PA-coated zeolites for selective adsorption. In the work described in Chapter 2, PAs with different alkyl chain length and steric configuration were coated on zeolite 5A. The PA coatings decreased gas adsorption rates, especially for C_3H_8, and improved kinetic selectivity of C_3H_6/C_3H_8 based on single-gas, pressure-decay adsorption measurements. The temperature dependence of adsorption selectivity was investigated for uncoated and

PA-coated zeolite 5A. The adsorption curves were fit with two kinetic models, including an internal diffusion model and a surface limitation model, to determine the dominate barrier for gas diffusion. The *n*-octadecylphosphonic acid (ODPA) coating changed the dominant diffusion barrier for gas molecules from pore channels to coating layers. By providing gas-specific resistance on zeolite surfaces, the PA coatings enhanced the kinetic adsorption selectivity.

The PA coatings on zeolite 5A enhanced the ideal kinetic selectivity of C_3H_6/C_3H_8 based on single-gas, pressure-decay adsorption measurements. Beyond that, understanding the competitive adsorption between C_3H_6 and C_3H_8 in mixtures is essential for developing an adsorptive separation process. The difference in diffusion rates of gas components and the interactions of gas components with adsorbent surfaces affect mixture selectivity. The work described in Chapter 3 investigated the selective adsorption of C_3H_6 over C_3H_8 in mixtures on zeolite 5A using a pulse injection method, followed by temperature-programmed desorption (TPD) to investigate desorption kinetics. The exposure-dependent trends in mixture selectivity were examined for mixtures with feed molar ratios of 50/50 and 90/10 C_3H_6/C_3H_8 and were compared with the ideal selectivity. The ODPA coating favored mixture selectivity of C_3H_6/C_3H_8 at low gas exposures, whereas uncoated 5A enabled high selectivity at high gas exposures due to the fast filling of the zeolite and displacement of C_3H_8 by C_3H_6. The findings demonstrated the importance of considering both barriers to gas diffusion and competitive adsorption between adsorbates for the design of adsorbents and separation processes.

Finally, to further extend the tunability of coating structure, PAs with terminal functional groups (amine or carboxylic acid group) and different coating densities were investigated. Single-gas, pressure-decay adsorption showed that the coatings of 4-phosphonobutyric acid ($COOHC_3PA$) and 3-aminopropyl phosphonic acid (NH_2C_3PA) had higher resistance to gas diffusion than *n*-butylphosphonic acid (BPA) with a similar ligand chain length. With the decrease of coating density, the initial adsorption rates of C_3H_6 and C_3H_8 increased, but the density-dependent trends varied drastically between NH_2C_3PA and *n*-octadecylphosphonic acid coatings. The TPD of a probe molecule, *n*-propylamine showed that the amine group bonded with hydroxyl group on the zeolite external surface, suggesting that at low coating densities of NH_2C_3PA, a bridge-shaped structure may form across the zeolite pore window to create high gas diffusion resistance. The gas adsorption rates and selectivities in zeolites are highly sensitive to the composition and density of monolayer films on material external surface.

5.2. Future directions

5.2.1. Zeolites coated with PAs for different gas separation systems

In this thesis, we focused on the adsorptive separation of C_3H_6 and C_3H_8 using PA-coated zeolite 5A, and gas adsorption rates were tuned by changing the properties of PAs, such as ligand chain lengths, steric configurations, functional groups, and coating densities. The PA modification technique can be employed for other zeolites with different aperture sizes and structures. The modified zeolites can be used for the

separation of other gases, such as linear from branched isomers and the separation of benzene derivatives. Potentially, the desired zeolite pore window and high selectivity could be achieved by PA coatings with suitable properties. Some preliminary results were obtained for single-gas, pressure-decay adsorption of CO_2, C_3H_6, and C_3H_8 on uncoated zeolites MOR and Y, as well as those coated with methylphosphonic acid (MPA) and *n*-octadecylphosphonic acid (ODPA). For zeolite MOR coated with MPA and ODPA, the loadings of C_3H_6 and C_3H_8 were <0.1 mmol/g at 10 min (Fig. D.1). For zeolite Y, the MPA coating had minimal effect on gas adsorption, whereas the ODPA coating decreased the equilibrium gas loadings (Fig. D.2). More experiments are needed to investigate PA coatings on wide-pore zeolites for adsorptive separation of C_{3+} hydrocarbons.

5.2.2. Zeolites coated with PAs for catalysis

The PA coating technique was used to modify zeolite surfaces for gas adsorptive separation. In this thesis, the PA coatings tuned gas adsorption rates and enhanced kinetic selectivity by changing the diffusion mechanism from pore channels to coating layers on the zeolite surface. Potentially, the selectivity control for PA-coated zeolites can be employed for catalysis, such as isomerization of butene, isomerization of xylene, and acetylene hydrogenation in a mixture with ethylene. For isomerization using zeolites as catalysts, benefited by the tuning effect of PA coating layers, linear configuration molecules may diffuse out of zeolite pores faster than branched, sterically bulky molecules, thereby facilitating the selectivity of linear molecules. For a catalytic reaction with a mixture as feed, smaller molecules may

diffuse into zeolite pores faster than the other molecules to access the active sites in the zeolite and result in high reaction selectivity.

5.2.3. Simulation of PA-coated zeolite 5A

PAs were utilized to modify zeolite 5A, and the PA coatings enhanced the kinetic selectivity of C_3H_6 and C_3H_8. However, the structures of PAs on zeolites are not well understood at the molecular scale. In Chapter 4, we investigated the effects of terminal functional groups (amine and carboxylic acid) of PAs on gas adsorption rates, and we proposed that at low coating densities, a hydrogen bond formed between the amine group of NH_2C_3PA and the hydroxyl group on the zeolite surface, creating a bridge-shaped ligand structure across the zeolite pore window. Computational techniques, such as density function theory (DFT) calculations and molecular dynamics (MD) simulations, could provide insights on the structure of PA coatings, such as the binding mode of PAs with zeolite surfaces, the molecular arrangements, the interactions between functional groups on the ligands, or between those groups and the zeolite surface. Also, simulations of the competitive adsorption between gas molecules in mixtures are helpful to comprehend the influence of PA coatings.

5.3. Final remarks

Coating modification is an important method to tune the properties of material surfaces. In this thesis, zeolites were modified with organic phosphonic acids (PAs) for gas adsorptive separation, specifically for C_3H_6 and C_3H_8 separation. Chapter 2 focused on tuning gas adsorption rates by changing the properties of PAs and

understanding the mechanism of selectivity control for zeolites modified with PAs. The work performed in Chapter 3 demonstrated the importance of competitive adsorption in dictating mixture selectivity. The work performed in Chapter 4 focused on the effects of PA terminal functional group and coating density on adsorption rates and selectivity. The work in this thesis provides insights for the design of adsorbents and adsorptive separation process, and potentially can be leveraged for other research areas, such as CO_2 capture, catalysis, and drug delivery.

Bibliography

S. Abbasi, M.R. Khosravi-Nikou, A. Shariati, Selective separation of propane from the propylene-propane mixture using pure silica zeolites: A molecular dynamic simulation, Chem. Eng. Process.: Process Intensif. 184 (2023) 109294. https://doi.org/10.1016/j.cep.2023.109294.

H. Abdi, H. Maghsoudi, All-silica DD3R zeolite for adsorptive separation of propylene from propane: Equilibrium and kinetic data, Microporous Mesoporous Mater. 307 (2020) 110513. https://doi.org/10.1016/j.micromeso.2020.110513.

H. Abedini, M. Asgari, M. Watt Coull, A. Shariati, M.R. Khosravi-Nikou, Efficient production of polymer-grade propylene from the propane/propylene binary mixture using Cu-MOF-74 framework, Sep. Purif. Technol. 276 (2021) 119172. https://doi.org/10.1016/j.seppur.2021.119172.

H. Abedini, A. Shariati, M.R. Khosravi-Nikou, Separation of propane/propylene mixture using MIL-101(Cr) loaded with cuprous oxide nanoparticles: Adsorption equilibria and kinetics study, Chem. Eng. J. 387 (2020) 124172. https://doi.org/10.1016/j.cej.2020.124172.

A. Akah, M. Al-Ghrami, Maximizing propylene production via FCC technology, Appl. Petrochem. Res. 5 (2015) 377–392. https://doi.org/10.1007/s13203-015-0104-3.

J.R. Alcántara-Avila, F.I. Gómez-Castro, J.G. Segovia-Hernández, K.I. Sotowa, T. Horikawa, Optimal design of cryogenic distillation columns with side heat pumps for the propylene/propane separation, Chem. Eng. Process.: Process Intensif. 82 (2014) 112–122. https://doi.org/10.1016/j.cep.2014.06.006.

A. Anson, C.C.H. Lin, T.M. Kuznicki, S.M. Kuznicki, Separation of ethylene/ethane mixtures by adsorption on small-pored titanosilicate molecular sieves, Chem. Eng. Sci. 65 (2010) 807–811. https://doi.org/10.1016/j.ces.2009.09.033.

C.C. Aquino, G. Richner, M.C. Kimling, D. Chen, G. Puxty, P.H.M. Feron, R.A. Caruso, Amine-functionalized titania-based porous structures for carbon dioxide postcombustion capture, J. Phys. Chem. C 117 (2013) 9747–9757. https://doi.org/10.1021/jp312118e.

Y.S. Bae, C.Y. Lee, K.C. Kim, O.K. Farha, P. Nickias, J.T. Hupp, S.T. Nguyen, R.Q. Snurr, High propene/propane selectivity in isostructural metal-organic frameworks with high densities of open metal sites, Angew. Chem. 124 (2012) 1893–1896. https://doi.org/10.1002/ange.201107534.

F. Bahmanzadegan, M.A. Pordsari, A. Ghaemi, Improving the efficiency of 4A-zeolite synthesized from kaolin by amine functionalization for CO_2 capture, Sci Rep 13 (2023) 12533. https://doi.org/10.1038/s41598-023-39859-z.

R. Bai, X. Song, W. Yan, J. Yu, Low-energy adsorptive separation by zeolites, Natl. Sci. Rev. 9 (2022) nwac064. https://doi.org/10.1093/nsr/nwac064.

P.J. Bereciartua, Á. Cantín, A. Corma, J.L. Jordá, M. Palomino, F. Rey, S. Valencia, E.W. Corcoran, P. Kortunov, P.I. Ravikovitch, A. Burton, C. Yoon, Y. Wang, C. Paur, J. Guzman, A.R. Bishop, G.L. Casty, Control of zeolite framework flexibility and pore topology for separation of ethane and ethylene, Science. 358 (2017) 1068–1071. https://doi.org/10.1126/science.aao0092.

A.I. Biaglow, D.J. Parrillo, R.J. Gorte, Characterization of H,Na-Y using amine desorption, J. Catal. 144 (1993) 193–201. https://doi.org/10.1006/jcat.1993.1323.

Z. Blanchette, J. Zhang, S. Yazdi, M.B. Griffin, D.K. Schwartz, J.W. Medlin, Investigating deposition sequence during synthesis of Pd/Al_2O_3 catalysts modified with organic monolayers, Catal. Sci. Technol. 12 (2022) 2306–2314. https://doi.org/10.1039/D1CY02131A.

E.D. Bloch, W.L. Queen, R. Krishna, J.M. Zadrozny, C.M. Brown, J.R. Long, Hydrocarbon separations in a metal-organic framework with open iron(II) coordination sites, Science 335 (2012) 1606–1610. https://doi.org/10.1126/science.1217544.

J.H. de Boer, B.C. Lippens, B.G. Linsen, J.C.P. Broekhoff, A. van den Heuvel, Th.J. Osinga, The t-curve of multimolecular N_2-adsorption, J. Colloid Interface Sci. 21 (1966) 405–414. https://doi.org/10.1016/0095-8522(66)90006-7.

S. Brunauer, P.H. Emmett, E. Teller, Adsorption of gases in multimolecular layers, J. Am. Chem. Soc. 60 (1938) 309–319. https://doi.org/10.1021/ja01269a023.

A. Cadiau, K. Adil, P.M. Bhatt, Y. Belmabkhout, M. Eddaoudi, A metal-organic framework-based splitter for separating propylene from propane, Science. 353 (2016) 137–140. https://doi.org/10.1126/science.aaf6323.

M.C. Campo, A.M. Ribeiro, A. Ferreira, J.C. Santos, C. Lutz, J.M. Loureiro, A.E. Rodrigues, New 13X zeolite for propylene/propane separation by vacuum swing adsorption, Sep. Purif. Technol. 103 (2013) 60–70. https://doi.org/10.1016/j.seppur.2012.10.009.

J.M. Castillo, M. Klos, K. Jacobs, M. Horsch, H. Hasse, Characterization of alkylsilane self-assembled monolayers by molecular simulation, Langmuir 31 (2015) 2630–2638. https://doi.org/10.1021/la504178g.

Y. Chai, X. Han, W. Li, S. Liu, S. Yao, C. Wang, W. Shi, I. da-Silva, P. Manuel, Y. Cheng, L.D. Daemen, A.J. Ramirez-Cuesta, C.C. Tang, L. Jiang, S. Yang, N. Guan, L. Li, Control of zeolite pore interior for chemoselective alkyne/olefin separations, Science. 368 (2020) 1002–1006. https://doi.org/10.1126/science.aay8447.

H. Chen, F. Yan, X. Jiao, H. Wu, X. Liang, X. Shen, H. Fan, Z. Zhang, Facile and efficient amine@AD-SiO_2 adsorbents from coal fly ash: Comparison of various amines for CO_2 adsorption capacity and cyclic stability, Sep. Purif. Technol. 346 (2024) 127469. https://doi.org/10.1016/j.seppur.2024.127469.

Y. Chen, Y. Yang, Y. Wang, Q. Xiong, J. Yang, S. Xiang, L. Li, J. Li, Z. Zhang, B. Chen, Ultramicroporous hydrogen-bonded organic framework material with a thermoregulatory gating effect for record propylene separation, J. Am. Chem. Soc. 144 (2022) 17033–17040. https://doi.org/10.1021/jacs.2c06585.

O. Cheung, N. Hedin, Zeolites and related sorbents with narrow pores for CO_2 separation from flue gas, RSC Adv. 4 (2014) 14480–14494. https://doi.org/10.1039/C3RA48052F.

M.L. Chng, Y. Xiao, T.S. Chung, M. Toriida, S. Tamai, Enhanced propylene/propane separation by carbonaceous membrane derived from poly (aryl ether ketone)/2,6-bis(4-azidobenzylidene)-4-methyl-cyclohexanone interpenetrating network, Carbon 47 (2009) 1857–1866. https://doi.org/10.1016/j.carbon.2009.03.032.

C.D. Chudasama, J. Sebastian, R.V. Jasra, Pore-size engineering of zeolite A for the size/shape selective molecular separation, Ind. Eng. Chem. Res. 44 (2005) 1780–1786. https://doi.org/10.1021/ie049333l.

P.D. Coan, L.D. Ellis, M.B. Griffin, D.K. Schwartz, J.W. Medlin, Enhancing cooperativity in bifunctional acid-Pd catalysts with carboxylic acid-functionalized organic monolayers, J. Phys. Chem. C 122 (2018) 6637–6647. https://doi.org/10.1021/acs.jpcc.7b12442.

P.D. Coan, M.B. Griffin, P.N. Ciesielski, J.W. Medlin, Phosphonic acid modifiers for enhancing selective hydrodeoxygenation over Pt catalysts: The role of the catalyst support, J. Catal. 372 (2019) 311–320. https://doi.org/10.1016/j.jcat.2019.03.011.

J. Cui, Z. Zhang, L. Yang, J. Hu, A. Jin, Z. Yang, Y. Zhao, B. Meng, Y. Zhou, J. Wang, Y. Su, J. Wang, X. Cui, H. Xing, A molecular sieve with ultrafast adsorption kinetics for propylene separation, Science (2023) eabn8418. https://doi.org/10.1126/science.abn8418.

F.A. Da Silva, A.E. Rodrigues, Vacuum swing adsorption for propylene/propane separation with 4A zeolite, Ind. Eng. Chem. Res. 40 (2001) 5758–5774. https://doi.org/10.1021/ie0008732.

Q. Ding, Z. Zhang, P. Zhang, J. Wang, X. Cui, C.H. He, S. Deng, H. Xing, Control of intracrystalline diffusion in a bilayered metal-organic framework for efficient kinetic separation of propylene from propane, Chem. Eng. J. 434 (2022) 134784. https://doi.org/10.1016/j.cej.2022.134784.

Q. Dong, Z. Song, F. Zhou, H. Li, M. Yu, Ultrathin, fine-tuned microporous coating modified 5A zeolite for propane/propylene adsorptive separation, Microporous Mesoporous Mater. 281 (2019) 9–14. https://doi.org/10.1016/j.micromeso.2019.02.038.

L.D. Ellis, S.T. Parker, J. Hu, S.F. Zaccarine, M.J. Stellato, H.H. Funke, C. Sievers, S. Pylypenko, J.L. Falconer, J.W. Medlin, Tuning gas adsorption selectivity and diffusion rates in zeolites with phosphonic acid monolayers, Cell Rep. Phys. Sci. 1 (2020) 100036. https://doi.org/10.1016/j.xcrp.2020.100036.

L.D. Ellis, R.M. Trottier, C.B. Musgrave, D.K. Schwartz, J.W. Medlin, Controlling the surface reactivity of titania via electronic tuning of self-assembled monolayers, ACS Catal. 7 (2017) 8351–8357. https://doi.org/10.1021/acscatal.7b02789.

R. Faiz, K. Li, Polymeric membranes for light olefin/paraffin separation, Desalination. 287 (2012) 82–97. https://doi.org/10.1016/j.desal.2011.11.019.

J.L. Falconer, J.A. Schwarz, Temperature-programmed desorption and reaction: applications to supported catalysts, Catal. Rev. 25 (1983) 141–227. https://doi.org/10.1080/01614948308079666.

B. Feichtenschlager, C.J. Lomoschitz, G. Kickelbick, Tuning the self-assembled monolayer formation on nanoparticle surfaces with different curvatures: Investigations on spherical silica particles and plane-crystal-shaped zirconia particles, J. Colloid Interface Sci. 360 (2011) 15–25. https://doi.org/10.1016/j.jcis.2011.03.035.

J. Gao, Y. Cai, X. Qian, P. Liu, H. Wu, W. Zhou, D. Liu, L. Li, R. Lin, B. Chen, A Microporous hydrogen - bonded organic framework for the efficient capture and purification of propylene, Angew. Chem. 133 (2021) 20563–20569. https://doi.org/10.1002/ange.202106665.

J. Gascon, W. Blom, A. van Miltenburg, A. Ferreira, R. Berger, F. Kapteijn, Accelerated synthesis of all-silica DD3R and its performance in the separation of propylene/propane mixtures, Microporous Mesoporous Mater. 115 (2008) 585–593. https://doi.org/10.1016/j.micromeso.2008.02.038.

M. Gehre, Z. Guo, G. Rothenberg, S. Tanase, Sustainable separations of C_4-hydrocarbons by using microporous materials, ChemSusChem. 10 (2017) 3947–3963. https://doi.org/10.1002/cssc.201700657.

M. Gnauck, E. Jaehne, T. Blaettler, S. Tosatti, M. Textor, H.-J.P. Adler, Carboxy-terminated oligo(ethylene glycol)-alkane phosphate: Synthesis and self-Assembly on titanium oxide surfaces, Langmuir 23 (2007) 377–381. https://doi.org/10.1021/la0606648.

C.A. Grande, J. Gascon, F. Kapteijn, A.E. Rodrigues, Propane/propylene separation with Li-exchanged zeolite 13X, Chem. Eng. J. 160 (2010) 207–214. https://doi.org/10.1016/j.cej.2010.03.044.

C.A. Grande, A. Lind, Ø. Vistad, D. Akporiaye, Olefin-paraffin separation using calcium-ETS-4, Ind. Eng. Chem. Res. 53 (2014) 15522–15530. https://doi.org/10.1021/ie5004703.

M. Guo, M. Kanezashi, Recent progress in a membrane-based technique for propylene/propane separation, Membranes. 11 (2021) 310. https://doi.org/10.3390/membranes11050310.

P. Gutfreund, O. Bäumchen, R. Fetzer, D. Van Der Grinten, M. Maccarini, K. Jacobs, H. Zabel, M. Wolff, Solid surface structure affects liquid order at the polystyrene-self-assembled-monolayer interface, Phys. Rev. E 87 (2013) 012306. https://doi.org/10.1103/PhysRevE.87.012306.

N. Gys, L. Siemons, B. Pawlak, K. Wyns, K. Baert, T. Hauffman, P. Adriaensens, F. Blockhuys, B. Michielsen, S. Mullens, V. Meynen, Experimental and computational insights into the aminopropylphosphonic acid modification of mesoporous TiO_2 powder: The role of the amine functionality on the surface interaction and coordination, Appl. Surf. Sci. 566 (2021) 150625. https://doi.org/10.1016/j.apsusc.2021.150625.

T. Hauffman, O. Blajiev, J. Snauwaert, C. Van Haesendonck, A. Hubin, H. Terryn, Study of the self-assembling of n-octylphosphonic acid layers on aluminum oxide, Langmuir 24 (2008) 13450–13456. https://doi.org/10.1021/la801978a.

R. Helmy, A.Y. Fadeev, Self-Assembled monolayers supported on TiO_2 : Comparison of $C_{18}H_{37}SiX_3$ (X = H, Cl, OCH_3), $C_{18}H_{37}Si(CH_3)_2Cl$, and $C_{18}H_{37}PO(OH)_2$, Langmuir 18 (2002) 8924–8928. https://doi.org/10.1021/la0262506.

E. Hoque, J.A. DeRose, G. Kulik, P. Hoffmann, H.J. Mathieu, B. Bhushan, Alkylphosphonate modified aluminum oxide surfaces, J. Phys. Chem. B 110 (2006) 10855–10861. https://doi.org/10.1021/jp061327a.

G. Horváth, K. Kawazoe, Method for the calculation of effective pore size distribution in molecular sieve carbon., J. Chem. Eng. Japan 16 (1983) 470–475. https://doi.org/10.1252/jcej.16.470.

M. Huelsekopf, R. Ludwig, Temperature dependence of hydrogen bonding in alcohols, J. Mol. Liq. 85 (2000) 105–125. https://doi.org/10.1016/S0167-7322(99)00168-3.

International Zeolite Association. https://america.iza-structure.org/IZA-SC/ftc_table.php.

D.K. Jacquelín, M.A. Pérez, E.M. Euti, N. Arisnabarreta, F.P. Cometto, P. Paredes-Olivera, E.M. Patrito, A pH-sensitive supramolecular switch based on mixed carboxylic acid terminated self-assembled monolayers on Au(111), Langmuir 32 (2016) 947–953. https://doi.org/10.1021/acs.langmuir.5b03807.

A.H. Jenkins, E.E. Dunphy, M.F. Toney, C.B. Musgrave, J.W. Medlin, Tailoring the near-surface environment of Rh single-atom catalysts for selective CO_2 hydrogenation, ACS Catal. 13 (2023) 15340–15350. https://doi.org/10.1021/acscatal.3c03768.

S. Kasahara, E. Kamio, R. Minami, H. Matsuyama, A facilitated transport ion-gel membrane for propylene/propane separation using silver ion as a carrier, J. Membr. Sci. 431 (2013) 121–130. https://doi.org/10.1016/j.memsci.2012.12.026.

M. Khalighi, Y.F. Chen, S. Farooq, I.A. Karimi, J.W. Jiang, Propylene/propane separation using SiCHA, Ind. Eng. Chem. Res. 52 (2013) 3877–3892. https://doi.org/10.1021/ie3026955.

Y. Kim, Thermal decomposition of octanethiolate self-assembled monolayers on Cu(111) in UHV, Bull. Korean Chem. Soc. 24 (2003) 610–612. https://doi.org/10.5012/BKCS.2003.24.5.610.

G.J. Kluth, M.M. Sung, R. Maboudian, Thermal behavior of alkylsiloxane self-assembled monolayers on the oxidized Si(100) surface, Langmuir 13 (1997) 3775–3780. https://doi.org/10.1021/la970135r.

O. Kresnawahjuesa, R. Heussner, C.C. Lee, G. Kuehl, R.J. Gorte, An examination of acid sites in H-LTA zeolites, Appl. Catal. A: General 199 (2000) 53–60. https://doi.org/10.1016/S0926-860X(99)00549-9.

C. Krishnaraj, H.S. Jena, K. Leus, H.M. Freeman, L.G. Benning, P. van der Voort, An aliphatic hexene-covalent triazine framework for selective acetylene/methane and ethylene/methane separation, J. Mater. Chem. A. 7 (2019) 13188–13196. https://doi.org/10.1039/C8TA11722E.

V. Kulkarni, D. Panda, S.K. Singh, Direct air capture of CO_2 over amine-modified hierarchical silica, Ind. Eng. Chem. Res. 62 (2023) 3800–3811. https://doi.org/10.1021/acs.iecr.2c02268.

H.T. Kwon, H.K. Jeong, *In Situ* Synthesis of thin zeolitic-imidazolate framework ZIF-8 membranes exhibiting exceptionally high propylene/propane separation, J. Am. Chem. Soc. 135 (2013) 10763–10768. https://doi.org/10.1021/ja403849c.

J. Lahann, S. Mitragotri, T.N. Tran, H. Kaido, J. Sundaram, I.S. Choi, S. Hoffer, G.A. Somorjai, R. Langer, A reversibly switching surface, Science 299 (2003) 371–374. https://doi.org/10.1126/science.1078933.

L. Li, R.B. Lin, R. Krishna, X. Wang, B. Li, H. Wu, J. Li, W. Zhou, B. Chen, Flexible-robust metal-organic framework for efficient removal of propyne from propylene, J. Am. Chem. Soc. 139 (2017) 7733–7736. https://doi.org/10.1021/jacs.7b04268.

L. Li, R.B. Lin, X. Wang, W. Zhou, L. Jia, J. Li, B. Chen, Kinetic separation of propylene over propane in a microporous metal-organic framework, Chem. Eng. J. 354 (2018) 977–982. https://doi.org/10.1016/j.cej.2018.08.108.

Y. Li, H.M. Guan, T.S. Chung, S. Kulprathipanja, Effects of novel silane modification of zeolite surface on polymer chain rigidification and partial pore blockage in polyethersulfone (PES)–zeolite A mixed matrix membranes, J. Membr. Sci. 275 (2006) 17–28. https://doi.org/10.1016/j.memsci.2005.08.015.

Y. Li, L. Li, J. Yu, Applications of zeolites in sustainable chemistry, Chem. 3 (2017) 928–949. https://doi.org/10.1016/j.chempr.2017.10.009.

L. Lin, S. Han, F. Meng, J. Li, K. Chen, E. Hu, J. Jiang, The influence of pore size and pore structure of silica-based material on the amine-modified adsorbent for CO_2 capture, Sep. Purif. Technol. 340 (2024) 126735. https://doi.org/10.1016/j.seppur.2024.126735.

J. Liu, J. Goss, T. Calverley, Y. Liu, C. Broomall, J. Kang, R. Golombeski, D. Anaya, B. Moe, K. Mabe, G. Watson, A. Wetzel, Carbon molecular sieve fiber with 3.4–4.9 angstrom effective micropores for propylene/propane and other gas separations, Microporous Mesoporous Mater. 305 (2020) 110341. https://doi.org/10.1016/j.micromeso.2020.110341.

J. Liu, Y. Liu, D.K. Talay, E. Calverley, M. Brayden, M. Martinez, A new carbon molecular sieve for propylene/propane separations, Carbon 85 (2015) 201–211. https://doi.org/10.1016/j.carbon.2014.12.089.

R. Luschtinetz, A.F. Oliveira, H.A. Duarte, G. Seifert, Self-assembled monolayers of alkylphosphonic acids on aluminum oxide surfaces – A theoretical study, Z. Anorg. Allg. Chem. 636 (2010) 1506–1512. https://doi.org/10.1002/zaac.201000016.

X. Ma, P. Kumar, N. Mittal, A. Khlyustova, P. Daoutidis, K.A. Mkhoyan, M. Tsapatsis, Zeolitic imidazolate framework membranes made by ligand-induced permselectivation, Science. 361 (2018) 1008–1011. https://doi.org/10.1126/science.aat4123.

I. Maege, E. Jaehne, A. Henke, H.P. Adler, C. Bram, C. Jung, M. Stratmann, Ultrathin organic layers for corrosion protection, Macromolecular Symposia 126 (1998) 7–24. https://doi.org/10.1002/masy.19981260104.

H. Maghsoudi, H. Abdi, A. Aidani, Temperature- and pressure-dependent adsorption equilibria and diffusivities of propylene and propane in pure-silica Si-CHA zeolite, Ind. Eng. Chem. Res. 59 (2020) 1682–1692. https://doi.org/10.1021/acs.iecr.9b05451.

J.G. Min, K.C. Kemp, S.B. Hong, Propylene/propane separation on a ferroaluminosilicate levyne zeolite, Microporous Mesoporous Mater. 294 (2020) 109833. https://doi.org/10.1016/j.micromeso.2019.109833.

J.G. Min, K.C. Kemp, K.S. Kencana, R.R. Mukti, S.B. Hong, Dealuminated Cs-ZK-5 zeolite for propylene/propane separation, Chem. Eng. J. 413 (2021) 127422. https://doi.org/10.1016/j.cej.2020.127422.

A. Ortiz, L.M. Galán, D. Gorri, A.B. de Haan, I. Ortiz, Reactive ionic liquid media for the separation of propylene/propane gaseous mixtures, Ind. Eng. Chem. Res. 49 (2010) 7227–7233. https://doi.org/10.1021/ie100576r.

J. Padin, S.U. Rege, R.T. Yang, L.S. Cheng, Molecular sieve sorbents for kinetic separation of propane/propylene, Chem. Eng. Sci. 55 (2000) 4525–4535. https://doi.org/10.1016/S0009-2509(00)00099-3.

Y. Pan, T. Li, G. Lestari, Z. Lai, Effective separation of propylene/propane binary mixtures by ZIF-8 membranes, J. Membr. Sci. 390–391 (2012) 93–98. https://doi.org/10.1016/j.memsci.2011.11.024.

D. Panda, E.A. Kumar, S.K. Singh, Amine Modification of binder-containing zeolite 4A bodies for post-combustion CO_2 capture, Ind. Eng. Chem. Res. 58 (2019) 5301–5313. https://doi.org/10.1021/acs.iecr.8b03958.

S. Pawsey, K. Yach, L. Reven, Self-assembly of carboxyalkylphosphonic acids on metal oxide powders, Langmuir 18 (2002) 5205–5212. https://doi.org/10.1021/la015749h.

Y.Y. Peng, S. Srinivas, R. Narain, Modification of polymers, Polymer Science and Nanotechnology, Elsevier. (2020) 95–104. https://doi.org/10.1016/B978-0-12-816806-6.00005-4.

T.D. Pham, R.F. Lobo, Adsorption equilibria of CO_2 and small hydrocarbons in AEI-, CHA-, STT-, and RRO-type siliceous zeolites, Microporous Mesoporous Mater. 236 (2016) 100–108. http://dx.doi.org/10.1016/j.micromeso.2016.08.025.

B.R. Pimentel, R.P. Lively, Propylene enrichment via kinetic vacuum pressure swing adsorption using ZIF-8 fiber sorbents, ACS Appl. Mater. Interfaces. 10 (2018) 36323–36331. https://doi.org/10.1021/acsami.8b08983.

S. Pookpanratana, J.W.F. Robertson, C. Jaye, D.A. Fischer, C.A. Richter, C.A. Hacker, Electrical and physical characterization of bilayer carboxylic acid-functionalized molecular layers, Langmuir 29 (2013) 2083–2091. https://doi.org/10.1021/la304225m.

P.A. Redhead, Thermal desorption of gases, Vaccum. 12 (1962) 203–211. https://doi.org/10.1016/0042-207X(62)90978-8.

D.M. Ruthven, Diffusion in type A zeolites: New insights from old data, Microporous Mesoporous Mater. 162 (2012) 69–79. https://doi.org/10.1016/j.micromeso.2011.12.025.

D.M. Ruthven, S.C. Reyes, Adsorptive separation of light olefins from paraffins, Microporous Mesoporous Mater. 104 (2007) 59–66. https://doi.org/10.1016/j.micromeso.2007.01.005.

M. Sakai, N. Fujimaki, Y. Sasaki, N. Yasuda, M. Seshimo, M. Matsukata, Preferential adsorption of propylene over propane on a Ag-exchanged X-type zeolite membrane, ACS Appl. Mater. Interfaces. 12 (2020) 24086–24092. https://doi.org/10.1021/acsami.0c01461.

D.K. Schwartz, Mechanisms and kinetics of self-assembled monolayer formation, Annu. Rev. Phys. Chem. 52 (2001) 107–137. https://doi.org/10.1146/annurev.physchem.52.1.107.

C. Selzer, A. Werner, S. Kaskel, Selective adsorption of propene over propane on hierarchical zeolite ZSM-58, Ind. Eng. Chem. Res. 57 (2018) 6609–6617. https://doi.org/10.1021/acs.iecr.8b00377.

J. Shang, G. Li, R. Singh, Q. Gu, K.M. Nairn, T.J. Bastow, N. Medhekar, C.M. Doherty, A.J. Hill, J.Z. Liu, P.A. Webley, Discriminative separation of gases by a "molecular trapdoor" mechanism in chabazite zeolites, J. Am. Chem. Soc. 134 (2012) 19246–19253. https://doi.org/10.1021/ja309274y.

D.S. Sholl, R.P. Lively, Seven chemical separations to change the world, Nature 532 (2016) 435–437. https://doi.org/10.1038/532435a.

S. Shrestha, P.K. Dutta, Modification of a continuous zeolite membrane grown within porous polyethersulfone with Ag(I) cations for enhanced propylene/propane gas separation, Microporous Mesoporous Mater. 279 (2019) 178–185. https://doi.org/10.1016/j.micromeso.2018.12.032.

D.M. Spori, N.V. Venkataraman, S.G.P. Tosatti, F. Durmaz, N.D. Spencer, S. Zürcher, Influence of alkyl chain length on phosphate self-assembled monolayers, Langmuir 23 (2007) 8053–8060. https://doi.org/10.1021/la700474v.

H. Strathmann, Membranes and membrane separation processes, Ullmann's Encyclopedia of Industrial Chemistry, Wiley-VCH Verlag GmbH & Co. KGaA, Weinheim, Germany. (2005) 16–187. https://doi.org/10.1002/14356007.a16_187.pub2.

R.J. Swaidan, B. Ghanem, R. Swaidan, E. Litwiller, I. Pinnau, Pure- and mixed-gas propylene/propane permeation properties of spiro- and triptycene-based microporous polyimides, J. Membr. Sci. 492 (2015) 116–122. https://doi.org/10.1016/j.memsci.2015.05.044.

V. Tejavath, V. Kasarabada, S. Gonuguntla, V. Perupoga, S.V. Nandury, S. Bojja, U. Pal, Technoeconomic investigation of amine-grafted zeolites and their kinetics for CO_2 capture, ACS Omega 6 (2021) 6153–6162. https://doi.org/10.1021/acsomega.0c05397.

M. Thommes, K. Kaneko, A.V. Neimark, J.P. Olivier, F. Rodriguez-Reinoso, J. Rouquerol, K.S.W. Sing, Physisorption of gases, with special reference to the evaluation of surface area and pore size distribution (IUPAC Technical Report), Pure Appl. Chem. 87 (2015) 1051–1069. https://doi.org/10.1515/pac-2014-1117.

C. Tudisco, M.T. Cambria, F. Sinatra, F. Bertani, A. Alba, A.E. Giuffrida, S. Saccone, E. Fantechi, C. Innocenti, C. Sangregorio, E. Dalcanale, G.G. Condorelli, Multifunctional magnetic nanoparticles for enhanced intracellular drug transport, J. Mater. Chem. B 3 (2015) 4134–4145. https://doi.org/10.1039/C5TB00547G.

C. Tudisco, V. Oliveri, M. Cantarella, G. Vecchio, G.G. Condorelli, Cyclodextrin anchoring on magnetic Fe_3O_4 nanoparticles modified with phosphonic linkers, Eur. J. Inorg. Chem. 2012 (2012) 5323–5331. https://doi.org/10.1002/ejic.201200510.

A. Ulman, Formation and structure of self-sssembled monolayers, Chem. Rev. 96 (1996) 1533–1554. https://doi.org/10.1021/cr9502357.

X. Wan, I. Lieberman, A. Asyuda, S. Resch, H. Seim, P. Kirsch, M. Zharnikov, Thermal stability of phosphonic acid self-assembled monolayers on alumina substrates, J. Phys. Chem. C 124 (2020) 2531–2542. https://doi.org/10.1021/acs.jpcc.9b10628.

H. Wang, X. Dong, V. Colombo, Q. Wang, Y. Liu, W. Liu, X. Wang, X. Huang, D.M. Proserpio, A. Sironi, Y. Han, J. Li, Tailor - made microporous metal-organic frameworks for the full separation of propane from propylene through selective size exclusion, Adv. Mater. 30 (2018) 1805088. https://doi.org/10.1002/adma.201805088.

T. Wang, F. Liu, W. Tang, S. Xu, H. Dong, Z. Chen, X. Gao, Ultra-highly efficient adsorbent for CO_2 capture from air by directional deprotonation regulation of MOFs-based amine grafting, Chem. Eng. J. 490 (2024) 151426. https://doi.org/10.1016/j.cej.2024.151426.

Y. Wang, T. Du, Y. Song, S. Che, X. Fang, L. Zhou, Amine-functionalized mesoporous ZSM-5 zeolite adsorbents for carbon dioxide capture, Solid State Sci. 73 (2017) 27–35. https://doi.org/10.1016/j.solidstatesciences.2017.09.004.

P. Wei, X. Qu, H. Dong, L. Zhang, H. Chen, C. Gao, Silane - modified NaA zeolite/PAAS hybrid pervaporation membranes for the dehydration of ethanol, J. Appl. Polym. Sci. 128 (2013) 3390–3397. https://doi.org/10.1002/app.38555.

M.H. Weston, Y.J. Colón, Y.S. Bae, S.J. Garibay, R.Q. Snurr, O.K. Farha, J.T. Hupp, S.T. Nguyen, High propylene/propane adsorption selectivity in a copper(catecholate)-decorated porous organic polymer, J. Mater. Chem. A. 2 (2014) 299–302. https://doi.org/10.1039/C3TA12999C.

S. Xu, W.C. Li, C. Wang, R. Liu, G.P. Hao, A.H. Lu, Beyond the selectivity-capacity trade-off: Ultrathin carbon nanoplates with easily accessible ultramicropores for high-efficiency propylene/propane separation, Nano Lett. 22 (2022) 6615–6621. https://doi.org/10.1021/acs.nanolett.2c01930.

X. Xu, X. Zhao, L. Sun, X. Liu, Adsorption separation of carbon dioxide, methane and nitrogen on monoethanol amine modified ß-zeolite, J. Nat. Gas Chem. 18 (2009) 167–172. https://doi.org/10.1016/S1003-9953(08)60098-5.

S.T. Yang, J.Y. Kim, J. Kim, W.S. Ahn, CO_2 capture over amine-functionalized MCM-22, MCM-36 and ITQ-2, Fuel 97 (2012) 435–442. https://doi.org/10.1016/j.fuel.2012.03.034.

G. Yu, L. Deng, A.A. Abdeltawab, S.S. Al-Deyab, X. Chen, J. Zhang, Functional solution composed of Cu(I) salt and ionic liquids to separate propylene from propane, Ind. Eng. Chem. Res. 53 (2014) 13430–13435. https://doi.org/10.1021/ie501522m.

I.W. Zapelini, D. Cardoso, Amine-grafted Na-LTA zeolite precursors as basic catalysts for Knoevenagel condensation, Microporous Mesoporous Mater. 324 (2021) 111270. https://doi.org/10.1016/j.micromeso.2021.111270.

H. Zeng, M. Xie, T. Wang, R.J. Wei, X.J. Xie, Y. Zhao, W. Lu, D. Li, Orthogonal-array dynamic molecular sieving of propylene/propane mixtures, Nature 595 (2021) 542–548. https://doi.org/10.1038/s41586-021-03627-8.

J. Zhang, L.D. Ellis, B. Wang, M.J. Dzara, C. Sievers, S. Pylypenko, E. Nikolla, J.W. Medlin, Control of interfacial acid-metal catalysis with organic monolayers, Nat. Catal. 1 (2018) 148–155. https://doi.org/10.1038/s41929-017-0019-8.

Z. Zhang, Q. Ding, X. Cui, X.M. Jiang, H. Xing, Fine-tuning and selective-binding within an anion-functionalized ultramicroporous metal-organic framework for efficient olefin/paraffin separation, ACS Appl. Mater. Interfaces. 12 (2020) 40229–40235. https://doi.org/10.1021/acsami.0c07800.

X. Zhou, J.L. Falconer, J.W. Medlin, Competitive adsorption between propylene and propane on zeolite 5A and the influence of organic phosphonic acid coatings, Sep. Purif. Technol. 346 (2024) 127435. https://doi.org/10.1016/j.seppur.2024.127435.

X. Zhou, J.L. Falconer, J.W. Medlin, Mechanism of selectivity control for zeolites modified with organic monolayers, Microporous Mesoporous Mater. 337 (2022) 111913. https://doi.org/10.1016/j.micromeso.2022.111913.

W. Zhu, F. Kapteijn, J.A. Moulijn, Shape selectivity in the adsorption of propane/propene on the all-silica DD3R, Chem. Commun. (1999) 2453–2454. https://doi.org/10.1039/a906465f.

Appendix

Appendix A: Supplement to Chapter 2

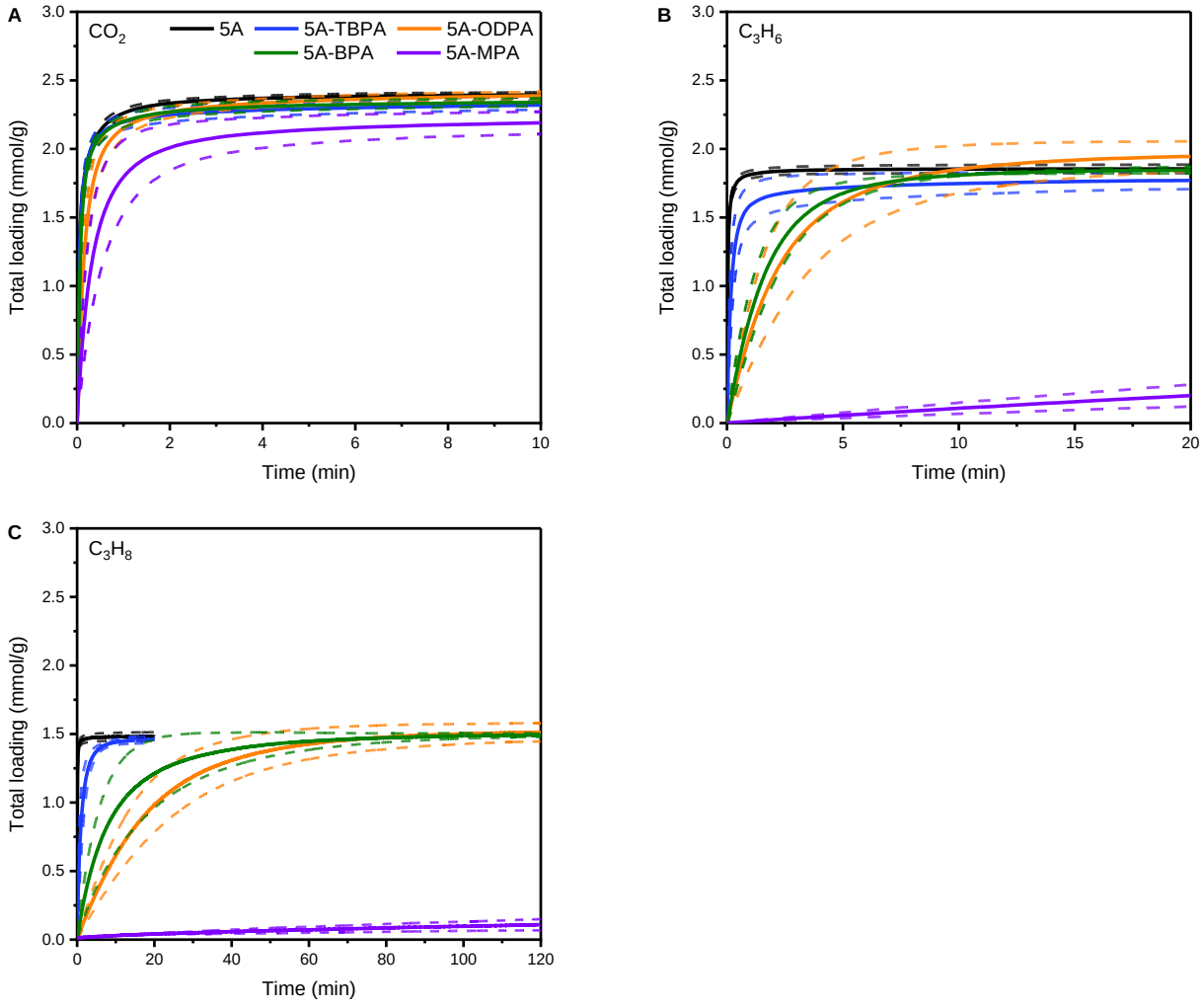

Figure A.1. (A) CO_2, (B) C_3H_6, and (C) C_3H_8 adsorption on uncoated, TBPA-, BPA-, ODPA-, and MPA-coated 5A at 25 °C. Uncertainty bounds are based on standard deviations of triplicate measurements for separately prepared samples, with the exception of C_3H_6 and C_3H_8 adsorption on 5A-MPA, where the dashed curves represent the span of duplicate measurements with separate samples.

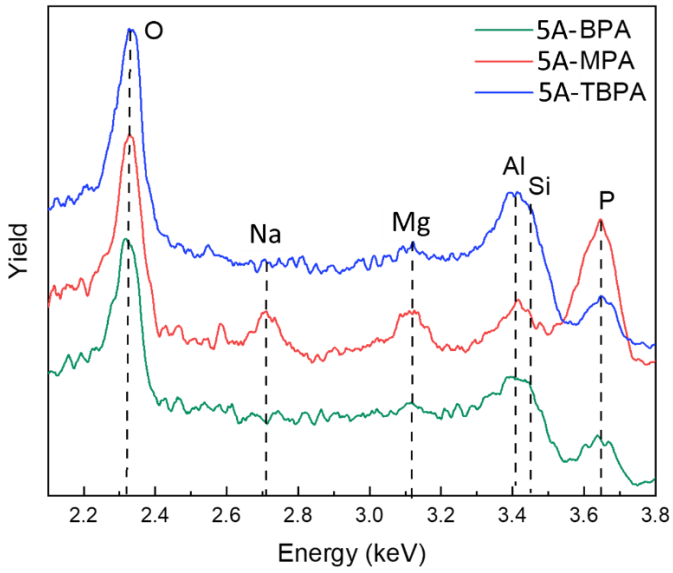

Figure A.2. Low energy ion scattering (LEIS) spectra of zeolite 5A coated with MPA, BPA and TBPA.

Table A.1. Elementary composition of the topmost surface layer from LEIS measurements for zeolite 5A coated with BPA, TBPA, and MPA.

Element	5A-BPA	5A-TBPA	5A-MPA
P	14.1%	7.9%	34.2%
Al+Si	39.3%	43.6%	11.0%
O	46.6%	48.5%	39.8%
Mg	0.0%	0.0%	6.4%
Na	0.0%	0.0%	8.5%
P:(Al+Si)	0.36	0.18	3.12

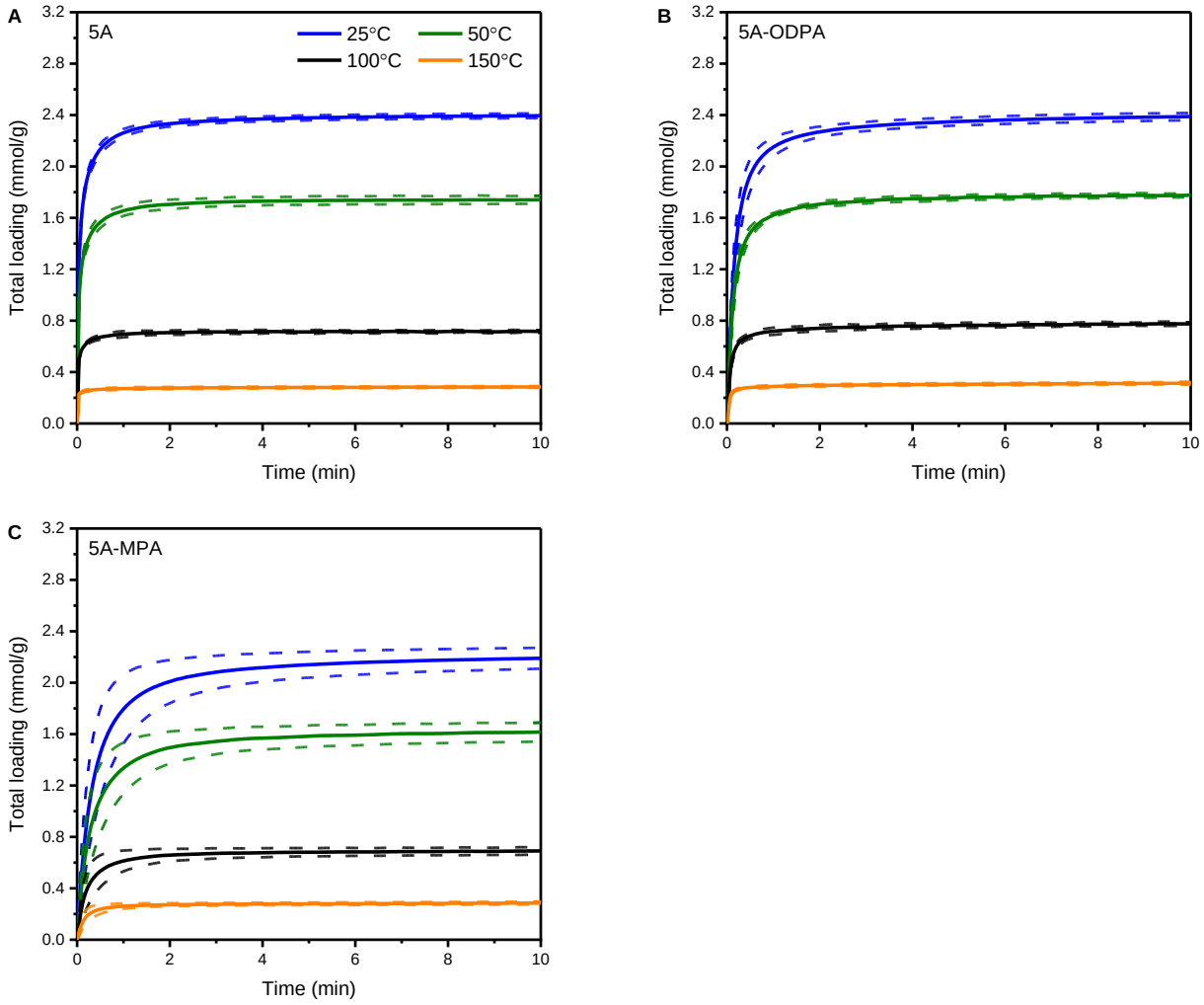

Figure A.3. Temperature dependence (25–150 °C) of CO_2 adsorption on (A) uncoated, (B) ODPA-, and (C) MPA-coated 5A. The dashed curves represent the uncertainty bounds based on standard deviations of triplicate measurements for separately prepared samples.

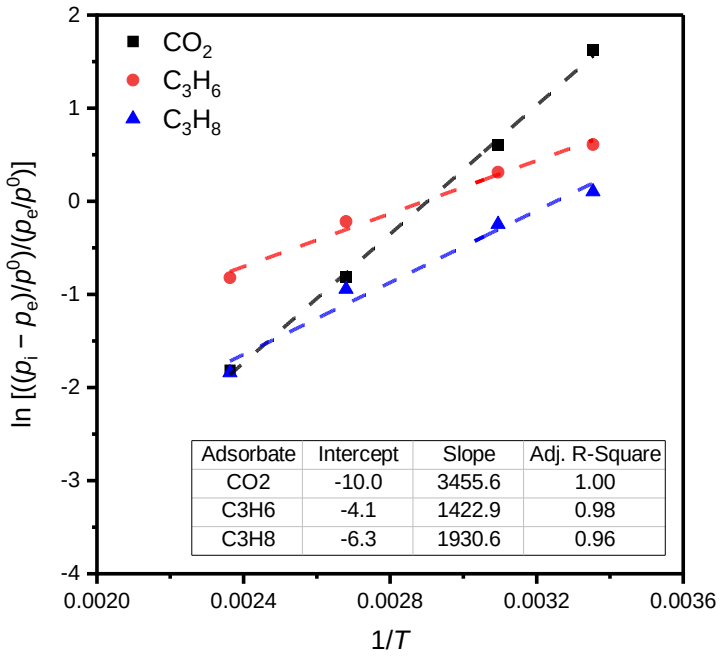

Figure A.4. Plots of ln $[((p_i - p_e)/p^0)/(p_e/p^0)]$ vs. $1/T$ for CO_2, C_3H_6, and C_3H_8 adsorption on uncoated 5A.

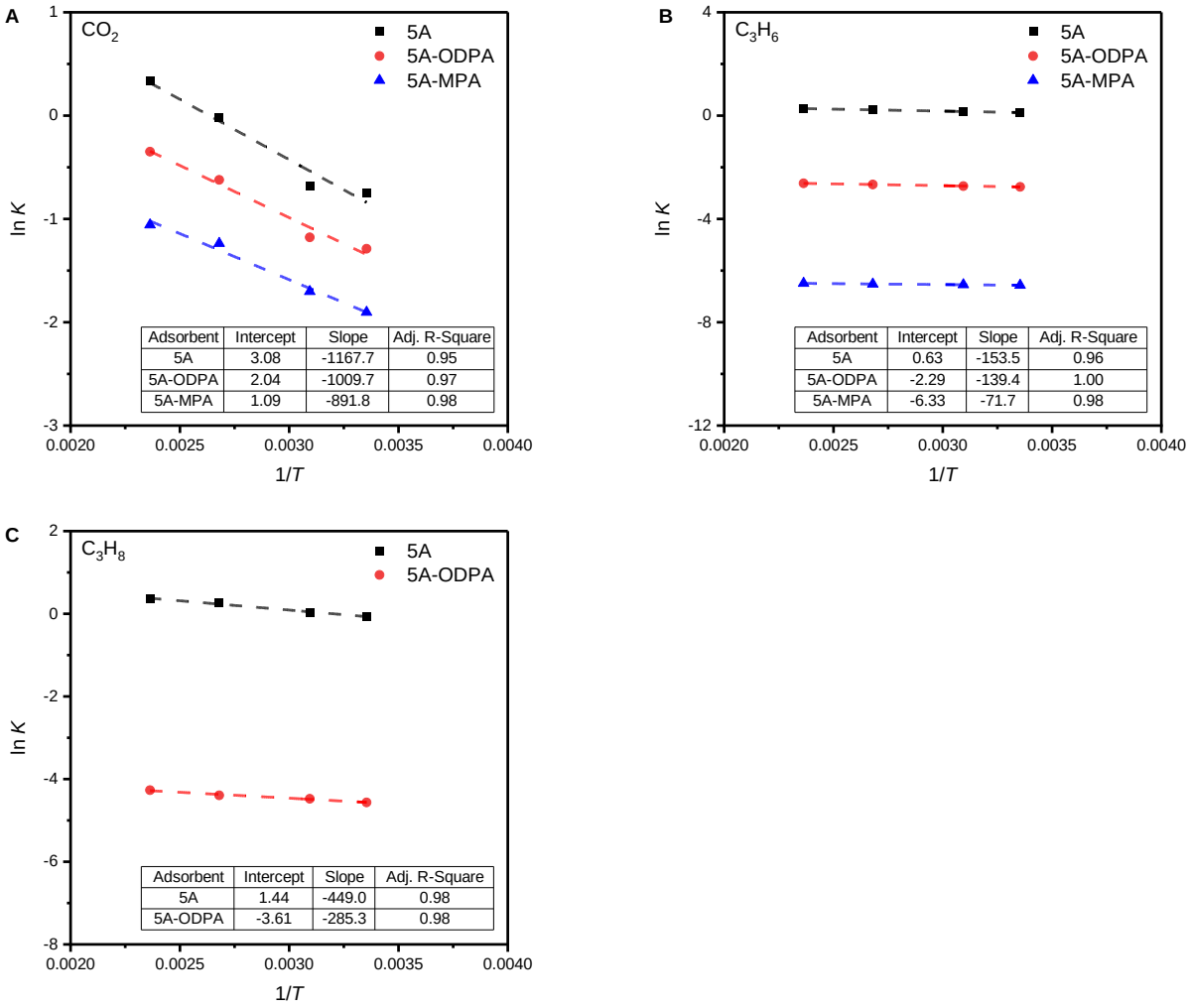

Figure A.5. Plots of ln K vs. $1/T$ for (A) CO_2, (B) C_3H_6, and (C) C_3H_8 adsorption on uncoated, ODPA-, and MPA-coated 5A. The diffusion rate constant K is D/R^2 for internal diffusion model or k/R for surface limitation model.

Table A.2. Pre-exponential factors A of diffusion rate constants (determined by Arrhenius analysis of fitted rate parameters) of C_3H_6, C_3H_8, and CO_2 adsorption on uncoated, ODPA-, and MPA-coated 5A.

Adsorbate	A (min^{-1})		
	5A	5A-ODPA	5A-MPA
C_3H_6	2.2 ± 0.2	0.16 ± 0.04	0.0024 ± 0.0007
C_3H_8	3.9 ± 0.3	0.04 ± 0.01	/
CO_2	24.8 ± 10.2	12.0 ± 6.6	3.0 ± 1.9

* The surface limitation model was employed for C_3H_6 and C_3H_8 adsorption on PA-coated 5A, and the internal diffusion model for the others.

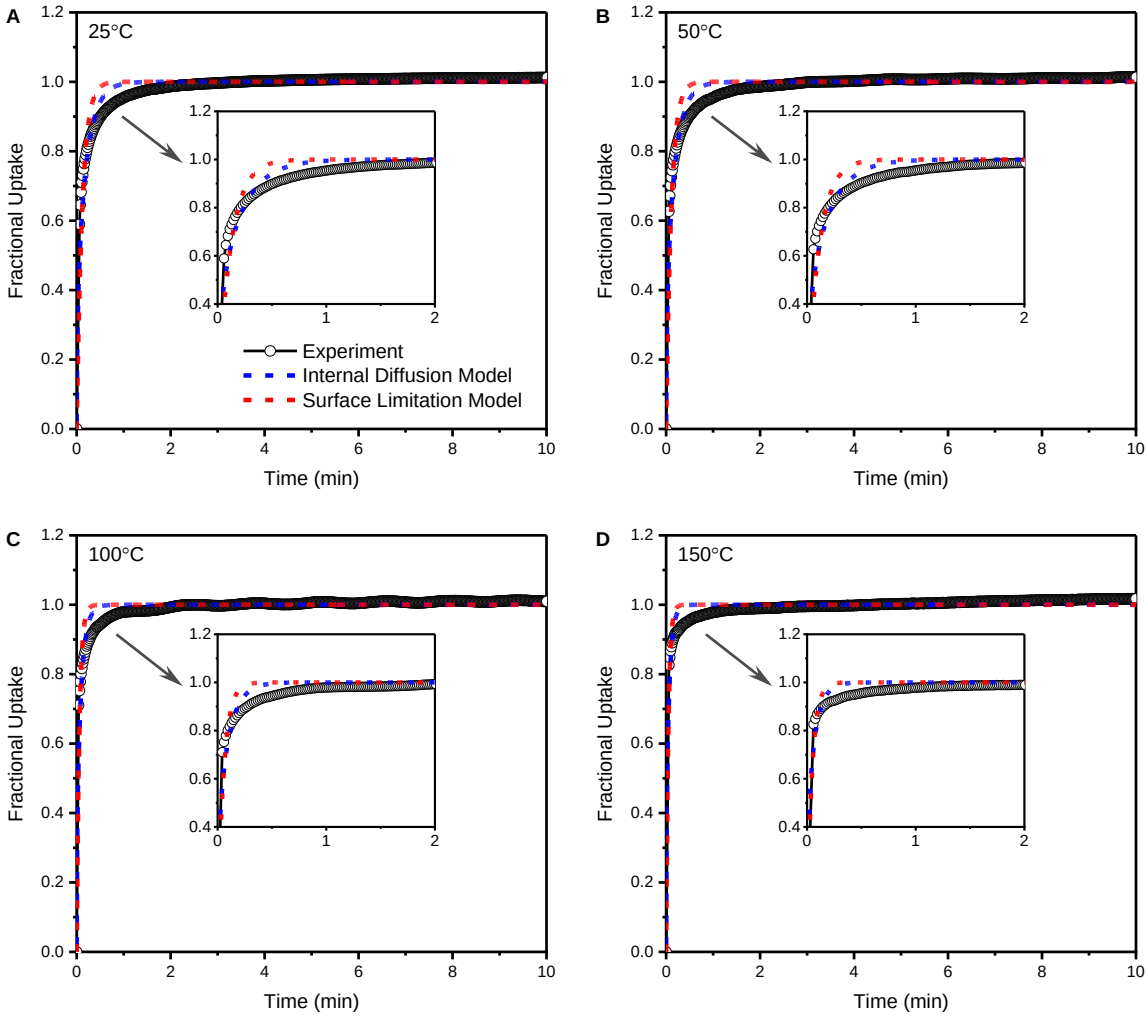

Figure A.6. Modeling of CO_2 uptake curves for uncoated zeolite 5A at (A) 25, (B) 50, (C) 100, and (D) 150 °C.

Table A.3. Diffusion rate constants D/R^2 in internal diffusion model and k/R in surface limitation model for CO_2 adsorption on uncoated 5A.

5A (CO_2)	Internal Diffusion Model		Surface Limitation Model	
T (°C)	D/R^2 (min^{-1})	Adj. R^2	k/R (min^{-1})	Adj. R^2
25	0.47	0.91	2.81	0.82
50	0.51	0.90	3.03	0.80
100	0.98	0.89	5.85	0.83
150	1.40	0.88	7.20	0.86

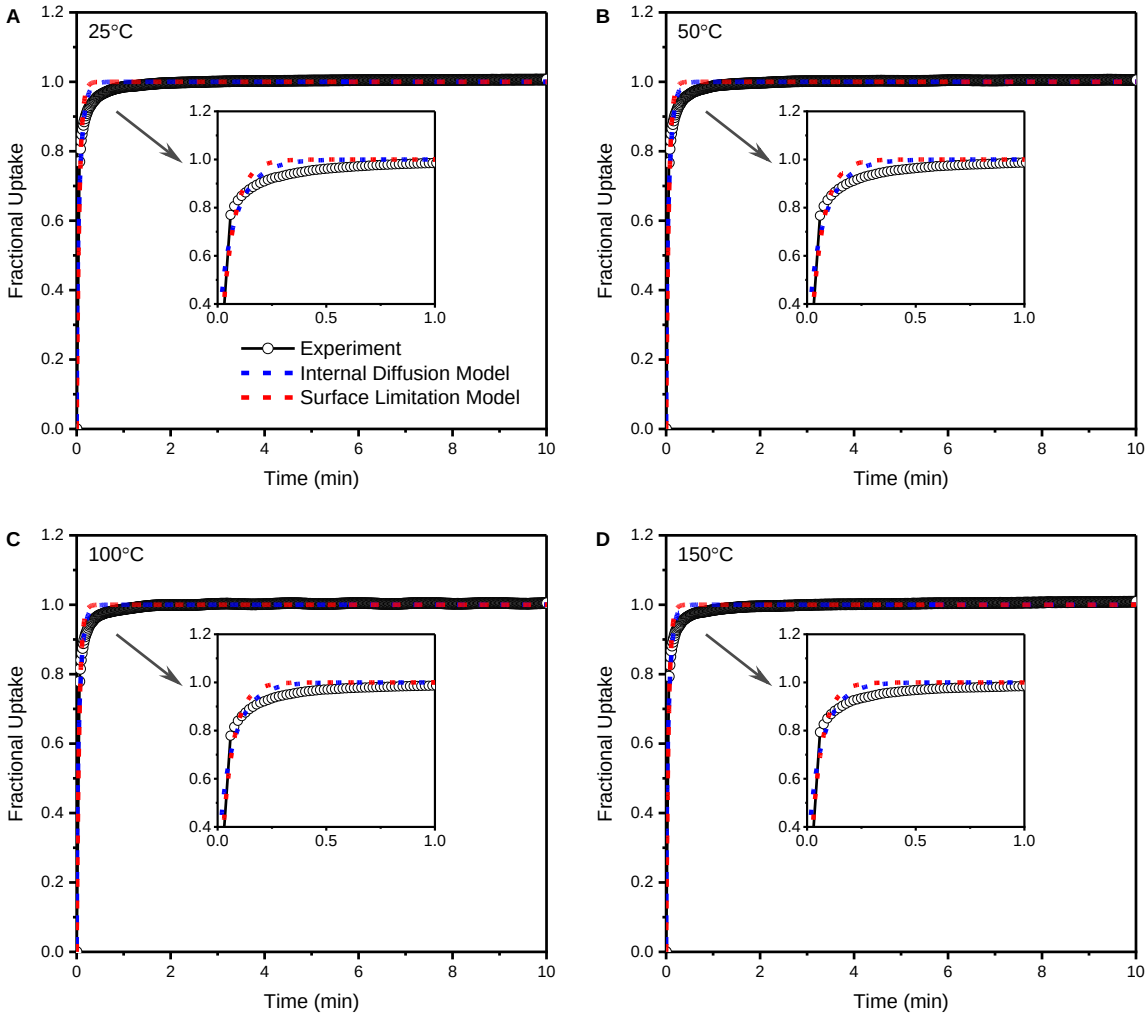

Figure A.7. Modeling of C_3H_6 uptake curves for uncoated zeolite 5A at (A) 25, (B) 50, (C) 100, and (D) 150 °C.

Table A.4. Diffusion rate constants D/R^2 in internal diffusion model and k/R in surface limitation model for C_3H_6 adsorption on uncoated 5A.

5A (C_3H_6)	Internal Diffusion Model		Surface Limitation Model	
T (°C)	D/R^2 (min^{-1})	Adj. R^2	k/R (min^{-1})	Adj. R^2
25	1.14	0.94	5.93	0.91
50	1.15	0.95	5.95	0.92
100	1.25	0.96	6.31	0.93
150	1.32	0.94	6.62	0.92

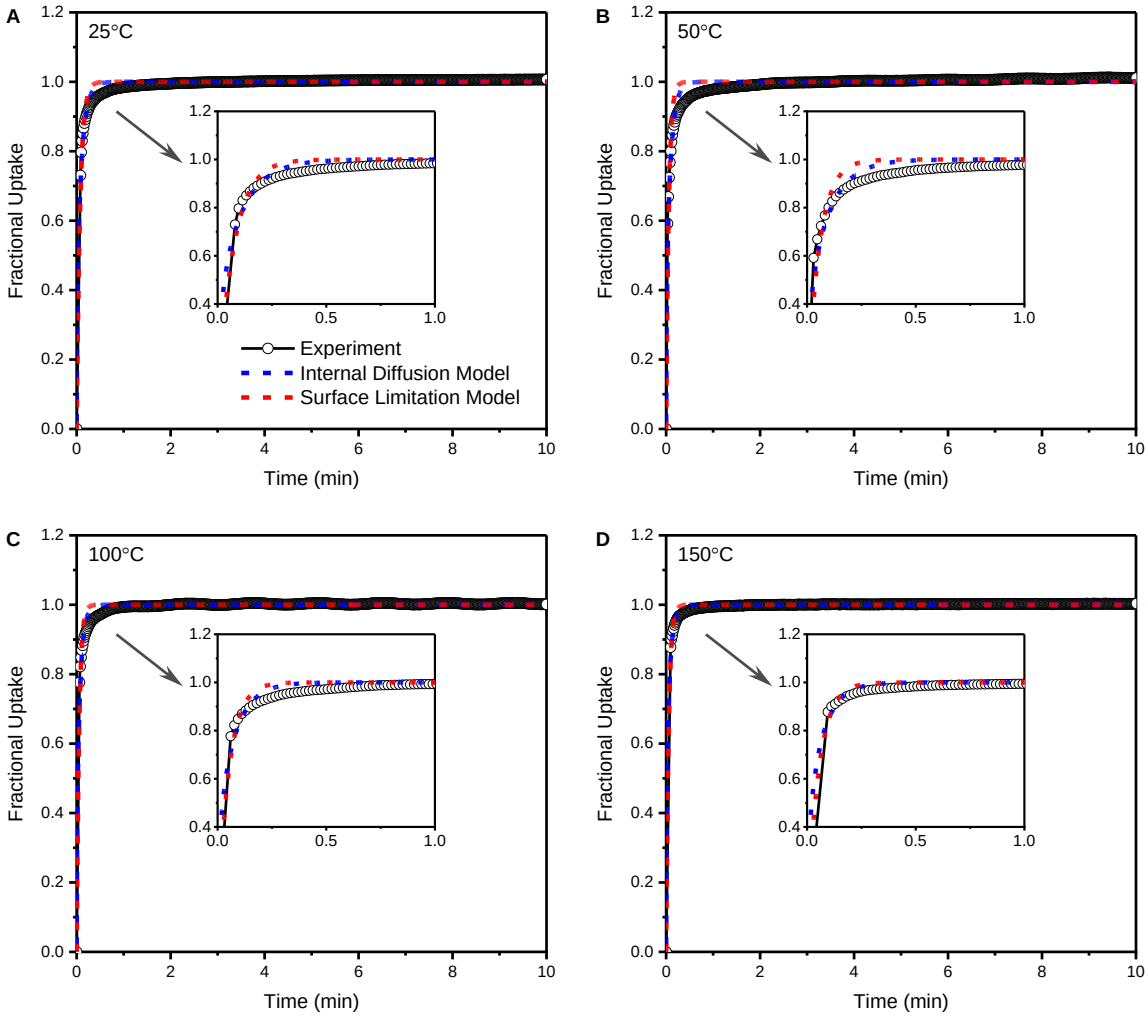

Figure A.8. Modeling of C_3H_8 uptake curves for uncoated zeolite 5A at (A) 25, (B) 50, (C) 100, and (D) 150 °C.

Table A.5. Diffusion rate constants D/R^2 in internal diffusion model and k/R in surface limitation model for C_3H_8 adsorption on uncoated 5A.

5A (C_3H_8)	Internal Diffusion Model		Surface Limitation Model	
T (°C)	D/R^2 (min^{-1})	Adj. R^2	k/R (min^{-1})	Adj. R^2
25	0.94	0.96	4.59	0.94
50	1.03	0.93	6.01	0.88
100	1.30	0.96	6.47	0.94
150	1.43	0.99	6.26	0.98

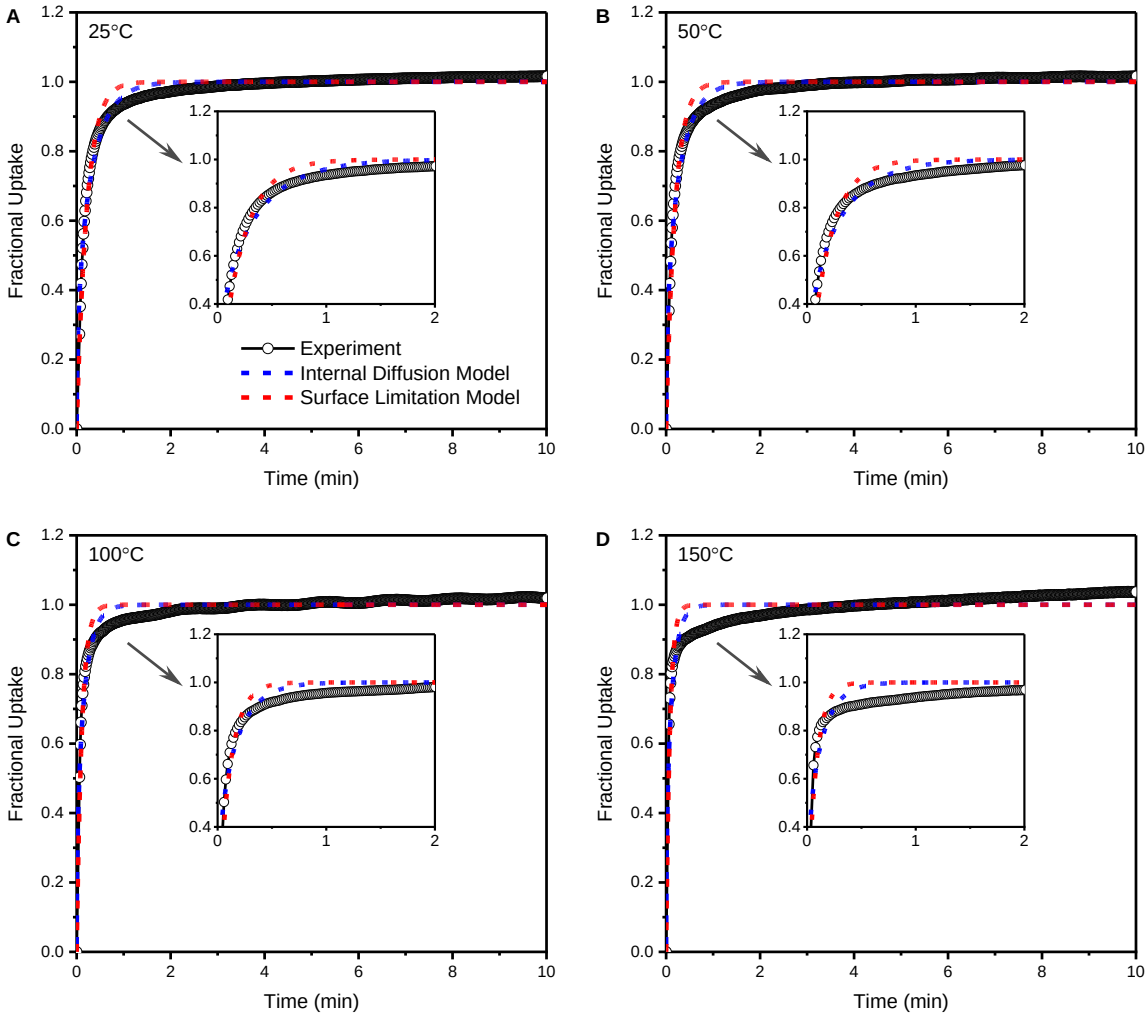

Figure A.9. Modeling of CO_2 uptake curves for ODPA-coated 5A at (A) 25, (B) 50, (C) 100, and (D) 150 °C.

Table A.6. Diffusion rate constants D/R^2 in internal diffusion model and k/R in surface limitation model for CO_2 adsorption on ODPA-coated 5A.

5A-ODPA (CO_2)	Internal Diffusion Model		Surface Limitation Model	
T (°C)	D/R^2 (min^{-1})	Adj. R^2	k/R (min^{-1})	Adj. R^2
25	0.28	0.96	1.54	0.93
50	0.31	0.95	1.76	0.90
100	0.54	0.90	3.03	0.85
150	0.71	0.73	4.21	0.68

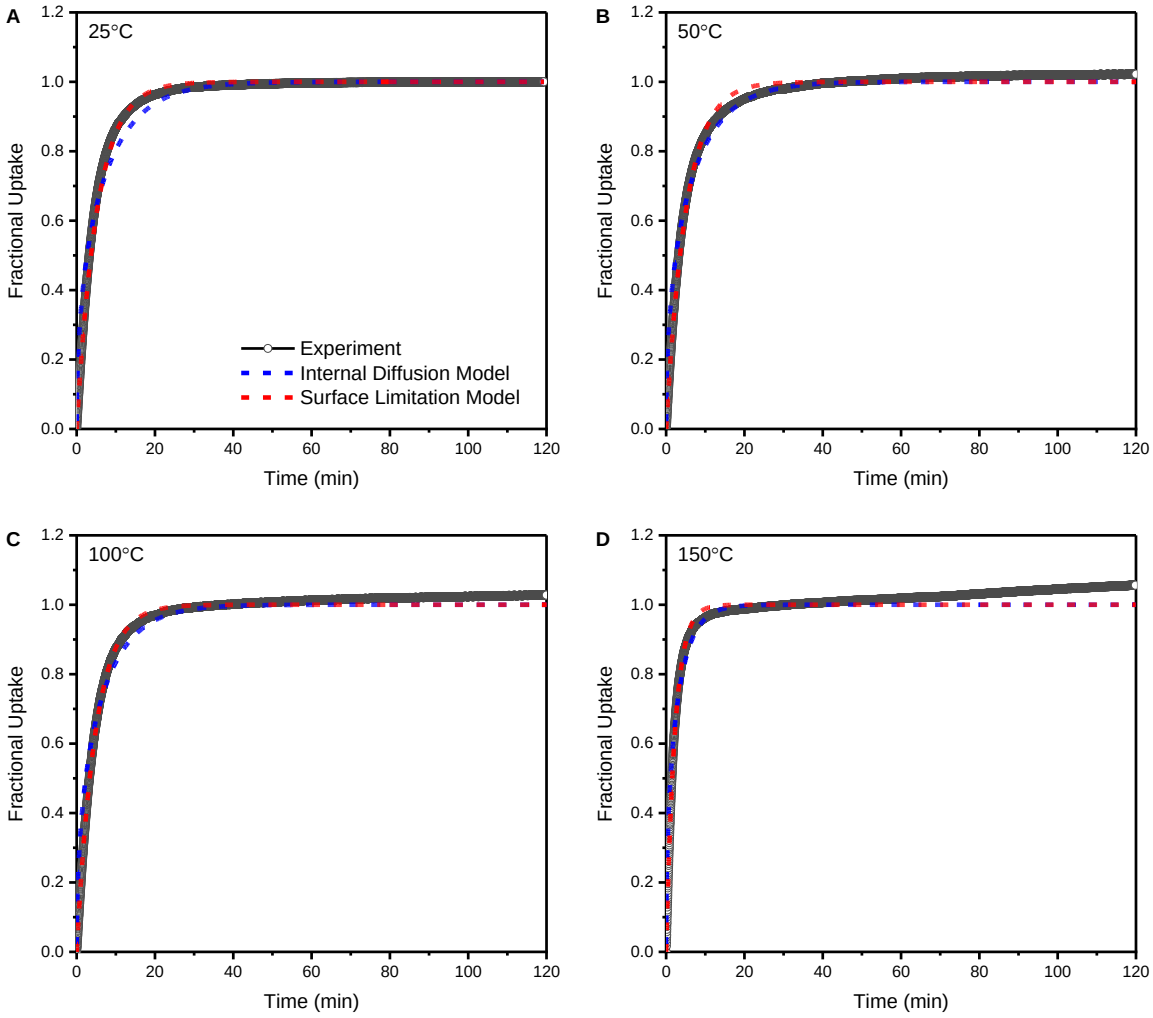

Figure A.10. Modeling of C_3H_6 uptake curves for ODPA-coated 5A at (A) 25, (B) 50, (C) 100, and (D) 150 °C.

Table A.7. Diffusion rate constants D/R^2 in internal diffusion model and k/R in surface limitation model for C_3H_6 adsorption on ODPA-coated 5A.

5A-ODPA (C_3H_6)	Internal Diffusion Model		Surface Limitation Model	
T (°C)	D/R^2 (min^{-1})	Adj. R^2	k/R (min^{-1})	Adj. R^2
25	0.012	0.95	0.063	0.96
50	0.012	0.97	0.065	0.98
100	0.013	0.95	0.069	0.99
150	0.015	0.65	0.073	0.69

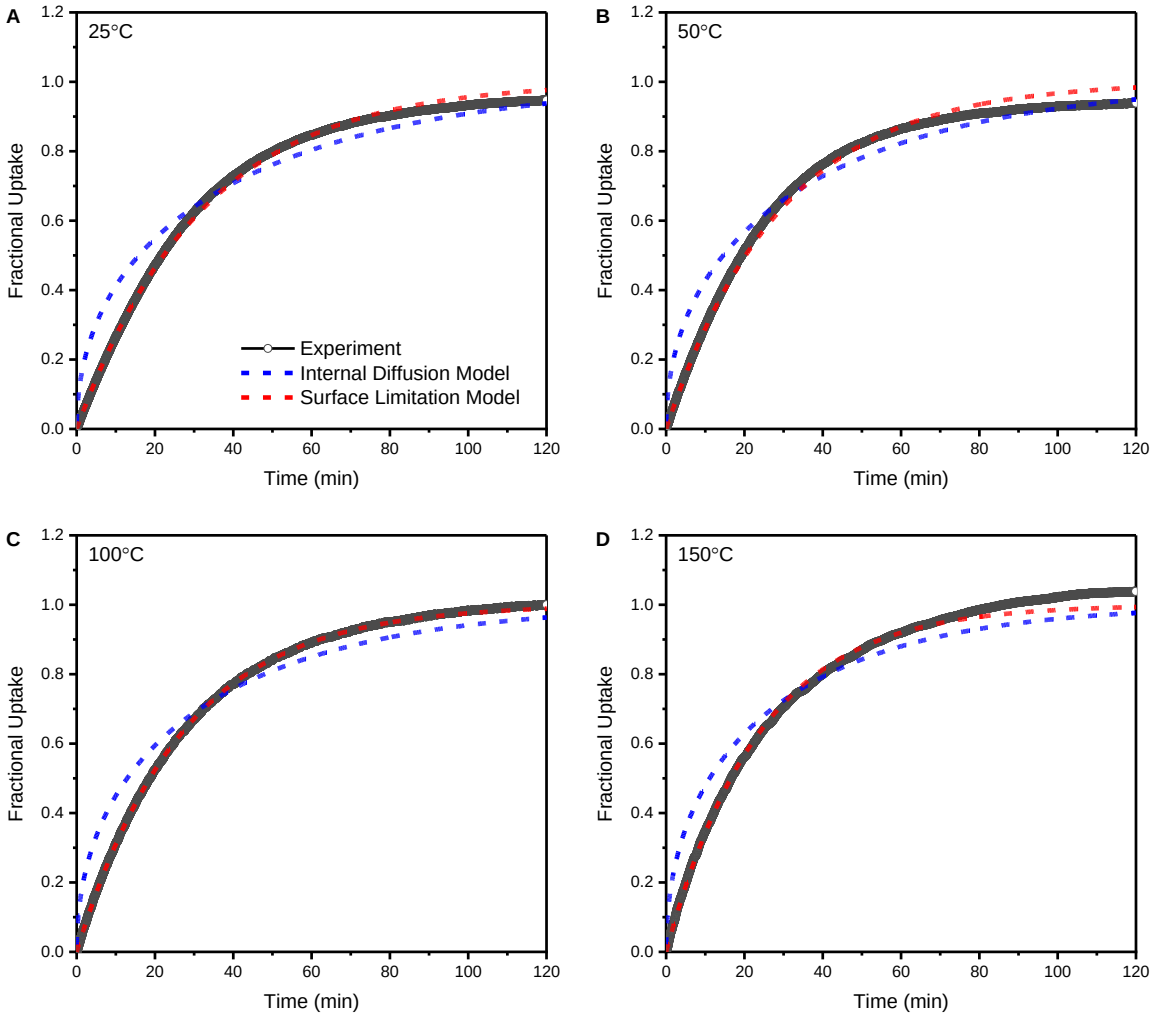

Figure A.11. Modeling of C_3H_8 uptake curves for ODPA-coated 5A at (A) 25, (B) 50, (C) 100, and (D) 150 °C.

Table A.8. Diffusion rate constants D/R^2 in internal diffusion model and k/R in surface limitation model for C_3H_8 adsorption on ODPA-coated 5A.

5A-ODPA (C_3H_8)	Internal Diffusion Model		Surface Limitation Model	
T (°C)	D/R^2 (min^{-1})	Adj. R^2	k/R (min^{-1})	Adj. R^2
25	0.0019	0.94	0.010	1.00
50	0.0021	0.95	0.011	0.99
100	0.0024	0.94	0.012	1.00
150	0.0028	0.93	0.014	0.99

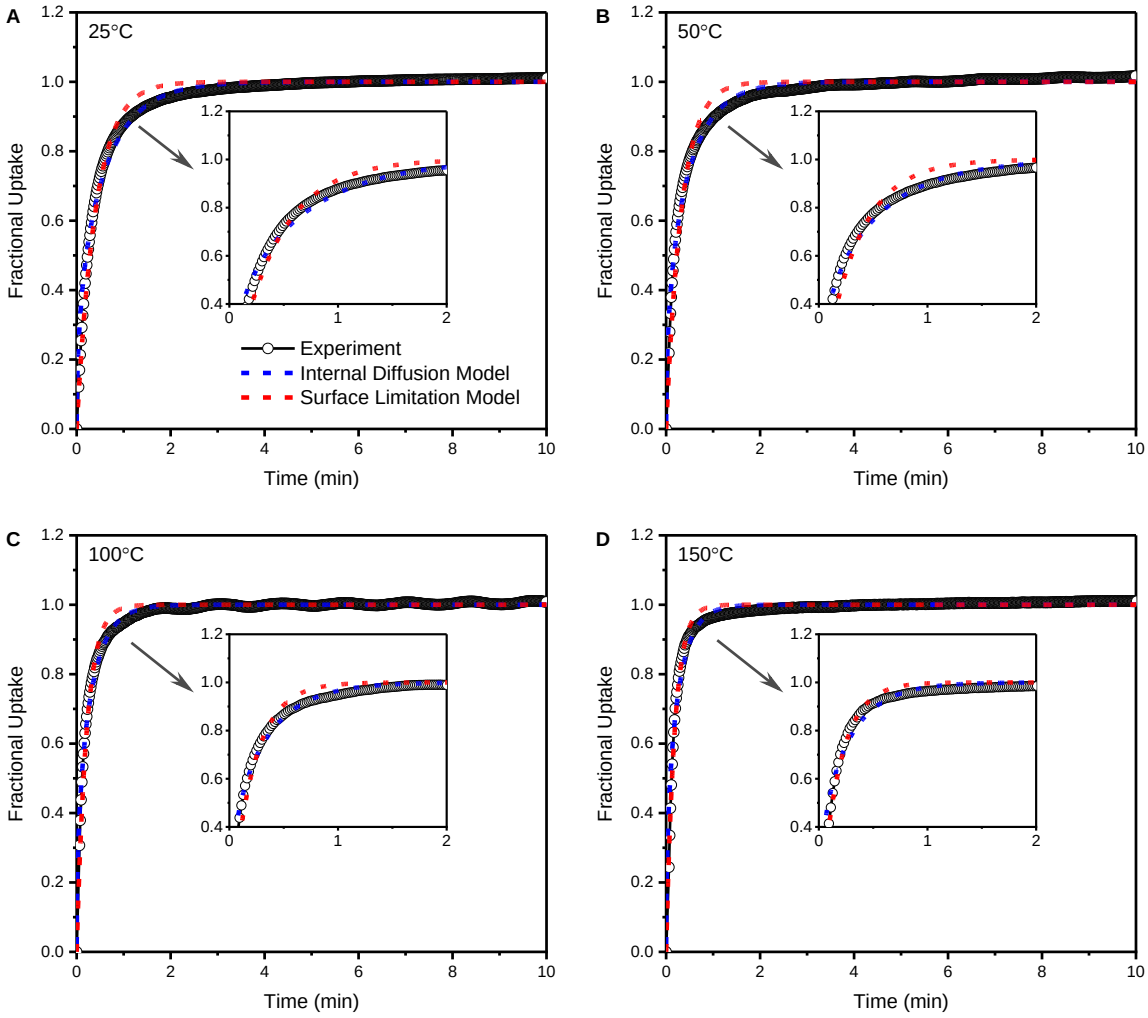

Figure A.12. Modeling of CO_2 uptake curves for MPA-coated 5A at (A) 25, (B) 50, (C) 100, and (D) 150 °C.

Table A.9. Diffusion rate constants D/R^2 in internal diffusion model and k/R in surface limitation model for CO_2 adsorption on MPA-coated 5A.

5A-MPA (CO_2)	Internal Diffusion Model		Surface Limitation Model	
T (°C)	D/R^2 (min^{-1})	Adj. R^2	k/R (min^{-1})	Adj. R^2
25	0.15	0.98	0.82	0.97
50	0.18	0.98	1.02	0.94
100	0.29	0.99	1.58	0.96
150	0.35	0.96	1.85	0.97

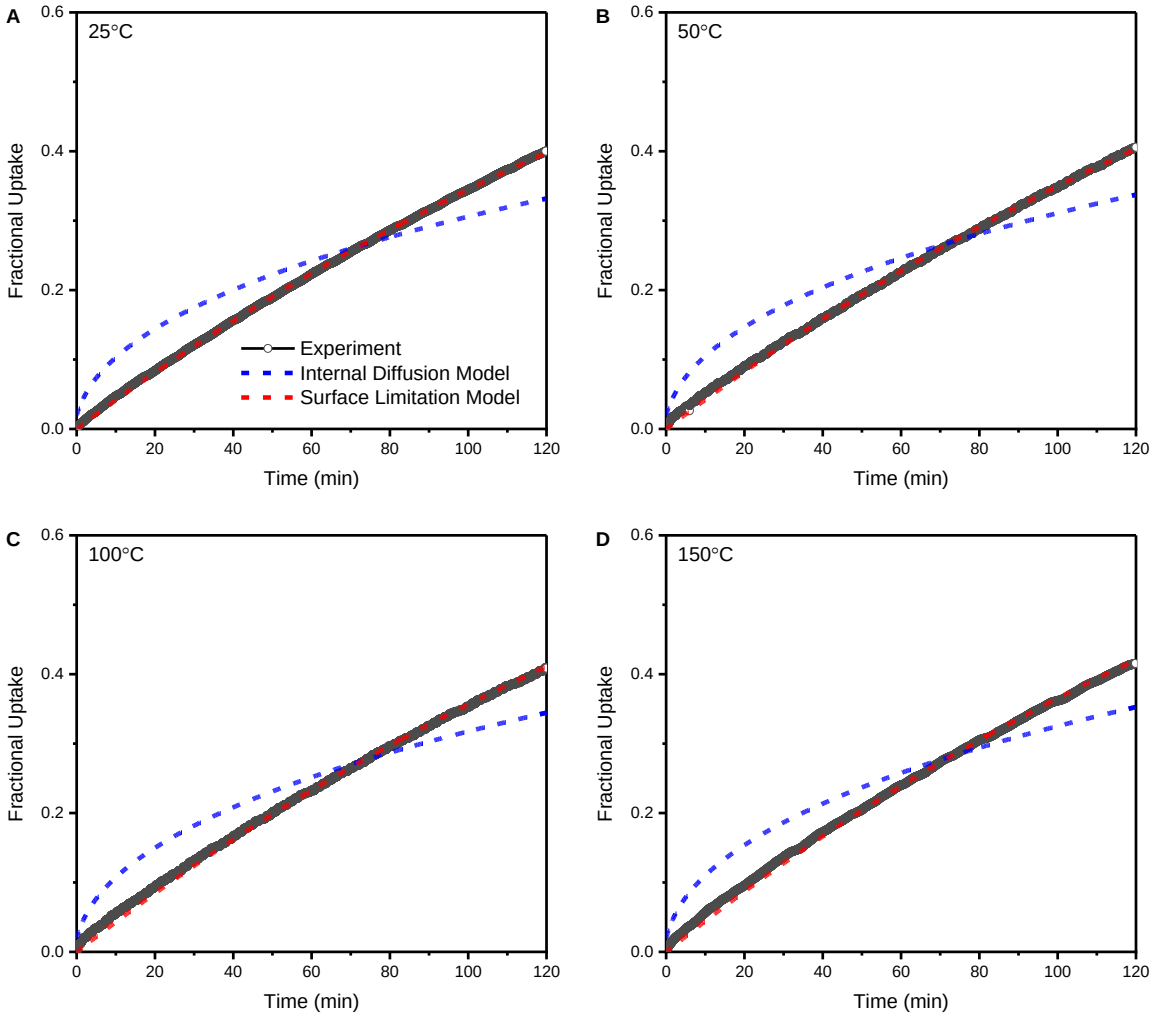

Figure A.13. Modeling of C_3H_6 uptake curves for MPA-coated 5A at (A) 25, (B) 50, (C) 100, and (D) 150 °C.

Table A.10. Diffusion rate constants D/R^2 in internal diffusion model and k/R in surface limitation model for C_3H_6 adsorption on MPA-coated 5A.

5A-MPA (C_3H_6)	Internal Diffusion Model		Surface Limitation Model	
T (°C)	D/R^2 (min^{-1})	Adj. R^2	k/R (min^{-1})	Adj. R^2
25	0.000098	0.86	0.00141	1.00
50	0.000102	0.87	0.00143	1.00
100	0.000107	0.88	0.00147	1.00
150	0.000112	0.88	0.00152	1.00

Table A.11. Diffusion rate constants D/R^2 in internal diffusion model, k/R in surface limitation model, and apparent activation energies E_a from the modelling with adsorption time of 0.2, 0.5, 1, and 10 min for CO_2 adsorption on uncoated 5A.

5A (CO_2)		Internal Diffusion Model			Surface Limitation Model		
t (min)	T (°C)	D/R^2 (min^{-1})	Adj. R^2	E_a (kJ/mol)	k/R (min^{-1})	Adj. R^2	E_a (kJ/mol)
0.2	25	0.64	0.98	7.8	3.51	0.90	6.8
	50	0.70	0.97		3.75	0.88	
	100	1.18	0.95		6.26	0.87	
	150	1.54	0.97		7.36	0.95	
0.5	25	0.53	0.92	8.8	2.89	0.73	8.4
	50	0.56	0.90		3.11	0.71	
	100	0.99	0.88		5.85	0.77	
	150	1.40	0.92		7.17	0.89	
1	25	0.48	0.88	9.6	2.81	0.70	8.7
	50	0.51	0.86		3.04	0.68	
	100	0.98	0.87		5.85	0.78	
	150	1.40	0.90		7.17	0.87	
10	25	0.47	0.91	9.7	2.81	0.82	8.7
	50	0.51	0.90		3.03	0.80	
	100	0.98	0.89		5.85	0.83	
	150	1.40	0.88		7.17	0.86	

Appendix B: Supplement to Chapter 3

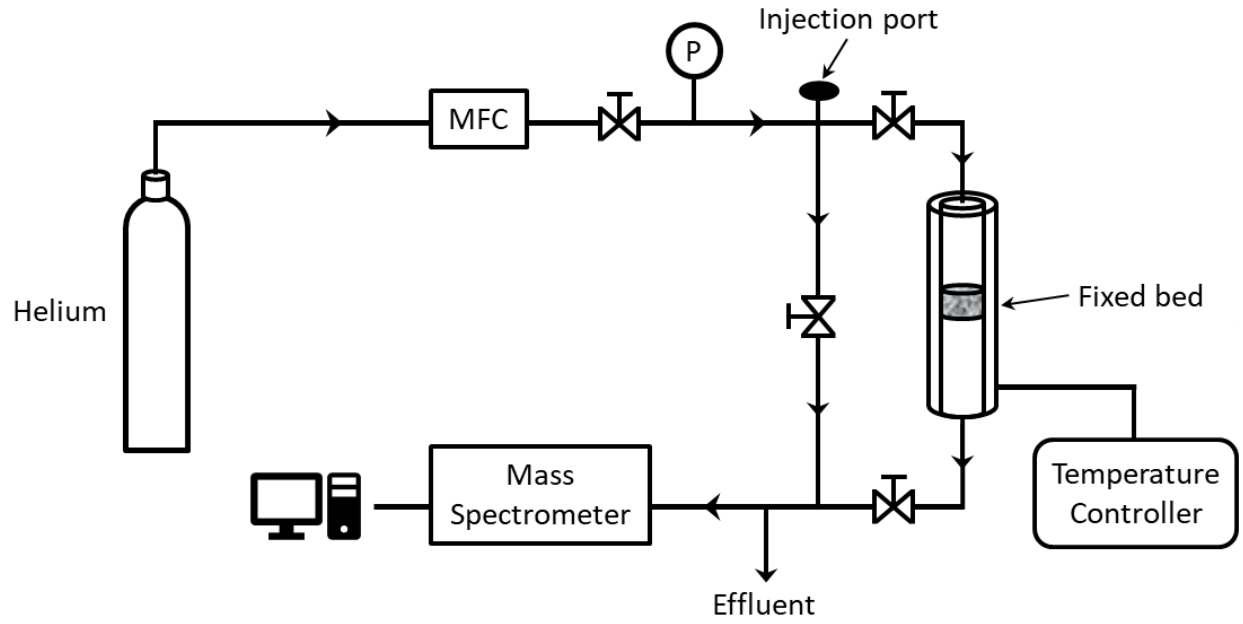

Figure B.1. Schematic illustration of the apparatus for adsorption and desorption measurements.

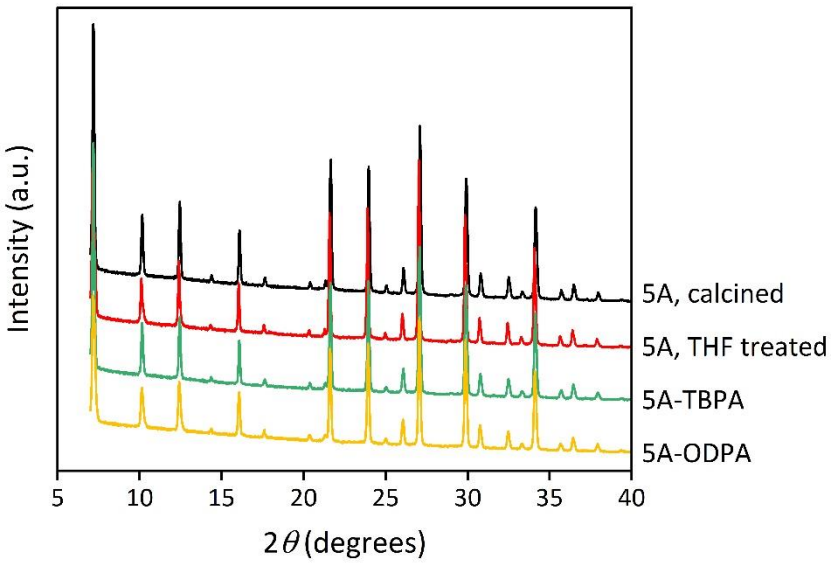

Figure B.2. XRD patterns of calcined zeolite 5A (heated in air at 673 K for 4 h), THF treated 5A (put through deposition process in THF solvent without a PA modifier), TBPA- and ODPA-coated 5A.

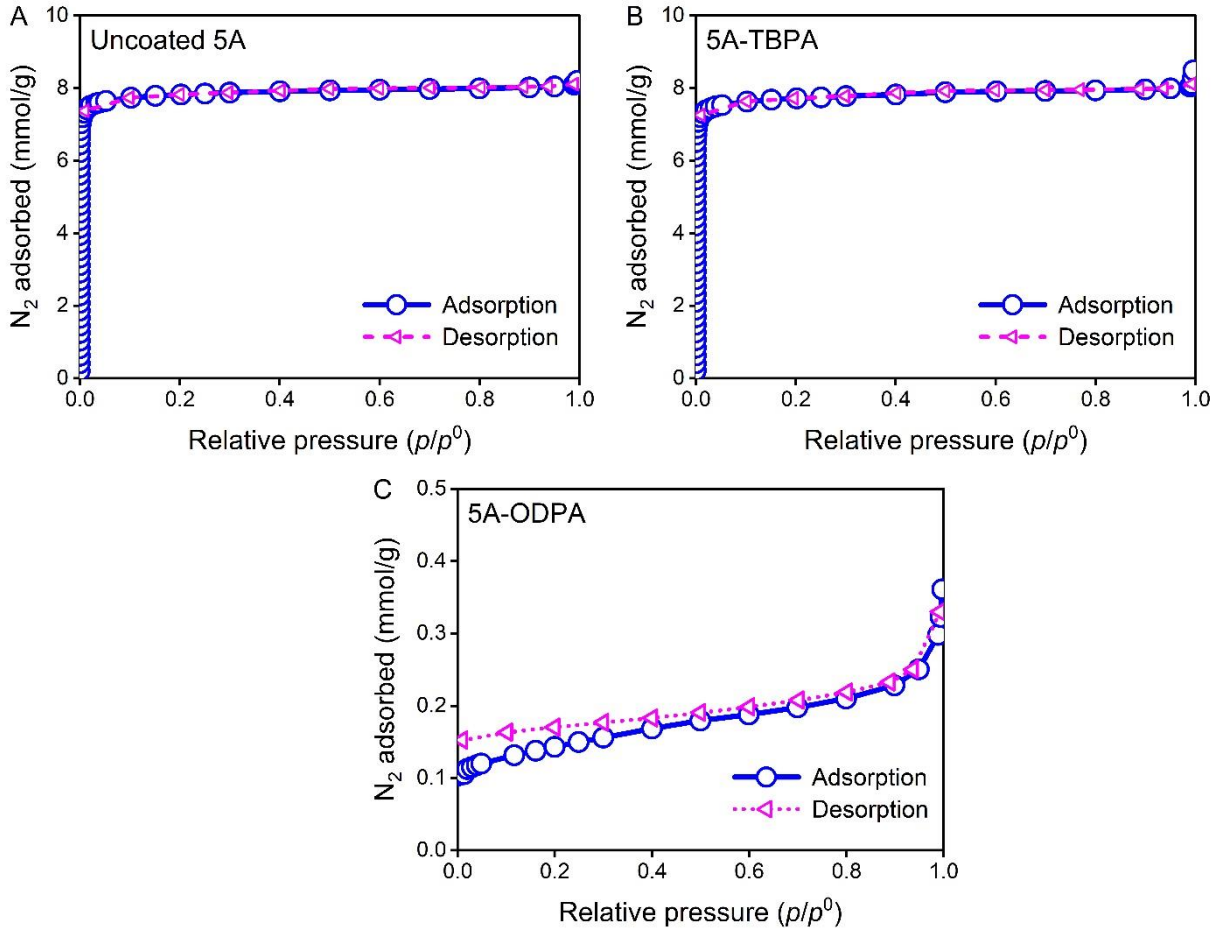

Figure B.3. Nitrogen adsorption isotherms at 77 K on (A) uncoated, (B) TBPA-, and (C) ODPA-coated 5A.

Table B.1. Surface area of uncoated and TBPA-coated zeolite 5A based on nitrogen adsorption isotherm at 77 K.

Material	Total surface area (m^2/g)[a]	External surface area (m^2/g)[b]	Micropore area (m^2/g)[c]
Uncoated 5A	715 ± 11	33 ± 2	681 ± 12
5A-TBPA	700 ± 3	33 ± 2	666 ± 1

a. The total surface area was determined with the Brunauer-Emmett-Teller multi-point method using relative pressure p/p^0 in the range of 10^{-7}–0.05.
b. The external surface area (pore size >2.5 nm) was determined with the t-plot method using p/p^0 in the range of 0.20–0.40.
c. The micropore area was calculated by the subtraction of external surface area from the total surface area.

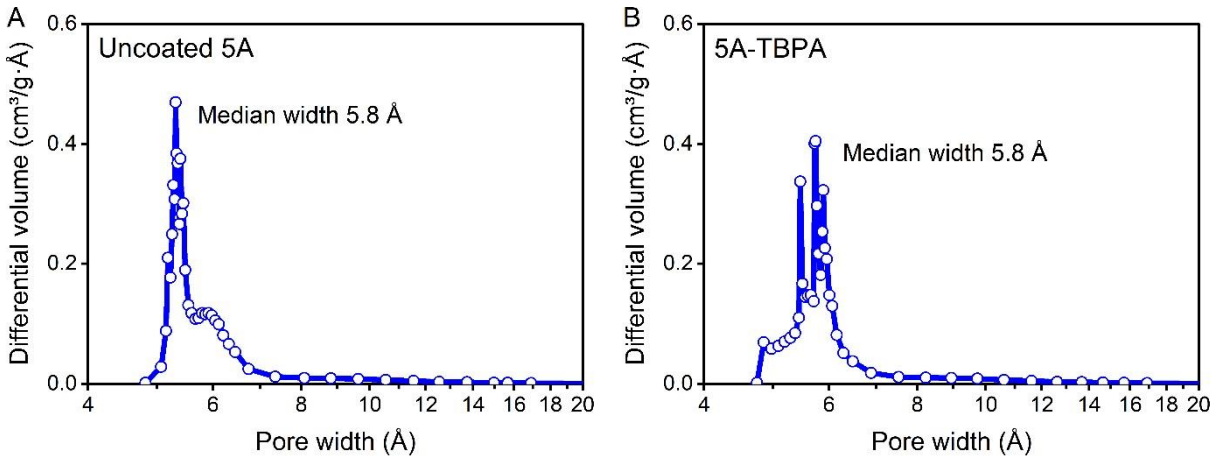

Figure B.4. Micropore size distribution of (A) uncoated and (B) TBPA-coated zeolite 5A determined with the Horvath-Kawazoe (HK) method.

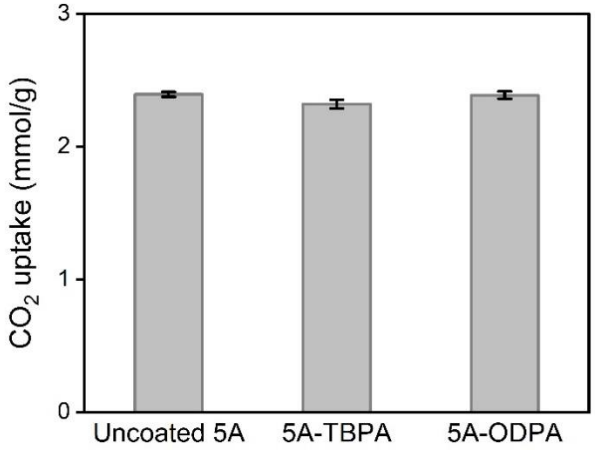

Figure B.5. Equilibrium uptakes of CO_2 on uncoated, TBPA-, and ODPA-coated zeolite 5A at 298 K under 3.5 kPa.

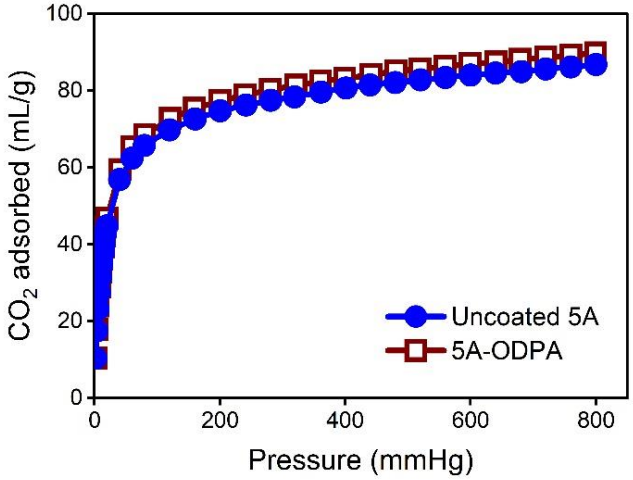

Figure B.6. CO_2 adsorption isotherms on uncoated and ODPA-coated zeolite 5A at 300 K.

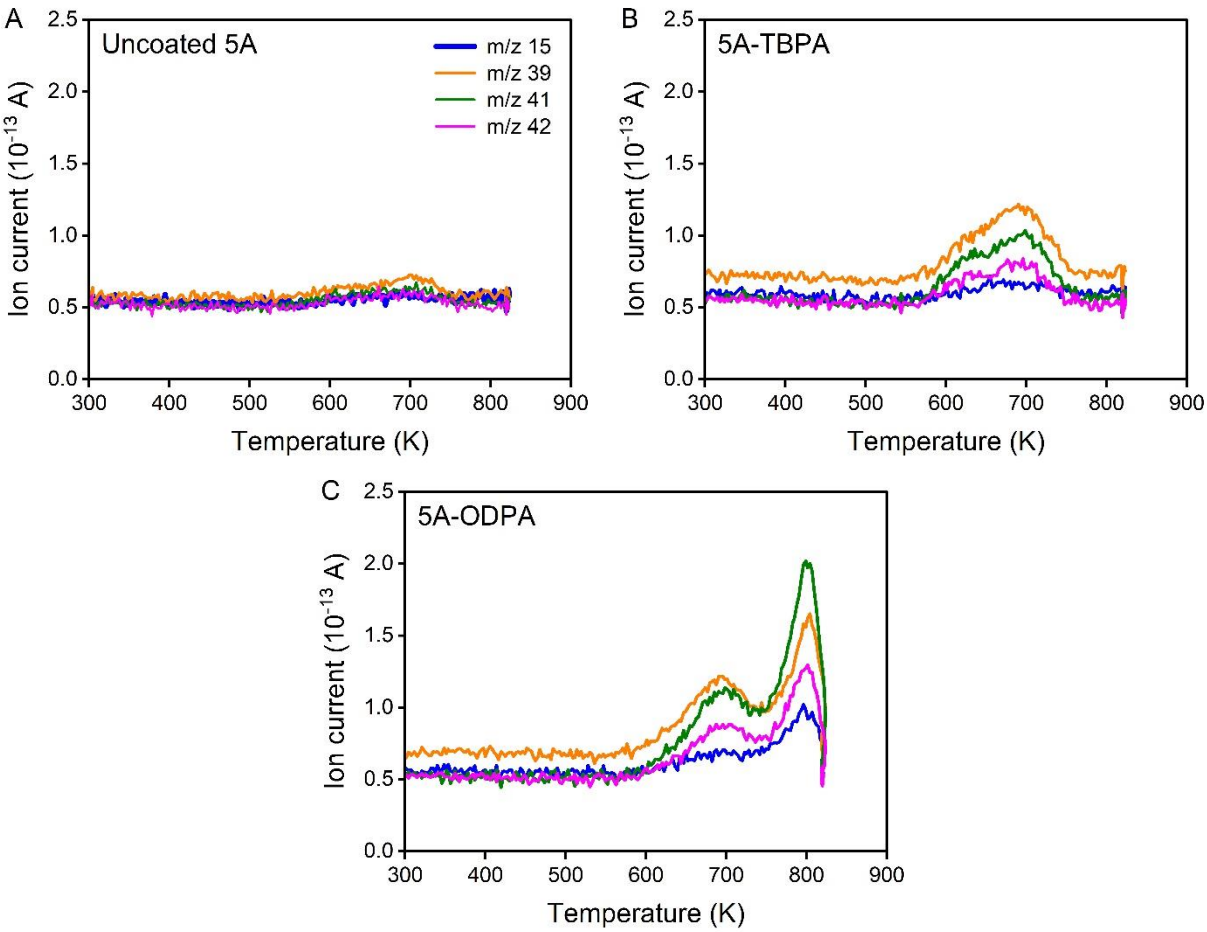

Figure B.7. TPD profiles of (A) uncoated, (B) TBPA-coated, and (C) ODPA-coated zeolite 5A. The samples were pretreated in 20 SCCM helium for 2 h at 523 K prior to 8 K/min ramp from 298 K to 823 K with 20 SCCM helium carrier gas.

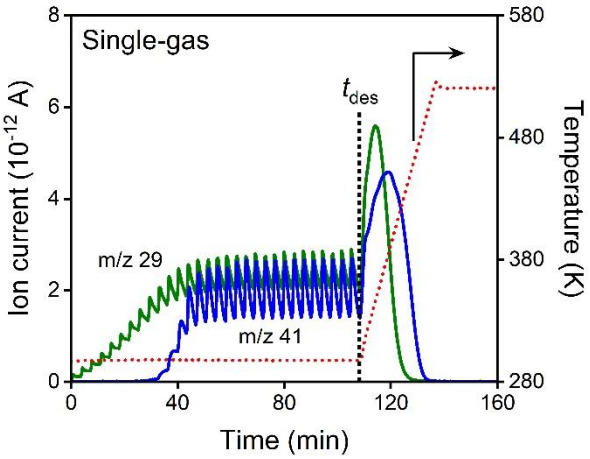

Figure B.8. Mass spectrometer signals from C_3H_6 (m/z 41) and C_3H_8 (m/z 29) in single-gas adsorption (start at time 0) on uncoated zeolite 5A with 30 doses (1.0 mL per dose) for each gas at 298 K, followed by TPD (start at time t_{des}), under 20 SCCM of helium.

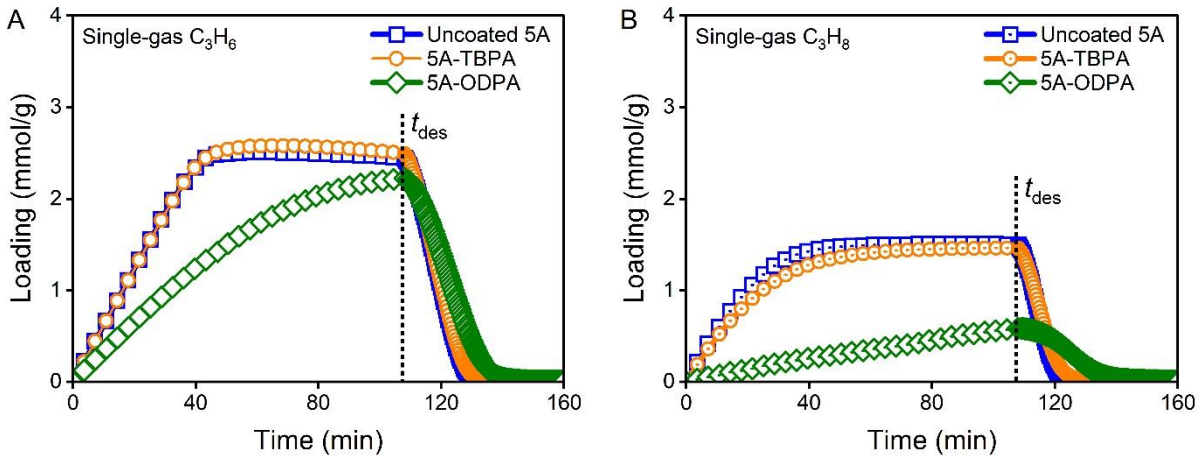

Figure B.9. Loadings of (A) C_3H_6 and (B) C_3H_8 in single-gas adsorption on uncoated, TBPA-, and ODPA-coated zeolite 5A with 30 doses (1.0 mL per dose) for each gas at 298 K, followed by TPD (start at time t_{des}), under 20 SCCM of helium.

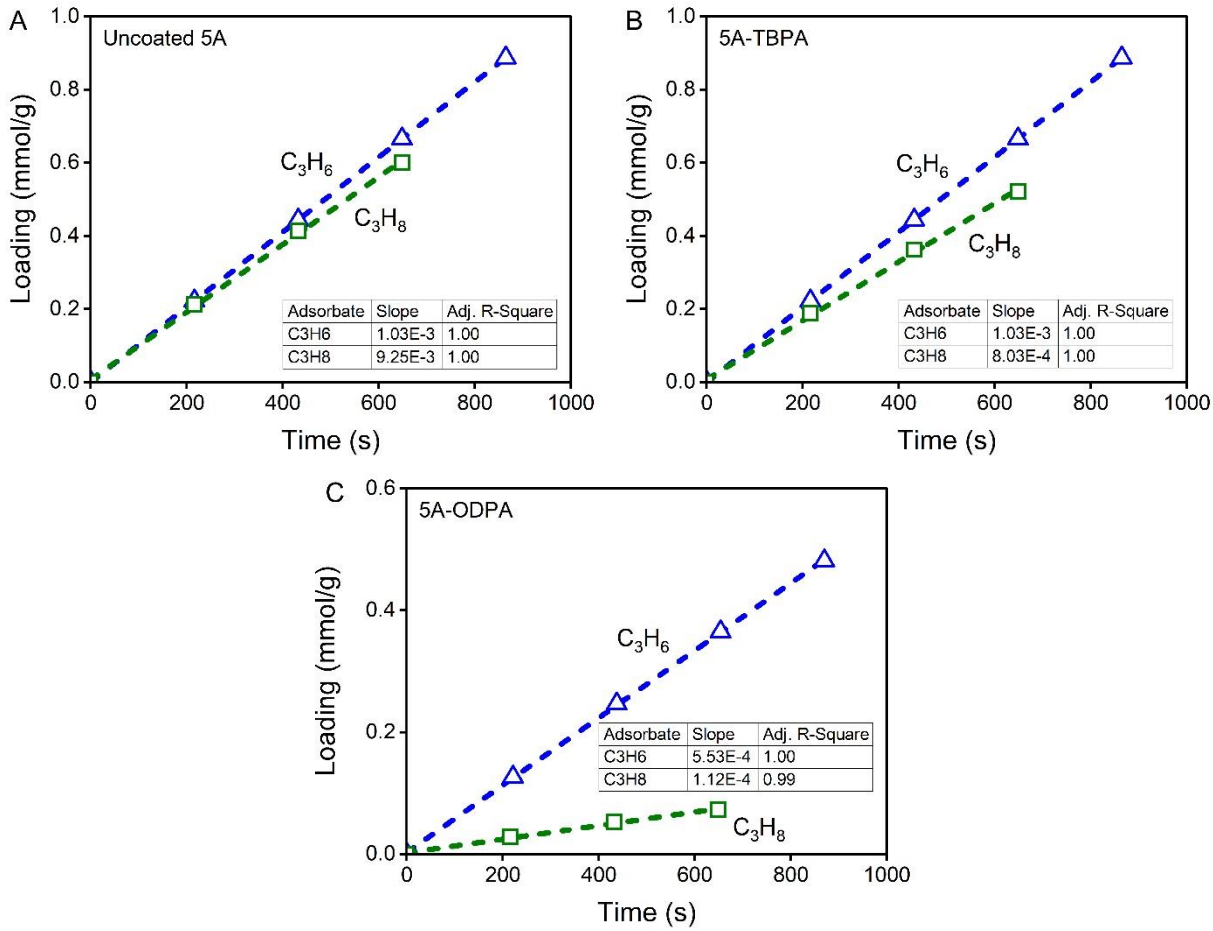

Figure B.10. Fittings for initial adsorption rates of C_3H_6 and C_3H_8 on (A) uncoated, (B) TBPA-, and (C) ODPA-coated 5A from single-gas adsorption.

Table B.2. Initial adsorption rates of C_3H_6 and C_3H_8 on uncoated, TBPA-, and ODPA-coated 5A from single-gas adsorption.

Adsorbate	Initial adsorption rate (mmol g^{-1} s^{-1})		
	Uncoated 5A	5A-TBPA	5A-ODPA
C_3H_6	1.03×10^{-3}	1.03×10^{-3} (100%*)	5.53×10^{-4} (54%)
C_3H_8	9.25×10^{-4}	8.03×10^{-4} (87%)	1.12×10^{-4} (12%)

* The percentage was the initial adsorption rate on 5A-TBPA or 5A-ODPA relative to the uncoated.

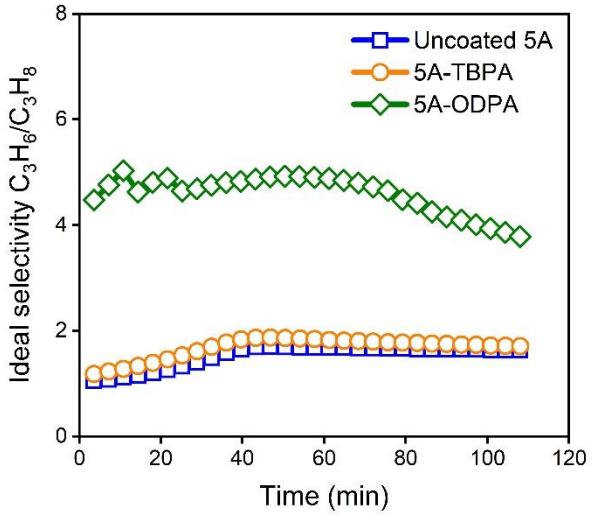

Figure B.11. Ideal selectivity of C_3H_6/C_3H_8 in single-gas adsorption on uncoated, TBPA-, and ODPA-coated zeolite 5A at 298 K as a function of adsorption time.

Table B.3. Loadings of C_3H_6 and C_3H_8 after single-gas adsorption on uncoated 5A with 30 doses (1.0 mL per dose) at 298 K under 20 SCCM of helium.

Adsorbate	Adsorption (mmol/g)	Desorption (mmol/g)
C_3H_6	2.44 ± 0.08	2.42 ± 0.05
C_3H_8	1.50 ± 0.20	1.50 ± 0.06

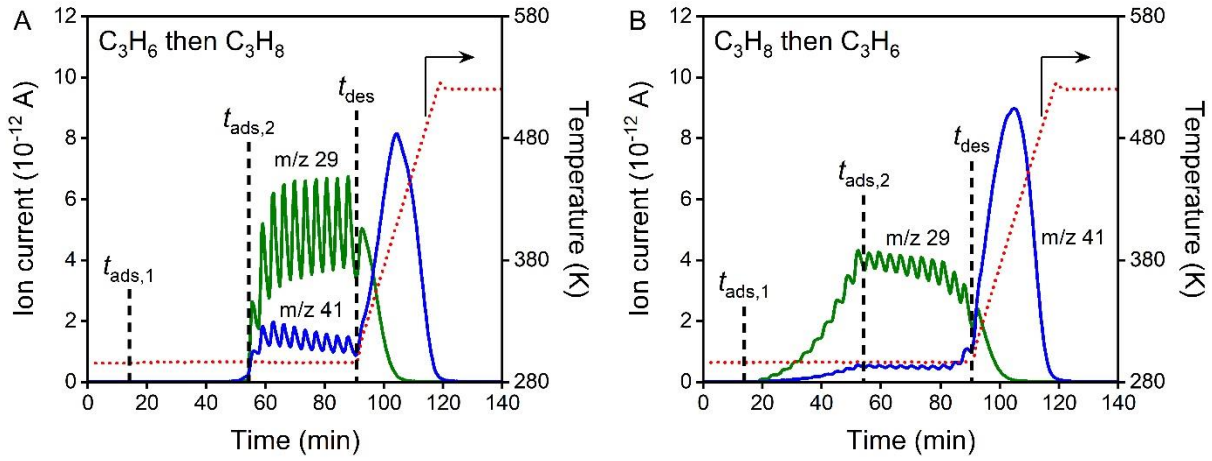

Figure B.12. Mass spectra of successive gas adsorption on uncoated zeolite 5A with (A) 10 doses (1.0 mL per dose) of C_3H_6 (start at time $t_{ads,1}$) then 10 doses of C_3H_8 (start at time $t_{ads,2}$) and (B) 10 doses of C_3H_8 then 10 doses of C_3H_6 at 298 K, followed by TPD (start at time t_{des}), under 10 SCCM of helium. The m/z fragment 29 was specific to C_3H_8, while the m/z 41 was for a fragment produced from both C_3H_6 and C_3H_8.

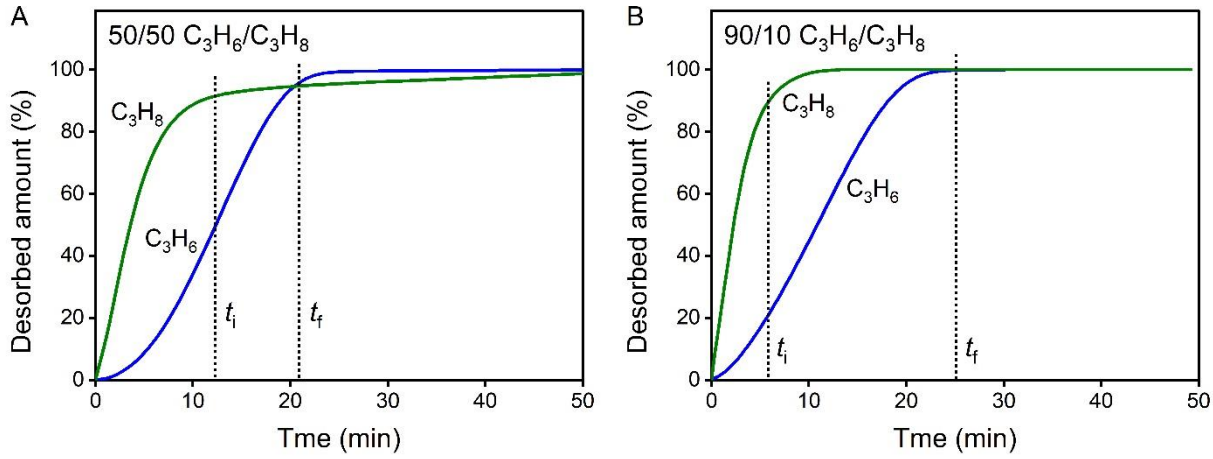

Figure B.13. Percentage of the desorbed gas after (A) equimolar and (B) 90/10 C_3H_6/C_3H_8 mixture adsorption on uncoated zeolite 5A with respect to desorption time. The desorption start time is set to 0. The collecting time for desorbed gas with high purity of C_3H_6 is represented by the interval t_i to t_f (corresponding to Fig. 3.5A3 and Fig. 3.5B3). The percentage of gas desorbed was calculated by the accumulated desorption mass over its maximum loading at the start of desorption.

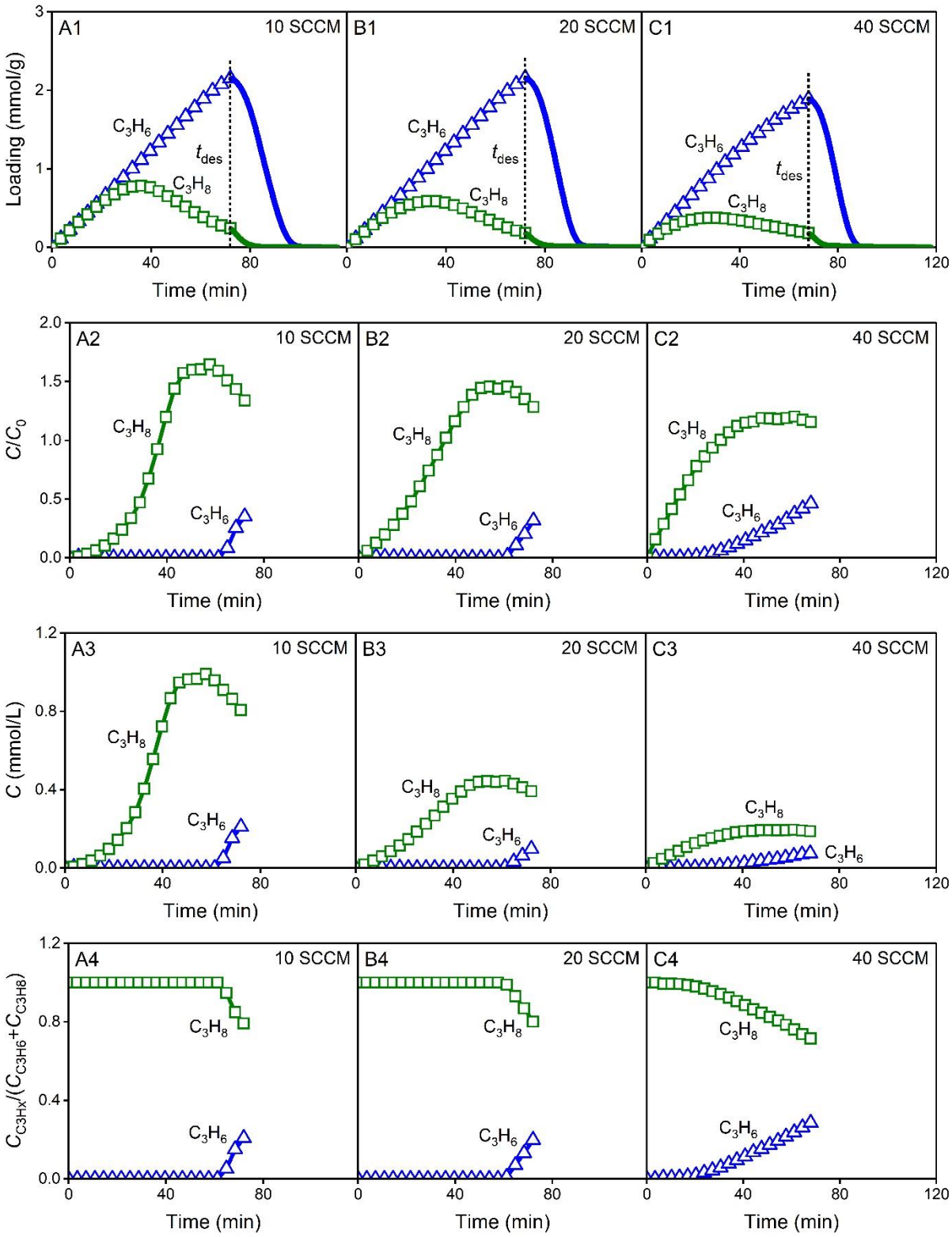

Figure B.14. Loadings of C_3H_6 and C_3H_8 in adsorption on uncoated zeolite 5A with 20 doses (1.0 mL per dose) of equimolar C_3H_6/C_3H_8 mixture at 298 K, followed by TPD (start at time t_{des}), relative concentrations C/C_0, concentrations C, and fractions $C_{C3Hx}/(C_{C3H6}+C_{C3H8})$ in adsorption under (A1–A4) 10 SCCM, (B1–B4) 20 SCCM, and (C1–C4) 40 SCCM of helium.

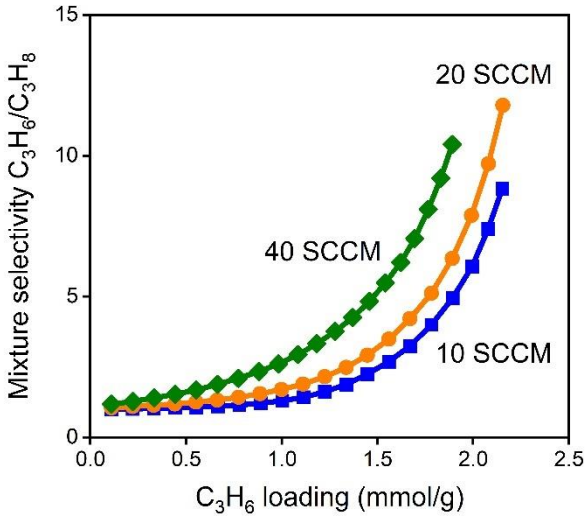

Figure B.15. Mixture adsorption selectivity versus C_3H_6 loading on uncoated zeolite 5A with 20 doses (1.0 mL for each dose) of equimolar C_3H_6/C_3H_8 mixture at 298 K under 10, 20, and 40 SCCM of helium.

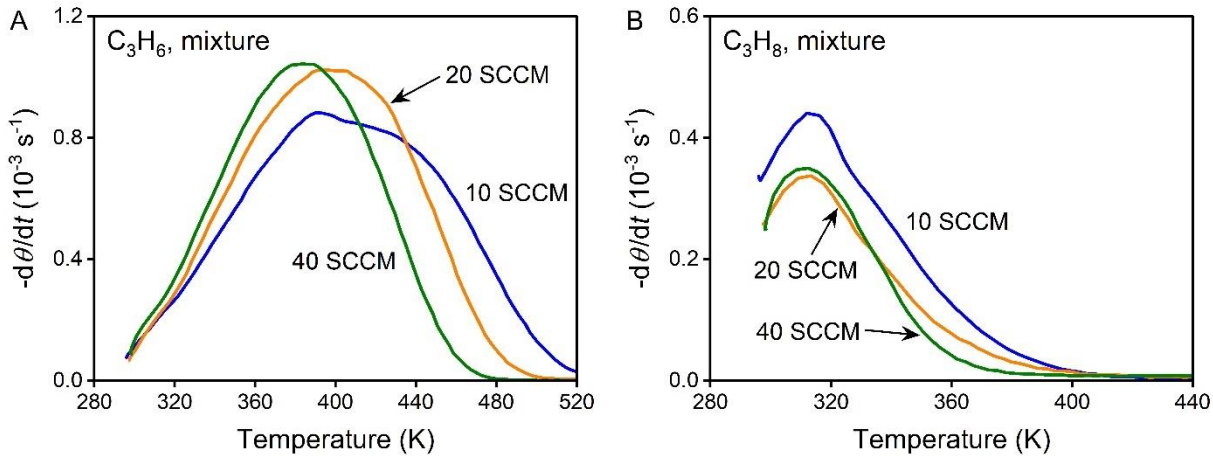

Figure B.16. TPD curves of (A) C_3H_6 and (B) C_3H_8 from uncoated zeolite 5A after adsorption at 298 K under 10, 20, and 40 SCCM of helium with 20 doses (1.0 mL per dose) of equimolar C_3H_6/C_3H_8 mixture.

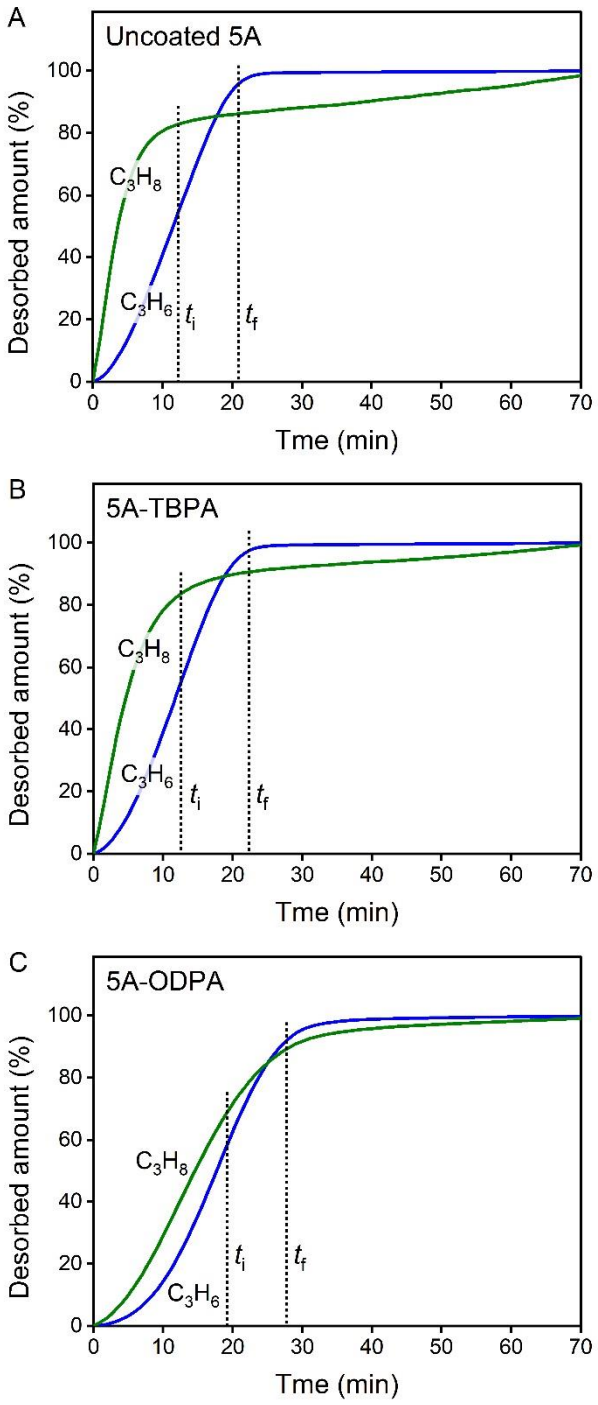

Figure B.17. Percentage of the desorbed gas from (A) uncoated, (B) TBPA-coated, and (C) ODPA-coated 5A with respect to desorption time. The desorption start time is set to 0. The collecting time for desorbed gas with high purity of C_3H_6 is represented by the interval t_i to t_f (corresponding to Fig. 3.7A3, B3, and C3). The percentage of gas desorbed was calculated by the accumulated desorption mass over its maximum loading at the start of desorption.

Table B.4. Loadings, coverages, and peak desorption temperatures of C_3H_6 after adsorption at 298 K with 5, 10, 20, 30 doses (1.0 mL per dose) of single gas on uncoated 5A.

Doses for adsorption	Loading (mmol/g)	Coverage*	Desorption peak temperature (K)
5	1.11	0.45	414
10	2.19	0.90	397
20	2.44	1.0	380
30	2.44	1.0	380

* The coverage is the ratio of the C_3H_6 loading after a certain number of gas doses to the equilibrium C_3H_6 loading.

Table B.5. Loadings, coverages, and peak desorption temperatures of C_3H_8 after adsorption at 298 K with 5, 10, 20, 30 doses (1.0 mL per dose) of single gas on uncoated 5A.

Doses for adsorption	Loading (mmol/g)	Coverage*	Desorption peak temperature (K)
5	0.92	0.61	351
10	1.35	0.90	345
20	1.48	0.99	345
30	1.50	1.0	345

* The coverage is the ratio of the C_3H_8 loading after a certain number of gas doses to the equilibrium C_3H_8 loading.

Table B.6. Loadings, coverages, and peak desorption temperatures of C_3H_6 after adsorption at 298 K with 5, 10, 20, 30 doses (1.0 mL per dose) of equimolar C_3H_6/C_3H_8 mixture on uncoated 5A.

Doses for adsorption	Loading (mmol/g)	Coverage*	Desorption peak temperature (K)
5	0.55	0.23	429
10	1.11	0.45	417
20	2.15	0.88	400
30	2.34	0.96	389

* For coverage calculation, the maximum loading of C_3H_6 in mixture adsorption is assumed to be the same as that in single-gas C_3H_6 adsorption, 2.44 mmol/g.

Table B.7. Loadings, coverages, and peak desorption temperatures of C_3H_8 after adsorption at 298 K with 5, 10, 20, 30 doses (1.0 mL per dose) of equimolar C_3H_6/C_3H_8 mixture on uncoated 5A.

Doses for adsorption	Loading (mmol/g)	Coverage*	Desorption peak temperature (K)
5	0.44	0.29	351
10	0.59	0.39	337
20	0.21	0.14	314
30	0.10	0.07	309

* For coverage calculation, the maximum loading of C_3H_8 in mixture adsorption is assumed to be the same as that in single-gas C_3H_8 adsorption, 1.50 mmol/g.

Table B.8. Loadings, coverages, and peak desorption temperatures of C_3H_6 after adsorption at 298 K with 5, 10, 20, 30 doses (1.0 mL per dose) of single gas on ODPA-coated 5A.

Doses for adsorption	Loading (mmol/g)	Coverage*	Desorption peak temperature (K)
5	0.58	0.24	455
10	1.07	0.44	446
20	1.87	0.77	423
30	2.20	0.90	417

* For coverage calculation, the maximum loading of C_3H_6 in single-gas adsorption on ODPA-coated 5A is assumed to be the same as that on uncoated 5A, 2.44 mmol/g.

Table B.9. Loadings, coverages, and peak desorption temperatures of C_3H_8 after adsorption at 298 K with 5, 10, 20, 30 doses (1.0 mL per dose) of single gas on ODPA-coated 5A.

Doses for adsorption	Loading (mmol/g)	Coverage*	Desorption peak temperature (K)
5	0.15	0.10	428
10	0.26	0.17	429
20	0.47	0.31	429
30	0.58	0.39	435

* For coverage calculation, the maximum loading of C_3H_8 in single-gas adsorption on ODPA-coated 5A is assumed to be the same as that on uncoated 5A, 1.50 mmol/g.

Table B.10. Loadings, coverages, and peak desorption temperatures of C_3H_6 after adsorption at 298 K with 5, 10, 20, 30 doses (1.0 mL per dose) of equimolar C_3H_6/C_3H_8 mixture on ODPA-coated 5A.

Doses for adsorption	Loading (mmol/g)	Coverage*	Desorption peak temperature (K)
5	0.29	0.12	466
10	0.55	0.23	463
20	1.07	0.44	446
30	1.50	0.61	435

* For coverage calculation, the maximum loading of C3H6 in mixture adsorption on ODPA-coated 5A is assumed to be the same as that in single-gas C3H6 adsorption on uncoated 5A, 2.44 mmol/g.

Table B.11. Loadings, coverages, and peak desorption temperatures of C_3H_8 after adsorption at 298 K with 5, 10, 20, 30 doses (1.0 mL per dose) of equimolar C_3H_6/C_3H_8 mixture on ODPA-coated 5A.

Doses for adsorption	Loading (mmol/g)	Coverage*	Desorption peak temperature (K)
5	0.06	0.04	438
10	0.09	0.06	429
20	0.17	0.11	409
30	0.21	0.14	394

* For coverage calculation, the maximum loading of C_3H_8 in mixture adsorption on ODPA-coated 5A is assumed to be the same as that in single-gas C_3H_8 adsorption on uncoated 5A, 1.50 mmol/g.

Appendix C: Supplement to Chapter 4

Table C.1. Concentrations of NH_2C_3PA in THF to prepare PA coatings with different coverages on zeolite 5A.

NH_2C_3PA coverage (monolayer)	NH_2C_3PA concentration in THF (mmol/L)
1	10*
0.8	0.68
0.2	0.14
0.1	0.08
0.04	0.03
0.02	0.02

* Twelve times more PA than the theoretical amount was used to form a full monolayer.

Table C.2. Concentrations of ODPA in THF to prepare PA coatings with different coverages on zeolite 5A.

ODPA coverage (monolayer)	ODPA concentration in THF (mmol/L)
1	10*
0.9	0.75
0.8	0.67
0.6	0.50
0.4	0.34
0.2	0.13

* Twelve times more PA than the theoretical amount was used to form a full monolayer.

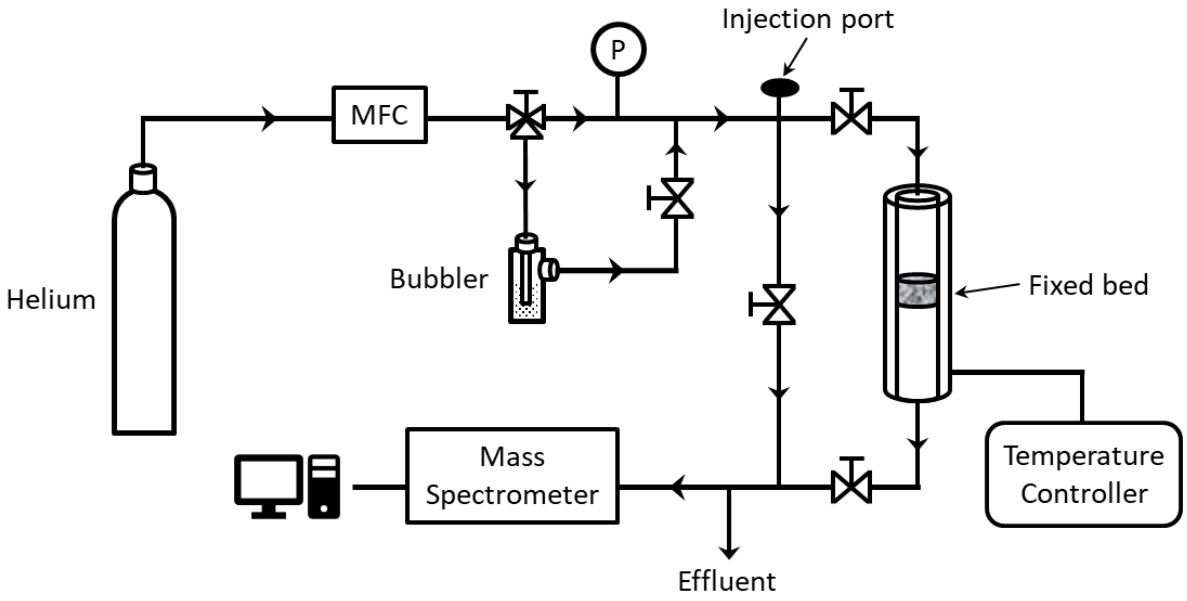

Figure C.1. Schematic illustration of the apparatus for propylamine adsorption and TPD measurements.

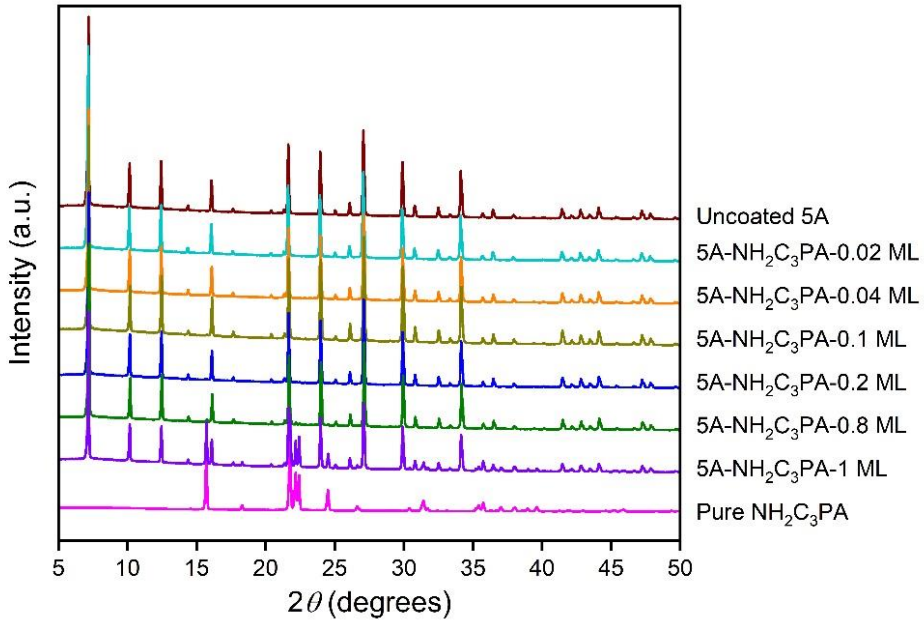

Figure C.2. XRD patterns of uncoated 5A and the 5A coated with different coverage of NH_2C_3PA.

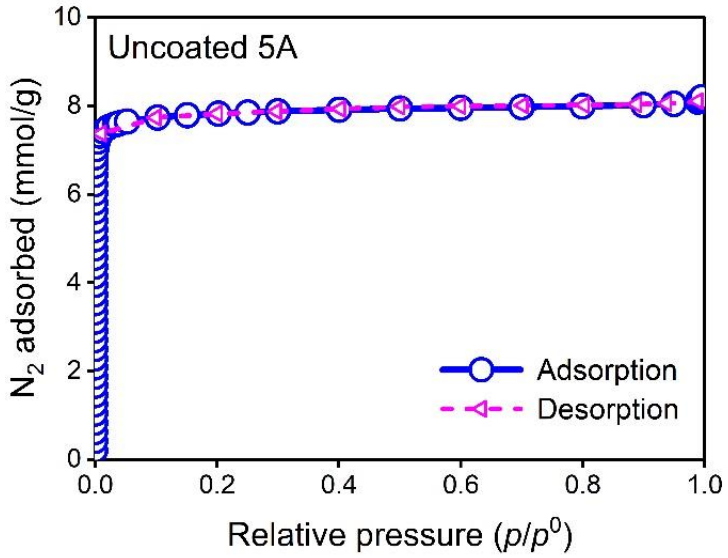

Figure C.3. Nitrogen ad/desorption isotherms at 77 K on uncoated zeolite 5A.

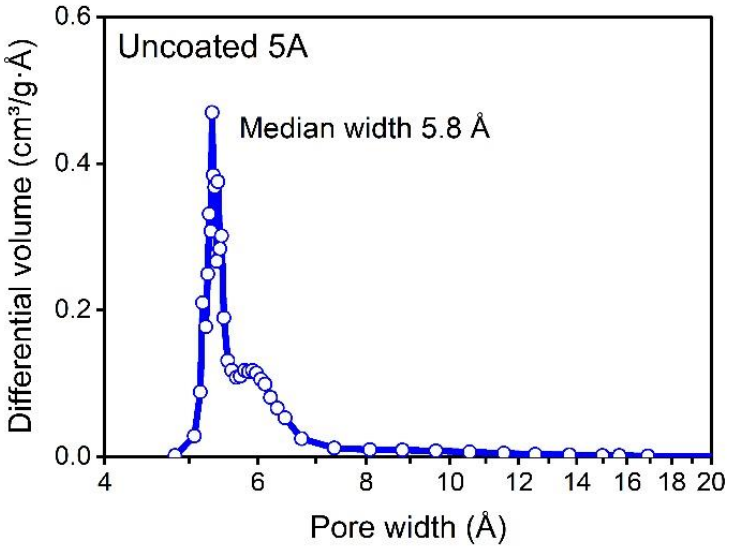

Figure C.4. Micropore size distribution of uncoated zeolite 5A determined with the Horvath-Kawazoe (HK) method.

A

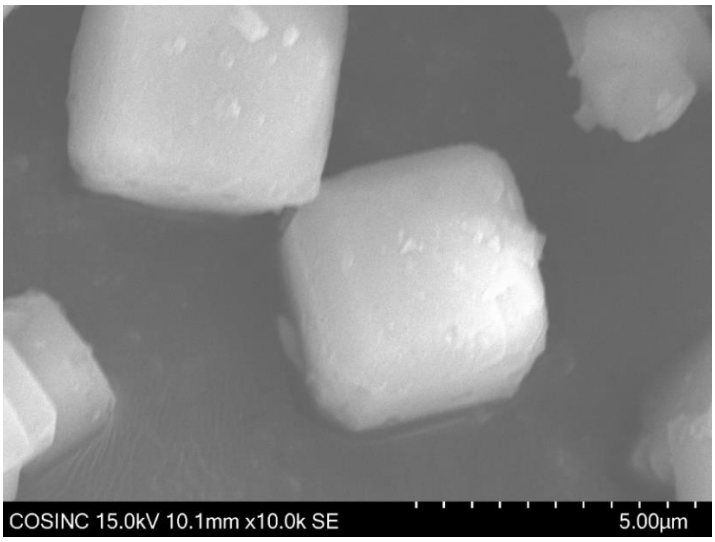

B

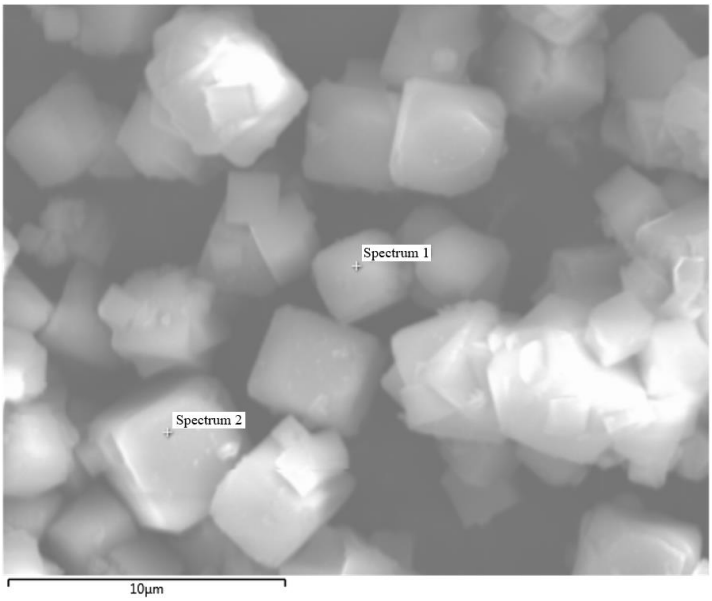

Figure C.5. SEM images of zeolite 5A-ODPA: scale bar of (A) 5 µm and (B) 10 µm.

Table C.3. Elemental composition of zeolite 5A-ODPA measured by SEM-EDS.

Element	Weight % *
Si	17.4
Al	17.0
O	46.4
Ca	8.5
Na	4.1
C	6.6

* The weight percent of element was obtained by averaging the compositions of "spectrum 1" and "spectrum 2" points marked in SEM image (Fig. C.5B). The content of phosphorus was below the detection limit of EDS, 1 wt%.

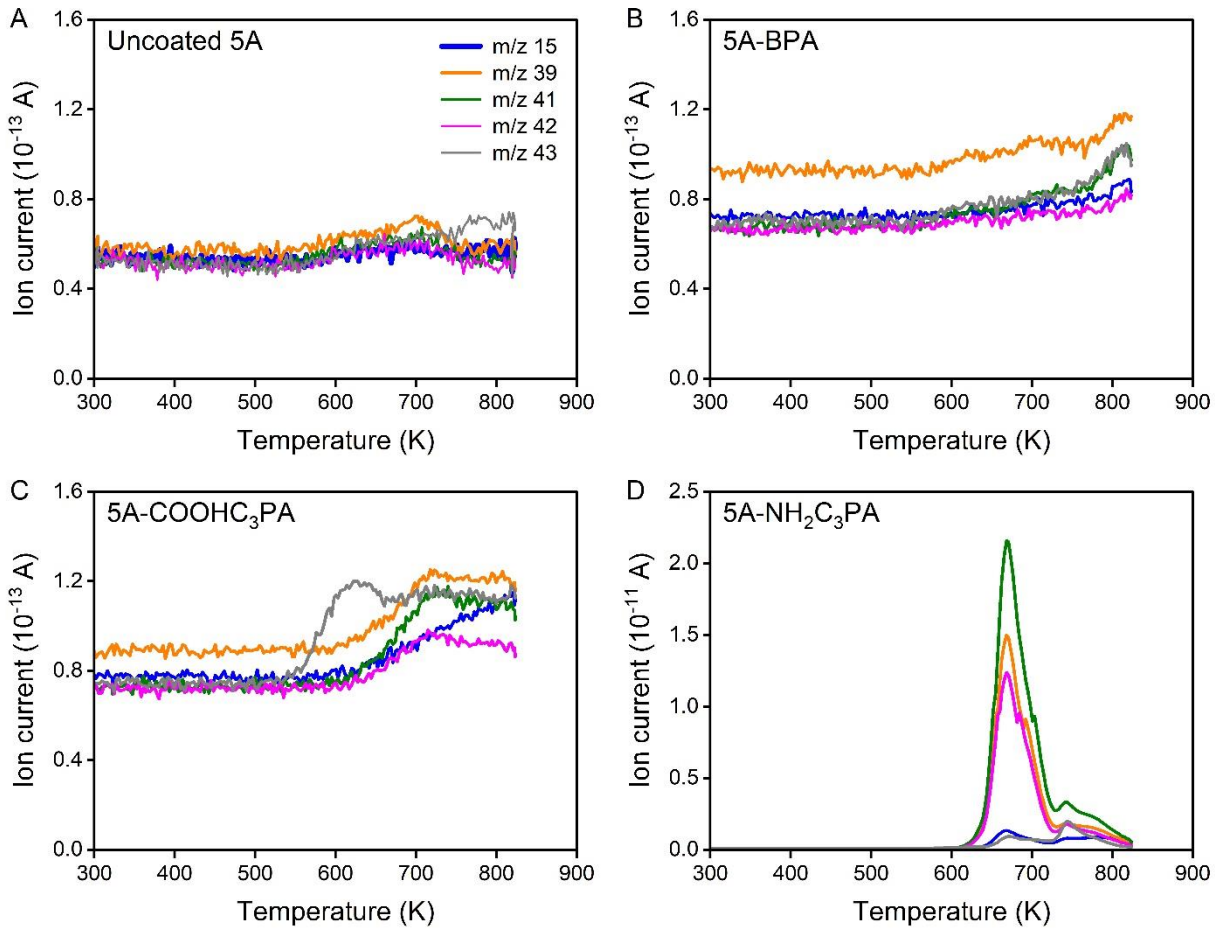

Figure C.6. TPD profiles of (A) uncoated, (B) BPA-, (C) $COOHC_3PA$-, and (D) NH_2C_3PA-coated zeolite 5A. The samples were pretreated at 523 K under 20 SCCM helium for 2 h prior to heating from 298 K to 823 K with ramp 8 K/min under 20 SCCM helium. The PA coatings were from saturating depositions of monolayers.

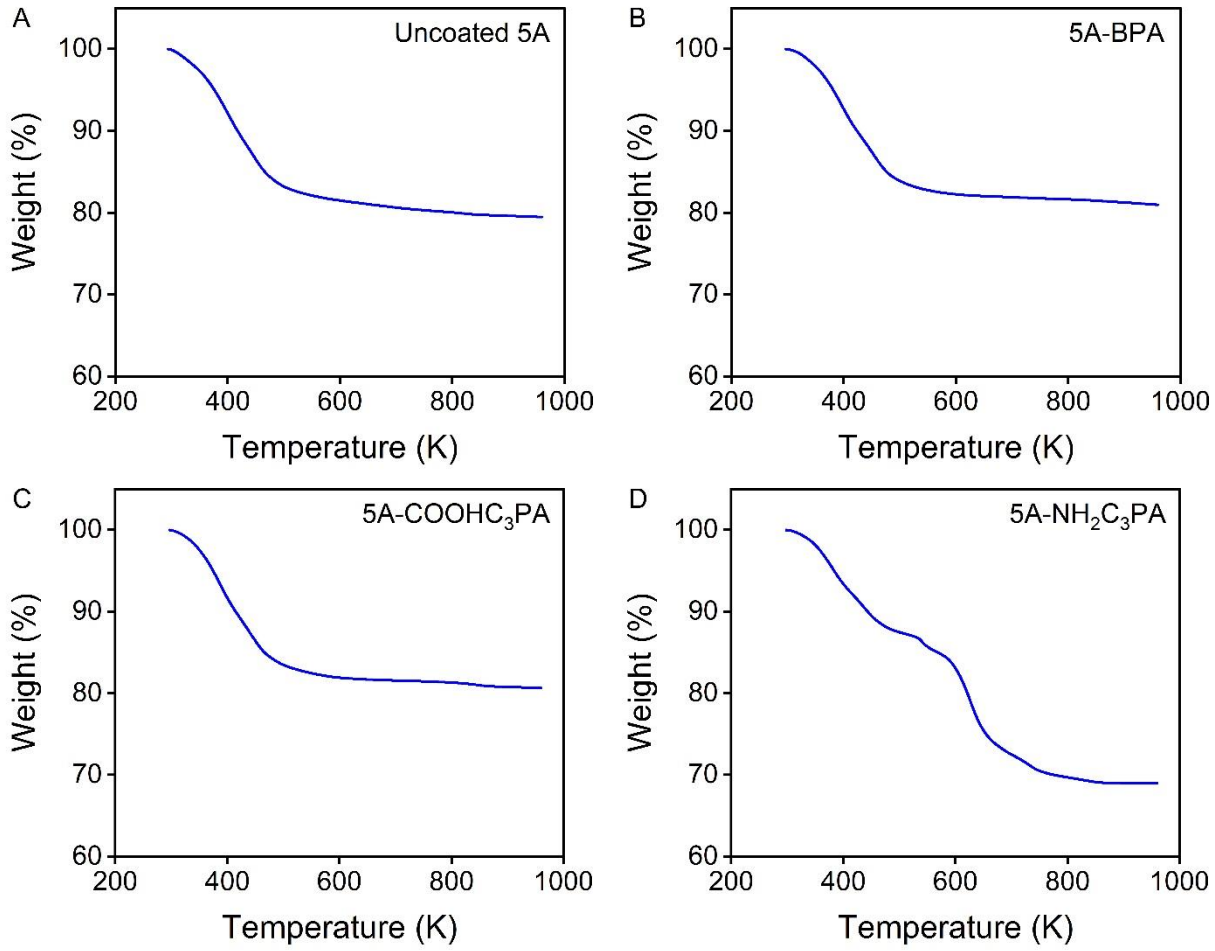

Figure C.7. TGA curves of (A) uncoated, (B) BPA-, (C) $COOHC_3PA$-, and (D) NH_2C_3PA-coated zeolite 5A. The PA coatings were from saturating depositions of monolayers.

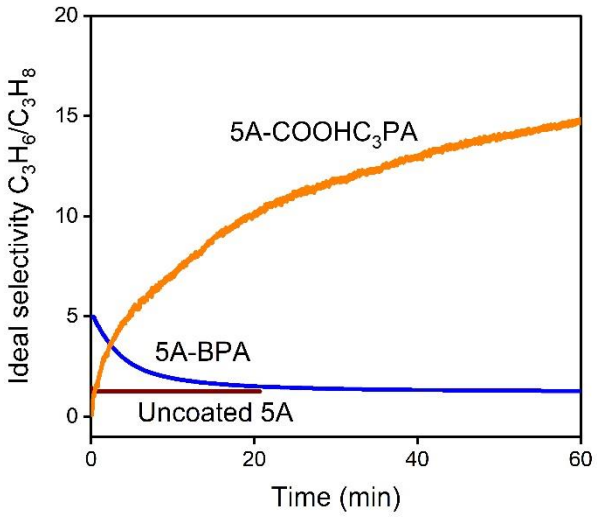

Figure C.8. Ideal selectivities of C_3H_6/C_3H_8 on uncoated, BPA-, and $COOHC_3PA$-coated zeolite 5A at 298 K. The PA coatings were from saturating depositions of monolayers.

Table C.4. Initial fractional rates of C_3H_6 adsorption at different temperatures on zeolite 5A coated with ODPA and $COOHC_3PA$ from saturating depositions of monolayers.

Temperature (K)	C_3H_6 initial rate (min^{-1})	
	5A-ODPA	5A-$COOHC_3PA$
298	0.33	0.0039
373	0.31	0.0071
423	0.29	0.010

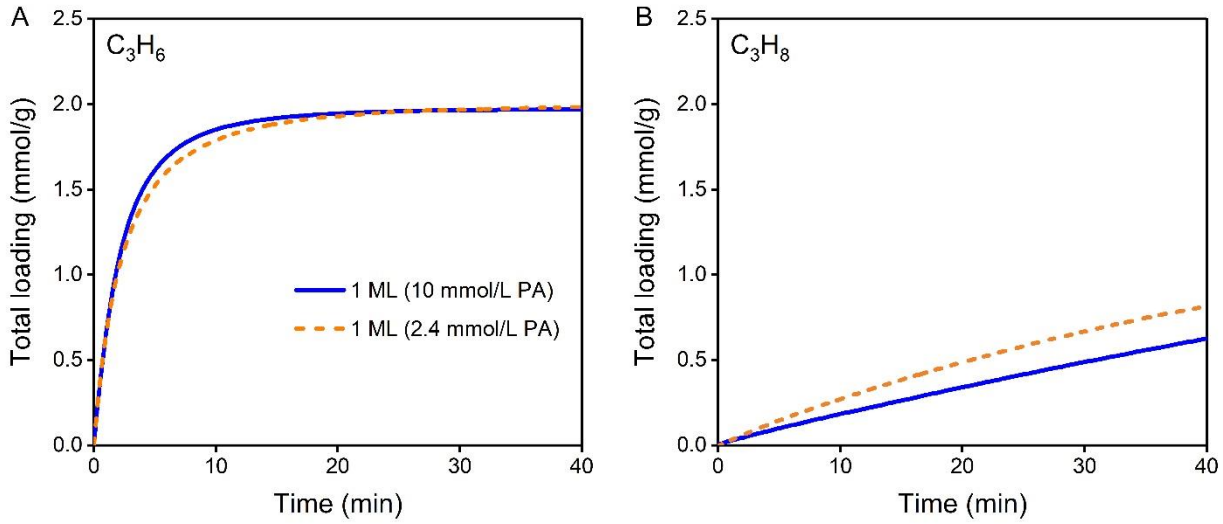

Figure C.9. Loadings of (A) C_3H_6 and (B) C_3H_8 in single-gas pressure-decay adsorption at 298 K on zeolite 5A coated with a full monolayer of ODPA using 10 or 2.4 mmol/L of PA (12 or 3 times the theoretical amount needed to form a full monolayer) in THF solvent for the deposition.

Table C.5. Initial fractional rates of C_3H_6 adsorption at different temperatures on zeolite 5A coated with 0.1 ML NH_2C_3PA.

Temperature (K)	C_3H_6 initial rate (min^{-1})
298	0.027
323	0.073
373	0.088

Appendix D: Supplement to Chapter 5

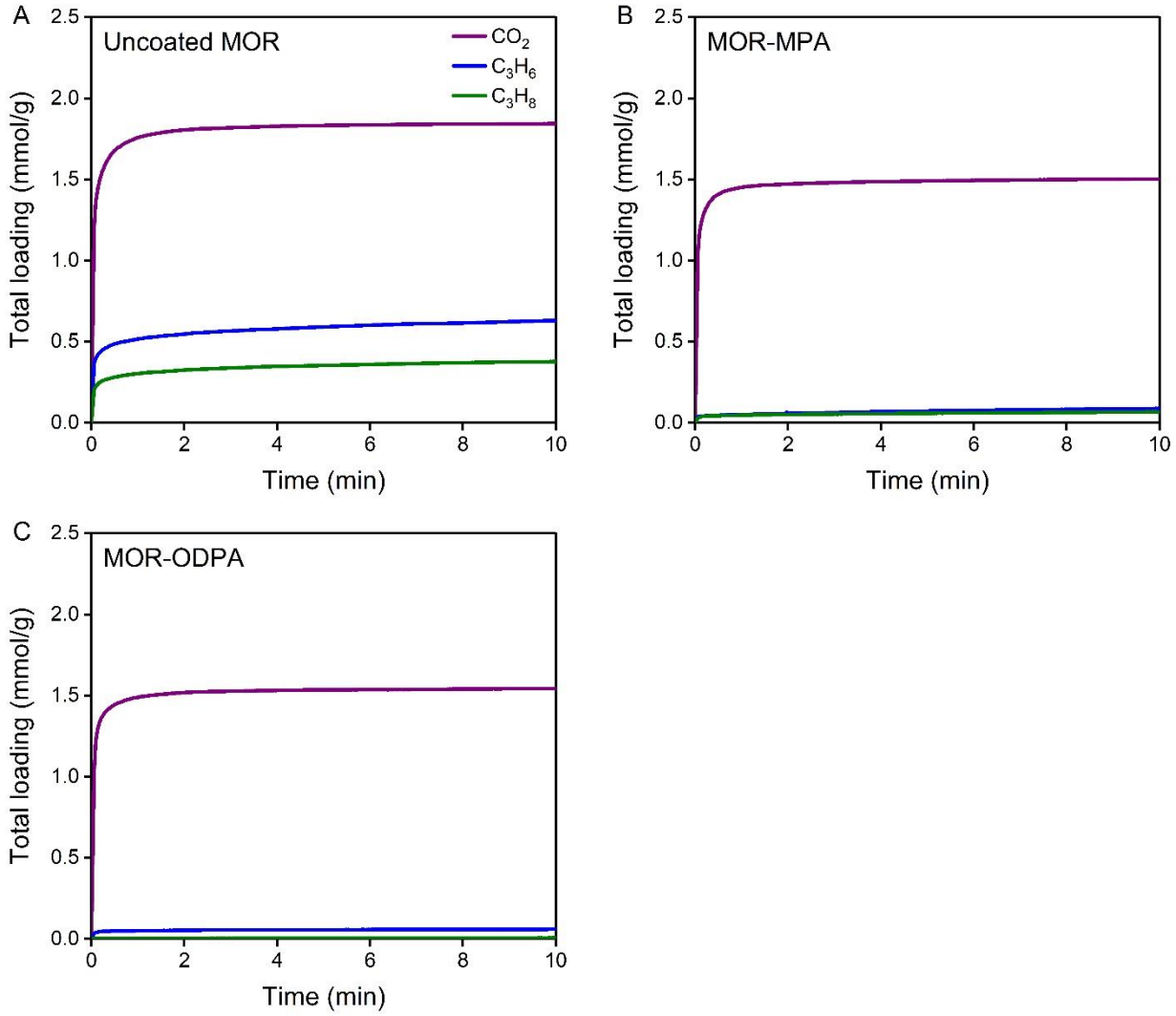

Figure D.1. Loadings of CO_2, C_3H_6, and C_3H_8 single-gas adsorption at 298 K on (A) uncoated, (B) MPA-, and (C) ODPA-coated zeolite MOR.

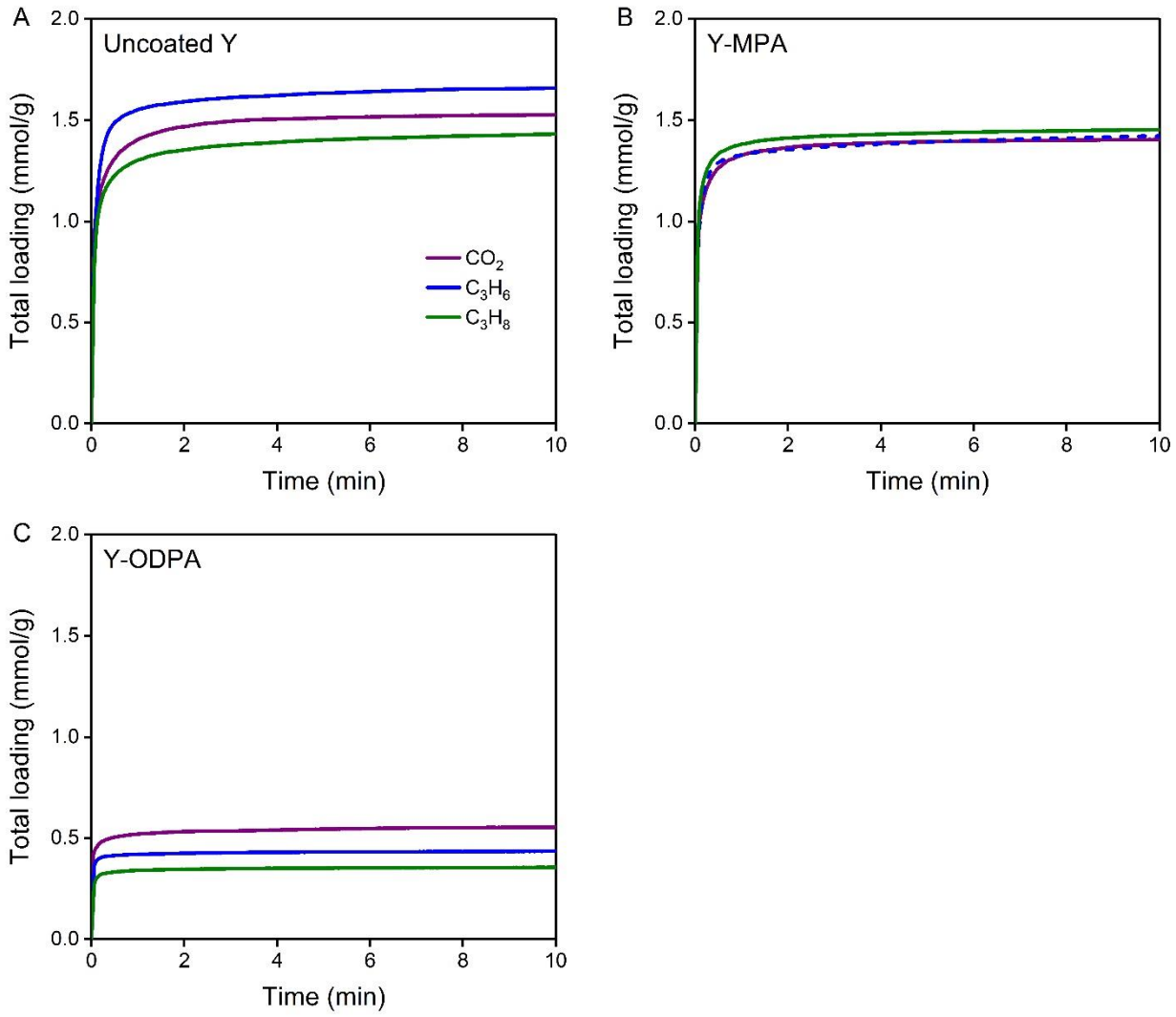

Figure D.2. Loadings of CO_2, C_3H_6, and C_3H_8 single-gas adsorption at 298 K on (A) uncoated, (B) MPA-, and (C) ODPA-coated zeolite Y.